2013

Development of Procedures for Accurate Finite Element Modeling of the Dynamic and Quasi-Static Performance of Automotive Chassis Components Incorporating Hyperelastic Materials

Matthew Bondy
University of Windsor

Development of Procedures for Accurate Finite Element Modeling of the Dynamic and Quasi-Static Performance of Automotive Chassis Components Incorporating Hyperelastic Materials

by

Matthew Bondy

A Thesis
Submitted to the Faculty of Graduate Studies
through Mechanical, Automotive, and materials Engineering
in Partial Fulfillment of the Requirements for
the Degree of Master of Applied Science at the
University of Windsor

Windsor, Ontario, Canada

2012

Development of Procedures for Accurate Finite Element Modeling of the Dynamic and Quasi-Static Performance of Automotive Chassis Components Incorporating Hyperelastic Materials

by

Matthew Bondy

APPROVED BY:

_____

Dr. Faouzi Ghrib
Department of Civil and Environmental Engineering

_____

Dr. Daniel Green
Department of Mechanical, Automotive and Materials Engineering

_____

Dr. William Altenhof, Advisor
Department of Mechanical, Automotive and Materials Engineering

_____

Dr. Andrzej Sobiesiak, Chair of Defense
Department of Mechanical, Automotive and Materials Engineering

January 22, 2013

Declaration of Originality

I hereby certify that I am the sole author of this thesis and that no part of this thesis has been published or submitted for publication.

I certify that, to the best of my knowledge, my thesis does not infringe upon anyone's copyright nor violate any proprietary rights and that any ideas, techniques, quotations, or any other material from the work of other people included in my thesis, published or otherwise, are fully acknowledged in accordance with the standard referencing practices. Furthermore, to the extent that I have included copyrighted material that surpasses the bounds of fair dealing within the meaning of the Canada Copyright Act, I certify that I have obtained a written permission from the copyright owner(s) to include such material(s) in my thesis and have included copies of such copyright clearances to my appendix.

I declare that this is a true copy of my thesis, including any final revisions, as approved by my thesis committee and the Graduate Studies office, and that this thesis has not been submitted for a higher degree to any other University or Institution.

Abstract

Finite element models of the vehicle for crashworthiness have traditionally included simplified representations of isolators intended to improve noise and vibration. However, the low stiffness of the hyperelastic material employed in such components allows for large deformations under impact conditions with a significant effect upon the accelerations experienced by the occupant. Modeling these components is challenging due to the non-linear behaviour of the material and the large deformations. The purpose of this research was to identify practices for developing accurate and efficient finite element models of chassis components incorporating hyperelastic materials. To maximize the comprehensiveness of this process, this research included quasi-static and dynamic material characterization; material model selection and implementation; finite element modeling techniques; quasi-static and dynamic component characterization; and model validation. Conclusions included the importance of comprehensive material characterization, material model selection, variation in results due to solver updates, and methodologies for model validation through component characterization.

Dedication

Dedicated to my parents and grandparents.

Acknowledgements

This research was associated with the double degree University of Windsor and Politecnico di Torino program supported by FIAT-Chrysler. I worry that it may be impossible to acknowledge everyone involved in organizing this program, the following is likely a partial list. At the Politecnico di Torino Dr. Giovanni Belingardi, Dr. Giancarlo Genta, and Raffaella Fiora were incredibly helpful and went out of their way to make myself and the other Canadians feel more than welcome. I would like to thank, in particular, Dr. Belingardi, as one my supervisors, for providing invaluable advice. Another individual at the Politecnico, Lorenzo Peroni, deserves special recognition for the significant investment of time to provide a great deal of assistance with this research. I would also like to thank Professor Donato Firrao for finding us a place to stay in Collegio Valentino.

FIAT engineers Massimo Barbi (Centro Ricerche FIAT) and Paolo Chiappero (Mirafiori FIAT polymer laboratory) provided invaluable advice and assistance with this research. The experience gained working with these individuals and their co-workers will undoubtedly be of great benefit to me in my future career. Several Chrysler engineers are equally deserving of my sincere gratitude. Mohammed Malik provided significant organizational and technical assistance from the Automotive Research and Development Center in Windsor. Dr. Sae Park and Hamid Keshtkar, crashworthiness engineers at Chrysler Technical Center, were a pleasure to work with and very supportive. At the University of Windsor I would like to thank Mike Houston for his advice before, throughout, and after the trip overseas. Dr. Peter Frise and Jan Stewart are forever owed a debt of gratitude for their work in developing this program and providing a great deal of support. To my Canadian advisor, Dr. William Altenhof, thank you. I was very fortunate to have such a dedicated advisor.

Contents

List of Figures

List of Tables

List of Abbreviations, Symbols, Nomenclature

AMD	Advanced Micro Devices
BOF	Body on frame
CAD	Computer aided design
CAE	Computer aided engineering
CDC	Center for disease control
CPU	Central processing unit
CTC	Chrysler Technical Center
DP	Double precision
EFG	Element free Galerkin
EPDM	Ethylene propylene diene monomer
EuroNCAP	European New Car Assessment Program
FE	Finite element
FIAT	Fabbrica Italiana Automobili Torino
GHz	Gigahertz
GPa	Gigapascal
GTM	Gassmann Theiss Messtechnik
IIHS	Insurance Institute for Highway Safety
ISO	International Organization for Standardization
LSTC	Livermore Software Technology Corporation
mm	Millimeter
MPa	Megapascal
MPP	Massively parallel processing
N	Newton
NCAP	New Car Assessment Program
NI	National Instruments
NVH	Noise, vibration, and harshness
PdT	Politecnico di Torino
PSSF	Penalty stiffness scaling factor
RAM	Random access memory

SHPB	Split Hopkinson pressure bar
SMP	Shared memory parallel
SP	Single precision
TSSF	Time step scaling factor
USB	Universal serial bus
WHO	World Health Organization

List of Nomenclature

$F_{excitation}$	Force exerted by the powertrain on the powertrain suspension
m_{engine}	Mass of the powertrain
x	Displacement of the powertrain
c_{mount}	Damping of the powertrain suspension
k_{mount}	Stiffness of the powertrain suspension
w	Excitation frequency of the powertrain
w_n	Natural frequency of the powertrain suspension
$F_{chassis}$	Force exerted by the powertrain suspension on the chassis
T	Powertrain suspension force transmissibility
s	Laplace variable
ζ	Damping ratio of the powertrain suspension
s^*	Laplace variable normalized with respect to the powertrain suspension natural frequency
m	Mass
c	Damping
k	Stiffness
F_{ext}	External Forces
Δt	Explicit time integration critical time step
M_1	Discrete element nodal mass
M_2	Discrete element nodal mass
L	Element length
ρ	Material density
E	Elastic modulus
ν	Poisson's ratio
λ_x	Stretch ratio in the x-direction
L_o	Initial element length
δ	Element deformation
ε_x	Strain in the x-direction
ε_y	Strain in the y-direction

ε_z	Strain in the z-direction
σ_x	Normal stress in the x-direction
σ_y	Normal stress in the y-direction
σ_z	Normal stress in the z-direction
τ_{xy}	Shear stress in the y-direction on a plane with a normal in the x-direction
τ_{xz}	Shear stress in the z-direction on a plane with a normal in the x-direction
τ_{yz}	Shear stress in the z-direction on a plane with a normal in the y-direction
W	Strain energy density
C_1	Mooney material model constant
C_2	Mooney material model constant
λ_1	Stretch ratio in the first principal direction
λ_2	Stretch ratio in the second principal direction
λ_3	Stretch ratio in the third principal direction
I_1	First stretch ration invariant
I_2	Second stretch ratio invariant
I_3	Third stretch ratio invariant
b_j	Ogden material model parameters
c_j	Ogden material model parameters
C_{100}	Frazer-Nash material model coefficient
U	Strain energy density
$N_i(x)$	Lagrange interpolation function
$w(x)$	Beam element deflection
$\Psi(x)$	Beam element angle of deflection
s_i	Angle of deflection of beam at node i
w_i	Deflection of beam at node i
x_A	Axial position on beam of node A
x_B	Axial position on beam of node B

δ_1	Deformation in the first principal direction
δ_2	Deformation in the second principal direction
δ_3	Deformation in the third principal direction
S	Simple tension stress
$S_{Pure\ shear}$	Pure shear (planar tension) stress
$S_{Biaxial}$	Equibiaxial tension radial stress
V	Error metric proposed by Oberkampf and Trucano
y	Numerical data being validated
Y	Experimental data for model validation
Z_{Bar}	Mechanical impedance of a bar of a split bar apparatus
A_{Bar}	Cross sectional area of bar of a split bar apparatus
C_{Bar}	Speed of sound in bar material
E_{Bar}	Elastic modulus of bar material
ρ_{Bar}	Density of bar material
$T_{Incident}$	Time duration of the incident pulse
$L_{Striker}$	Length of the striker bar
$C_{Striker}$	Speed of sound in the striker bar material
$\sigma_{Incident}$	Stress magnitude of the incident pulse
$v_{Striker}$	Velocity of the striker bar
$\varepsilon_{Incident}$	Strain magnitude of the incident pulse
$\varepsilon_{Reflected}$	Strain magnitude of the reflected pulse
$\varepsilon_{Transmitted}$	Strain magnitude of the transmitted pulse
v_1	Velocity of the surface of the input bar at the input bar-specimen interface
v_2	Velocity of the surface of the output bar at the specimen-output bar interface
$L_{Specimen}$	Length of the split Hopkinson pressure bar specimen
$\sigma_{Uniaxial}$	Uniaxial stress (simple tension and compression)
$\varepsilon_{Uniaxial}$	Uniaxial strain (simple tension and compression)
$\sigma_{Pure\ shear}$	Pure shear (planar tension) stress

$\sigma_{Equibiaxial}$	Equibiaxial tension radial stress
$\sigma_{Simple\ compression}$	Simple compression stress
$\varepsilon_{Equibiaxial}$	Equibiaxial tension radial strain
$\sigma_{Fixture}$	Approximate maximum stress in steel plates of fixture
M	Moment applied to beam approximation of fixture
c	Thickness of beam approximation of fixture plate
I	Moment of area of fixture plate
$\sigma_{Bolt\ preload}$	Approximation of stress in fixture plate due to bolt preload
$F_{Bolt\ preload}$	Fixture bolt preload
$r_{washer\ inner}$	Inner radius of fixture bolt washer
$r_{washer\ outer}$	Outer radius of fixture bolt washer

Chapter 1: Introduction

From 2011 to 2020 the United Nations General Assembly has instituted a Decade of Action for Road Safety. This initiative seeks to save 5 million lives over this ten year period (WHO, 2011). It is estimated that over 1 million fatalities and 50 million injuries occur each year worldwide as a result of motor vehicle incidents (WHO, 2004). Over the next 20 years these figures are projected to increase by 65%. In the USA motor vehicle incidents are the leading cause of death in the 5-34 age group (CDC, 2010) with over 2.3 million motor transport incident related admissions to emergency departments in 2009 (CDC, 2011). Crash related fatalities in 2005 cost an estimated $41 billion in medical costs and work loss.

Vehicle collisions are the second leading cause of death in Canada and the third leading cause of both hospitalizations and disabilities (SMARTRISK, 2009). The economic impact of transportation incidents is staggering at approximately $4 billion each year. Additionally, injuries resulting from transportation incidents are the leading cause of economic losses in the form of reduced productivity. Consistent with North America, in the European Union road traffic incidents are the leading cause of death for the population under 45 years of age (Genta G, 2009). Government crashworthiness standards dictate impact performance requirements and are consistently updated to ensure improved protection of the occupant. Additionally, in the USA the new car assessment program (NCAP) and the insurance institute for highway safety (IIHS) rate vehicles on their impact performance and this data is provided to consumers to consider when purchasing a vehicle.

Safety may be one of the more important vehicle characteristics for consumers considering the purchase of a new vehicle. A study in Europe found that European New Car Assessment Program (EuroNCAP) ratings and safety related features were the highest priorities among consumers that had recently purchased a new vehicle (Koppel S, 2008). This study was completed using questionnaires in Sweden, a European country with a low number of fatalities resulting from transport incidents, and telephone interviews in Spain, a European country with a high number of deaths from transport

incidents. In Sweden potential participants with a recent new vehicle purchase were identified through insurance records. A consulting group in Spain conducted telephone interviews. Eligibility criteria for the telephone interviews were defined by the demographics of the Swedish participants.

Other important considerations for consumers are ride quality and levels of noise, harshness, and vibration (NVH). A variety of elastomeric materials are used in vehicles as isolators, dampers, and mounts between body and frame, on the engine cradle, etc. These flexible isolators are mainly made of rubber and other polymeric materials. They are usually enclosed in a metallic tube to protect and contain the flexible elements. These components are critical components of modern vehicles because of their effect on the perceived quality in terms of ride and NVH.

The term crashworthiness originated in the aerospace industry in the 1950s. In the automotive industry this term refers to the design of a vehicle's structure to deform in a controlled manner in a crash and absorb energy to protect the occupants. There are several requirements in designing a vehicle for crashworthiness. The passenger compartment must be stiff to prevent harmful intrusions. However, there must be zones where structural elements, crash boxes for example, can dissipate energy through progressive deformation reducing accelerations experienced by the occupant to tolerable levels. Additionally, the fuel system must be protected and the roof must be structurally sound in rollover type events.

The connections between the car body and subframe may have a significant effect on the impact performance of modern vehicles. These connections consist of a bolt in a rubber bushing which is commonly contained in a metal tube. As an example of the importance of these connections, the occupant compartment, as part of the automotive body, may be connected to a front subframe by connections of this type. By allowing relative displacement between the occupant compartment and the front subframe, which is designed to manage energy in a frontal crash, the accelerations experienced by the occupant may be influenced by these connections. However, the rubber components are difficult to implement in computer models of the full vehicle.

Similar rubber components can also be found in the engine mounts and chassis suspension connections. Researchers at Ford Motor Company have documented the importance of suspension lower control arm bushings on the impact performance of the vehicle (Eguia M H. M., 2005). In many computer models the suspension connections are rigid body joints (e.g. spherical, revolute, and cylindrical joints). Another common technique to model these rubber components replaces the component with discrete spring and damper elements (Park S, 2004). However, these approaches result in a model that may not be suitable for the complex loading resulting from an impact. Additionally, the resulting models are poor predictors of failure modes and may give misleading results in the design phase. Airbag deployment strategies for low speed impacts may also be affected.

However, modeling the mechanical behaviour of rubber is difficult due to the nonlinear properties of the material and the large deformations that are commonly encountered with rubber components. The structural finite element (FE) method solves partial differential equations of motion coupled with mechanical material behaviour over a discretized domain (elements). For nearly incompressible materials (e.g. rubber) a problem known as element locking can introduce error into the model in the form of increased element stiffness reducing the level of deformation for a given load.

The purpose of this research was to develop methodologies for modelling components employing hyperelastic materials. A primary consideration was the application: full vehicle models for crashworthiness assessment and design. These methodologies were developed through extensive parametric studies of modelling techniques. Furthermore, material characterization was performed to obtain suitable, high quality material data and to start from the most fundamental stage of the modeling process to have a thorough understanding of the many factors and their interdependence. Ultimately, this research concluded with quasi-static and dynamic experimental characterization of a Chrysler engine mount and model validation.

This thesis documents this research as follows. A literature review summarizes fundamental knowledge for the completion of the methodology of this work as well as recent or important contributions to scientific and engineering literature on the topic of the crash performance influence of rubber noise and vibration isolators. This is followed by a detailed description of the methodology for this research. The corresponding results are presented for each step of the methodology. Finally, these results are discussed and conclusions are stated. Appendices for important but verbose data and resources are provided at the end of the document.

Chapter 2: Literature Review

2.1 Powertrain Suspension

The most important chassis isolators for noise and vibration may be those supporting the powertrain. These components may also have critical roles to play in vehicle crashworthiness. The frequency range of the dynamic excitation of the chassis by the powertrain is directly proportional to the range of possible engine speeds (Morello L, 2011). These frequencies for the engine and transmission are functions of the number of cylinders, the cylinder configuration, and the gear ratios in the transmission. The suspension of the engine is designed considering two relatively simple considerations: minimize transmission of dynamic forces to the chassis and minimize engine displacement with respect to the chassis. If the suspension of the engine is simplified to a one degree of freedom mass-spring-damper system a simple analysis of this system can aid in its design. If the chassis is assumed to be stationary the forces acting upon the engine and the chassis and the force transmissibility transfer function can be defined as shown in Equations 1 through 4.

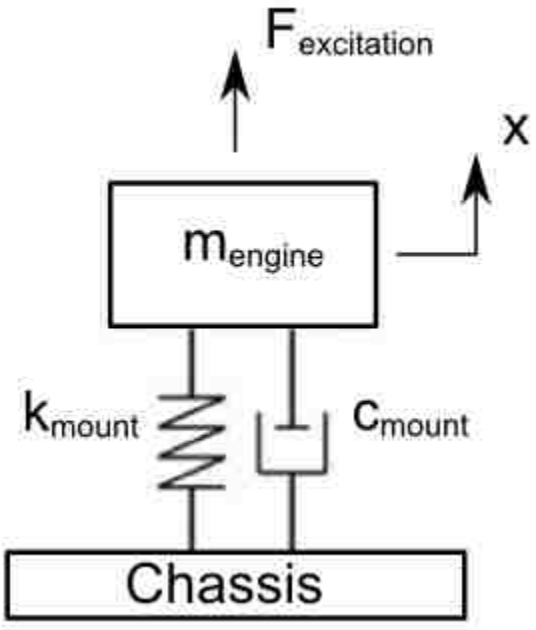

Figure 1: One degree of freedom, mass-spring-damper model of the engine suspension

$$F_{excitation} = m_{engine}\ddot{x} + c_{mount}\dot{x} + k_{mount}x \qquad \text{(Equation 1)}$$

$$F_{chassis} = c_{mount}\dot{x} + k_{mount}x \qquad \text{(Equation 2)}$$

$$T = \frac{F_{chassis}}{F_{excitation}} = \frac{c_{mount}\dot{x} + k_{mount}x}{m_{engine}\ddot{x} + c_{mount}\dot{x} + k_{mount}x} \qquad \text{(Equation 3)}$$

$$T(s) = \frac{c_{mount}s + k_{mount}}{m_{engine}s^2 + c_{mount}s + k_{mount}} \qquad \text{(Equation 4)}$$

The force transmissibility function can be non-dimensionalized to consider damping ratio rather than damping and by normalizing the Laplace variable with respect to the natural frequency. The resulting form of this equation is given by Equation 5. This transfer function is plotted with respect to excitation frequency and damping ratio in Figure 2. For any amount of damping the engine suspension reduces the transmitted force when the ratio of excitation frequency to natural frequency is greater than the √2. Therefore, for the minimum excitation frequency (directly proportional to the minimum engine speed) a maximum suitable natural frequency may be calculated. Since the mass of the engine is essentially fixed it is the stiffness of the engine mount that is the primary design variable. To reduce the transmissibility the natural frequency of the engine suspension should be minimized which is achieved by minimizing the stiffness. However, if the stiffness is excessively low large displacements of the powertrain will be possible. It is clear that displacements must be within reasonable limits to avoid undesirable contact between the engine and surrounding components and structures.

$$T(s^*) = \frac{2\zeta s^* + 1}{s^{*2} + 2\zeta s^* + 1} \qquad \text{(Equation 5)}$$

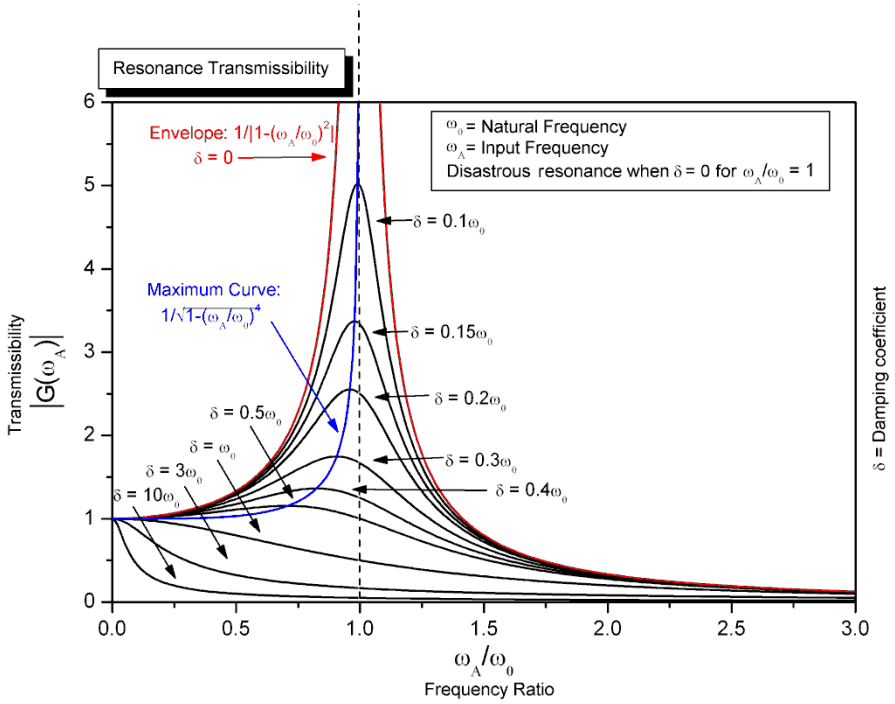

Figure 2: Engine suspension (under-damped 2nd order system) frequency response **(MasterHD, 2008)**.

Many engine support structures are designed with a non-linear force-displacement response to minimize stiffness for low displacements but with a marked increase in stiffness after sufficient displacement. Elastomers are often used for their low stiffness and internal damping. After sufficient displacement internal contact may occur within the engine mount such that small additional displacements result in relatively large compressive strains. The incompressibility of the rubber further increases the stiffness. As shown in Figure 2 the damping is a more complex characteristic. At low frequencies, particularly close to the natural frequency, damping should be maximized to reduce transmissibility. However, at high frequencies increased damping increases transmissibility. Elastomers used for such components exhibit varying internal damping with respect to frequency but many high end vehicles may use hydraulic mounts which allow near ideal damping characteristics to be achieved.

2.2 Review of Research on Automotive Chassis Components Incorporating Hyperelastic Materials

Rubber bushings, isolators, and dampeners for automotive applications commonly consist of a hollow elastomer cylinder between two metal cylindrical sleeves. Many are of the mold bonded type which is manufactured using injection molding to inject the elastomer between the metal sleeves where it then cures and bonds with the metal. This may be followed by a process known as swaging where the outer sleeve is compressed to eliminate residual tensile stresses in the elastomer due to shrinkage during the curing process. Researchers in the USA at Rowan University (NJ) and the University of Michigan performed experimental tests and numerical simulations (FEM) of this type of bushing under several types of loading (Kadlowec J, 2003). Radial loads were applied by loading the internal sleeve normal to the axis of the bushing and fixing the outer sleeve. Torsional loading was applied to the internal sleeve about the axis of the bushing with the outer bushing again fixed. For the combined radial and torsional loading the bushing was loaded in torsion to a pre-set angle after which the radial load was applied. Test specimens were subjected to several loading cycles to precondition the material before running the tests against which the finite element models would be compared.

The finite element modeling was completed using ABAQUS. It was not indicated how the material model parameters were obtained. The cooling and swaging manufacturing processes were first simulated to capture the prestress in the material. The resulting model correlated well with experimental data for radial and torsional loading applied separately. However, the model did not correlate well with the combined radial and torsional loading. It was proposed that through more extensive material testing better material model data could be obtained which may improve the finite element model.

Morman and Pan (Morman K, 1988) modeled the mechanical behaviour of several elastomeric automotive components. The simplest model was a bonded cylindrical block: a rubber cylinder bonded to two steel end plates. The authors of this publication also modeled a specific automotive rubber bushing known as a Silentbloc. With this type of bushing the metal sleeves are pressed around/into an oversized rubber bushing with

draft angles using lubricant and severe deformation of the rubber occurs. The rubber is not bonded to the metal of the sleeves. Morman and Pan created finite element models of the assembly process, axial loading, and radial loading. The FE model was compared with experimental data and simple analytical models. The FE model did not correlate well with the experimental data but the response of the FE model was improved by modeling the preload. The lack of accuracy may partially be the result of the use of a very simple, 2 parameter material model.

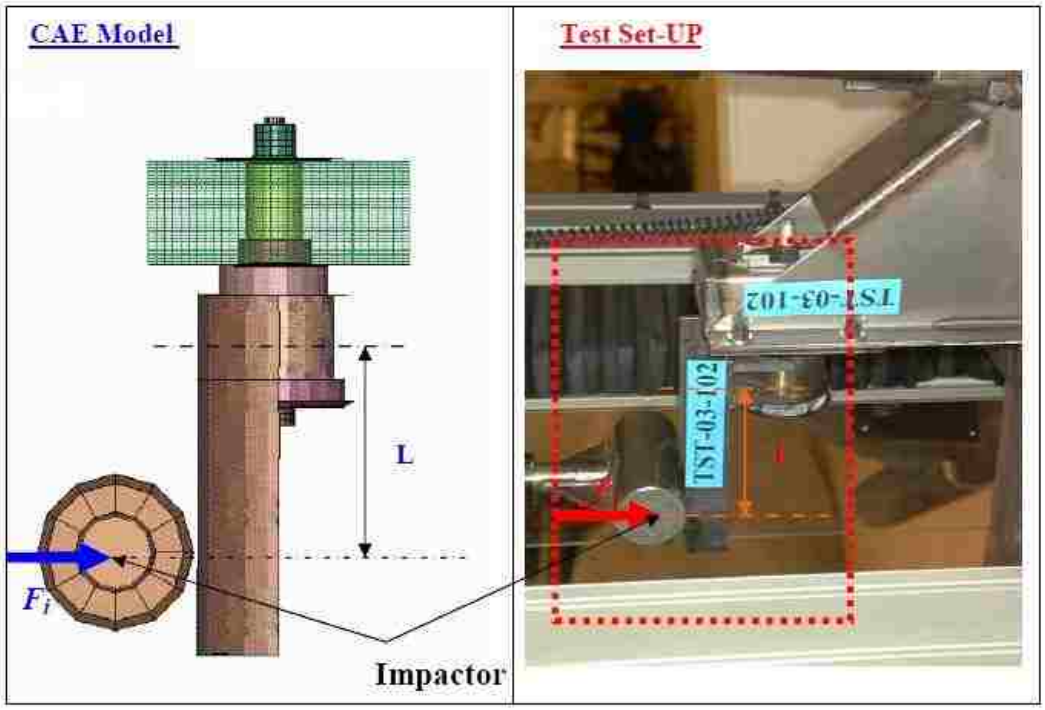

Figure 3 - Chrysler rubber bushing CAE model and experimental validation.

Researchers at Daimler Chrysler presented a paper at the 8th International LS-DYNA Users Conference in 2004 on their models of a rubber vehicle mount (Park S, 2004). Their model used the Mooney-Rivlin rubber material model (MAT_27) and included preloading of the bolt holding the assembly together as shown in Figure 3. The bolt was preloaded by dividing the bolt into upper and lower halves and applying forces to draw these two components together thereby compressing the rubber bushing. When the proper preload had been reached a tied contact algorithm was used to connect the two halves of the bolt. Stress-strain behaviour for the rubber material were provided by the

supplier. The steel bolts and the plates connected by the isolator used the piecewise linear plasticity material model (MAT_24). An impact test, as shown in Figure 3, was used to validate the model which exhibited a strong correlation with the experimental results (Figure 4).

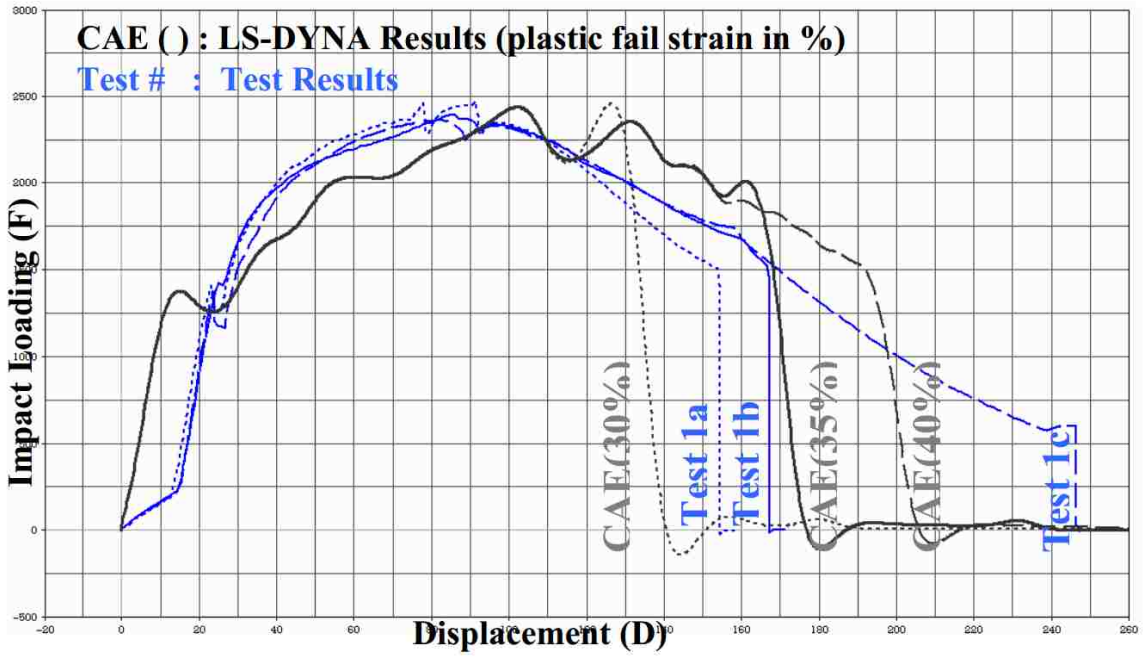

Figure 4: Force-displacement responses of Chrysler body mount CAE models validated with respect to mechanical characterization of a physical component.

Researchers at the University of Iowa compared analytical, numerical, and experimental load-deflection responses for rubber bushings subjected to several different types of loading (Chen J, 1997). Two rubber material models are used for the finite element modelling: the Mooney-Rivlin model and a Cubic model proposed by Yeoh (Yeoh, 1990). A comprehensive review of the Mooney-Rivlin material model is presented in a later section of this thesis. The finite element modelling was completed using the pressure projection method which avoids volumetric locking. The bushing was loaded axially, in torsion, and radially (each type of loading was applied separately). The authors compared their models with analytical 2D plane stress and plane strain solutions. Their conclusions include that for very short bushings a 3D analysis is necessary for accurate predictions of behaviour of the mechanical characteristics of the isolator.

In a more recent investigation Dharwadkar and Adivi investigated the modelling of engine suspension components for crash simulations (Dharwadkar N, 2011). The authors of this thesis modeled the left hand side engine suspension mount (the connection between the gearbox and chassis structural members) used in most Volvo vehicles. The mount is manufactured by Trelleborg Automotive in Germany. This engine mount consists primarily of rubber and aluminum. Modelling was completed using LS-DYNA. The rubber components used MAT_77 (MAT_HYPERELASTIC_RUBBER). The aluminum components used a user defined material model (MAT_48). This rubber material model cannot consider strain rate effects.

The model was validated with respect to bench testing of an engine mount with strong correlation between the numerical model and the experimental results. The validated engine mount model was utilized in a full vehicle model of a Volvo V60 and simulations of full width frontal impacts and offset frontal impacts were completed. In experimental full vehicle crash testing there was a failure in the aluminum of the engine mount. The authors tuned their aluminum material model to obtain a similar failure. The effects of the revised model of the engine mount on the crash pulse or response of the occupant were not considered at the time of publication.

Engineers at Ford Motor Company published a technical paper with SAE in 2003 on their efforts to model body mounts in body on frame (BOF) configuration vehicles (Chen Y, Dynamic Testing and CAE Modeling of Body Mount - An Application in the Frontal Impact Analysis of a Body-on-Frame Vehicle, 2003). This publication contains a great deal of information on experimental testing carried out by Ford engineers. There are many interesting observations. Connections between the body and frame were found to fail due to failure of the body mount itself or due to floor pan rupture. Preloading of the body mounts as is completed during vehicle assembly was accounted for in component level testing. Preloading due to the weight of the body was also considered. Neither was found to be significant. Additionally, the elastomer portion was not found to have a significant effect on the structural behaviour. However, the unloading behaviour of the mount was deemed important. In a related publication Ford engineers modeled an engine mount and a body mount using non-linear spring elements (Chen Y, Dynamic Testing

and CAE Modeling of Engine Mounts and the Application in Vehicle Crash Analysis, 2003) (Li M, 2005).

Researchers at Ford Motor Company have extensively studied suspension lower control arm structure behaviour in impact conditions (Eguia M H. M., 2005). Rubber bushings are used at the connections between the lower control arm and structural elements of the sprung mass of the vehicle. It was observed that these bushings allow for significant relative movement between the lower control arm and the frame for degrees of freedom normally constrained by the suspension mechanism. The lower control arm assembly can be critical in achieving optimal energy absorption since the lower control arm reinforces the vehicle frame and may prevent or influence plastic deformation of this critical region.

In one of many related publications the same researchers from Ford Motor Company document their investigations into the impact performance of lower control arms using numerical simulation (Huang M, 2005). The authors modeled the rubber bushings using beam elements with customized properties. One challenge highlighted by the authors was the need to complete physical testing to obtain data to accurately model the bushings using the beam element technique. A specific challenge was the press fit between the bushings and the lower control arm.

These researchers at Ford Motor Company also investigated the mechanical performance of suspension bushings experimentally (Eguia M T. T., 2006). These investigations considered lower control arm bushings from two vehicles loaded axially, radially, and in bending about axes running radially. The loads were applied by an impact using a form of sled test at speeds of 6, 8, 10, 15, and 17 mph (10, 13, 16, and 24 km/h). The publication documents deficiencies in their apparatus (plastic deformation of the fixtures) yielding invaluable advice for further research on this topic. Bushing stiffness varied considerably for the different types of bushing and the direction in which the load was applied. The highest stiffness encountered was 100 000 lbf/inch (17500 N/mm) for a bushing loaded axially. Another bushing recorded the lowest stiffness, also in the axial direction, of 5200 lbf/inch (910 N/mm). The peak load reached in testing, resulting in bushing failure, was 42 000 lbf (187 000 N).

2.3 Structural, Transient Finite Element Method

In the transient structural finite element method the momentum equation, coupled with material stress-strain relationships, is solved to obtain displacements, velocities, and accelerations for all nodes of a structure. The coupling equations between stress (force in the momentum equation) and strain (calculated from displacements) are known as constitutive equations or, more commonly, the material model. For each node the mass (m), dampening (c), and stiffness (k) is determined by the material surrounding each node (the elements). External forces are denoted F_{ext}. A node can be connected to several elements, each of which will contribute to the nodal mass, damping, and stiffness. The mass, stiffness, and dampening contributions of elements to nodes are determined using the finite element (FE) method.

$$m\ddot{x} + c\dot{x} + kx = F_{ext} \qquad \text{(Equation 6)}$$

This equation is solved numerically with respect to time using a central difference scheme to numerically approximate derivates with respect to time. Two types of time integration are commonly employed: explicit time integration and implicit time integration. With explicit time integration the solution marches forward in time with the solution at each timestep calculated using existing information (e.g. nodal displacements and velocities and stiffness and damping of the structure at the beginning of the time step). The numerical algorithm can be found in section 24 of the LS-DYNA Theory Manual (Hallquist, 2006). The maximum timestep is restricted to the transit time for the stress wave propagation speed across the smallest element. For a beam element this speed depends on the modulus of elasticity (E), the density of the material (ρ), and the characteristic length of the element (L). The function is given in Equation 7. Similar relationships are given by Equations 8, 9, and 10 for discrete, shell, and solid elements (positive, nonzero strain rates) respectively (v is Poisson's ratio). For solid elements the minimum time step of equation 10 assumes a constant bulk modulus. The implicit time integration scheme does not have such a limitation on the time step but is iterative at each time step due to a dependence on future (unknown) nodal displacements (section 34 of the LS-DYNA Theory Manual).

$$\Delta t \leq L\sqrt{\frac{\rho}{E}} \qquad \text{(Equation 7)}$$

$$\Delta t \leq 2\sqrt{\frac{2M_1M_2}{k(M_1+M_2)}} \qquad \text{(Equation 8)}$$

$$\Delta t \leq L\sqrt{\frac{\rho(1-v^2)}{E}} \qquad \text{Equation 9)}$$

$$\Delta t \leq L\sqrt{\frac{(1+v)(1-2v)\rho}{E(1-v)}} \qquad \text{(Equation 10)}$$

By default the explicit time integration solver in LS-DYNA finds the element with the smallest minimum time step. This time step is then adjusted depending upon a time step scaling factor (TSSF) that can be modified by the user. The explicit time integrator can be forced to use larger time steps if mass scaling is used. The solver will add mass to the model to allow a specified larger time step without instabilities. For quasi-static analyses mass scaling has little effect on the results. However, the ratio of kinetic energy to total energy should be monitored to ensure this approach is reasonable.

The discrete element critical time step (Equation 8) is significant due to the use of discrete elements in modelling contact between entities. The nodal masses at either end of the element are denoted M_1 and M_2. Contact algorithms search for entities with node through segment penetrations and insert discrete elements (springs and dampers) to model the contact phenomenon. The critical time steps for all contact related discrete elements are not calculated at each time step. However, the LS-DYNA solver will display a message upon starting a simulation estimating the minimum time step for stable contact and will suggest to the user that a smaller explicit time integration time step be used.

2.4 Hyperelastic Materials

Rubber originally referred to the compound obtained from latex of the Hevea Braziliensis tree. This natural rubber is a hydrocarbon with the chemical formula $(C_5H_8)_n$ (Treloar L. , 2009). The typical molecular weight is approximately 350 000 u. Natural rubber is in the form of small particles (0.1 to 1 µm) in a water-based solution with rubber accounting for approximately 35 percent. The rubber particles would aggregate if not for a protein coating. The rubber is obtained from the latex by removing the water or by acid precipitation; the latter produces a more pure rubber. Elastomer generally refers to synthetic materials with properties similar to rubber.

The properties of rubber stem from the molecular structure of the material. As an example, double bonds between carbon atoms in the continuous hydrocarbon chain react with sulfur or other reagents during vulcanization. This process creates links between the hydrocarbon chains. The double bonds are also the sites at which material degradation initiates. A raw rubber that has not been vulcanized may exhibit mechanical properties similar to vulcanized rubber for short time duration deformations as a result of entanglements in the hydrocarbon chains. If a non-vulcanized rubber is loaded for an extended period of time the entanglements will break down resulting in stress relaxation and creep.

Rubber and similar elastomeric materials are capable of large deformations before ultimate failure. Ultimate strain can be as high as 500 to 1000 percent. Stress-strain or force-displacement curves for rubber specimens are generally quite non-linear with no constant value for Young's modulus. A constant Young's modulus may be applied for very small deformations in which case the value can be 5 orders of magnitude smaller than Young's modulus for steel. Rubber and similar elastomers also exhibit interesting thermodynamic properties. There are two thermoelastic effects observed by Gough and Joule in the 19^{th} century: 1) rubber contracts upon heating when under a constant tensile load and 2) rubber emits heat when loaded (Treloar L. , 2009). This heat emission is associated with the hysteresis effects rubber exhibits with cyclic loading.

There are two contributors to the mechanical behaviour of rubber materials: elastic and hysteresis (non-reversible) effects. If hysteresis effects are observed the stress-strain

curve will be different for loading and unloading. The earliest strain energy density phenomenological rubber material models did not account for hysteresis effects commonly observed for rubbers with additional ingredients like sulfur or black carbon (Charlton D, 1993). However, natural gum rubbers have less significant hysteresis effects and can be better modelled using a strain energy density function. Ingredients like sulfur or black carbon can significantly alter the molecular structure. These changes in the molecular structure can result in a relatively high sensitivity to temperature, environment, strain rate, loading history, and strain magnitude. When material samples are tested to failure the data may not be reproducible due to the variability in defects.

Two methods are commonly used to model the mechanical characteristics of rubber materials. The statistical thermodynamics method arises from the observation that rubber in a natural state is highly irregular but as it is deformed in tension the rubber molecular networks become more structured and the entropy is reduced (Charlton D, 1993). However, this approach is only accurate up to approximately 50% strain (Shaw M, 1988). Most rubber material models are based on the phenomenological approach: observation and mathematical description of mechanical behaviour. In these models rubber is assumed to be isotropic with random orientation of molecules in the non-deformed condition. These assumptions of isotropy allow the use of the strain energy density function. This approach, the use of a strain energy density function, is used due to its capability to model non-linear elastic deformation. Rubber material models commonly formulate this energy as a function of strain tensor invariants or stretch ratios. Stretch ratios are calculated as shown by Equation 11 where L_0 is the original length of the specimen and $L = L_0 + \delta$ where δ is the elongation.

$$\lambda_x = \frac{L}{L_0} = \frac{L_0 + \delta}{L_0} = \varepsilon_x + 1 \qquad \text{(Equation 11)}$$

$$W = C_1(\lambda_1^2 + \lambda_2^2 + \lambda_3^2 - 3) + C_2\left(\frac{1}{\lambda_1^2} + \frac{1}{\lambda_2^2} + \frac{1}{\lambda_3^2} - 3\right) \qquad \text{(Equation 12)}$$

Mooney (Mooney, 1940) developed a phenomenological material model based on assumptions that rubber is incompressible (ie. constant volume), isotropic when unstrained, and consistent with Hooke's law for simple shear. The Mooney strain energy

function is given by Equation 12 where C_1 and C_2 are constants. Rivlin (Rivlin, 1956) extended Mooney's work by considering the symmetry of the strain energy function with respect to the stretch ratios as required by isotropy. Many implementations of this material model use the strain energy function given in Equation 16 where C_{ij} are constants.

$$I_1 = \lambda_1^2 + \lambda_2^2 + \lambda_3^2 \quad \text{(Equation 13)}$$

$$I_2 = \frac{1}{\lambda_1^2} + \frac{1}{\lambda_2^2} + \frac{1}{\lambda_3^2} \quad \text{(Equation 14)}$$

$$I_3 = \lambda_1^2 \lambda_2^2 \lambda_3^2 = 1 \quad \text{(Equation 15)}$$

$$W = \sum_{i=0,j=0}^{\infty} C_{ij} (I_1 - 3)^i (I_2 - 3)^j \quad \text{(Equation 16)}$$

A particularly important characteristic of rubber is the near incompressibility. The assumption of incompressibility results in a value of unity for the third stretch ratio invariant (Equation 15). Incompressible materials undergo no change of volume when loaded and correspondingly have a Poisson's ratio of approximately 0.5, the upper limit on Poisson's ratio. This upper limit can be observed for isotropic elastic materials by considering Hooke's law as shown by Equation 17. A Poisson's ratio of 0.5 results in singularities when using the stress-strain constitutive equations for isotropic elastic materials as shown in equation 18.

$$(1 + \varepsilon_x)(1 + \varepsilon_y)(1 + \varepsilon_z) - 1 = \frac{1 - 2v}{E}(\sigma_x + \sigma_y + \sigma_z) \quad \text{(Equation 17)}$$

$$\begin{Bmatrix} \sigma_x \\ \sigma_y \\ \sigma_z \\ \tau_{xy} \\ \tau_{yz} \\ \tau_{zx} \end{Bmatrix} = \frac{E}{(1+v)(1-2v)} \begin{bmatrix} 1-v & v & v & 0 & 0 & 0 \\ v & 1-v & v & 0 & 0 & 0 \\ v & v & 1-v & 0 & 0 & 0 \\ 0 & 0 & 0 & \frac{1-2v}{2} & 0 & 0 \\ 0 & 0 & 0 & 0 & \frac{1-2v}{2} & 0 \\ 0 & 0 & 0 & 0 & 0 & \frac{1-2v}{2} \end{bmatrix} \begin{Bmatrix} \varepsilon_x \\ \varepsilon_y \\ \varepsilon_z \\ \gamma_{xy} \\ \gamma_{yz} \\ \gamma_{zx} \end{Bmatrix} \quad \text{(Equation 18)}$$

$$S = 2(\lambda - \lambda^{-2})(c_1 + c_2 \lambda^{-1}) \quad \text{(Equation 19)}$$

$$\frac{S}{2(\lambda - \lambda^{-2})} = c_1 + c_2\lambda^{-1} \qquad \text{(Equation 20)}$$

Finney and Kumar (Finney R, 1988) have published a guide to finding the parameters of the Mooney-Rivlin, Ogden, Peng, and Peng-Landel material models. They show that the Mooney-Rivlin material strain energy density function can be manipulated to obtain a relationship between engineering stress and stretch ratio for material in simple tension (Equation 19). This relationship can be rearranged as shown to obtain the equation of a straight line where c_2 is the slope and c_1 is the y-intercept. These quantities can be obtained from a simple tensile test provided the linear relationship is a suitable representation. Similar expressions for the Ogden material model (Equation 21) are shown below in Equations 22, 23, and 24.

$$W = \sum_{i=1}^{3}\sum_{j=1}^{m}\frac{c_j}{b_j}\left(\lambda_i^{\,b_j} - 1\right) \qquad \text{(Equation 21)}$$

$$S = \sum_{j=1}^{m} c_j\left[\lambda^{\,b_j-1} - \lambda^{\,-(1+0.5b_j)}\right] \qquad \text{(Equation 22)}$$

$$S_{Pure\ shear} = \sum_{j=1}^{m} c_j\left[\lambda^{\,b_j-1} - \lambda^{\,-(1+b_j)}\right] \qquad \text{(Equation 23)}$$

$$S_{Biaxial} = \sum_{j=1}^{m} c_j\left[\lambda^{\,b_j-1} - \lambda^{\,-(1+2b_j)}\right] \qquad \text{(Equation 24)}$$

The principal stretch ratios, as shown in Equations 25 - 27, can be derived by considering the volume of a body to be constant. For a simple shape like a cube uniaxial tension will result in elongation (δ_1) along one axis while along the other principal axes the dimensions of the body (initial edge length is denoted L) will decrease by equal amounts (δ_2). Therefore, the volume, which is constant, is equal to L^3 or $(L+\delta_1)\cdot(L-\delta_2)\cdot(L-\delta_2)$. Taking the quotient of these two alternative expressions for the (constant) volume must yield unity. The relationship $\lambda\cdot\lambda_2\cdot\lambda_2 = \lambda\cdot\lambda_2^{\,2}=1$ or $\lambda_2 = \lambda_3 = \lambda^{-0.5}$ is then obtained where λ is the stretch ratio along the axis of loading and λ_2 and λ_3 are the stretch ratios for the

other 2 orthogonal axes. Different values for the variable 'a' yield the principal stretch ratios for different material characterization processes. For simple tension or compression a=0.5. For planar tension (pure shear) a=0 and for equibiaxial tension a=1.

$$\lambda_1 = \lambda \qquad \text{(Equation 25)}$$

$$\lambda_2 = \lambda^a \qquad \text{(Equation 26)}$$

$$\lambda_3 = \lambda^{-a-1} \qquad \text{(Equation 27)}$$

2.5 Mullins' Effect

The Mullin's effect is the asymptotic softening of vulcanized polymers observed with cyclic loading (Mullins, 1969). Depending upon the specific material and the application it may be important to consider this material behaviour. One of the earliest publications on this phenomenon was by Holt (Holt, 1931) in which it was found that a vulcanized natural rubber exhibited a progressive decrease in stiffness with cyclic loading as well as a lack of complete recovery. Mullins advised that after three or four loading and unloading cycles of tire tread rubber decreases in stiffness were not significant. Additionally, this researcher observed that material recovery was more rapid at higher temperatures. Hysteresis is also affected by cyclic loading with findings by Hock & Bostroem (Hock L, 1926) that energy absorption decreased with cyclic loading to a constant level of stress with increasing strains due to material softening.

2.6 Temperature Dependency

The theory that the deformation of rubber consists of rearranging long, tangled molecules (known as the kinetic theory) implies that the stress at a given strain is proportional to the absolute temperature (Treloar L. , 2009). For large strains this is generally observed but for small strains the opposite can occur (up to the thermoelastic inversion point). Hysteresis is also predicted by the kinetic theory since external work does not increase

internal energy as a result of straining. At sufficiently low temperatures molecular motion is inhibited such that the material is very stiff and brittle and can be considered a glass (Dick, 2001).

2.7 Hyperelastic Material Models in LS-DYNA

There are several material models for hyperelastic materials in LS-DYNA ranging in complexity and capability. Several hyperelastic material models in LS-DYNA require only uniaxial stress-strain or force-displacement data to determine material model parameters (MAT 027, 031, 077, 181, & 183). However, it is generally recommended (Kadlowec J, 2003) (Charlton D, 1993) that material model parameters be determined by several different types of mechanical testing including tension, compression, and pure shear testing. The accuracy of any material model is highly dependent on the quality of the material model data. Finney and Kumar (Finney R, 1988) tested four material models (Mooney-Rivlin, Ogden, Valanis and Landel, and Peng-Landel) and found that the Ogden material model (MAT 077_O in LS-DYNA) was the most accurate model performing well over a large range of strains (0 to 500%). However, a superior choice within LS-DYNA may be MAT_181 which uses a tabulated Ogden strain energy function and can replicate experimental data essentially verbatim since it fits the strain energy function piecewise. It also simplifies the modeling of strain rate sensitivity. Additionally, there are options with this model which can account for hysteresis and failure.

MAT_006 (MAT_VISCOELASTIC) models viscoelastic behaviour and can be applied to beams, shells, and solids (viscoelasticity is the dependency of stress and strain on time) (LSTC, 2007). The term viscoelasticity is derived from considering the material to be a combination of a Hookean elastic solid and a Newtonian viscous fluid. In MAT_006 the deviatoric stress tensor is a function of time. Inputs to the material model that control this time dependency are the short and long time shear moduli and a decay constant.

MAT_007 (MAT_BLATZ-KO_RUBBER) is a simple two parameter (shear modulus and density) model for rubber. Poisson's ratio is fixed at 0.463. Stress is a function of the shear modulus, Poisson's ratio, and change in volume.

MAT_027 (MAT_MOONEY-RIVLIN_RUBBER) is a four parameter model for rubber. Inputs to the model include mass density, Poisson's ratio (between 0.49 and 0.5 recommended), and two parameters A & B. This material model is based on the phenomenological material models of Mooney and Rivlin in which the constitutive equations consist of a function where strain energy is dependent on strain invariants. In MAT_027 the constants A and B can be input directly or load displacement data from a uniaxial mechanical test can be input from which the solver will determine the constants A and B. However, the low number of parameters will limit the response that can be captured. This may limit the usefulness of this material model.

MAT_031 (MAT_FRAZER_NASH_RUBBER_MODEL) is a 10 parameter rubber material model. These parameters consist of mass density, Poisson's ratio (between 0.49 and 0.50 suggested), and 8 coefficients of a strain energy density function dependent on strain invariants. These coefficients can be input directly. Alternatively, load-displacement data from a uniaxial test can be input from which the solver will determine the coefficients. Other options in this material model include maximum and minimum strain limits. The strain energy function is given in Equation 28.

$$U = C_{100}I_1 + C_{200}I_1^2 + C_{300}I_1^3 + C_{400}I_1^4 + C_{110}I_1I_2 + C_{210}I_1^2I_2 + C_{010}I_2 + C_{020}I_2^2 + f(J)$$

(Equation 28)

MAT_076 (MAT_GENERAL_VISCOELASTIC) is a viscoelastic material model which can account for the effects of temperature on viscoelasticity through Arrhenius and Williams-Landau-Ferry shift functions. The time dependency of the stress is implemented through a 6 term Prony series where each term consists of an exponential where the units are determined by a shear modulus and the exponent is dependent on time which is scaled by a decay factor. A similar Prony series exists for defining volumetric stress relaxation. MAT_175 (MAT_VISCOELASTIC_THERMAL) is another form of this model that can be combined with a thermal material model.

MAT_077_H (MAT_HYPERELASTIC RUBBER) is based on a Mooney-Rivlin type material model where the constitutive equations for stress and strain are a function of the

strain energy density which is dependent on strain invariants. The LS-DYNA implementation adds a linear viscoelasticity model. The strain energy density function is a polynomial with 6 coefficients that can be input directly or determined by the solver through input of load-displacement data from mechanical material testing (uniaxial only). MAT_077_O (MAT_OGDEN_RUBBER) is similar to MAT_077_H but uses the Ogden form of the strain energy density function.

MAT_127 (MAT_ARRUDA_BOYCE_RUBBER) is an Ogden strain energy functional based model which only requires the user to specify the bulk modulus, the shear modulus, and the number of statistical links between hydrocarbon chains. The LS-DYNA implementation includes an optional linear viscoelasticity model.

MAT_181 (MAT_SIMPLIFIED_RUBBER/FOAM) is a material model for rubbers and foams which is unique (among rubber models) in allowing multiple load-displacement curves (at different strain rates) to be input directly to account for strain rate effects. These load-displacement curves must be uniaxial stress-strain or force-displacement data. If this material model is used with foams a Poisson's ratio must be provided by the user. Other material model parameters include: mass density, linear bulk modulus, shear modulus for frequency independent damping, limit stress for this damping, and material failure parameters. MAT_183 (MAT_SIMPLIFIED_RUBBER _WITH_DAMAGE) is similar to MAT_181 but allows unloading curves to be specified which allows for the modeling of hysteresis due to internal energy dissipation.

2.8 Solid Element Formulations in LS-DYNA

The finite element code LS-DYNA offers the user a wide-ranging selection of element formulations. For this research solid hexahedron element formulations 1, 2, 3, and 41 may be suitable. Element formulation 1 is an under-integrated constant stress element. Element formulation 2 is a fully integrated element but with selectively reduced integration for shear stresses. Element formulation 3 is fully integrated with 8 nodes visible to the user as well as rotational degrees of freedom. Internally to the software this element has mid-span nodes from which the nodal rotations are calculated. Element

formulation 41 is a mesh-free or element free Galerkin (EFG) formulation. Element formulation 41 may also be used with an initial mesh of tetrahedrons.

Additionally, there are a number of element formulations specifically for tetrahedron elements available to a user of LS-DYNA. Formulations potentially suitable for this research include: 4, 10, 13, 16, and 17. Element formulation 4 is a selectively reduced integration element with nodal rotations (mid-span nodes internal to the code and not visible to the user). Element formulation 10 is a one point integration element. A similar element specifically designed for nearly incompressible materials is element formulation 13. Element formulations 16 and 17 are tetrahedron element formulations with 10 nodes visible to the user. The number of integration points can be controlled by the user through the keyword *CONTROL_SOLID.

2.9 Locking

The structural finite element method can suffer from a problem known as locking which commonly appears as two types: shear locking and pressure locking. Shear locking arises with certain element formulations and large aspect ratios whereas pressure locking occurs with nearly incompressible materials. Shear locking can be easily demonstrated for an Euler-Bernoulli beam element (Reddy, 1993). If Lagrange interpolation is used (Equations 29 and 30) the displacement and rotation fields are of the form in Equations 31 and 32 where x_A denotes the axial position (x axis) of the left end of the element, x_B denotes the right end, and h is the length of the element. Considering the left and right ends of the element ($x=x_A$ and $x=x_B$, Equation 33) it can be shown that the rotation field is constant. However, if the rotation field is constant the bending energy is zero as shown in Equation 34.

$$N_1(x) = \frac{x-x_2}{x_1-x_2} = \frac{x-x_B}{-h} \qquad \text{(Equation 29)}$$

$$N_2(x) = \frac{x-x_1}{x_2-x_1} = \frac{x-x_A}{h} \qquad \text{(Equation 30)}$$

$$w = w_1 \frac{x - x_B}{-h} + w_2 \frac{x - x_A}{h} \quad \text{(Equation 31)}$$

$$\psi = -\frac{dw}{dx} = s_1 \frac{x_B - x}{h} + s_2 \frac{x - x_A}{h} = \frac{w_1 - w_2}{h} \quad \text{(Equation 32)}$$

$$\psi(x) = s_1 = s_2 = \frac{w_1 - w_2}{h} \quad \text{(Equation 33)}$$

$$\int_{x_A}^{x_B} \frac{EI}{2} \left(\frac{d\psi}{dx}\right)^2 dx \quad \text{(Equation 34)}$$

Pressure locking is associated with Poisson's ratio approaching 0.5 and the use of solid elements. Under these conditions the number of constraints is equal to the product of the number of elements and the number of Gauss (integration) points used for each element (Cook, 1995). A penalty matrix (relatively large stiffnesses associated with violating constraints) can be separated from the element derived stiffness matrix. If the penalty matrix is not singular pressure locking occurs.

2.10 Oberkampf-Trucano (OT) Error Metric

Researchers in the Uncertainty Estimation Department of Sandia National Laboratories have proposed error metrics to be used to validate numerical models with respect to experimental data (Oberkampf W, 2002). These error metrics, given in Equations 29 and 30, ideally compare two sets of data over a domain rather than simply comparing discrete data points such as peak load or peak displacement. These specific error metrics approach zero when the relative error is large and approach unity with minimal relative error.

$$V = 1 - \frac{1}{I} \sum_{i=1}^{i=I} tanh \left| \frac{y(x_i) - Y(x_i)}{Y(x_i)} \right| \quad \text{(Equation 35)}$$

$$V = 1 - \frac{1}{L} \int_0^L tanh \left| \frac{y(x) - Y(x)}{Y(x)} \right| dx \quad \text{(Equation 36)}$$

2.11 American Society for Testing and Materials (ASTM) Standards

There are several ASTM standards relevant to mechanical testing of hyperelastic materials. Procedures for measurement of dimensions for rubber specimens are outlined in standard D3767-03 (ASTM International, 2008). Standard D3183-10 (ASTM International, 2010) covers standard practices for preparation of rubber specimens for test purposes. Standard D575-91 (ASTM International, 2012) consists of standard test methods for obtaining rubber properties in compression. Standard D412-06a (ASTM International, 2009) covers standard simple tension test methods for vulcanized rubber and thermoplastic elastomers. Each standard is discussed in greater detail below.

ASTM standard D3767-03 (measurement of dimensions) consists of 7 procedures: A through E. Specimens with length, width, thickness, or diameters less than 30mm (1.2in) are measured with a micrometer as per procedure A. A suitable device is depicted in procedure A in Figure 1 of standard D3767. One important aspect of the device depicted and described is the ability to control the forces applied to the specimen (and therefore the deformation) by the measuring device. Secondary procedures (within procedure A) provide guidance for measuring specimens with irregular, convex, or concave surfaces and flexible cellular materials. Procedure B applies to specimens with dimensions of length, width, thickness, diameter, and circumference from 30 to 100mm (1.2 to 4in). Specimens with dimensions of length, width, thickness, diameter, and circumference over 100mm can be measured with a rule or tape graduated to the nearest 1mm as per procedure C. Procedure D applies to soft, thin materials measured optically. Procedure E is used to measure inner diameter/circumference using a plug gage.

Standard D3183-10 provides guidance for preparation of specimens for material testing. If specimens cannot be obtained from the product being tested and rubber sheets can be molded, standard thicknesses are suggested. Processes and equipment are also suggested for cutting and buffing the material. Standard D575-91 (test methods for rubber properties in compression) consists of two test methods: A and B. With test method A the standard specimen is 12.5±0.5mm thick with a diameter of 28.6±0.1mm. Compressive forces are applied and removed in three successive cycles where the first two cycles condition the specimen. Sandpaper is to be placed between the platens of the

testing machine and the specimen. The deflection rate should be 12±3 mm/min (0.5±0.1 in/min). Test method B is intended for material characterization with a constant force testing apparatus. The force is applied for 3 seconds at which time the displacement is measured.

Standard D412-06a (standard test methods for rubber – tension) covers procedures used to evaluate the tensile properties of vulcanized rubbers. The standard consists primarily of two test methods: A & B. The geometry of the specimen may be of the dumbbell shape (test method A), straight pieces of uniform cross section (A), or rings (B). It is noted that straight specimens tend to fail in the grips. Testing to failure may require specimens of the dumbbell shape. The tensile testing machine employed should be capable of a displacement rate of 500±50 mm/min (20±3 in/min) for a total displacement of at least 750mm (30in). For materials with low yield strains the loading rate can be reduced to as low as 5±0.5 mm/min. The specimens are cut from rubber sheets of a thickness between 1.3 and 3.3mm using dies, designs of which are provided for the dumbbell geometry.

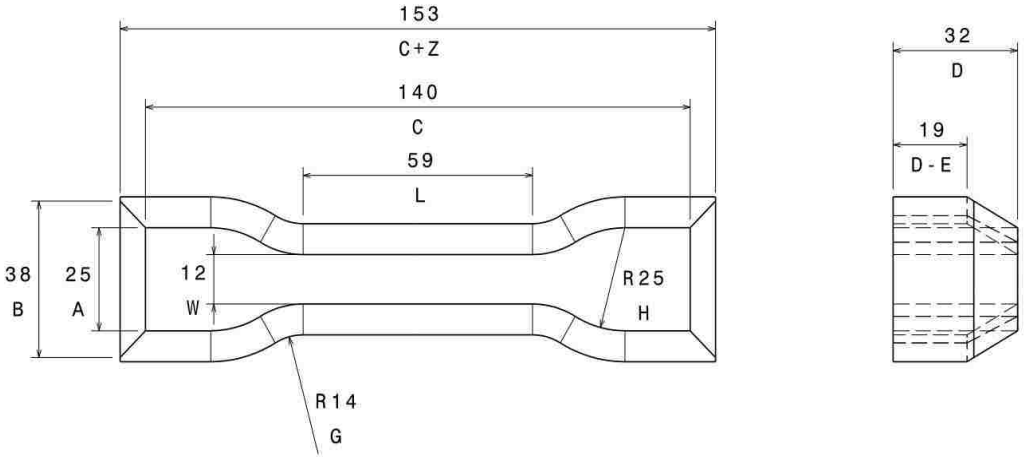

Figure 5: ASTM tensile specimen die **(ASTM International, 2009)**.

Table 1: Standard ASTM D412 Dumbbell Dies.

Dimension	Tolerance	Die A	Die B	Die C	Die D	Die E	Die F
A (mm)	± 1	25	25	25	16	16	16
B (mm)	Max	40	40	40	30	30	30
C (mm)	Min	140	140	115	100	125	125
D (mm)	± 6	32	32	32	32	32	32
E (mm)	± 1	13	13	13	13	13	13
F (mm)	± 2	38	38	19	19	38	38
G (mm)	± 1	14	14	14	14	14	14
H (mm)	± 2	25	25	25	16	16	16
L (mm)	± 2	59	59	33	33	59	59
W (mm)	± 0.05	12	6	6	3	3	6
Z (mm)	± 1	13	13	13	13	13	13

2.12 Split-Hopkinson Pressure Bar (SHPB) Material Testing

In 1914 Bertram Hopkinson (Hopkinson, 1914) proposed a method to determine the pressure resulting from the impact of a projectile or by the detonation of explosives. If a projectile is directed to impact the end of a metal bar a pressure (stress) wave is induced to travel through the bar. Over the very brief duration of the impact the stress changes with time. For a perfectly elastic bar the stress wave travels through the bar without being altered. On the first pass through the bar this stress wave is purely compressive. As it reaches the end of the bar it is reflected back as a tensile wave and the stress state at a given point in the bar can be a combination of the compressive stress wave and the reflected tensile stress wave. If the end of the bar is cut off and replaced with a thin film of grease to hold it in place the compressive stress wave will be transmitted across this

joint. However, a significant tensile stress wave will not be transmitted. The cut off end will be propelled away from the original bar and can be caught to measure its momentum. In the original method proposed by Hopkinson the cut off end of the bar varies in length to capture multiple data points.

However, there are serious deficiencies of the Hopkinson method that outweigh the advantages stemming from the simplicity. It is assumed that the pressure wave is evenly distributed over the cross section of the bar. However, this is often not the case when the pressure bar method is used to determine pressure time data for a bullet impacting the end of the bar where the diameter of the bullet is considerably smaller than the diameter of the bar (Davies, 1948). The original method by Hopkinson gives a pressure-time integral for each length of cut off bar. Additionally, these integrals are taken with respect to different, random time intervals for each length of cut off bar (Kolsky, 1949). With Hopkinson's original method the quantities obtained were: 1) maximum amplitude of the pressure and 2) the time duration over which pressure exceeded a certain magnitude. However, the original method also assumes that the stress wave is not significantly distorted as it travels through the bar. This is only true when the pulses have a large wavelength with respect to the diameter of the bar and there are no sudden changes in pressure. The joint also introduces error and prevents measurement of small pulses.

Davies (Davies, 1948) refined the Hopkinson pressure bar by using a continuous bar and measuring the displacement of the free end using a parallel plate condenser (condenser microphone). The use of the condenser allowed continuous pressure-time data to be acquired. Kolsky (Kolsky, 1949) was one of the first researchers to use an apparatus based on a Hopkinson pressure bar to study the mechanical behaviour of materials at high rates of strain. As shown in Figure 6 the specimen is a thin disk placed between two sections of the pressure bar (the term split Hopkinson pressure bar originates with the work of Kolsky) within a close fitting steel collar.

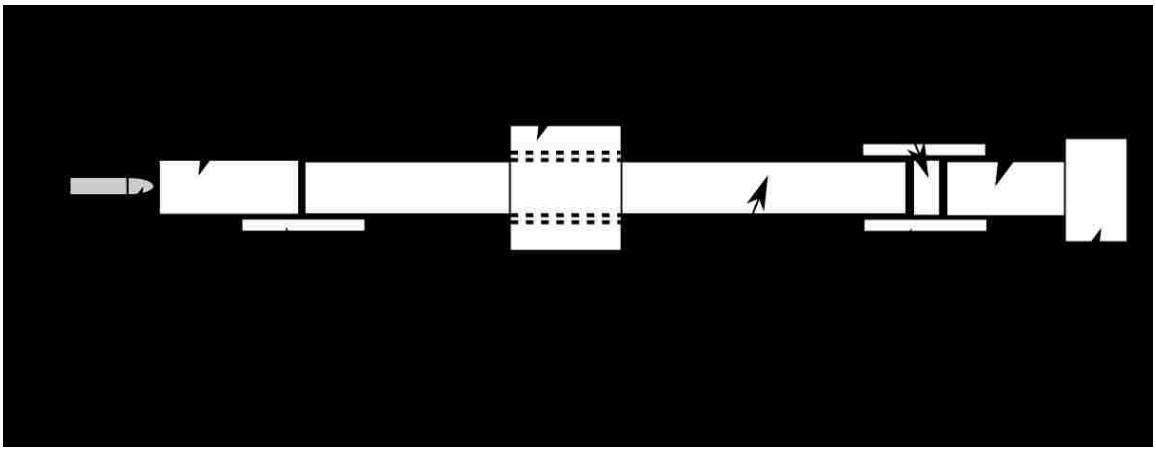

Figure 6: Kolsky pressure bar apparatus.

Other notable publications in the history of the split Hopkinson pressure bar (SHPB) include a publication by Bancroft (Bancroft, 1941) on wave dispersion in a cylinder and a publication by Hauser (Hauser, 1966) on the use of strain gauges rather than condenser microphones. Strain gauges are now the most common sensors used in acquisition of data with a SHPB apparatus. A third bar, known as a momentum bar, may be found after the transmission bar and is used in conjunction with a momentum trap to dissipate the kinetic energy of the apparatus. Loading is sometimes achieved with a hydraulic cylinder by clamping the end of the input bar, deforming the bar with the hydraulic cylinder, and quickly releasing the clamp. One method is to use a sintered metal clamp which is designed to fracture at a specific load thereby relieving the clamping force very rapidly.

In a SHPB the loading of the input bar results in a longitudinal stress (or strain) wave that travels through the bar at the speed of sound (for the material from which the bar is made). Three separate waves are referred to in the analysis of a SHPB: the incident pulse (generated by the impact and transmitted through the input bar essentially unaltered), the transmitted pulse (the portion of the incident pulse that is transmitted through the specimen and not reflected, measured in the output or transmission bar), and the reflected pulse (a portion of the incident pulse reflected back due to the difference in the impedance between the input bar and the specimen, measured at the input bar) (Weinong W Chen, 2011). The impedance of the bar is given by Equation 31 where A_{Bar} is the cross sectional area of the bar, C_{Bar} is the speed of sound in the bar, ρ_{Bar} is the density,

and E_{Bar} is the elastic modulus. The pulse is again transmitted and reflected as it reaches the interface between the specimen and the output (transmission) bar. However, the length of the specimen is very small when compared to the other longitudinal dimensions of the system. The strain gauge on the input bar measures the reflected pulse and the strain gauge on the transmission (output) bar measures the transmitted pulse.

$$Z_{Bar} = A_{Bar}\rho_{Bar}C_{Bar} = A_{Bar}\rho_{Bar}\sqrt{\frac{E_{Bar}}{\rho_{Bar}}} = A_{Bar}\sqrt{E_{Bar}\rho_{Bar}} \quad \text{(Equation 37)}$$

The most common implementation of the SHPB uses a striker bar propelled by a gas gun. This is the method employed in loading the SHPB for compressive material testing at the Politecnico di Torino campus in Vercelli, Piemonte, Italy. The time duration of the pulse is determined by the material and length of the striker bar as shown by Equation 32 where $T_{Incident}$ is the time duration of the pulse, $L_{Striker}$ is the length of the striker bar and $C_{Striker}$ is the wave speed of the striker bar material. The magnitude of the incident pulse, in terms of both stress and strain, can be calculated as shown in Equations 33 and 34 where v_{st} is the speed of the striker bar immediately prior to impact. These formulae can be used to design the SHPB material testing experiment as they impose an upper limit on the stress and strain in the specimen.

$$T_{Incident} = \frac{2L_{Striker}}{C_{Striker}} \quad \text{(Equation 38)}$$

$$\sigma_{Incident} = \frac{1}{2}\rho_{Bar}C_{Bar}v_{Striker} \quad \text{(Equation 39)}$$

$$\varepsilon_{Incident} = \frac{v_{Striker}}{2C_{Bar}} \quad \text{(Equation 40)}$$

Figure 7: Split Hopkinson pressure bar.

If it is assumed that there is no wave dispersion in the bar (the strain measured by each strain gauge is identical to the strain at the respective bar-specimen interface) the velocity at each end of the specimen can be related to the strains measured. These Equations (35 and 36) are given below where $\varepsilon_{Incident}$ is the magnitude of the incident pulse in terms of strain, $\varepsilon_{Reflected}$ is the magnitude of the reflected pulse in terms of strain, $\varepsilon_{Transmitted}$ is the magnitude of the transmitted pulse in terms of strain, v_1 is the velocity at the input bar-specimen interface, and v_2 is the velocity at the specimen-output bar interface.

$$v_1 = C_{Bar}\left(\varepsilon_{Incident} - \varepsilon_{Reflected}\right) \qquad \text{(Equation 41)}$$

$$v_2 = C_{Bar}\varepsilon_{Transmitted} \qquad \text{(Equation 42)}$$

The average engineering strain and engineering strain rate in the specimen can be calculated as shown in Equations 37 and 38 where ε is the average engineering strain and $L_{Specimen}$ is the length of the specimen. These equations also assume there is no wave dispersion. The stresses at each end of the specimen can be calculated as shown in Equations 39 and 40 where σ_1 is the stress at the input bar-specimen interface and σ_2 is the stress at the specimen-output bar interface. The SHPB method for high strain rate material testing assumes that the stress is uniform throughout the specimen. With this assumption ($\sigma_1 = \sigma_2$) the incident pulse, reflected pulse, and transmitted pulse strains are related by Equation 41.

$$\dot{\varepsilon} = \frac{v_1 - v_2}{L_{Specimen}} = \frac{C_{Bar}}{L_{Specimen}}\left(\varepsilon_{Incident} - \varepsilon_{Reflected} - \varepsilon_{Transmitted}\right) \quad \text{(Equation 43)}$$

$$\varepsilon = \int_0^t \dot{\varepsilon} dt = \frac{C_{Bar}}{L_{Specimen}} \int_0^t \left(\varepsilon_{Incident} - \varepsilon_{Reflected} - \varepsilon_{Transmitted}\right) dt \quad \text{(Equation 44)}$$

$$\sigma_1 = \frac{A_{Bar}}{A_{Specimen}} E_{Bar}\left(\varepsilon_{Incident} + \varepsilon_{Reflected}\right) \quad \text{(Equation 45)}$$

$$\sigma_2 = \frac{A_{Bar}}{A_{Specimen}} E_{Bar} \varepsilon_{Transmitted} \quad \text{(Equation 46)}$$

$$\varepsilon_{Incident} + \varepsilon_{Reflected} = \varepsilon_{Transmitted} \quad \text{(Equation 47)}$$

2.13 Split Hopkinson Pressure Bar Testing of Soft Materials

Many publications exist on the subject of SHPB testing of soft materials including different hyperelastic materials. W. Chen et al. (Chen W L. F., 2002) used an aluminum SHPB and a range of specimen aspect ratios and materials to study the feasibility of testing soft materials with a SHPB. Their analysis began with a traditional SHPB with aluminum bars with diameters of 19mm. The lengths of the striker, input, and output bars were 305, 1802, and 762 mm respectively. Strain gauges were located 560mm from the input bar – specimen interface and 203 mm from the specimen – output bar interface. The diameter of the specimen was 12.7 mm. A high speed camera was used to observe the deformation of the specimen and conclude that the specimen deformation was not homogeneous. Furthermore, a very low load was transmitted through the specimen as determined by the minimal amplitude of the transmitted strain pulse. Additionally, specimen failure occurred in the form of a large fracture. Further experiments were performed with quartz crystal force transducers at the input bar – specimen and specimen – output bar interfaces. The forces observed at the ends of the specimen were of significantly different magnitudes for all aspect ratios. The error was reduced as the specimen length was reduced but still remained significant.

The authors then introduced pulse shaping. Pulse shaping likely originated with Duffy et al. (Duffy J, 1971). Duffy et al. used pulse shaping to smooth pulses generated by explosive loading of a torsional SHPB. Pulse shaping is used to control the rate of change of the incident pulse. A gradual build-up of the incident pulse aids in achieving stress equilibrium (or force equilibrium as studied by W. Chen et al.) and the reduction in high frequency components of the incident pulse limits the effects of wave dispersion. Pulse shapers can also assist in obtaining a constant strain rate. Using pulse shaping and a specimen with a small aspect ratio (1.53 mm thickness, 12.7 mm diameter) W. Chen et al. (Chen W L. F., 2002) observed near perfect force equilibrium across an RTV 630 silicon rubber specimen at a strain rate of 3200 s^{-1}. A low density polyurethane foam specimen was also utilized with force equilibrium observed at a strain rate of 1000 s^{-1}.

In another publication W. Chen et al. (Chen W Z. B., 1999) document the development of a SHPB for testing of low impedance materials. This apparatus consisted of aluminum bars (identical dimensions to previously discussed publication) with a hollow transmission (output) bar (inner diameter: 16 mm) thereby increasing the magnitude of the transmitted strain. Pulse shaping was also used to more gradually develop strain in the incident bar and in the specimen to aid in developing stress equilibrium across the specimen. A small aluminum end cap was positioned between the specimen and the hollow transmission bar. The specimen consisted of RTV 630 silicon rubber with an initial diameter of 12.7 mm and thickness ranging from 1.54 to 6.34 mm. The strain rate varied with specimen thickness, strain rates of 7960, 6380, and 4480 s^{-1} were observed. The largest specimen did not produce satisfactory results as a result of poor dynamic stress equilibrium. The 1.54 and 3.14 mm thickness specimens yielded similar, satisfactory results.

Collaboration between researchers in Canada and China (Chen R, 2009) has produced a modified SHPB for soft materials at intermediate strain rates. This apparatus consists of an 800 mm long, 25 mm diameter steel striker bar; a 12.5 mm diameter, 2.5 mm thick rubber pulse shaper; and 25 mm diameter 7075 aluminum input and output bars. To achieve low strain rates the incident pulse length must increase such that incident and transmission bars must be very long to avoid overlapping pulses. If the bars are not

sufficiently long and the pulses overlap, multiple strain gauges can be used to separate the pulses. To avoid these difficulties the authors used a laser based device to measure the length of the specimen directly and from this data calculated the specimen strain. To determine the stress in the specimen quartz crystal force transducers were positioned at both ends of the specimen. The specimen consisted of a silicon foam rubber purchased from McMaster-Carr. Stress-strain curves were obtained for strain rates of 29, 63, 94, and 177 s^{-1}.

Nie et al. at Purdue University (Nie X, 2009) have developed a split Hopkinson tension bar for dynamic tensile characterization of soft materials. Their apparatus consists of a tubular striker concentric to a flanged incident bar. The momentum of the striker is transferred to the incident bar when the striker impacts the flange. To ensure repeatability the impact speed was higher than necessary: a momentum diversion bar was located adjacent to the incident bar (opposite the specimen) to immediately absorb a portion of the energy transferred to the incident bar by the striker. The specimen (ethylene-propylene-diene monomer (EPDM) rubber) consisted of a tubular sample, shown to reduce inertial effects, clamped to the incident and transmission bars. The stress-strain response of the tubular sample was compared with solid and hollow samples and a significant difference was observed in favour of the tubular sample. Quartz crystal force transducers were used to ensure dynamic stress equilibrium of the sample. Stress-strain curves were obtained for strain rates of 1000 and 2000 s^{-1}.

Song et al. at Purdue University in Indiana (Song B S. C., 2008) have developed a long split Hopkinson pressure bar (LSHPB) for characterizing soft materials at intermediate strain rates. The LSHPB consists of 7075-T6 aluminum bars 19.05 mm in diameter with an overall length of 27.4 m including the 4.6 m gas gun. Manufacturing limitations required the incident and transmission bars to each be separated into three segments each with a length of 3.66 m. The overall length of the bars allows loading pulses with a long duration required for low to intermediate strain rates without pulse overlap. Multiple strain gauges on the incident and transmission bars, which were not necessary since the pulses do not overlap, were used to assess wave propagation disturbances resulting from the joints. Additionally, pulse shaping was used to eliminate the need for wave

dispersion correction and to benefit from other advantages of this technique including a more constant strain rate. The apparatus was validated with a polymeric isocyanate (PMDI) rigid foam, the mechanical characteristics of which were also evaluated with a conventional material testing system (MTS). The two apparatuses for material characteristic evaluation produced comparable results for similar strain rates.

Song et al. (Song B G. Y., 2007) have also thoroughly investigated the effects of radial inertia in soft materials on the results of SHPB material testing. When using a SHPB apparatus to investigate the mechanical properties of soft materials a significant local maximum with short duration occurs early in the stress time history. The authors provide strong evidence that this stress spike is due to the radial inertia of the specimen and several methods to reduce this systematic error are discussed in the publication. It was observed that radial inertia effects can be controlled through specimen geometry and initial acceleration. Solid disk and annular ring specimen geometries were investigated with significant reductions in inertial effects with use of an annular ring. Pulse shaping was also successfully used to limit the initial acceleration. Another important topic in this publication, although not featured prominently, is the discussion of interface friction. With numerical simulation the authors found that interface friction did not affect the specimen response significantly. All further numerical analyses assumed that the interfaces were frictionless.

Zhao et al. (Zhao H, 1997) have documented the use of viscoelastic materials (polymers) in the construction of a SHPB. Polymeric materials, with their reduced stiffness, density, and wavespeed with respect to metals are well suited for SHPB apparatuses for soft materials. The authors recommend that polymeric SHPBs use bars with a large diameter due to the decreased stiffness of the material which may permit buckling of bars with a small diameter. It is also noted that a striker bar consisting of a material with a higher impedance than the input bar would produce an incident pulse similar in profile to a staircase. A striker bar with low impedance rebounds and produces an incident pulse with a low magnitude. A polymeric striker bar will produce an incident pulse with a long wavelength with respect to the length of the striker and can therefore be shorter in length.

Chapter 3: Scope of Research

The contribution of NVH isolators to the crash performance of the automobile has clearly been a topic of interest for Ford, Volvo, and Chrysler engineers. In the case of Ford existing research has focused on studying this contribution experimentally. Their published research is also dated and focuses on the development of methodologies for idealizing these isolators as a combination of springs and dampers. Consistent with key findings from Ford, publications by Chrysler engineers focused on the bolted connections between these isolators and the vehicle body. However, as this research evolved issues with numerical instabilities were observed as a result of the large deformations of the hyperelastic material.

This research consisted of a thorough development of methodologies for finite element modeling of automotive noise and vibration isolators with a focus on the crashworthiness application. To ensure the comprehensiveness of this research every step in the modeling process including material characterization, material model selection, the development of finite element models, and experimental validation was included. At each step the crashworthiness application and its requirements were also considered.

Chapter 4: Methodology

The methodology employed in this research consisted of three fundamental processes: material characterization, finite element modeling of a Chrysler powertrain suspension component, and model validation with respect to data from experimental characterization of this component. This process is depicted in Figure 8. Material characterization consisted of quasi-static and dynamic material characterization completed primarily by Chrysler engineers working with AXEL Products Physical Testing Services in Michigan. To have a thorough understanding of this process additional quasi-static material characterization was completed in a FIAT polymer laboratory. To optimize the process of using the acquired material data, finite element models of the material characterization processes were developed to complete extensive parametric studies of modeling techniques including, but not limited to, material model selection and implementation. Once a thorough understanding of the fundamentals of hyperelastic material modeling had been developed, finite element models of a Chrysler powertrain suspension component were built and further parametric studies were completed to consider additional modeling parameters. This research was concluded by experimental mechanical characterization of the powertrain suspension component under quasi-static and dynamic conditions and model validation with respect to the data acquired.

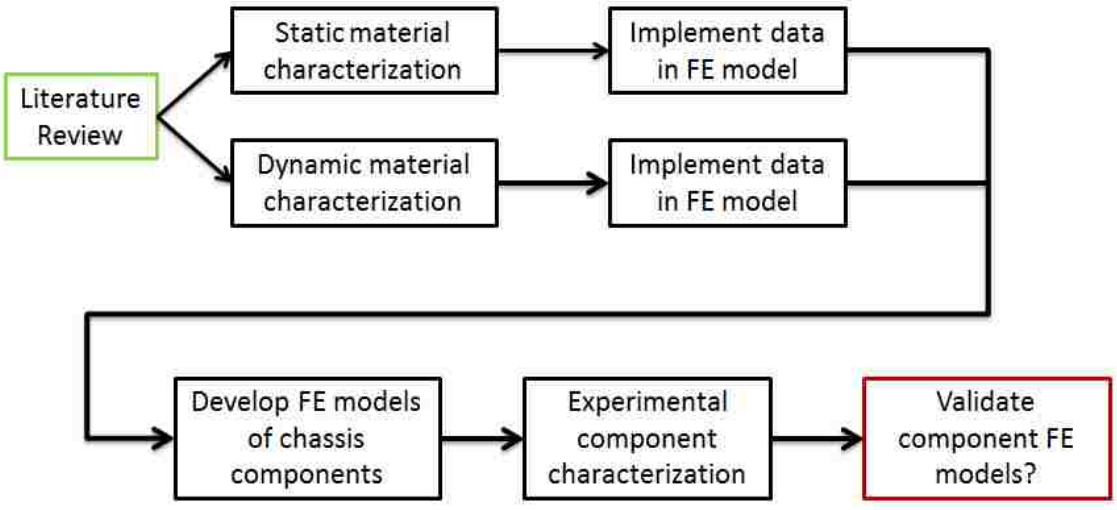

Figure 8: Methodology roadmap.

4.1 Quasi-Static Material Characterization

Static material characterization was completed in the FIAT Mirafiori polymer laboratory under the supervision of Paolo Chiappero and with the assistance and guidance from other staff in this laboratory. The static material characterization process consisted of three test configurations: tensile, compressive, and shear testing. Simple tension material characterization was completed consistent with ASTM standard D412 and simple compression consistent with D575. Material testing specimens were extracted from three Chrysler RT platform engine/transmission mounts supplied by Chrysler (part number 05273996AE). Three ASTM D412 die D tensile testing specimens (dumb-bell type) were extracted from one engine/transmission mount. This was consistent with ASTM standard D412 which recommends each test be completed three times to assess and ensure repeatability.

Static and dynamic material characterization was also completed by Chrysler Technical Center (CTC) engineers in conjunction with AXEL Products Physical Testing services in Ann Arbor Michigan. AXEL's procedures included tensile, compression, pure shear, and equibiaxial tension material testing. The data from this testing was compared to the data obtained in the FIAT laboratory with the goal of producing consistent results. However, procedures may have varied particularly for the shear testing since there is no standard for this method of material characterization. For tensile and compression testing non-standard specimen sizes were used in the FIAT laboratory due to the geometrical restrictions resulting from the extraction of specimens from the Chrysler engine/transmission mount.

Figure 9: Removal of rubber segments to prepare quasi-static material characterization specimens (simple compression specimen preparation shown).

The procedure for extracting specimens consisted of 5 steps: removal of the stamped steel brackets with a hacksaw (Figure 9); division of rubber portion to improve accessibility for future steps; removal of rubber with a sharp knife with a long, thin, and flat blade; dissection of rubber into pieces suitable for extracting the given specimen size; accurately reducing section thickness prior to specimen extraction; use of a die and a press to cut specimens. As rubber segments were removed from the engine mounts the position of each piece of rubber was tracked by marking each piece and taking photographs as shown by Figure 9. In this figure rubber is being extracted to prepare specimens for simple compression testing. The notation indicated that this was engine mount #2 and compression specimens 1 through 4. The thicknesses of rubber pieces extracted from the mount were finely controlled using a Fortuna leather scarfing or skiving machine (Figure 10). A piece of rubber with a non-uniform cross section was run through this device which reduces the irregular thickness to a highly controlled uniform thickness with a good surface finish. This machine can also be used to extract slabs of a precise but minimal thickness; on each pass of a piece of material through the machine a thin layer is removed. The thickness of this layer can be controlled and any material removed after the first pass through the machine is of a reasonably consistent thickness.

Figure 10: Fortuna leather skiving machine in FIAT Mirafiori polymer laboratory.

All specimen dimensions were identified using an optical measurement system (optical comparator) in the FIAT polymer laboratory developed by Microtechnica (Figure 12). Specimens were placed on a platen directly between a lens and a light source. The shadow is projected upon a screen with an increase in size due to the magnification of the lens. There were 3 lenses to select from: 5X, 10X, and 20X. The projected image was then measured using a ruler or a digital position readout similar to those found on milling machines. The platform on which the specimen was placed could be translated and a point on the projection tracked to determine dimensions. The specimen was also traced upon tracing paper so that it might be studied or digitized later. Apparatuses consistent with Figures 2, 4, and 5 of ASTM standard D3767, an example of which is shown in Figure 11, were also used to quickly assess specimen thickness but with less precision. The nature of the projected image and the contact area of the device in Figure 11 make it difficult to clearly identify which is more accurate.

Figure 11: Mitotoyo measuring device consistent with ASTM standard D3767 for measuring thickness of rubber components with a specified force of compression.

Figure 12: Microtechnica optical metrology system.

Tensile, compression, and pure shear tests were performed with a Zwick/Roell Z020 testing machine. This testing machine is equipped with two cameras which were used to optically measure strain during tensile tests. The strain is automatically calculated by Zwick Roell TestXpert proprietary software which is included with the testing apparatus.

Two different load cells were used in the course of this research, one for tensile tests and another for compression tests due to the different force magnitudes expected. For tensile testing a Zwick Roell Xforce HP load cell with a nominal force capacity of 500 N was used (S/N 753 066). For compression tests a Zwick Roell Xforce K load cell was used (nominal force of 20 kN, S/N 752 780).

Planar tension (pure shear) and equibiaxial tension material characterization was completed by Chrysler engineers in conjunction with AXEL Products Physical Testing Services. The pure shear test is depicted in Figure 13. The specimen consists of a long and thin rectangular prism of material. In the undeformed state the specimen width must be at least 10 times the height and thickness which are commonly identical or determined by sample dimensions from which specimens are extracted. Pure shear specimens were prepared at the FIAT Mirafiori polymer laboratory but the testing was not completed. Specimens were 50mm x 5mm x 5mm. The equibiaxial tension test is shown in Figure 14 followed by a drawing of the specimen in Figure 15.

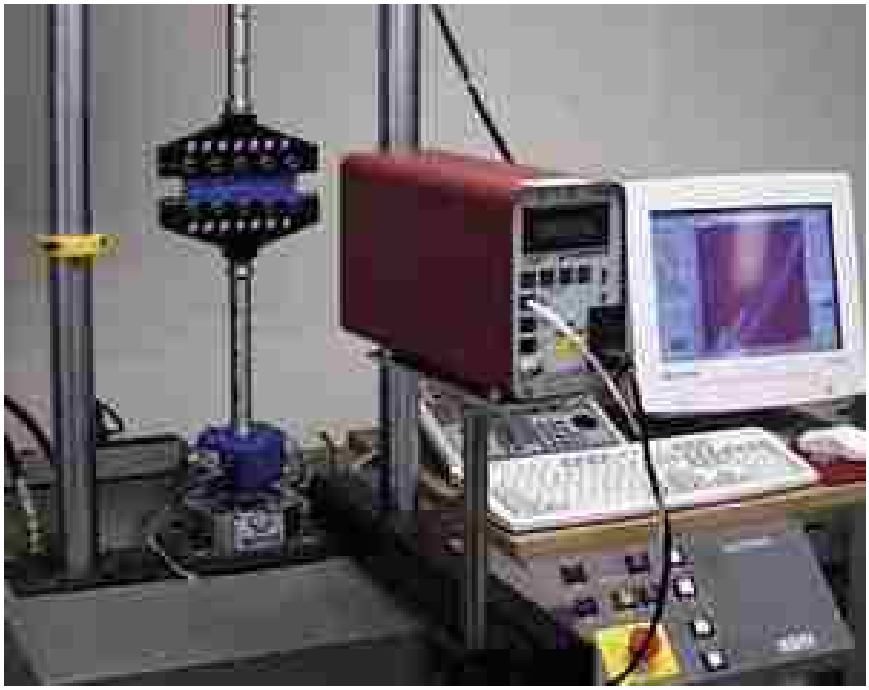

Figure 13: Pure shear (planar tension) material characterization.

Figure 14: Equibiaxial tension material characterization.

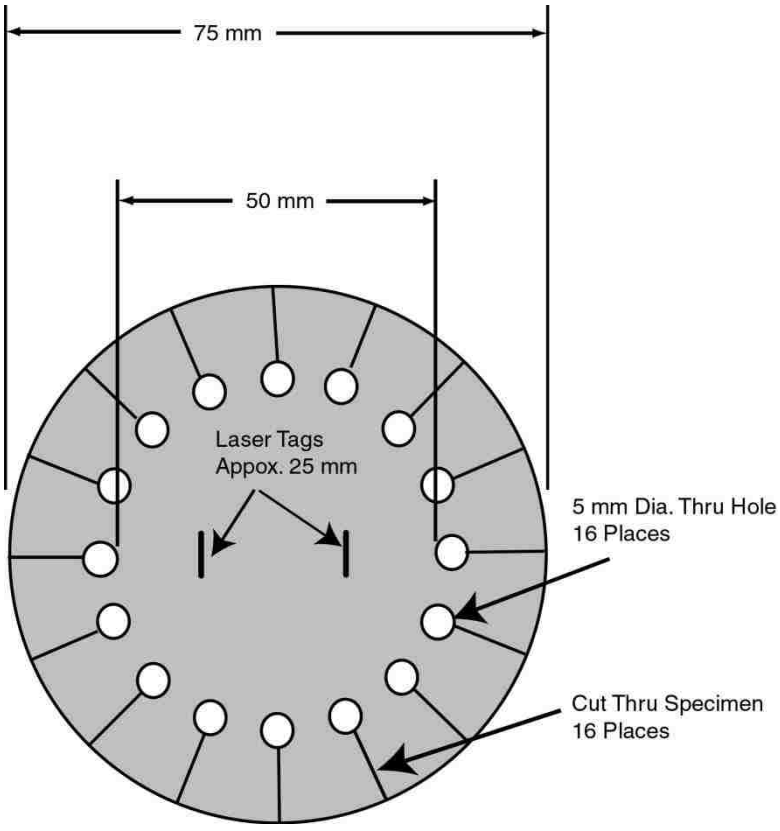

Figure 15: Equibiaxial tension specimen dimensions.

4.2 Dynamic Material Characterization

Dynamic material characterization was completed by AXEL Products Physical Testing Services. This material characterization consisted of simple tension and simple compression processes at different loading rates and using different specimen geometries to obtain desired strain rates. Split Hopkinson Pressure Bar material characterization was also partially completed at the DYNLab in the Vercelli campus of the Politecnico di Torino in Italy. The difficulties presented in the literature review for SHPB testing of soft materials resulted in challenges in obtaining high quality data.

4.3 Finite Element Modeling of Quasi-Static Material Characterization

Finite element models of the quasi-static material characterization procedures were developed as a simple assessment of modelling parameters including but not limited to material models. These finite element models also ensured that the material data was implemented into the finite element code correctly both by the user and internally within the software. Finite element models were developed for simple tension, simple compression, planar tension (pure shear), and equibiaxial tension material characterization procedures. This process was critical in assessing the capabilities of various material models to accurately capture the response of a hyperelastic material with different loading configurations.

4.3.1 Single Element Models

The modeling portion of this research began with the creation of very simple models of single element in pure tension. These models consisted of a single element with boundary conditions consisting of three planes of symmetry on three faces of a perfect cube sharing a vertex and prescribed displacement of one of the other faces in the normal direction. Three different material models were compared: MAT 181 (Simple Rubber/Foam), MAT 77H (Hyperelastic), and MAT 77O (Ogden). The engineering stress-strain input to these models was from simple tension tests completed at the FIAT polymer laboratory with ASTM standard D412 type D specimens and from material

testing completed for Chrysler by AXEL Products Physical Testing Services. A critical analysis compared models with material model inputs of solely tensile engineering stress-strain data or with uniaxial (tension and compression) stress-strain input.

4.3.2 Simple Tension Finite Element Models

After the very simple analyses of a single element more complex models of common material testing processes were developed. The simple tension models consisted of specimen type D from ASTM standard D412. Coarse and fine discretizations were constructed using both hexahedron and tetrahedron elements. The coarse meshes had an approximate average element edge length of 2.5 mm; the respective length for the fine meshes was 1 mm. Hexahedron element formulations 1, 2, and 3 in LS-DYNA were compared as were tetrahedron element formulations 4, 10, 13, 16, and 17. Formulations 1, 10, and 13 are under-integrated; formulations 2, 4, 16, and 17 use selectively reduced integration; and formulation 3 is fully integrated with additional degrees of freedom: nodal rotations. Initially MAT 181 Simple Rubber/Foam was employed with stress-strain data obtained by Chrysler through AXEL Physical Testing Services. As shown in Figure 16, one end of the specimen was fixed using nodal constraints applied with the keyword *BOUNDARY_SPC_SET. A node set was used to create a nodal rigid body at the opposite end of the specimen using the keyword *CONSTRAINED_NODAL_RIGID_BODY_SPC. This rigid body was translated using *BOUNDARY_PRESCRIBED_MOTION_RIGID_BODY. Meshing was completed, where possible, consistent with Chrysler protocols which can be found in Table 3 in which the mesh quality of the models is also tabulated. The quality of each mesh was assessed in ANSA. In this software the warping metric is calculated for each face of a solid element and the least optimal value is assigned to the element.

Table 2: Chrysler meshing guidelines and simple tension model quality, tetrahedron meshes.

Mesh Characteristic	Limit	Coarse mesh	Refined mesh
Critical length (mm)	N/A	1.41	0.570
Aspect ratio	8 (max)	6.99	5.21
Skewness	0.5 (max)	0.971	0.808
Min. angle, tetrahedrons	30°	14.20°	20.90°
Max. angle, tetrahedrons	120°	156.7°	141.4°

Table 3: Chrysler meshing guidelines and simple tension model quality, hexahedron meshes.

Mesh Characteristic	Limit	Coarse mesh	Refined mesh
Critical length (mm)	N/A	1.5	0.57
Aspect ratio	8 (max)	3.8	3.8
Warping	10	0.0065	0.0065
Jacobian	0.6	0.662	0.648
Min. angle, pentahedrons	30°	50.4°	N/A
Max. angle, pentahedrons	120°	90.0°	N/A
Min. angle, hexahedrons	30°	48.4°	57.7°
Max. angle, hexahedrons	140°	126.1°	132.1°

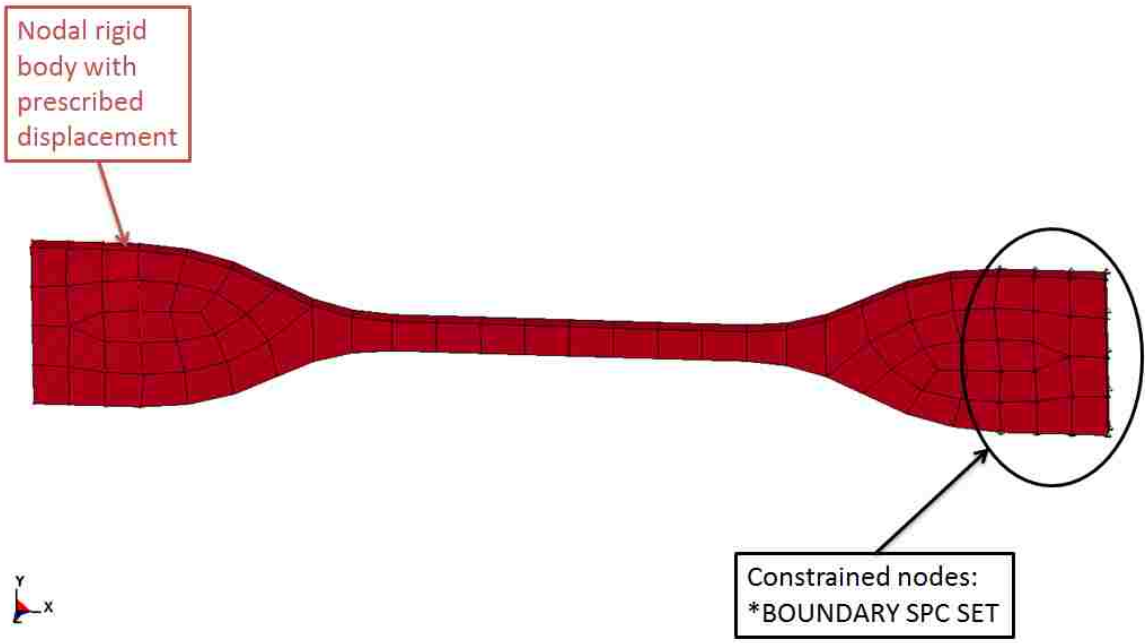

Figure 16: Simple tension (ASTM D412 Type D) finite element model, coarse mesh.

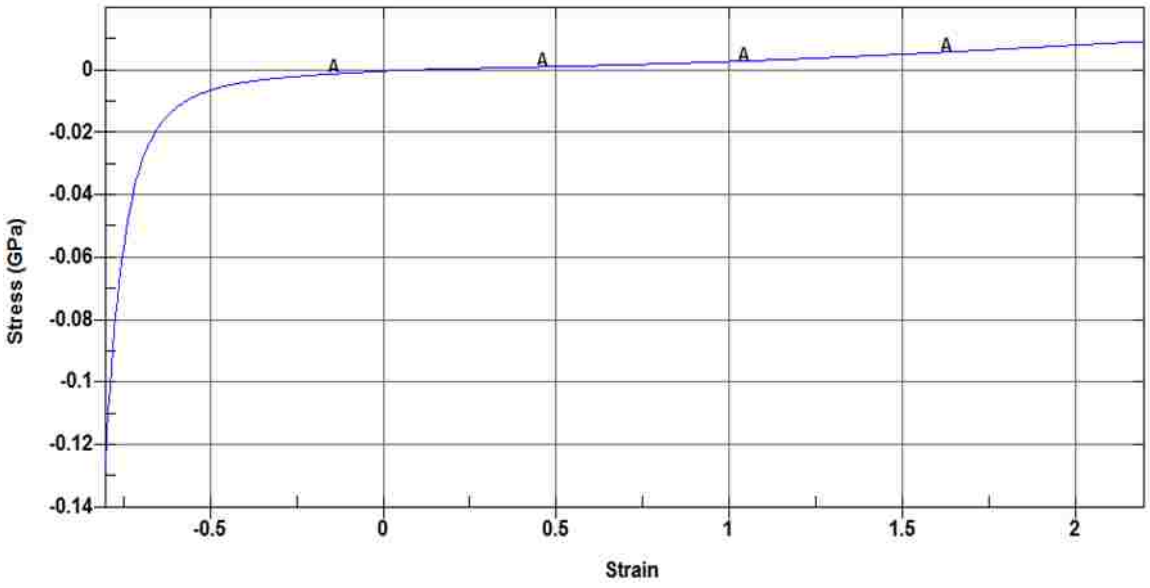

Figure 17: Engineering stress-strain input to MAT 181 for finite element models of quasi-static material characterization processes.

4.3.3 Simple Tension Finite Element Models with Automatic Tetrahedron Remeshing

In an attempt to use the automatic 3D solid tetrahedron remeshing capabilities of LS-DYNA, models of the simple tension material characterization process were developed compatible with the requirements of this tool. Building a model compatible with automatic tetrahedron remeshing can be challenging since node and element numbering change. Contact algorithms must use part numbers or part sets and data output is restricted since node sets cannot be used for nodes for which the node numbers may change. The methodology employed for this model was to use rigid bodies to apply boundary conditions (constraints and prescribed motion). As shown in Figure 18, a single deformable element was a separate part and remeshing for this part was not activated allowing the output of nodal displacements and/or element stress and strain. The rigid bodies and deformable parts were connected using a tied contact algorithm (*CONTACT_AUTOMATIC_SURFACE_TO_SURFACE_ TIEBREAK) with the default OPTION=1 for which nodes initially tied by contact are permanently connected.

Table 4: Chrysler meshing guidelines and mesh quality for simple tension model with automatic re-meshing

Mesh Characteristic	Limit	Coarse mesh
Critical length (mm)	N/A	1.41
Aspect ratio	8 (max)	6.99
Skewness	0.5 (max)	0.971
Min. angle, tetrahedrons	20°	14.2°
Max. angle, tetrahedrons	120°	156.7°

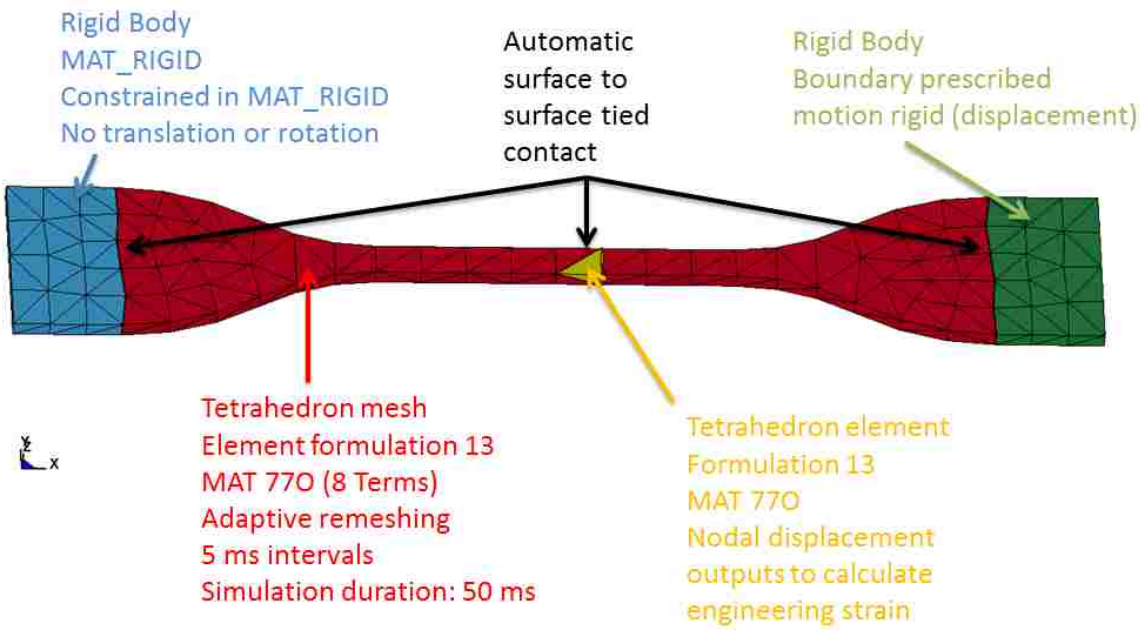

Figure 18: Simple tension finite element model compatible with automatic tetrahedron remeshing.

4.3.4 Simple Compression Finite Element Models

Simple compression models were based upon the specimen in ASTM standard D575: a cylinder with a diameter of 28.8 mm and a thickness of 12.5mm. Fine and coarse meshes of hexahedron and tetrahedron elements were constructed with average element edge lengths of 5 mm for coarse meshes and 1 mm for the fine discretizations. The same element formulations employed for the simple tension models were used in these analyses. As shown in Figure 19, three planes of symmetry were considered to increase the computational efficiency and provide constraints. If planes of symmetry were not considered and the specimen was not constrained, rigid body translation in a radial direction occurred. Hourglass control type 7 ($Q_M = Q_B = Q_W = 0.01$) was used with element formulation 1. Nodal rigid bodies were not used here since this would restrict the lateral expansion of the specimen.

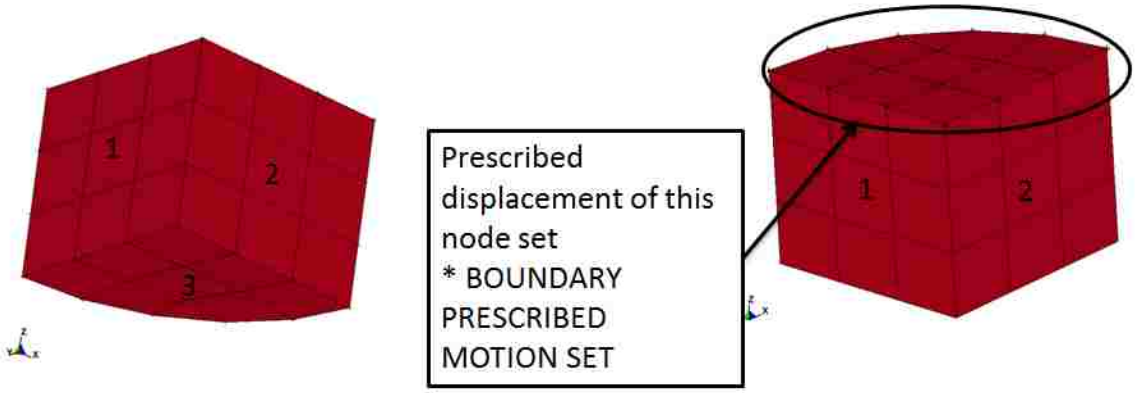

Figure 19: Simple compression finite element model, coarse mesh. Three planes of symmetry labeled 1, 2, and 3.

Table 5: Chrysler meshing guidelines and simple compression model quality, tetrahedron meshes.

Mesh Characteristic	**Limit**	**Coarse mesh**	**Refined mesh**
Critical length (mm)	N/A	3.64	1.18
Aspect ratio	8 (max)	3.02	4.38
Skewness	0.5 (max)	0.506	0.760
Min. angle, tetrahedrons	30°	32.5°	19.0°
Max. angle, tetrahedrons	120°	126°	148°

Table 6: Chrysler meshing guidelines and simple compression model quality, hexahedron meshes.

Mesh Characteristic	Limit	Coarse mesh	Refined mesh
Critical length (mm)	N/A	3.64	1.18
Aspect ratio	8 (max)	1.29	1.77
Warping	10	~ 0	~ 0
Jacobian	0.6	0.817	0.794
Min. angle, pentahedrons	30°	52.0°	47.7°
Max. angle, pentahedrons	120°	90.0°	90.0°
Min. angle, hexahedrons	30°	67.8°	61.5°
Max. angle, hexahedrons	140°	118°	126.2°

4.3.5 Planar Tension (Pure Shear) Finite Element Models

The planar tension (pure shear) specimen was modeled based upon the specimen used in the FIAT Mirafiori polymer laboratory. This specimen is a 5 mm x 5 mm x 50 mm rectangular prism bonded (using an adhesive) on two opposite 5 mm x 50 mm faces to aluminum blocks through which a tensile load is applied. A state of pure shear exists in this specimen on a plane at 45 degrees to the bonded surfaces. The finite element model of this material characterization procedure was very similar to the simple tension model with the exception of the geometry. All of the nodes on one of the faces adhered to an aluminum fixture were fixed to not permit translation or rotation. The nodes on the opposite face were specified to be a nodal rigid body with only one degree of translational freedom. A prescribed motion was then applied to this nodal rigid body. A model with a coarse mesh is depicted in Figure 20. Nodal displacement data was extracted for two nodes of the specimen to approximate the laser displacement transducer used by AXEL to acquire the strain/time data. This model was validated with respect to data provided by AXEL; correspondingly the method of acquiring the numerical strain/time history was chosen to be consistent with their testing methodology. The specimen geometry was chosen to be consistent with the FIAT procedure due to familiarity with their methodology.

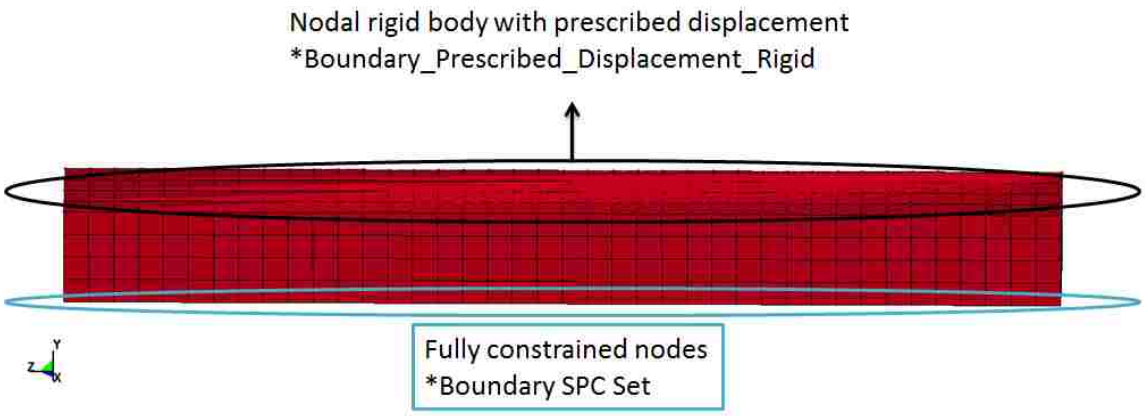

Figure 20: Planar tension (pure shear) finite element model, coarse mesh.

Table 7: Chrysler meshing guidelines and planar tension (pure shear) model quality, tetrahedron meshes.

Mesh Characteristic	**Limit**	**Coarse mesh**	**1st level of mesh refinement**	**2nd level of mesh refinement**	**3rd level of mesh refinement**
Critical length (mm)	N/A	1.77	0.783	0.457	0.195
Aspect ratio	8 (max)	4.24	4.25	6	5.49
Skewness	0.5 (max)	0.863	0.736	0.929	0.848
Min. angle, tetrahedrons	30°	20.8°	18.8°	17.5°	16.1°
Max. angle, tetrahedrons	120°	139°	147°	153°	154°

Table 8: Chrysler meshing guidelines and planar tension (pure shear) model quality, hexahedron meshes.

Mesh Characteristic	**Limit**	**Coarse mesh**	**1st level of mesh refinement**	**2nd level of mesh refinement**	**3rd level of mesh refinement**
Critical length (mm)	N/A	2.5	1.25	0.625	0.3125
Aspect ratio	8 (max)	1	1	1	1
Warping	10	0	0	0	0
Jacobian	0.6	1	1	1	1
Min. angle, pentahedrons	30°	N/A	N/A	N/A	N/A
Max. angle, pentahedrons	120°	N/A	N/A	N/A	N/A
Min. angle, hexahedrons	30°	90°	90°	90°	90°
Max. angle, hexahedrons	140°	90°	90°	90°	90°

4.3.6 Equibiaxial Tension Finite Element Models

The finite element model of the biaxial tension material characterization procedure was constructed to be consistent with the testing completed by AXEL. This method of material characterization was not completed in the FIAT polymer laboratory. One challenge would have been the extraction of a suitable specimen from the engine mounts supplied by Chrysler. The finite element model is depicted in Figure 21. Similar to previous models nodal rigid bodies were created where boundary conditions were prescribed to the model. These rigid bodies were constrained to not allow translation in the z-direction or any rotation. Rigid body displacements in the x and y directions were calculated for each nodal rigid body to obtain purely radial translations of each rigid body. Strains were measured near the origin where the two planes of symmetry met by outputting the displacements of two neighbouring nodes. This is consistent with the laser displacement transducer used by AXEL.

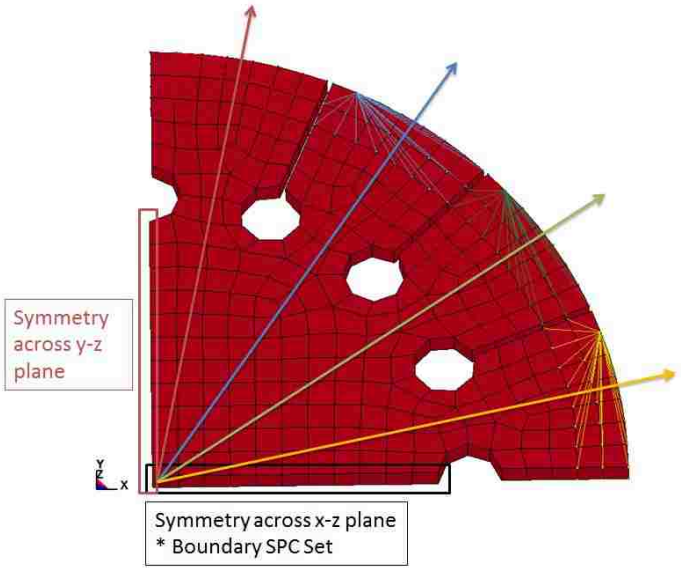

Figure 21: Equibiaxial tension finite element model, coarse mesh.

Table 9: Chrysler meshing guidelines and equibiaxial tension model quality, tetrahedron meshes.

Mesh Characteristic	**Limit**	**Coarse mesh**	**1st level of mesh refinement**	**2nd level of mesh refinement**
Critical length (mm)	N/A	1.23	0.591	0.283
Aspect ratio	8 (max.)	4.09	4.59	6.71
Skewness	0.5 (max.)	0.751	0.793	0.929
Min. angle, tetrahedrons	30°	24.9°	22.6°	13.6°
Max. angle, tetrahedrons	120°	132°	148.6°	157°

Table 10: Chrysler meshing guidelines and equibiaxial tension model quality, hexahedron meshes.

Mesh Characteristic	**Limit**	**Coarse mesh**	**1st level of mesh refinement**	**2nd level of mesh refinement**
Critical length (mm)	N/A	1.23	0.591	0.283
Aspect ratio	8 (max.)	2.34	1.92	2.30
Warping	10 (max.)	~ 0	~ 0	~ 0
Jacobian	0.6	0.457	0.591	0.543
Min. angle, pentahedrons	30°	N/A	47.1°	N/A
Max. angle, pentahedrons	120°	N/A	90°	N/A
Min. angle, hexahedrons	30°	39.8°	42.6°	41.2°
Max. angle, hexahedrons	140°	161°	140.1°	138°

4.3.7 Single Element Models to Validate Strain Rate Sensitivity Capabilities of MAT 181

Single element models were used to assess the capability of MAT 181 to model the strain rate sensitivity of the material. This capability requires uniaxial stress-strain data be input in a tabular format with each stress-strain data set associated with a strain rate. This strain rate can be an engineering strain rate or a true strain rate. As shown in Figure 22 and Figure 23 the strain rate sensitivity data provided by AXEL contained inconsistencies. In tension the behaviour of the material was reasonable with the only slight discrepancy at a strain of approximately 125% where the stress, at this strain, was higher for the two lowest strain rates with respect to the stress associated with the 3rd largest strain rate (1 1/s). The simple compression data was less ideal. The stiffest response (and the highest stress for a given strain) at large strains (>70% compressive) was associated with the 2nd lowest stain rate (0.1 1/s). For strains less than 70% this stress-strain curve was also unexpectedly stiff. The stress-strain curve associated with the lowest strain rate (0.01 1/s) was also surprisingly stiff but only at very large strains.

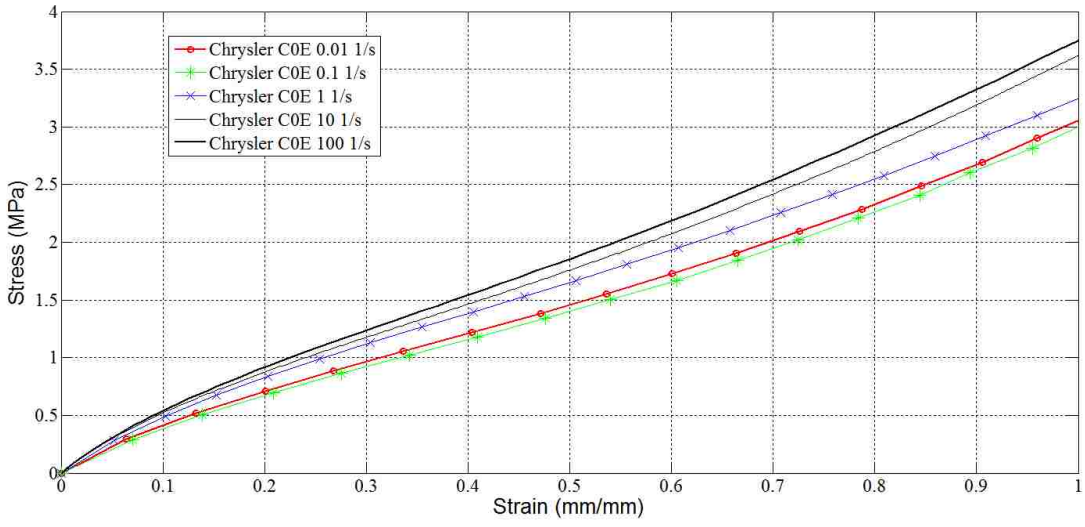

(a)

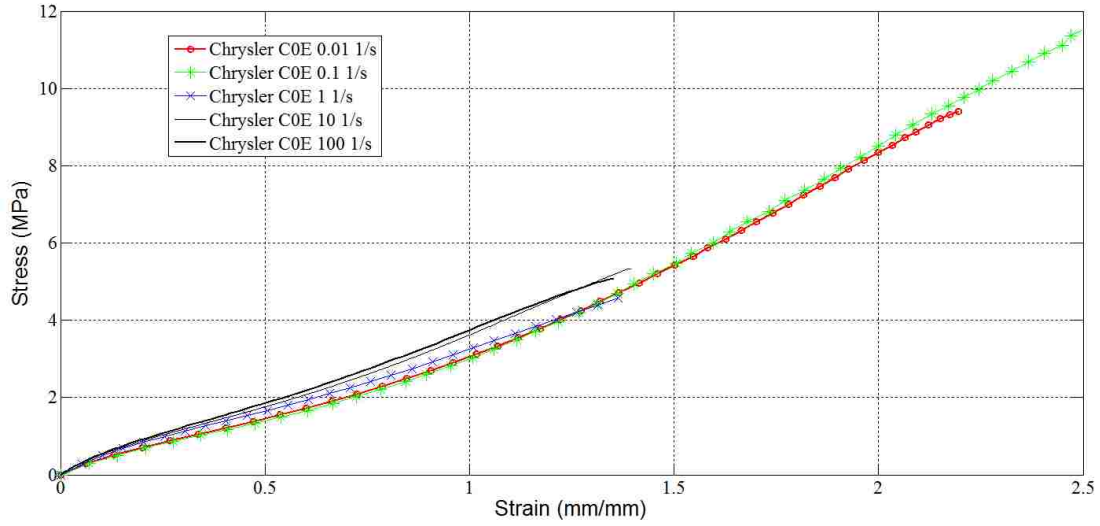

(b)

Figure 22: AXEL simple tension data, rubber C0E, strain rate sensitivity analysis, (a) small strains, (b) complete stress-strain response.

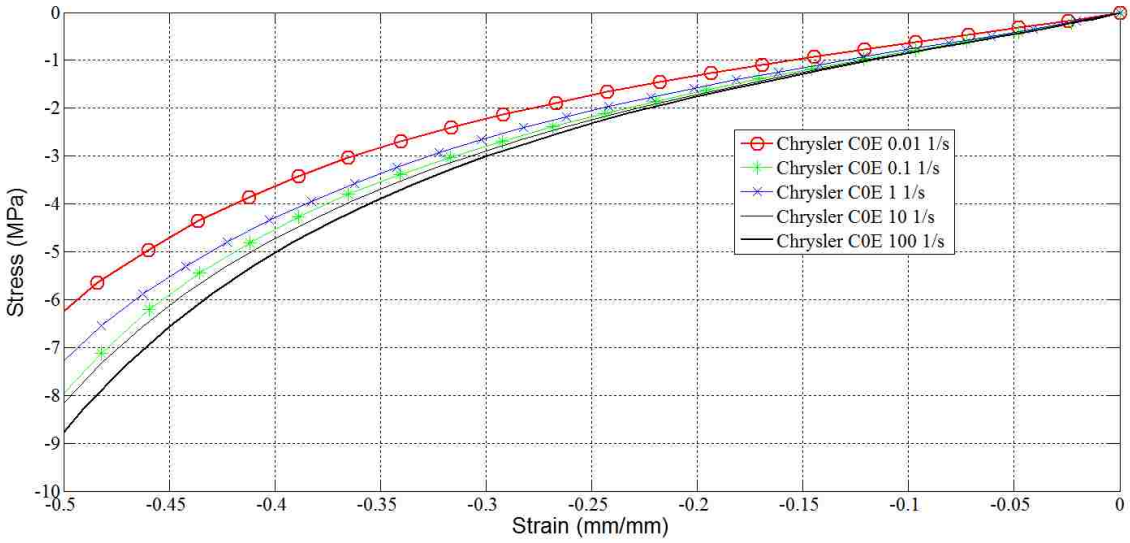

(a)

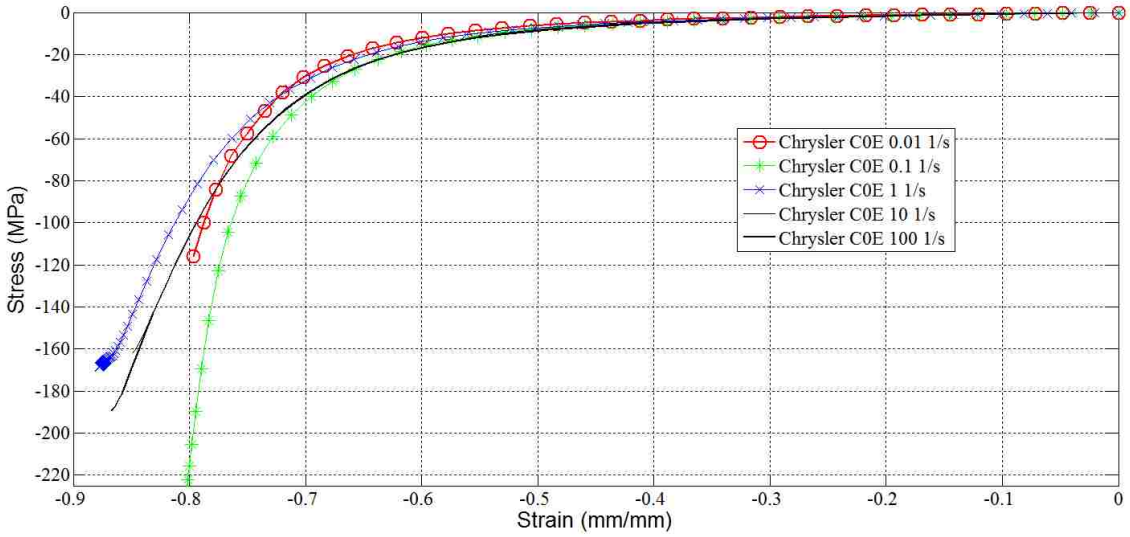

(b)

Figure 23: Simple compression AXEL data, strain rate sensitivity analysis, (a) small strains, (b) full stress-strain curves.

The relatively small increase in stiffness with increasing strain rate and the inconsistent results resulted in a decision to select two stress-strain curves, one at a low strain rate and the other at a high strain rate. The lowest and highest strain rate data sets were selected (0.01 and 100 1/s). However, to eliminate the intersection between the two curves, stress strain data for compressive strains larger than 70% were eliminated for both sets of data. At this level of strain there is an approximately constant offset between the two curves. The input data for LS-DYNA is shown in Figure 24.

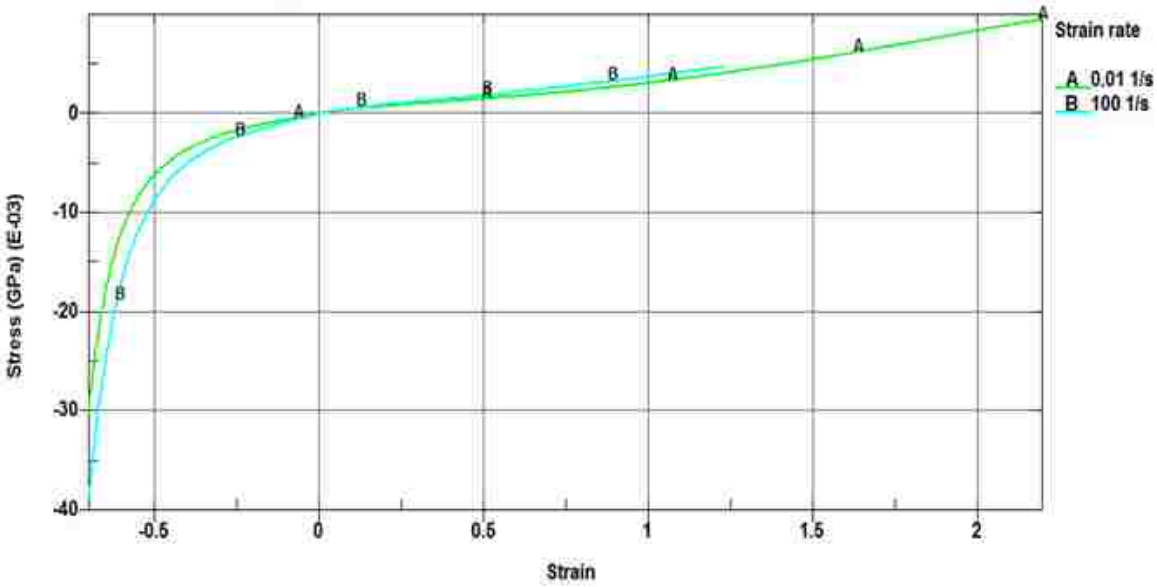

Figure 24: LS-DYNA uniaxial stress-strain input.

Single element models were developed to validate the material model's ability to capture strain rate sensitivity. Single element models were used since the strain rate of 0.01 1/s requires a termination time on the order of 100 seconds to achieve a strain of 100 %. A specimen of realistic dimensions would require elements with an average edge length on the order of 1 mm with a critical time step of approximately 2E-5 seconds. Therefore, the number of time steps required is approximately 5 million. While a larger element size could be used the approach taken was to use a reasonable element size and one element. Previous work modelling ASTM specimens and using single element models did not reveal an especially significant difference in the capability of capturing a uniaxial state of stress.

4.4 Finite Element Modeling of Quasi-Static Material Characterization with MAT 77O (Ogden)

Several approaches were taken to implementing the Ogden material model. As shown previously with single element models, MAT 77O was specified with material stress-strain data input directly. LS-DYNA internally determined the coefficients for the Ogden strain energy density function. However, the LS-DYNA user's manual suggests that the curve fit should be investigated by the user by extracting the Ogden strain energy function coefficients identified by LS-DYNA and output to the d3hsp file. The function should be plotted in a suitable software package and a comparison drawn with the input data. A similar approach was taken using MATLAB. However, to aid in this process and provide a concomitant method, a student version of the finite element software package MARC-Mentat was used. MARC-Mentat features a simple interface for plotting several types of material characterization data, determining material model coefficients, and plotting the material model alongside the material data for comparison. A similar interface exists in ABAQUS CAE but is more restrictive. As an example, MARC-Mentat permits any data (ie. pure shear, equibiaxial tension, uniaxial, or any combination) to be used to determine Ogden material model coefficients. ABAQUS CAE requires a certain minimum amount of data, for example, uniaxial and pure shear, to determine material model coefficients. In any case the documentation available for these student software packages may not provide the level of detail necessary to be certain that the coefficients have been obtained correctly. A greater familiarity with the software from experience would be valuable.

The use of MARC-Mentat may be beneficial in obtaining material model coefficients that will yield a stable model. There are options to obtain only positive Ogden model coefficients and to perform mathematical checks. It is unknown what these mathematical checks are but positive coefficients may be beneficial in obtaining a stable model since they will prevent negative derivatives (with respect to strain or stretch ratio) of the strain energy functional. To be certain that MARC-Mentat was being used correctly, calculations were completed using MATLAB starting with the most basic concept of strain energy density. Hyperelastic material models like the Ogden model are based upon

strain energy density functions that relate the strain energy density to the strain. However, principal stretch ratios often replace principal engineering strain. The relationships between the principal stretch ratios for the material characterization processes are given in Table 11 where λ is the stretch ratio obtained from the engineering strain measured during the characterization process.

Table 11: Relationships between principal stretch ratios for common material characterization processes.

	λ_1	λ_2	λ_3
Simple tension or compression	λ	$\lambda^{-0.5}$	$\lambda^{-0.5}$
Pure shear (planar tension)	λ	1	λ^{-1}
Equibiaxial tension	λ	λ	λ^{-2}

These relationships are simple to derive as they are based on the near incompressibility of rubber and the boundary conditions of the material characterization specimen. With these conditions the Ogden strain energy functional can be greatly simplified to obtain a simplified form only valid for specific boundary conditions. Additionally, when the definition of strain energy density is considered one can obtain relationships between stress and stretch ratio. As an example, for a simple tension test the strain energy density is the integral of the stress-strain curve. By taking the derivative of the strain energy function with respect to the stretch ratio (see Equations 42 and 44) one obtains stress as a function of the stretch ratio. This yields the simplified form of the Ogden model in Equation 45. Similarly, relationships between stress and stretch ratio can be derived for pure shear (planar tension) and equibiaxial tension. These equations were derived after identification in a publication (Finney R, 1988).

$$d\lambda = \mathrm{d}\varepsilon \qquad \text{(Equation 48)}$$

$$W = \int \sigma_{uniaxial} \cdot d\varepsilon_{uniaxial} \qquad \text{(Equation 49)}$$

$$\sigma_{\text{uniaxial}} = \frac{\mathrm{dW}}{\mathrm{d}\lambda} \qquad \text{(Equation 50)}$$

$$\sigma_{uniaxial} = \sum_{j=1}^{n} \mu_j \left[\lambda^{\alpha_j - 1} - \lambda^{-\left(1+0.5\alpha_j\right)} \right] \qquad \text{(Equation 51)}$$

$$\sigma_{pure\ shear} = \sum_{j=1}^{n} \mu_j \left[\lambda^{\alpha_j - 1} - \lambda^{-\left(1+\alpha_j\right)} \right] \qquad \text{(Equation 52)}$$

$$\sigma_{equibiaxial\ tension} = \sum_{j=1}^{n} \mu_j \left[\lambda^{\alpha_j - 1} - \lambda^{-\left(1+2\alpha_j\right)} \right] \qquad \text{(Equation 53)}$$

Using these relationships Ogden material model coefficients identified in MARC-Mentat were used to compute the Ogden predicted stresses associated with the strains of the stress-strain curves from AXEL. Experimental curves and Ogden models were plotted for comparison with each other and with the Ogden model in MARC-Mentat and in MATLAB (see Figure 25). The Ogden model plotted in MATLAB was identical to the model plotted in MARC-Mentat.

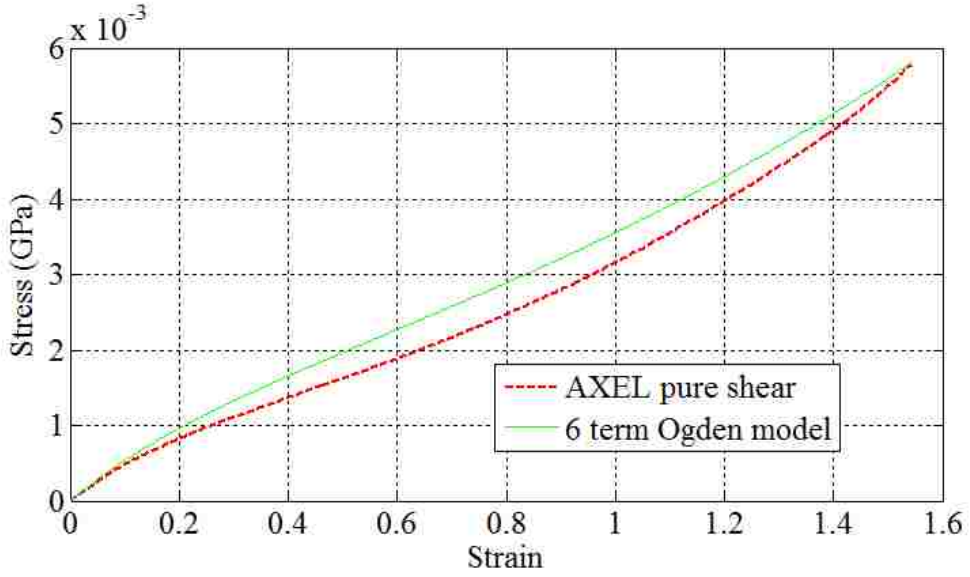
x 10^-3
Stress (GPa)
Strain
AXEL pure shear
6 term Ogden model

(a)

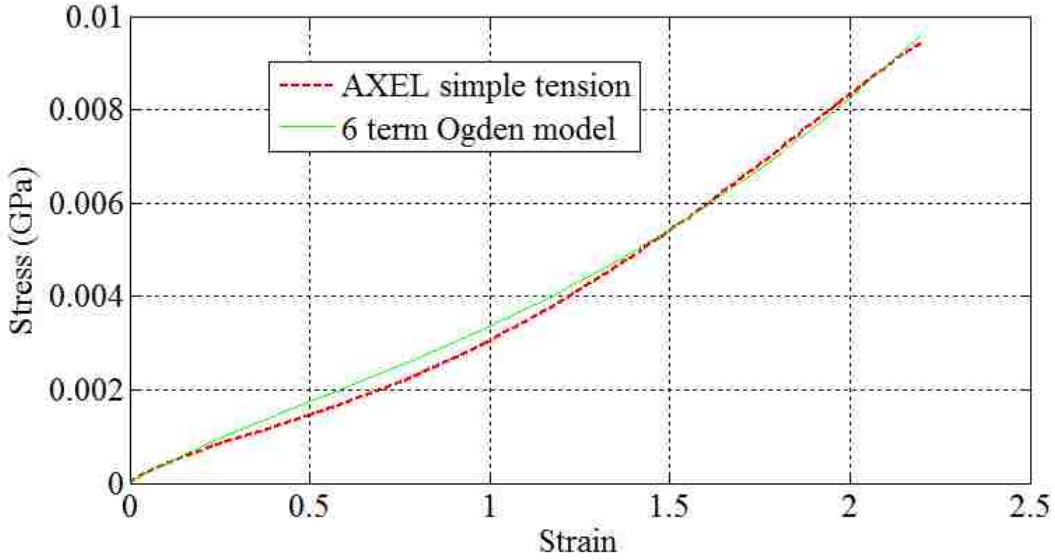
Stress (GPa)
Strain
AXEL simple tension
6 term Ogden model

(b)

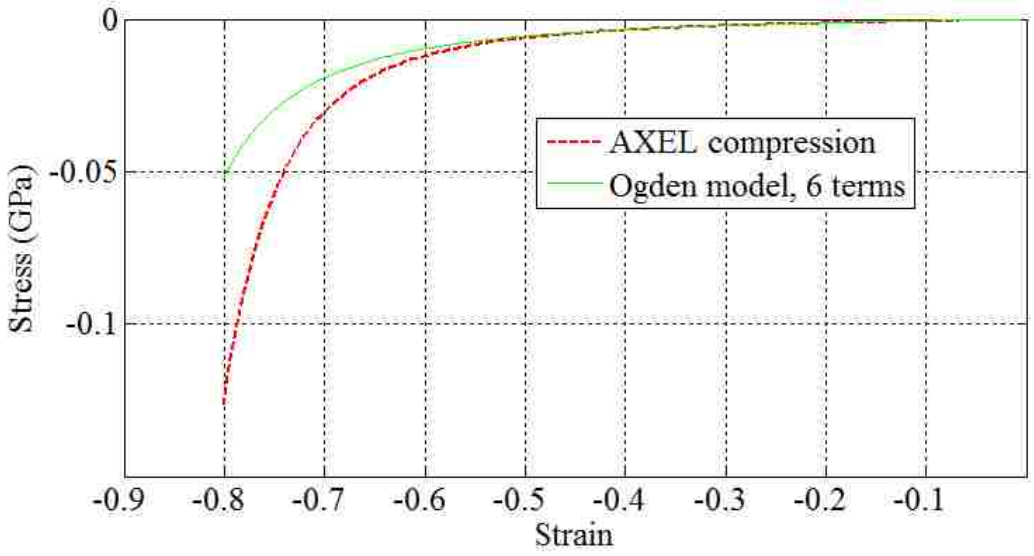

(c)

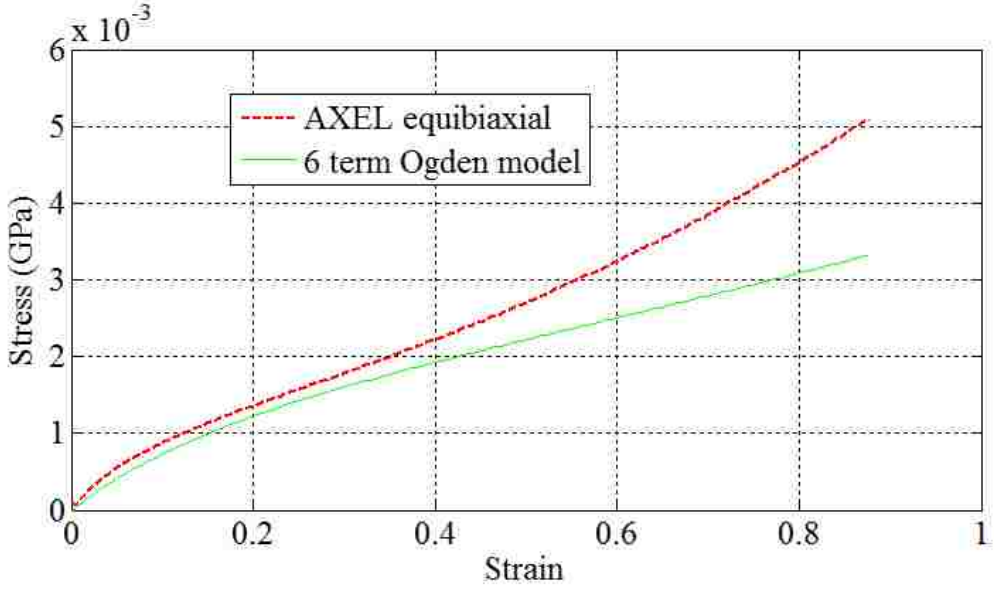

(d)

Figure 25: Comparison between AXEL material characterization data and Ogden model (6 terms), coefficients determined using MARC, (a) pure shear (planar tension), (b) simple tension, (c) simple compression, (d) equibiaxial tension.

Table 12: 6 term Ogden model obtained using MARC-Mentat.

c_1	0.000222631	b_1	1.96928
c_2	0.000199656	b_2	1.13113
c_3	6.38978E-5	b_3	3.13473
c_4	0.000294451	b_4	2.1394
c_5	0.000143757	b_5	4.20627
c_6	0.000719426	b_6	1.32728

Table 13: Oberkampf-Trucano validation metrics for 6 term Ogden model from MARC-Mentat.

Simple tension	0.91892
Simple compression	0.80931
Pure shear (planar tension)	0.86574
Equibiaxial tension	0.79863

These six coefficients were implemented into the Ogden material model in LS-DYNA which was added to the quasi-static material characterization finite element models previously developed. There were no other changes to these finite element models. However, the determination of Ogden material model coefficients was further considered since the use of MARC-Mentat may not be acceptable since it is possible Chrysler engineers may have limited access to MARC-Mentat. In any case it would be ideal to have an independent solution for determining the material model parameters. Therefore, an algorithm in MATLAB was developed with the secondary goal of compatibility with Octave, an open source MATLAB clone. Using the relationships between stress and stretch ratio given in Equations 42 through 44, a least squares non-linear regression scheme was developed to determine Ogden material model coefficients to minimize the error between the Ogden model and the material characterization data from AXEL. The MATLAB code can be found in Appendices A through C.

The form of the error metric (last segment of MATLAB code in Appendix C) resulted from an attempt to weight the error metric contribution for each type of testing completed by AXEL. As an example, compressive stresses were considerably larger than any other stresses, which were quite small since the unit system resulted in stresses in GPa. As a result, the non-linear regression algorithm would find Ogden model coefficients that would accurately capture simple compression stresses with mixed results for simple tension, pure shear, and equibiaxial tension. One may also observe the use of absolute value functions which were used to replace the need to square error terms to prevent positive and negative error cancellation. This was employed as it may be more computationally efficient and reduced the change in magnitude associated with the use of exponential operations. Normalizing each error contribution (i.e. pure shear, simple tension, etc.) would be a logical further step.

An eight term Ogden model is shown in Figure 26. An attempt was made to force the MATLAB algorithm to find positive coefficients but the resulting Ogden model (not used for the results documented in this thesis) was not a significant improvement on the 6 term model with positive coefficients from MARC-Mentat. The algorithm designed to identify positive Ogden coefficients was very sensitive to the initial estimate of the Ogden model parameters with respect to the earlier MATLAB functions that did not exhibit such behaviour. This may be behaviour that would be expected since the methodology to obtain positive coefficients included a discontinuity: when the optimization process identified one or more negative coefficients the error metric was increased by an order of magnitude.

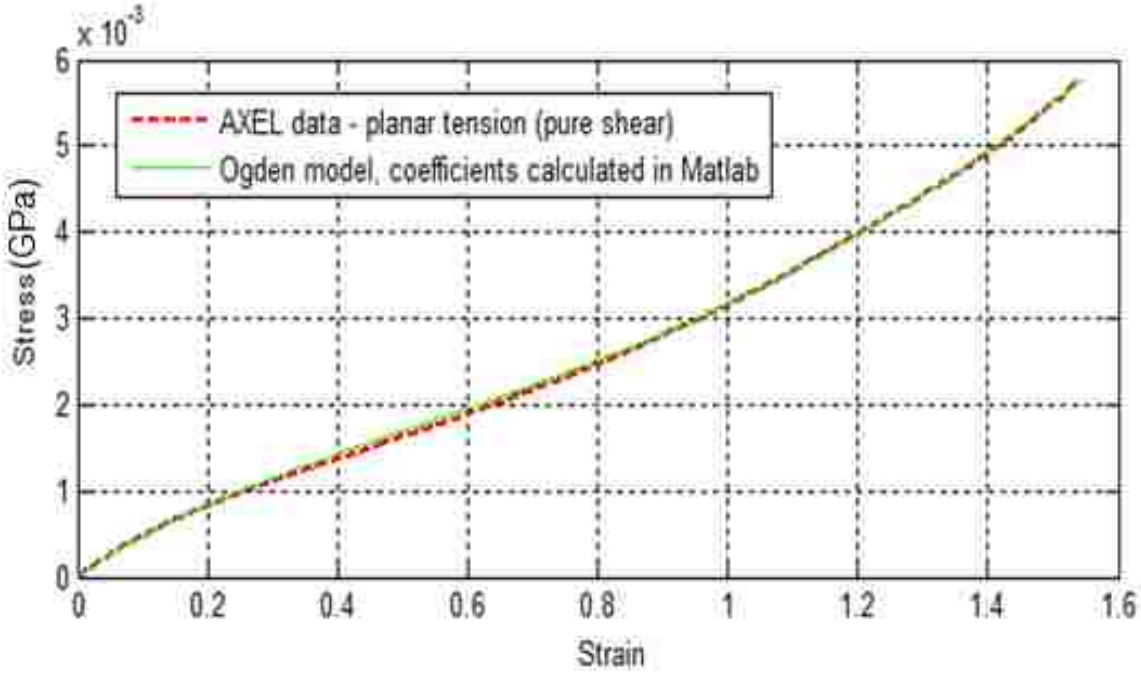
x 10^-3
AXEL data - planar tension (pure shear)
Ogden model, coefficients calculated in Matlab
Stress (GPa)
Strain
0
1
2
3
4
5
6
0
0.2
0.4
0.6
0.8
1
1.2
1.4
1.6

(a)

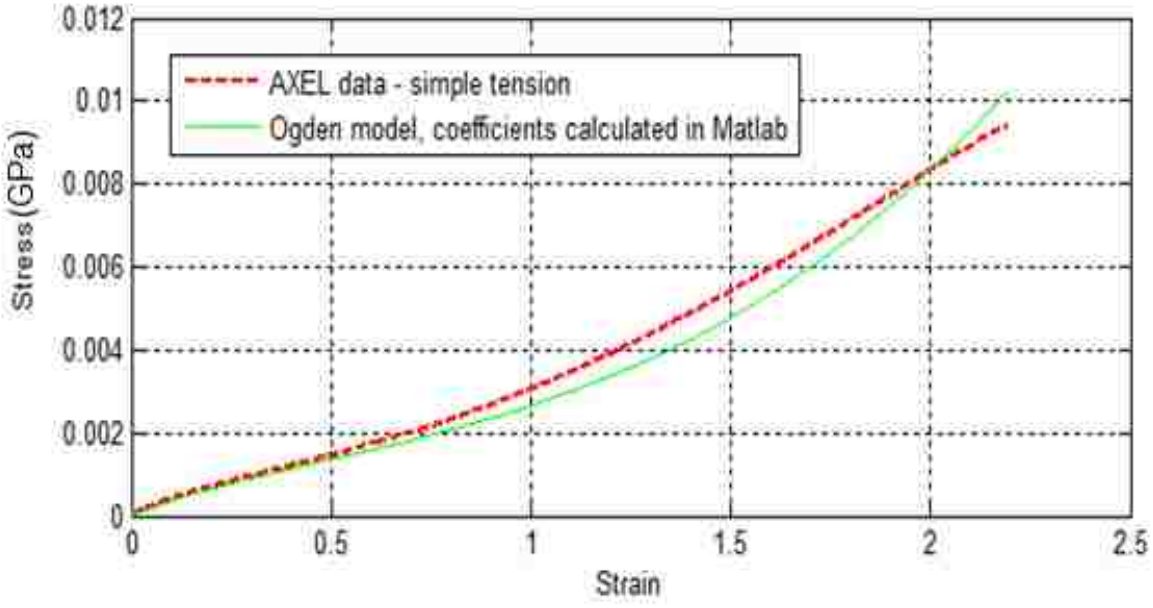
AXEL data - simple tension
Ogden model, coefficients calculated in Matlab
Stress (GPa)
Strain
0
0.002
0.004
0.006
0.008
0.01
0.012
0
0.5
1
1.5
2
2.5

(b)

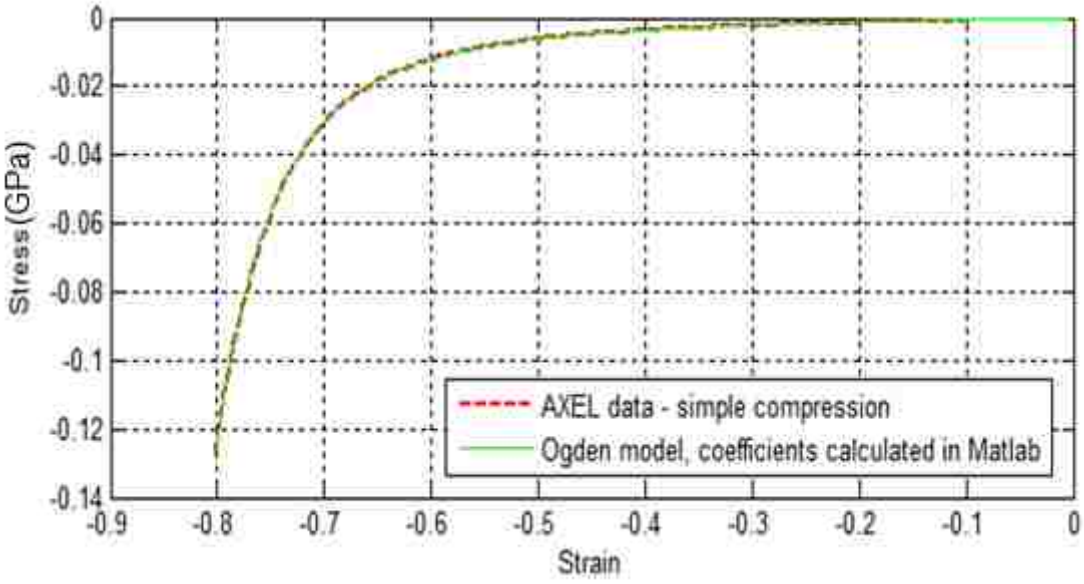

(c)

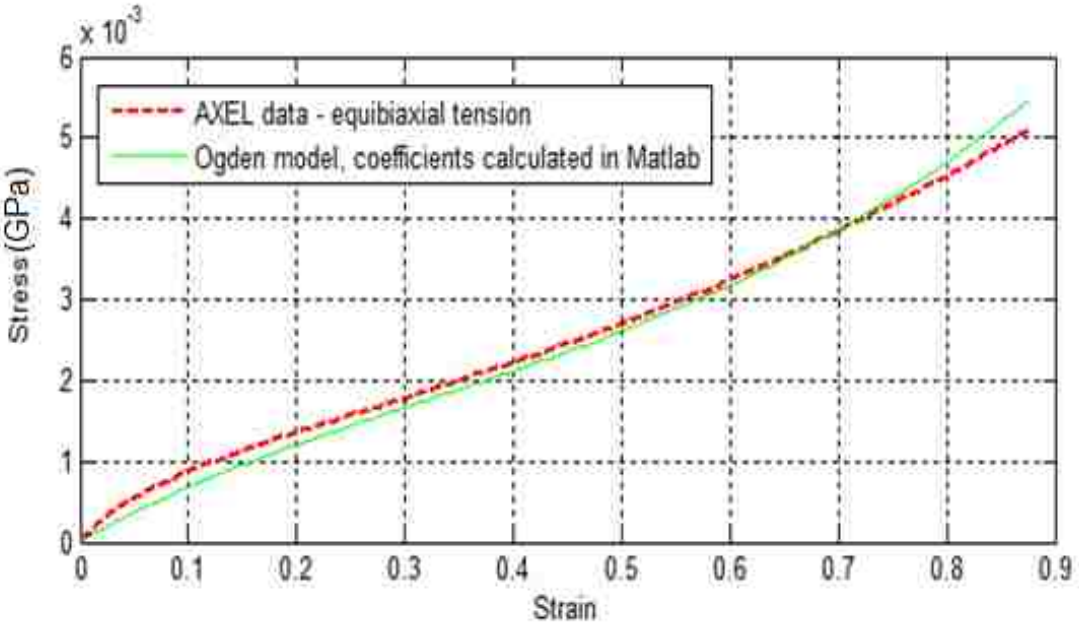

(d)

Figure 26: 8 Term Ogden Material Model (coefficients identified using MATLAB), (a) pure shear (planar tension), (b) simple tension, (c) simple compression, (d) equibiaxial tension.

Table 14: 8 term Ogden model, coefficients identified using MATLAB.

c_1	-0.00914727	b_1	-0.72655344
c_2	0.001202727	b_2	-1.78726458
c_3	-0.00161635	b_3	-2.27110004
c_4	0.001172715	b_4	-0.03172023
c_5	0.003519742	b_5	-1.59542126
c_6	0.000116893	b_6	4.749009080
c_7	0.000214484	b_7	0.337388949
c_8	0.001347245	b_8	-0.34671495

Table 15: Oberkampf-Trucano validation metric, 8 term Ogden model, MATLAB coefficients.

Simple tension	0.90459
Simple compression	0.902785
Pure shear (planar tension)	0.97863
Equibiaxial tension	0.91012

4.5 Development of Finite Element Model of Chrysler RT Platform Transmission Mount

Dr. Sae Park at Chrysler Tech Center (CTC) provided computer aided design (CAD) data and finite element models of a transmission mount (part number P05273883AD). A new finite element mesh was developed from the provided CAD data using the Hypermesh workbench in Altair's Hyperworks software package. Material model data from the Chrysler supplied finite element models was used for preliminary analyses prior to the completion of material characterization in the FIAT polymer laboratory and by AXEL Products Physical Testing Services.

Initial models assumed that the aluminum ‘inner pipe’ (so-named in the Chrysler supplied CAD data) or ‘hub’ and other metallic components were rigid as shown in Figure 28. Therefore, the type of elements and mesh quality were only considered for contact purposes where contact with these components was to be modelled. Many initial analyses disregarded aspects of contact to study the stability of various modelling techniques. These simplifications to the model allowed extreme deformation of the rubber to be studied. Such deformation would be impossible in the physical component. Many aspects of finite element modelling were studied including solver version (R3.2.1 and R5.1.1), element size (minimum critical length ranging from approx. 1 mm to 8 mm), element formulation (LS-DYNA formulations 1, 2, 3, 10, 13, 16, and 17), and hourglass energy control (LS-DYNA types 1, 3, 5, 6, 7, and 9).

The material model for the rubber was MAT_Simplified_Rubber/Foam (MAT 181). This hyperelastic material model is unique within LS-DYNA in that it does not globally fit one strain energy density function to model the constitutive relationship between stress and strain for the material. All other hyperelastic material models in LS-DYNA, and in many other finite element codes, will exhibit some error due to this curve fitting process. MAT 181 fits a pre-tabulated function piecemeal to replicate input data with minimal error. The use of a tabulated function may increase the stability of the model. This material model is also very suitable for this model with its ability to model strain rate sensitivity, hysteresis (MAT 183, a further development of MAT 181), and failure. For all studies of modelling parameters and stability using the model of the engine mount the stress-strain input data was provided by Chrysler in the initial stages of this research project (included in an ANSA CAE model). For many models the metallic elements were assumed to be rigid and therefore used MAT_RIGID (MAT 020).

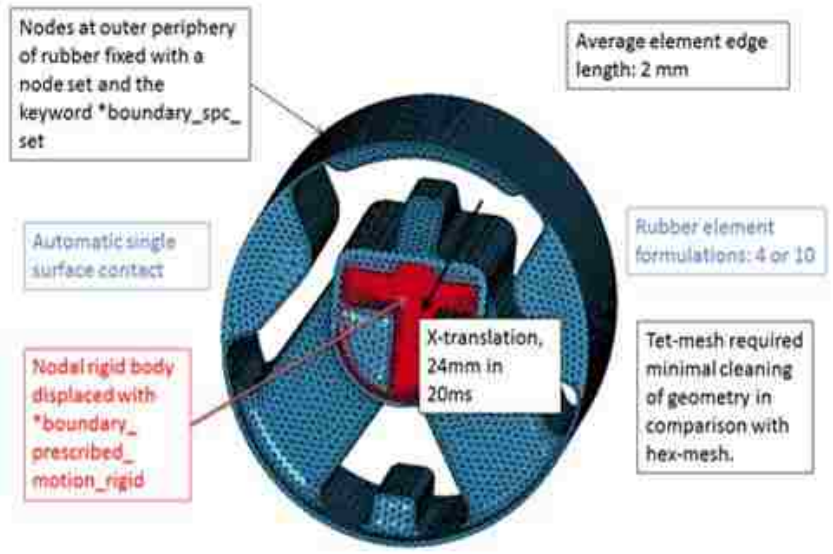

(a)

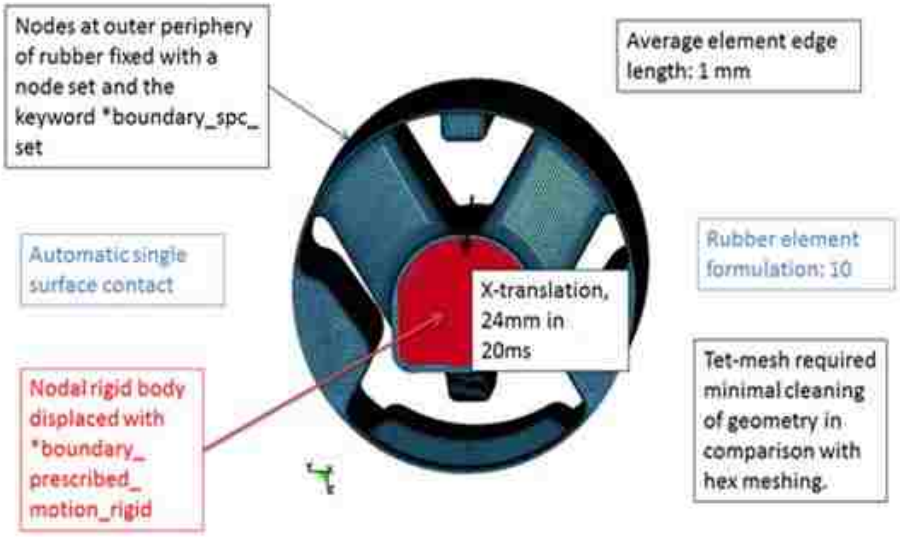

(a)

Figure 27: (a) 2mm and (b) 1 mm average element edge length tetrahedron element mesh, finite element model of Chrysler RT platform transmission mount.

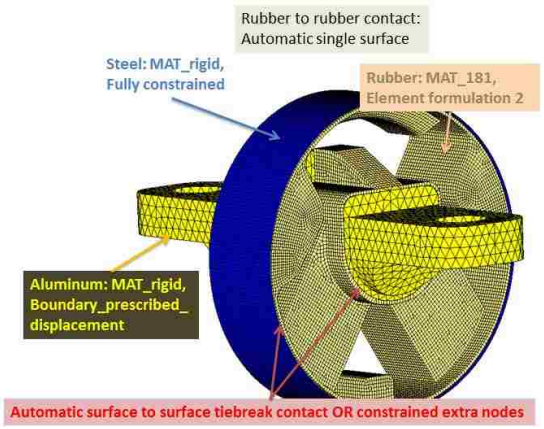

Figure 28: 1mm average edge length hexadron mesh, finite element model of Chrysler RT platform transmission mount.

The first models to be built consisted of a very fine mesh of solid elements (Figure 27 & Figure 28). In separate models hexahedron and tetrahedron elements were used. With hexahedron elements many simplifications of the geometry (i.e. removing fillets) were required to simplify the meshing process. Tetrahedron elements had a significant advantage in this regard, for a given element critical length far fewer simplifications had to be made and the meshing process was therefore highly automated. However, a mesh consisting of tetrahedron elements requires approximately twice as many elements for the same average element size. Summaries of the quality of the various meshes are provided in Table 17 and Table 18. After running a simulation LS-DYNA provides the user with data on the usage of CPU time. As shown in Table 16, which is a typical breakdown for an engine mount model, element processing is the most significant consumer of CPU time. A model with under-integrated hexahedron elements (1-point Gaussian quadrature) will generally have a lower computational expense than under-integrated tetrahedron elements with the same average element size.

Table 16: CPU time breakdown, FIAT computing cluster, MPP solver.

T i m i n g i n f o r m a t i o n

	CPU(seconds)	%CPU	Clock(seconds)	%Clock
Initialization	1.2100E+00	1.35	1.4359E+00	1.59
Element processing ...	7.2555E+01	81.01	7.2898E+01	80.83
Binary databases	9.9000E-01	1.11	1.0014E+00	1.11
ASCII database	4.2900E+00	4.79	4.4528E+00	4.94
Contact algorithm	8.9625E+00	10.01	8.8775E+00	9.84
Interface ID 1	1.7463E+00	1.95	1.7958E+00	1.99
Interface ID 2	5.4750E+00	6.11	5.4855E+00	6.08
Contact entities	0.0000E+00	0.00	0.0000E+00	0.00
Rigid bodies	1.5525E+00	1.73	1.5180E+00	1.68
Implicit Nonlinear ...	0.0000E+00	0.00	0.0000E+00	0.00
Implicit Lin. Alg. ...	0.0000E+00	0.00	0.0000E+00	0.00
T o t a l s	8.9560E+01	100.00	9.0183E+01	100.00

Table 17: Chrysler meshing guidelines and simple compression model quality, tetrahedron meshes of the Chrysler powertrain suspension component.

Mesh Characteristic	**Limit**	**Coarse mesh**	**Coarse mesh, cleaned geometry**	**Refined mesh**
Critical length (mm)	N/A	0.527	0.945	0.342
Aspect ratio	8 (max)	12.1	5.37	13.4
Skewness	0.5 (max)	0.994	0.844	0.999
Min. angle, tetrahedrons	30°	8.31°	14.3°	7.32°
Max. angle, tetrahedrons	120°	158°	147°	162°

Table 18: Chrysler meshing guidelines and simple compression model quality, hexahedron meshes of the Chrysler powertrain suspension component.

Mesh Characteristic	**Limit**	**8 mm mesh**	**4 mm mesh**	**2 mm mesh**	**1 mm mesh**
Critical length (mm)	N/A	3.25	1.61	0.839	0.334
Aspect ratio	8 (max)	2.81	2.54	3.33	3.01
Warping	10	27.6	51.9	47.1	32.6
Jacobian	0.6	0.459	0.465	0.479	0.492
Min. angle, pentahedrons	30°	32.5°	38.5°	26.8°	29.7°
Max. angle, pentahedrons	120°	143°	109°	153°	97.6°
Min. angle, hexahedrons	30°	41.9°	35.3°	25.7°	38.1°
Max. angle, hexahedrons	140°	149°	148°	163°	157°

The use of tetrahedron and hexahedron elements also allowed the effect of geometrical simplifications to be assessed. While tetrahedron elements allowed for fewer geometrical simplifications, these types of elements were also used to mesh a geometry simplified for hexahedron meshing. The resulting mesh is shown in Figure 29. For tetrahedron meshing two element formulations were used: tetrahedron element formulation 10 (under-integrated) and 4 (selectively reduced integration). Selectively reduced integration reduces element locking (excessive stiffness), a phenomenon that is more problematic for tetrahedron elements than hexahedron. Initially, three hexahedron element formulations were used: element formulation 1 (under-integrated), formulation 2 (selectively reduced integration), and formulation 3 (fully integrated). Element formulation 41 was not used as it was not compatible with MAT 181.

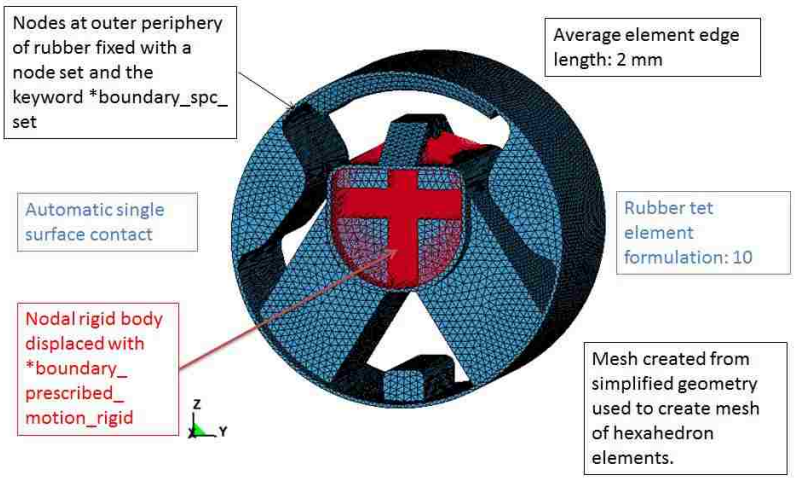

Figure 29: 2mm average edge length tetrahedron mesh from hexahedron-meshing simplified geometry.

A series of coarser meshes were also developed to identify the coarsest level of discretization that would yield reasonable results. This model replaced thin regions of rubber, previously modelled with solid elements, with shell elements. This provided a significant advantage with respect to computational efficiency since the critical timestep for a shell element is not dependent on the thickness of the shell element. An example of this model is shown in Figure 30. Finally, a very coarsely meshed model provided by Chrysler, shown in Figure 31, was modified to have similar boundary conditions providing another level of discretization for comparison.

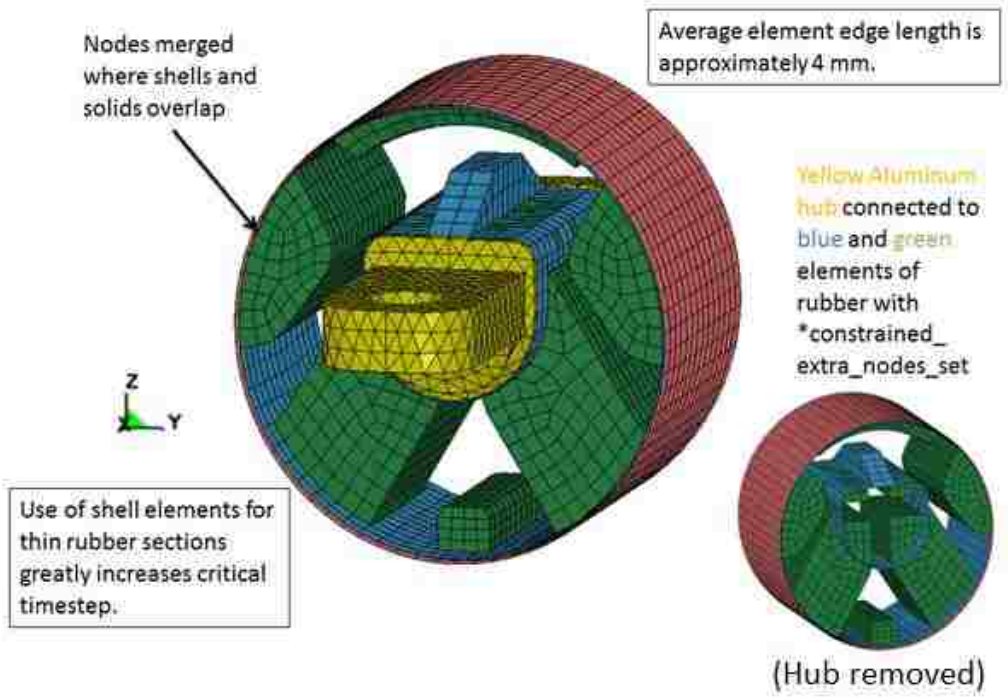

Figure 30: Coarse mesh using a combination of shell and solid element to represent the rubber regions.

Each model was loaded such that the outer steel sleeve was fixed and the inner hub (also known as the inner pipe) translated linearly (24 mm in the x-direction or 12 mm in the y or z-directions) or rotated about axes parallel to those of the global axes but passing through the center of mass of the hub. All rotations were limited to 90 degrees. Physically such a rotation is likely impossible for rotations about the local y and z axes since the inner aluminum hub would contact the outer steel sleeve. Contact between these two components was not modelled to assess the level of deformation of the mesh of the rubber regions permissible by the solver prior to severe instabilities. Contact was accurately modeled for loading by hub translation. All simulations had a termination time of 20 ms and used a loading curve specified using the keyword *DEFINE_CURVE_SMOOTH with a start time of 0.01 ms, an end time of 20ms, and a rise time of 4ms. This method of specifying load curves was assumed to minimize instabilities due to discontinuities that may exist with a manually specified curve.

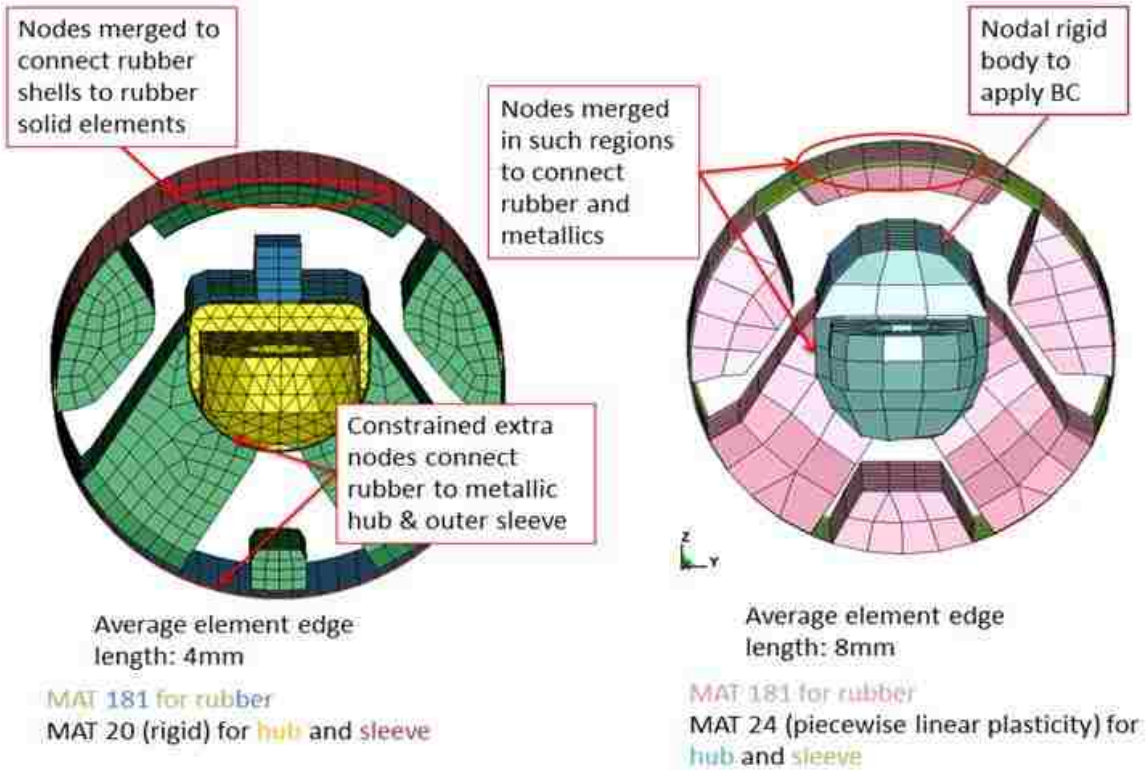

Figure 31: Comparison between two of the coarsest meshes used in this research, (a) 4 mm average element edge length, (b) Chrysler supplied mesh, 8 mm average element edge length.

4.5.1 Tied Contact

As part of an effort to use automatic tetrahedron re-meshing the use of tied contact was studied. With the use of a combination of shell and solid elements there often arises a need to connect parts with these two different types of elements. The simplest connection was to merge nodes. However, the only hexahedron (solid) element with nodal rotational degrees of freedom is element formulation 3. This element formulation has been found to be particularly poorly suited for modeling near incompressible materials. An alternative to merging nodes is to use a tied contact. The revised model to use tied contact is shown in Figure 32.

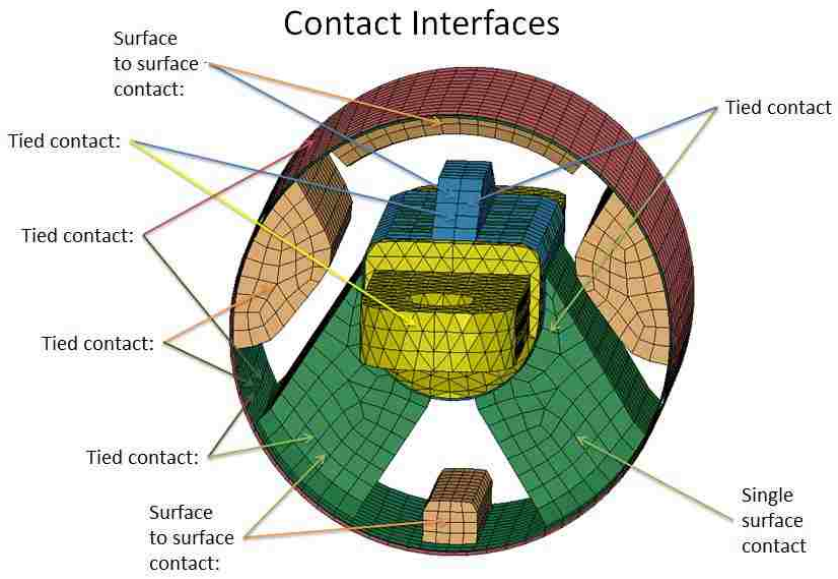

Figure 32: Contact interfaces for model with tied contact replacing merged nodes.

4.6 Component Level Testing – Chrysler Engine Mount

4.6.1 Fixture Design

Force-displacement characteristics for the Chrysler engine mount were obtained in the DYNLab (Impact and high strain rate testing laboratory) at the Politecnico di Torino campus in Vercelli, Italy. After determining suitable equipment to be used, a fixture was developed to mount the Chrysler engine support. The fixture was designed to use standard steel structural shapes available from the Italian steel producer the Beltrame Group which has facilities near Torino, Italy. An initial design is shown in Figure 33. Finite element models of the fixture were developed with the engine mount modeled as rigid through which an estimated peak load was applied. The finite element models of the fixture were significantly different than models of the engine mount due to the different applications. The engine mount finite element models were designed to be computationally efficient and capable of capturing the force-displacement response. Low computational cost was achieved through reduced integration element formulations and coarse discretizations. This resulted in a model poorly suited for identifying the stress state in the material. Alternatively, the fixture models were designed to accurately capture

the stiffness of the structure and the state of stress. This required a much finer mesh which is not suitable for use with explicit time integration. Implicit time integration was used to complete a static analysis of the structure with a minimal number of intermediate steps between the unloaded and fully loaded conditions.

To reduce the computational expense of the fixture/engine mount combined models the rubber portion of the engine mount was removed since MAT 181 Simple Rubber/Foam is not implemented at this time in the implicit LS-DYNA solver. The stamped steel sheet metal brackets of the engine mount were modeled as rigid and were connected to each other using the keyword *CONSTRAINED_RIGID_BODIES. Contact between the rigid bodies of the engine mount and the fixture was carefully designed to ensure the infinite stiffness of the rigid bodies did not improperly affect the design of the fixture. Bolt preloading was accomplished by applying forces to the nodes of the deformable washers.

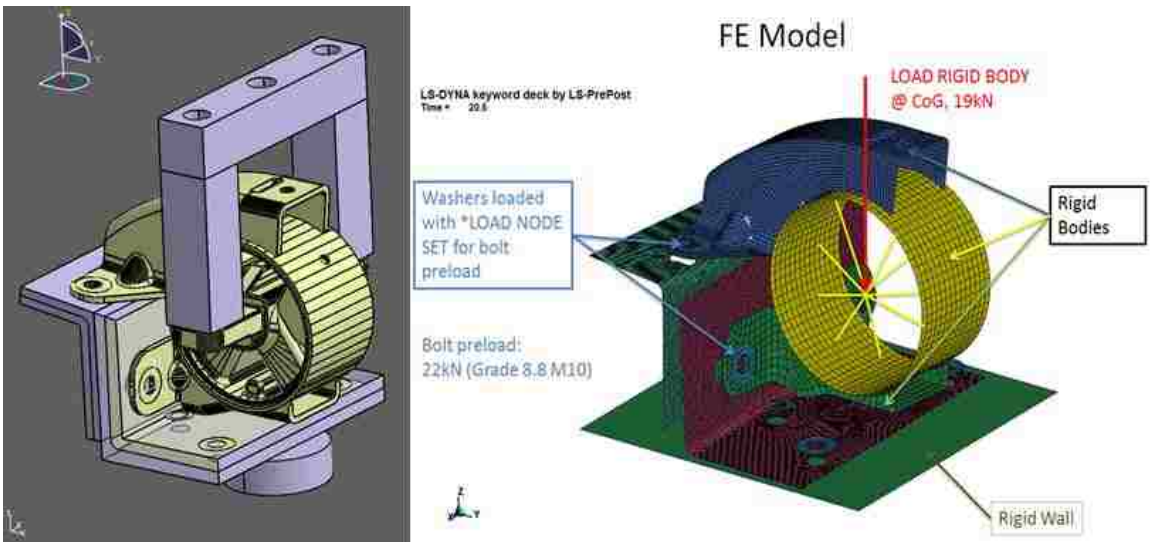

Figure 33: Initial fixture design and finite element model.

As shown in the results section the initial fixture design was found to have deficiencies. It was assumed that the yield strength of structural steel is approximately 250 MPa, a figure obtained from the Canadian industrial supplier McMaster Carr (McMaster-Carr). The 90 degree equal angle selection was revised to use a more substantial piece of material. This necessitated a revision of the design as shown in Figure 34. The modified

design could no longer use shell elements for the steel sections since not all holes were through holes. Linear tetrahedron and quadratic tetrahedron solid elements were used to simplify the meshing process. In addition to mesh refinement the element formulation was enhanced to assess the mesh dependency.

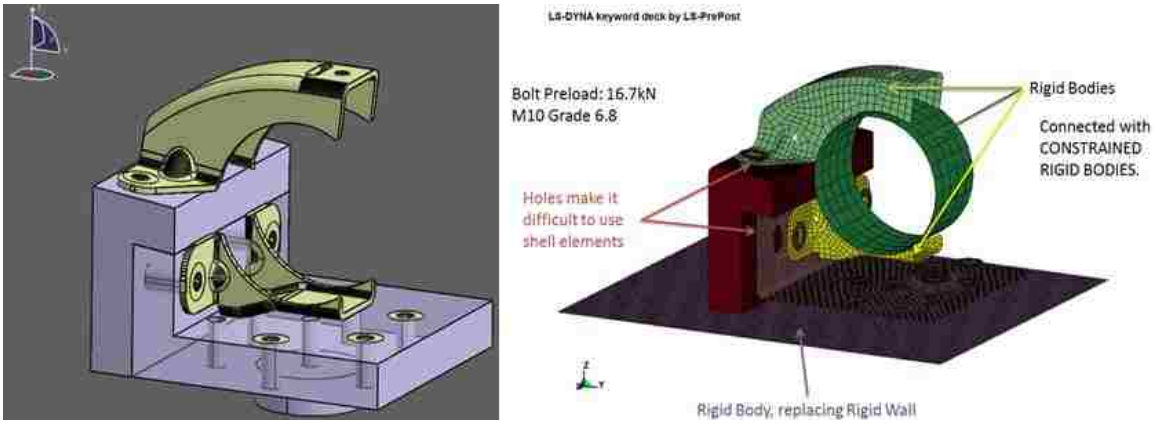

Figure 34: Revised fixture design and finite element model.

4.6.2 Quasi-Static Component Characterization

Quasi-static component characterization was completed under the supervision of Lorenzo Peroni and other researchers in DYNLab at the Politecnico di Torino campus in Vercelli, Piemonte, Italy. A Zwick/Roell Z100 testing machine with a GTM Series K 100 kN load cell was used to obtain the quasi-static force-displacement response of the Chrysler engine mount. Zwick/Roell TestXpert software was used for data acquisition. The characterization process was displacement controlled with the displacement profile shown in Figure 35. Each engine mount was loaded and unloaded in tension (4 mm displacement of the hub of the engine mount) and loaded and unloaded in compression (22 mm displacement of the hub of the engine mount) with this process repeated for a total of five cycles for each test. Four separate tests were completed. Two complete component characterization processes were completed with engine mount specimen #1. Specimens #2 and #3 each underwent one complete characterization process. High resolution images were captured every 2 seconds for the duration of each test (approximately 5 minutes) with a PixeLINK 5 megapixel (MP) camera.

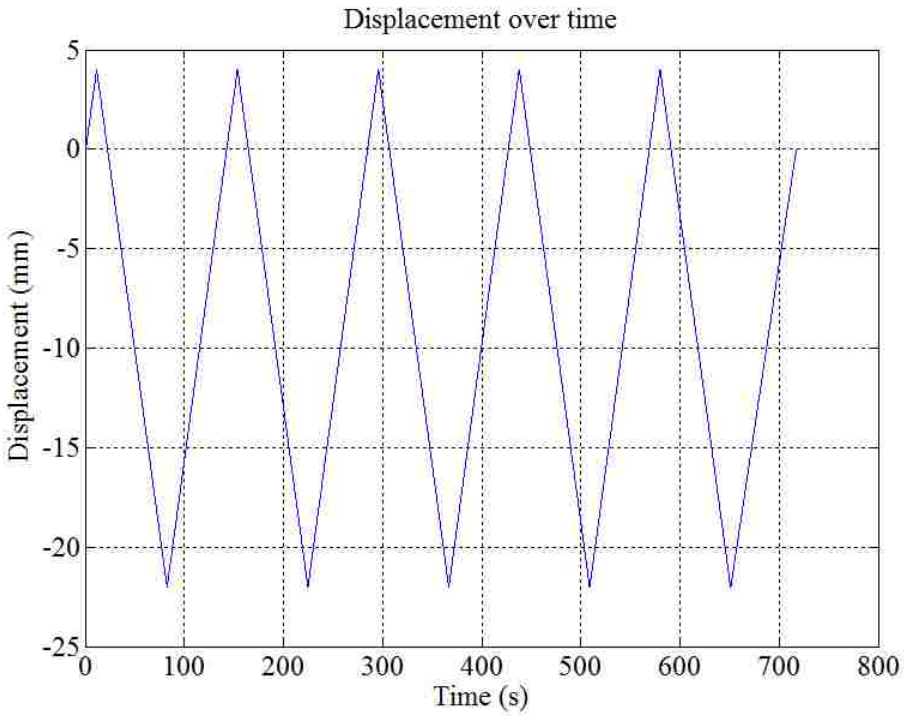

Figure 35: Quasi-static component characterization displacement profile.

4.6.3 Dynamic Component Characterization

Dynamic component characterization of the Chrysler engine mount was also completed in DYNLab at the Politecnico di Torino campus in Vercelli using a DARTEC servo-hydraulic testing machine. Force and displacement data were obtained using a Kistler 120 kN (model 9371B) piezoelectric load cell and a Keyence laser displacement transducer (LK-G402) both of which were connected to a PC with a National Instruments (NI) high speed USB hub (NI USB-9162). DARTEC software was used to specify loading conditions and acquire data. To provide data for digital image correlation (DIC) a Citius Imaging C100 Centuri high speed video camera was employed. This camera features a resolution of 1280 x 1024 with a maximum frame rate of 424 frames per second at full resolution increasing to 111111 frames per second at a resolution of 64 x 10. Three specimens were characterized with each specimen characterized twice for a total of 6 sets of data. Each characterization process consisted of loading and unloading

the specimen in a configuration consistent with the compressive loading of the quasi-static component characterization process.

To dynamically load the engine mount, the structure was bolted to the piston of a hydraulic cylinder using a fixture. To apply a dynamic load a velocity-time profile was input to the DARTEC software for the hydraulic cylinder. As shown in Figure 36 the engine mount was loaded by impacting the upper half of the fixture, a relatively rigid entity with respect to the mount itself, against a relatively rigid platen of the testing machine. The displacement and velocity of the hydraulic cylinder, for both the actual and the prescribed conditions, are shown in Figure 37. As shown in Figure 36, a small initial gap between the upper half of the fixture and the fixed platen of the testing machine was included to allow the hydraulic cylinder to reach a relatively constant velocity prior to impact. Specimen #3, one of the specimens used for quasi-static characterization, was used to adjust the gains of a proportional-integral-derivative (PID) closed feedback loop controller in the DARTEC apparatus to obtain an actual velocity profile with minimal deviation from the prescribed profile. Two sets of force-displacement data for each of engine mount specimens 4, 5, and 6 were obtained.

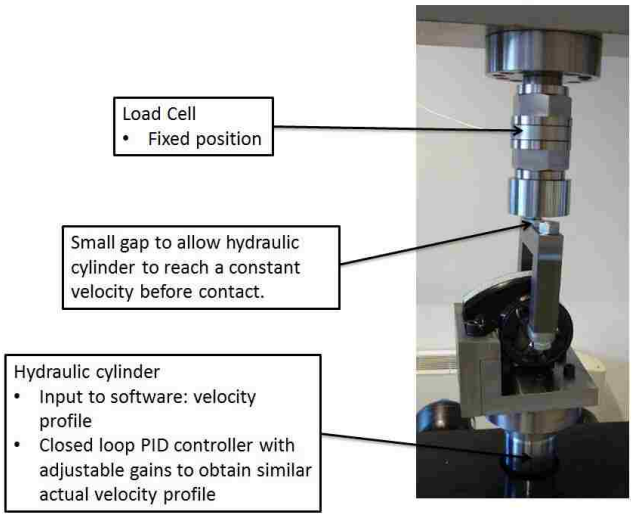

Figure 36: Dynamic characterization apparatus.

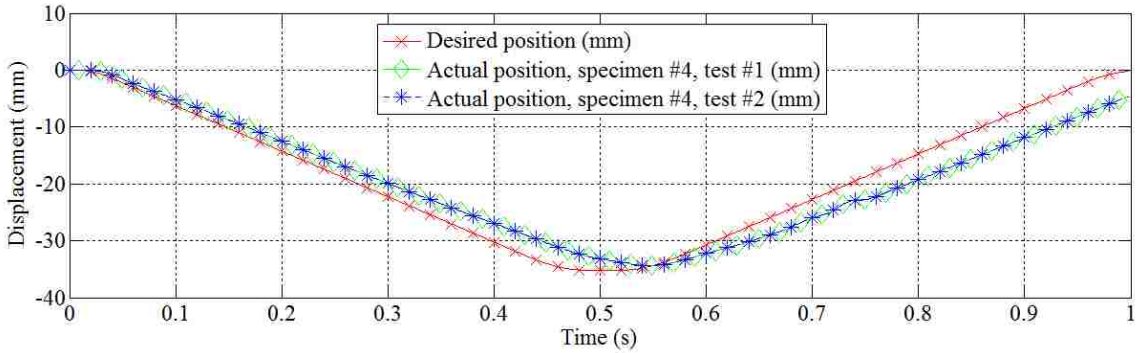

(a)

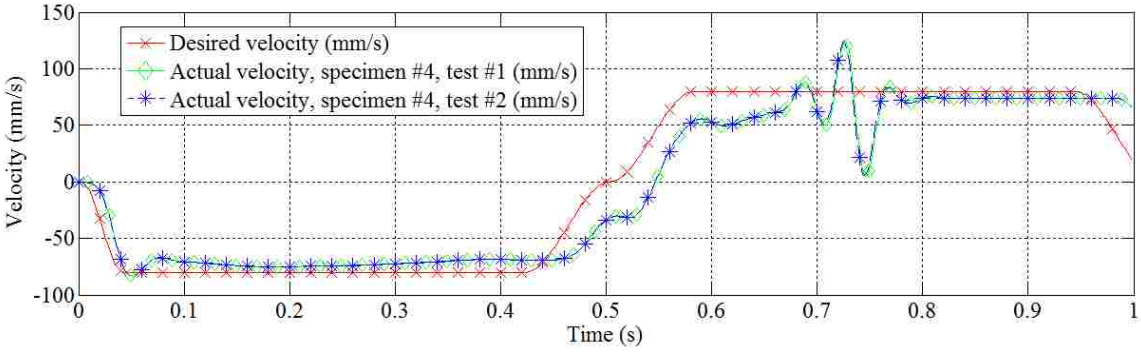

(b)

Figure 37: (a) Prescribed and actual displacement and (b) velocity of the hydraulic cylinder over time, specimen #4.

4.7 Finite Element Model Validation

4.7.1 Quasi-Static Force-Displacement Response

To validate the finite element models of the Chrysler engine mount, models were developed which included the stamped steel brackets. It was observed during the experimental component characterization that although the deformation of the rubber was the most significant contributor to the measured displacement there was a contribution associated with deformation of the steel brackets. The resulting models were developed in Hypermesh with minimal alterations to the methodology for meshing and modelling the rubber regions. Tied contact was used to model any bonding between rubber and another material and any press fits. The material model was also updated to include rate

effects, consistent with the single element finite element models to investigate strain rate sensitivity modelling with MAT 181.

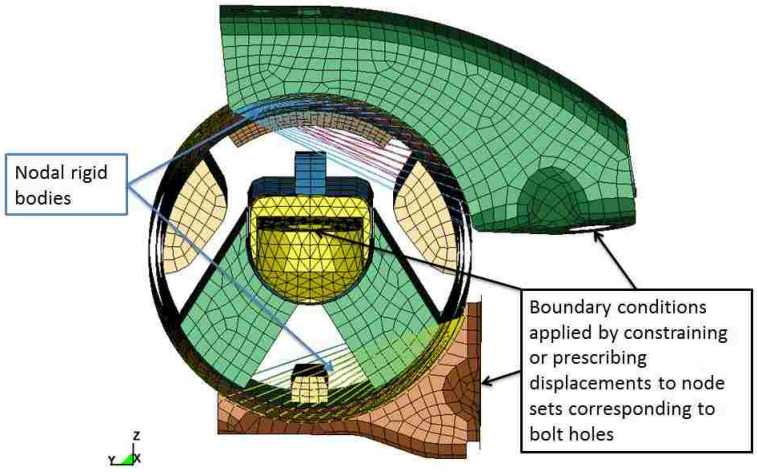

Figure 38: Finite element model of engine mount including steel brackets.

Several models were used for validation with respect to the data from the quasi-static component characterization process. The data from the quasi-static component characterization process was divided into loading and unloading in tension and compression. The complete loading and unloading in tension and in compression of the quasi-static component characterization process were not simulated together since the material model was not selected to be capable of capturing hysteresis effects. Another version of MAT 181 (MAT 183, Simple Rubber/Foam With Damage) is capable of modelling hysteresis but requires stress-strain data for the unloading behaviour.

One of the most significant alterations to the engine mount model, required due to the addition of the steel brackets, was the use of nodal rigid bodies. These rigid bodies may result in an excessive stiffness contribution. An attempt was made to use tied contact for all connections but the approximately perpendicular orientation of tied elements presented difficulties. A better solution may be to use merged nodes.

4.7.2 Dynamic Force-Displacement Response

A separate finite element model was developed to be validated with respect to the dynamic component characterization data obtained at the DYNLab at the PdT in Vercelli, Italy using a Zwick/Roell DARTEC servo-hydraulic mechanical testing system. The model included portions of the fixture which it was thought might contribute significant inertia forces. Significant time scaling was employed with a time step of -4.5E-4 ms specified. If the steel brackets of the engine mount were modeled as deformable the increase in mass was significant (70%). However, the ratio of kinetic energy to internal energy was less than 1%. Modeling the steel brackets as rigid resulted in a negligible increase in mass with this time step (<1%).

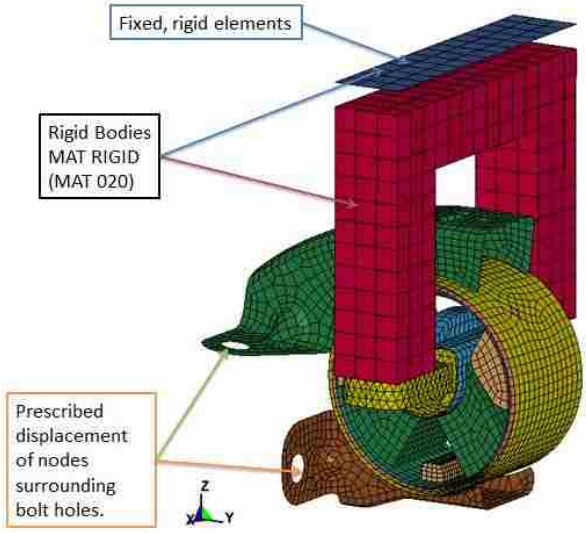

Figure 39: Finite element model of dynamic component characterization process.

Chapter 5: Results

5.1 Quasi-Static Material Characterization

AXEL Physical Testing Services completed extensive material characterization on two types of rubber for Chrysler. Comparisons between data from AXEL and the FIAT polymer laboratory are shown in Figure 40. There was notable variation between the results for simple compression when comparing results from FIAT and AXEL. There is also significant variation between different tests completed in the FIAT polymer laboratory. A significant amount of time was spent to try to identify the most important contributing factors to this variation.

Simple tension stress-strain data obtained from the three ASTM D412 type D specimens cut from engine mount #1 are shown in Figure 40 (a). For simple tension there was near ideal consistency between the data obtained in the FIAT Mirafiori polymer lab and from AXEL Testing Services. However, there was significant variation for the simple compression data as is shown in Figure 40 (b). For all FIAT simple compression tests the specimen was 24 mm in diameter with a nominal thickness of 8.8 mm (ratio consistent with ASTM D575 specimen). More accurate dimensions were input to the data acquisition and processing software accompanying the Zwick-Roell testing apparatus. For tests 1 through 5 the specimens were extracted from Chrysler engine/transmission mount #1. The general orientation and position from which the specimens were extracted was noted (the radial 'arms' of the engine mount) but of the four specimens (specimen number 3 was tested twice, tests 3 and 4) it was not known precisely where each specimen had been extracted from.

Additionally, it was noted that two specimens were prepared several hours prior to testing while two specimens were prepared immediately prior to testing. (two specimens were extracted from each radial arm of the engine mount). Specimen 3 was tested twice to assess the effect of varying the amount of lubricant applied. After noting the significant variation between these four specimens further testing was conducted with greater attention to detail. As shown in Figure 41 the precise positions of specimens 1 through 4 for engine mount #2 were documented. It was found that within each radial arm the

material properties were reasonably consistent but between the two radial arms of each engine mount there can be significant variation but this was not always observed. The time between specimen preparation and specimen testing was not identified to be associated with any trend in the data.

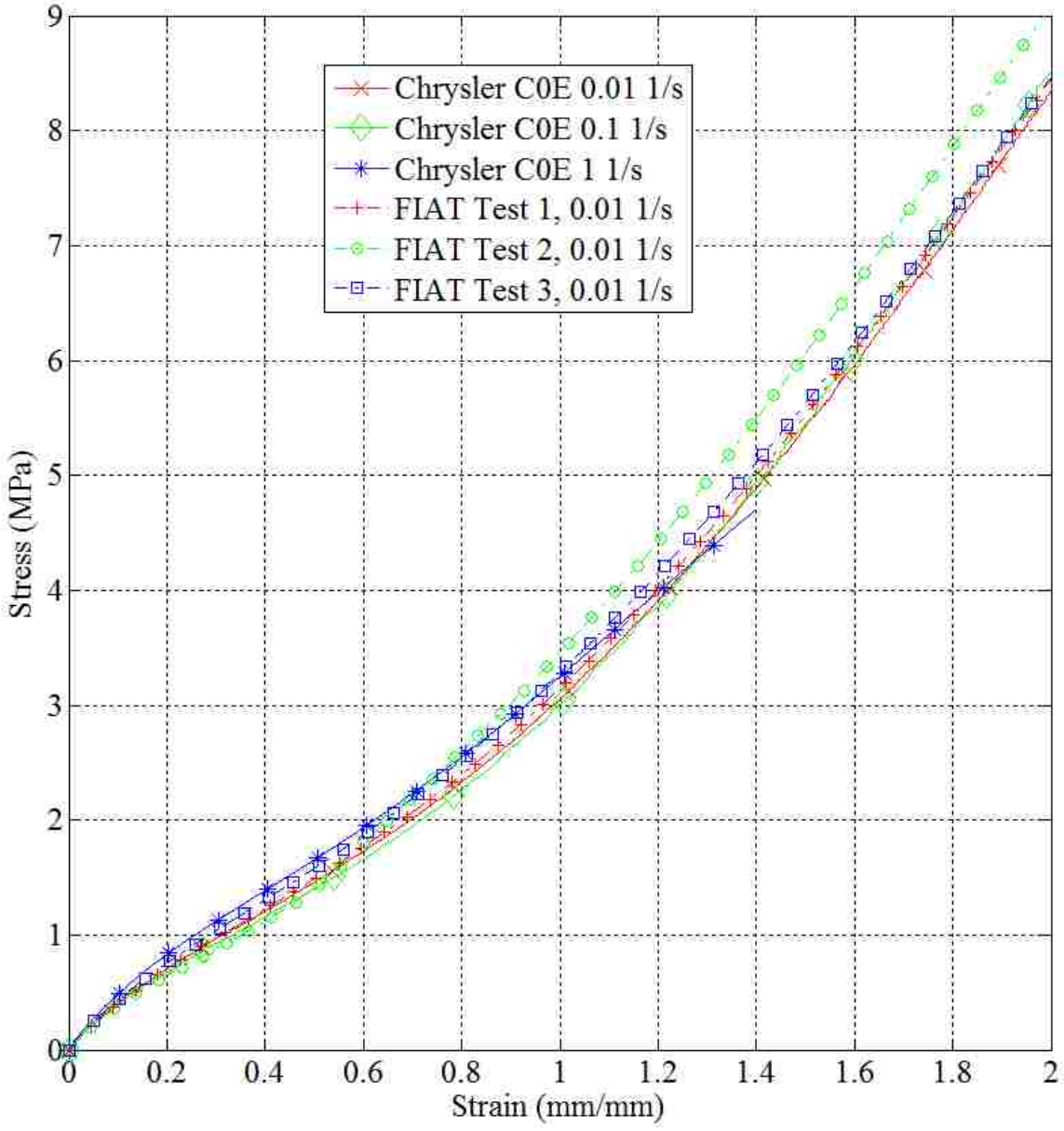

(a)

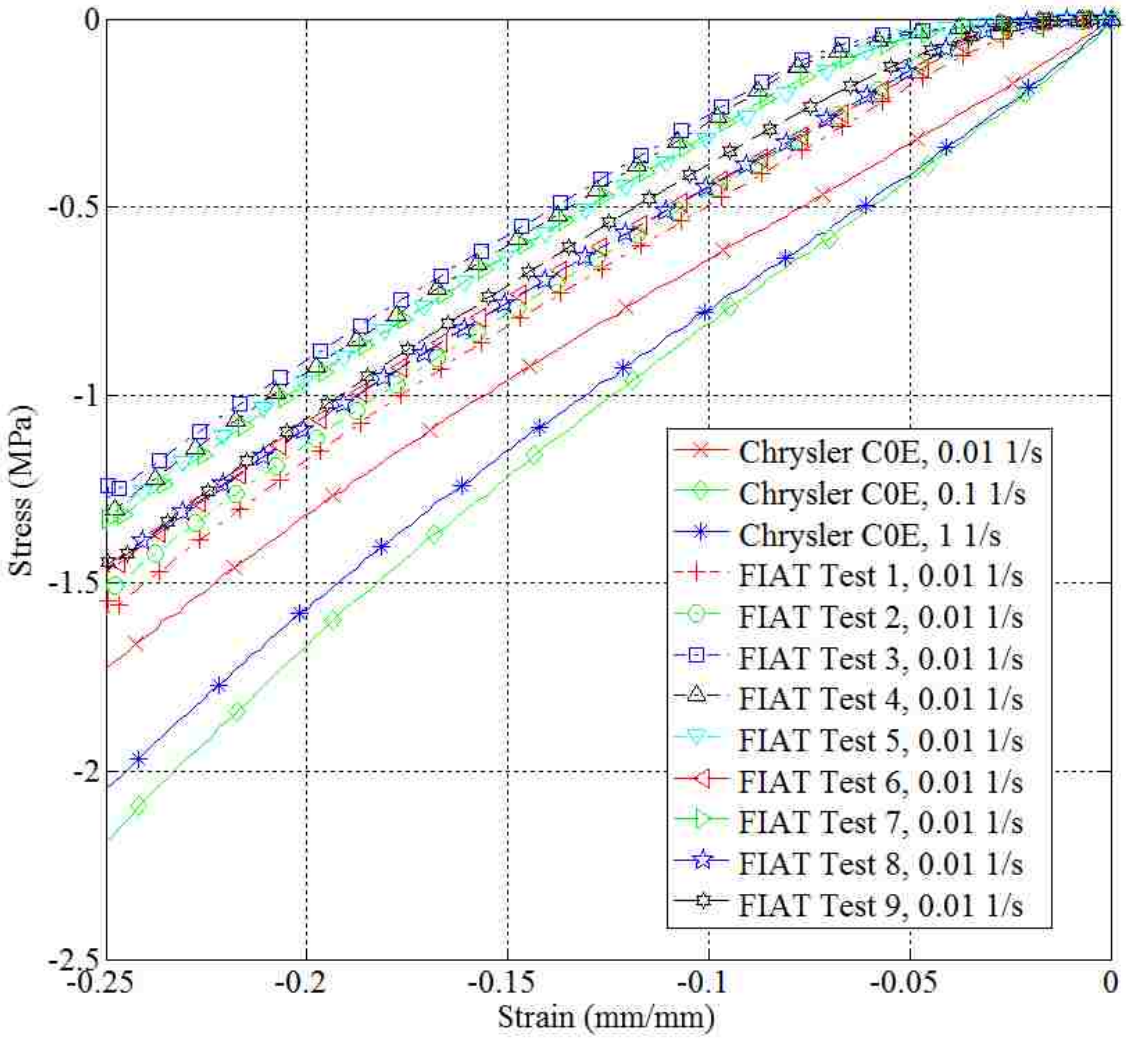

(b)

Figure 40: Quasi-static uniaxial stress-strain data. Sources: FIAT polymer laboratory and AXEL Testing Services, (a) simple tension, (b) simple compression.

Figure 41: Specimen tracking methodology.

AXEL Physical Testing Services completed additional types of material characterization: planar tension (pure shear) and equibiaxial tension. The planar tension test is essentially a simple tension test but with a very wide specimen. In the FIAT Mirafiori polymer laboratory this material characterization procedure uses a rectangular prism specimen that is 5mm x 5mm x 50mm with the load applied through two aluminum fixtures adhered to two opposite 5 mm x 50 mm faces. The aspect ratio of this cross section results in essentially no strain in one principal direction. The constant volume due to incompressibility results in a simple relationship between the other two strains. This arrangement yields a state of pure shear with the proper stress transformation. The data for this test from AXEL, which is obtained using the same methods used for a simple tension test, is shown in Figure 42.

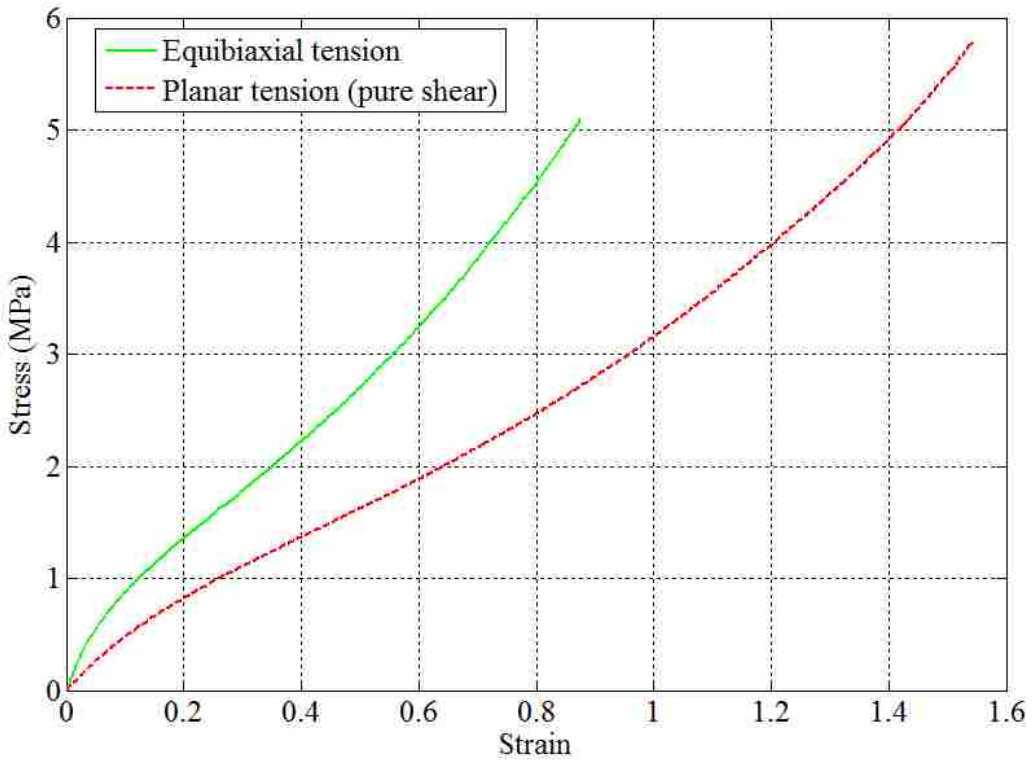

Figure 42: AXEL planar tension (pure shear) and equibiaxial tension stress-strain data, rubber C0E, 0.01 1/s.

The equibiaxial tension test completed by AXEL can be used to assess the characterization of material using simple compression testing. The radial stress strain data provided by AXEL for rubber C0E is shown in Figure 42. As studied by Day and Miller (Day JR, 2000) friction can significantly affect the ASTM D575 simple compression method of material characterization. Simple stress and strain transformations, shown in Equations 48 and 49, allow for the conversion of the radial stress and strain from the equibiaxial test to an ideal stress-strain curve for simple compression. A comparison between the experimental simple compression data and the converted AXEL equibiaxial data is shown in Figure 43.

$$\sigma_{Simple\ compression} = \sigma_{Equibiaxial}\left(1 + \varepsilon_{Equibiaxial}\right)^3 \qquad \text{(Equation 54)}$$

$$\varepsilon_{Simple\ compression} = \frac{1}{\left(\varepsilon_{Equibiaxial} + 1\right)^2} - 1 \qquad \text{(Equation 55)}$$

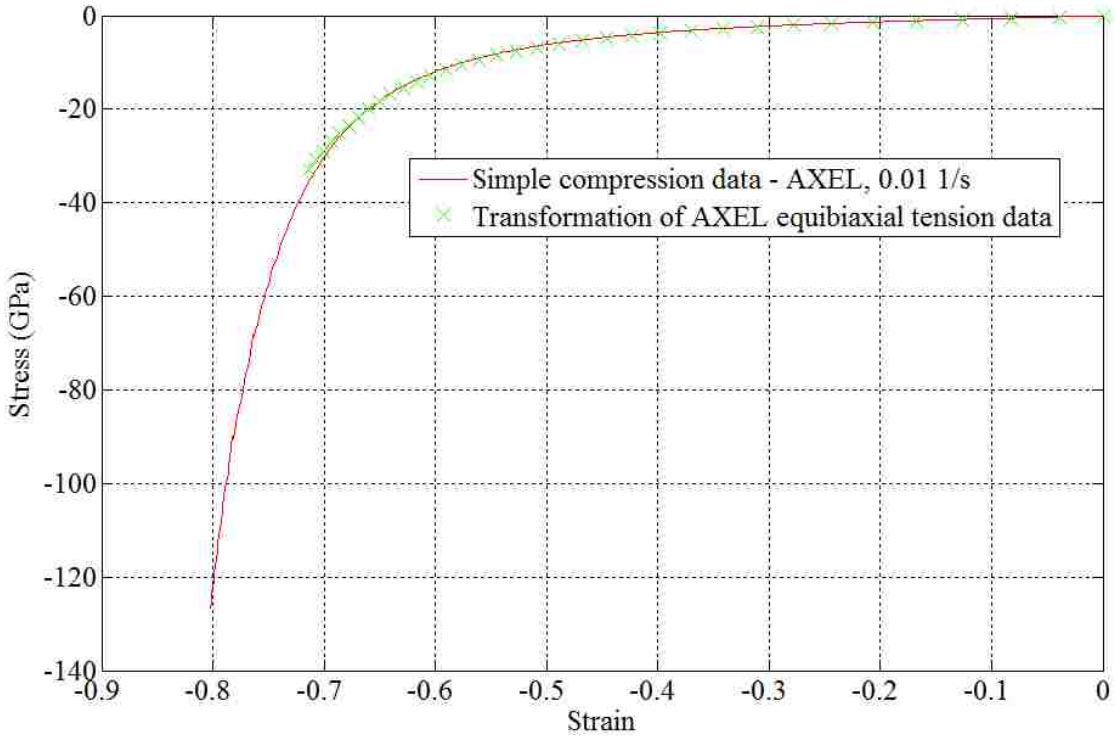

Figure 43: Comparison between simple compression material characterization and equibiaxial tension with stress transformation.

5.2 Finite Element Modeling of Quasi-Static Material Characterization with MAT 181 (Simple Rubber/Foam)

5.2.1 Single Element Models (MAT 181, MAT 77H, & MAT 77O)

The first models developed were a single element with three planes of symmetry sharing a vertex. A displacement (translation) was prescribed to the nodes of a face (segment) opposite one of the symmetry boundary conditions. Three material models were compared: MAT 77H which uses a strain energy density function of the form given by Equation 11, MAT 77O where the O denotes Ogden and the strain energy density function is of the form of Equation 21, and MAT 181 Simple Rubber/Foam. MAT 31 (Frazer Nash Rubber Model) was also considered but performed poorly with error terminations at small strains (input to model was the same uniaxial stress-strain data used with MAT 181 and MAT 77). For these simple models the material models were defined by including a uniaxial simple tension stress strain curve in the input file and fitting a curve automatically and internally by the LS-DYNA solver. Referring to Figure 44, the simple tension stress-strain response was from the first ASTM D412 tensile test completed in the FIAT polymer laboratory. An error metric was calculated (Oberkampf W, 2002) to quantify the performance of the material model and other modelling parameters studied. Similar models were created using data from the other simple tension tests completed in the FIAT laboratory and using data from AXEL. The different data sets had no pronounced effect on the results; other modelling parameters were of greater importance with the material model likely being the most critical.

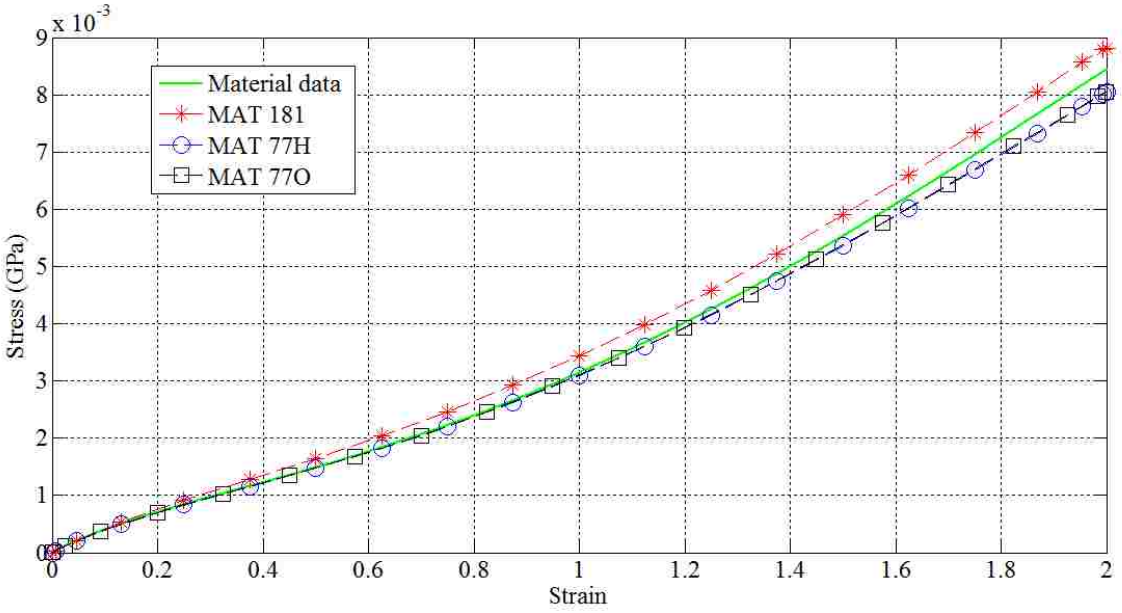

Figure 44: One element simple tension model, FIAT data.

Table 19: Single element models, material model comparison, Oberkampf-Trucano validation metrics.

Material model	**Validation metric**
MAT 181 Simple Rubber/Foam	0.91863
MAT 77H	0.98003
MAT 77O	0.98164

In a surprising result the inclusion of compressive stress strain data significantly improved the performance of MAT 181 in simple tension while, as expected, it reduced the performance of the other material models studied. These results are given in Figure 45. The next models developed represented the ASTM D412 type D dumb-bell simple tension specimen. The simple one element model had confirmed expectations that MAT 181 would outperform other material models for simple compression and tension. Therefore, MAT 181 became the focus of further studies. However, other material models were still assessed to provide a thorough analysis of modelling techniques.

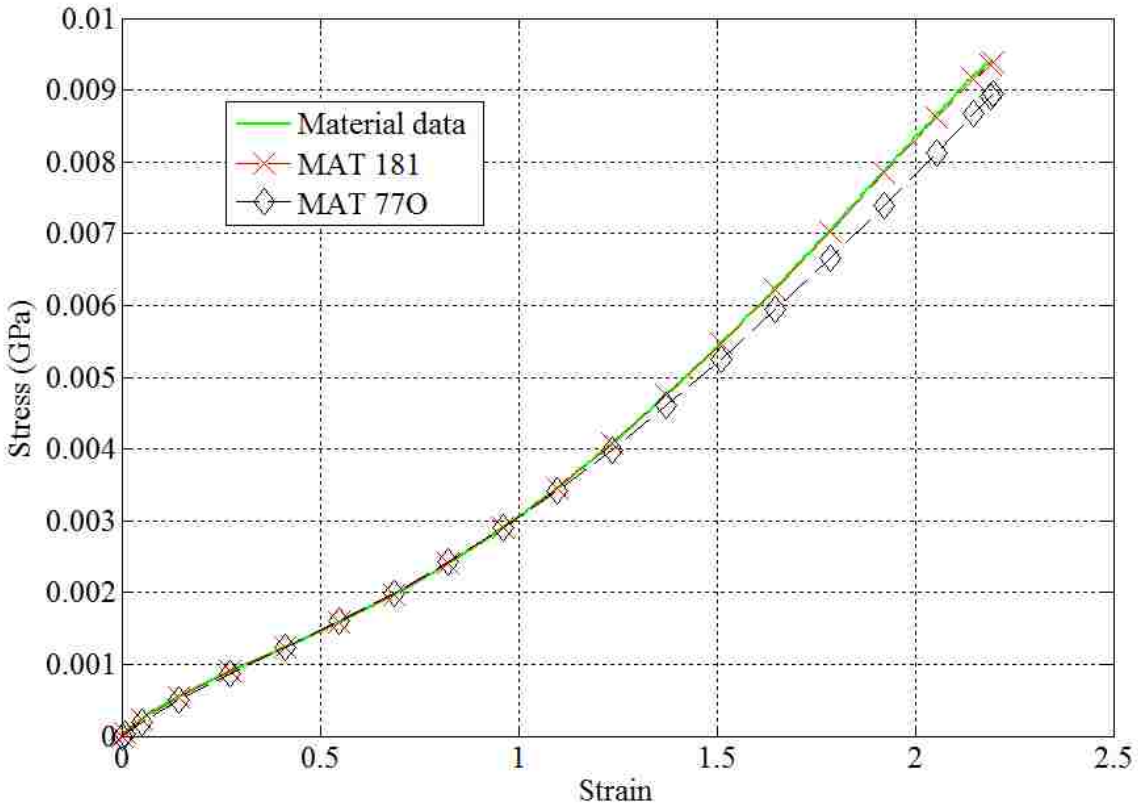

Figure 45: Material model performance in simple tension with uniaxial tension-compression input data.

Table 20: Oberkampf-Trucano validation metrics for single element models to compare material models with uniaxial stress-strain input.

Material model	**Validation metric**
MAT 181 Simple Rubber/Foam	0.99511
MAT 77H	Error termination, out of range nodal velocities
MAT 77O	0.96090

5.2.2 Simple Tension Finite Element Models (MAT 181)

Two sets of simple tension finite element models were developed. One set used hexahedron formulations 1, 2, and 3. The other set of models used tetrahedron element formulations 4, 10, 13, 16, and 17. Element formulations 1, 10, and 13 are under-integrated. Element formulations 4, 16, and 17 employ selectively reduced integration. Element formulation 3 is fully integrated. For each type of element different levels of mesh discretization were studied. It was attempted to identify reasonable limits for the optimal average element critical length to yield acceptable results with an efficient model. These models were run on a workstation with a dual core Intel Xeon CPU with a clock speed of 2.5 GHz and 12 GB of RAM. The default solver version was a single precision R3.2.1 solver for AMD64 processors. Studies of the solver version included the use of a double precision solver and a release 6.0.0 double precision solver.

A coarse hexahedron element mesh of the ASTM D412 type D specimen is shown in Figure 16. The three hexahedron element formulations for this mesh are compared in Figure 46. The error metric is the Oberkampf-Trucano metric. Element formulation 3 performed very poorly with respect to the input stress-strain data and element formulations 1 and 2. At this relatively coarse level of discretization element formulation 2 performed quite well. With a refined mesh the performance of element formulation 1 exceeded that of formulation 2 quantified using the error metric, and, as expected, the CPU time of formulation 1 was much lower. Element formulation 3 again performed quite poorly with an error termination and a large CPU time. The error termination occurred after the maximum strain of the experimental data against which the model was validated. However, all models were identical in terms of the displacement of the nodal rigid body. Error terminations may therefore provide evidence of modeling parameters with reduced capabilities of modeling large deformations.

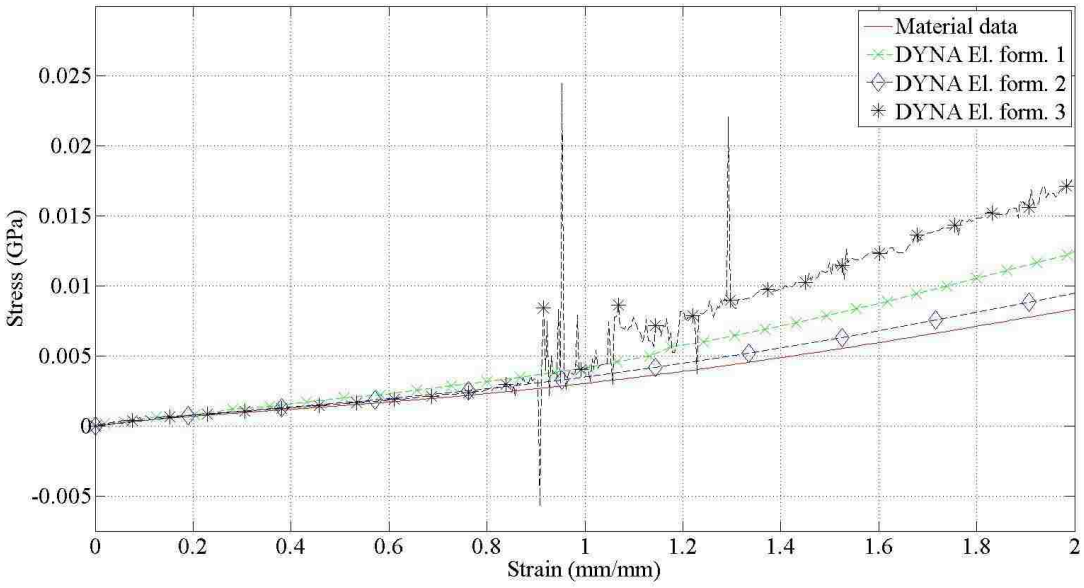

Figure 46: Coarse hexahedron mesh, ASTM D412 Type D specimen.

Tetrahedron element formulations 4, 10, 13, and 16 were similarly compared. Element formulation 17 was also employed but performed very poorly. Element formulation 4 terminated with an error. The post-processing technique, which used the open source Matlab clone Octave, extrapolated the stress-strain response in this particular case. The normal operation is to interpolate the LS-DYNA model results to determine the stresses computed by the models corresponding to the entries in the strain vector of the material model input. The engineering stress was calculated from an output of boundary condition force from LS-DYNA (BNDOUT) and the initial cross sectional area of the specimen. These calculated stresses were then compared to the stresses of the input material model data through the calculation of the Oberkampf-Trucano metric. The Octave script can be found in the appendices. Element formulations 10 and 13 exhibited comparable and relatively accurate responses. Formulation 13 performed slightly better which may be associated with the specialization of this formulation for incompressible materials. Formulation 16 produced the most accurate response but was much more computationally expensive. This is to be expected since these 10 point tetrahedron elements have sub-elements which approximately halve the critical timestep. Element

formulation 17 exhibited an interesting erroneous response whereby the volume was not near-constant but instead increased drastically (~5000%) with deformation. With a refined mesh all models terminated normally with very accurate results.

5.2.3 Simple Compression Finite Element Models (MAT 181)

Similar analyses to those performed for simple tension were completed for the models of simple compression. Figure 47 shows the engineering stress strain responses with a coarse hexahedron mesh for element formulations 1, 2, and 3. Element formulation 1 exhibited an instability that may be associated with hourglassing, a conclusion reached considering the energy balance (shown in Figure 48). With a refined mesh element formulation 1 still exhibited the instability also observed with the coarse mesh. Element formulation 2 also terminated with an error but this was studied and found to be associated with a reduction in initial element quality. It should be noted that the discretization quality was very high with near unity aspect ratios and Jacobians.

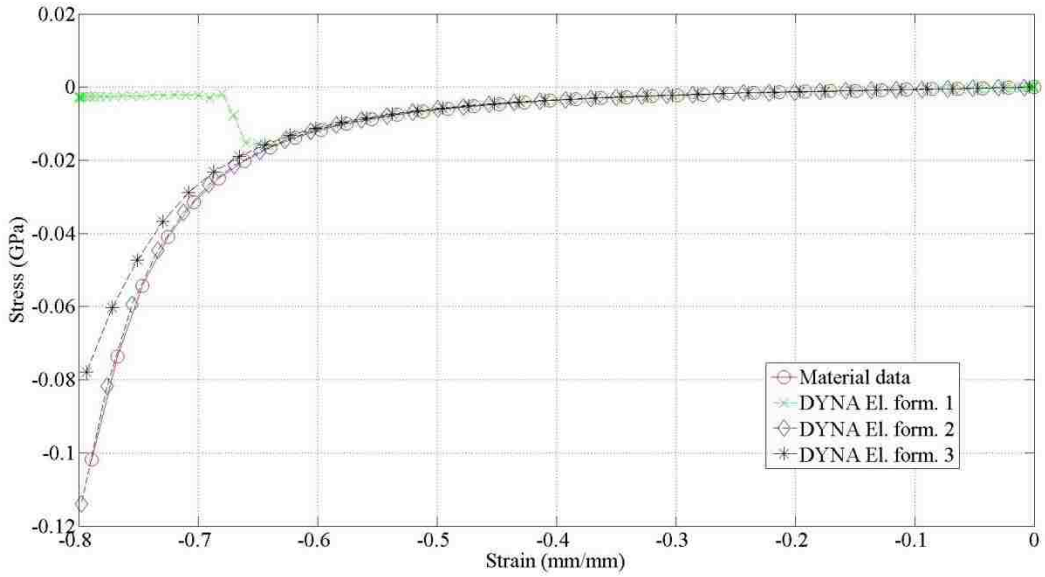

Figure 47: Model of simple compression test, coarse hexahedron mesh.

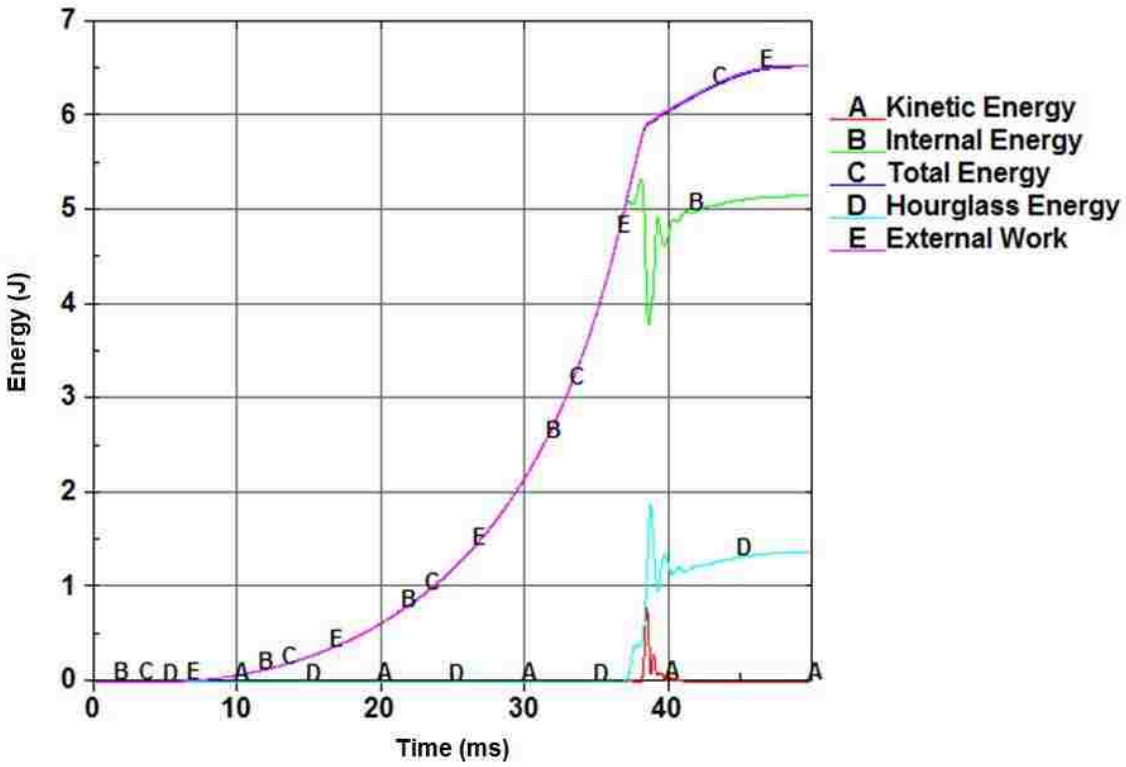

Figure 48: Energy balance for element formulation 1, coarse discretization.

Models were also developed with a coarse tetrahedron mesh. Element formulation 10 exhibited increased stiffness at large compressive strains which may be associated with the locking of the element. Element formulation 13, which is similar to formulation 10 but specialized for incompressible materials, was slightly less stiff. Instabilities were encountered with the 10 node tetrahedron elements (formulations 16 and 17). The model using element formulation 16 exhibited non-uniform deformation such that while some elements collapsed driving the critical timestep to a very small value, other elements remained essentially undeformed. The simulation did not terminate with an error but was manually terminated due to the extremely small time step. Element formulation 17 exhibited an interesting response akin to its erroneous behaviour in tension. The volume of material decreased significantly eventually resulting in an error termination. These results were dependent on the version of the solver. With release 3.2.1 of LS-DYNA the simulation would terminate immediately after initialization. A release 6.0.0 solver would

achieve 50% of the termination time but with the loss of volume noted. A refined mesh significantly increased the accuracy of elements 4, 10, and 13 and eliminated the error terminations. The refined mesh had no effect on models using element formulations 16 and 17.

5.2.4 Planar Tension (Pure Shear) Finite Element Models (MAT 181)

The planar tension models were the first models that provided a valuable analysis of the capabilities of MAT 181 simple rubber/foam. This material model accepts a uniaxial stress-strain input and is capable of performing with high accuracy with respect to this data. However, it cannot accept pure shear data as an input. Other material models, such as the Ogden material model (MAT 77O), allow the analyst to determine a best fit of the Ogden strain energy density function for all available material data. The stress-strain response of the LS-DYNA planar tension (pure shear) model utilizing MAT 181 with a coarse hexahedron element mesh is shown in Figure 49. Element formulation 3 generally performed quite poorly. Element formulation three required several levels of mesh refinement to exhibit a reasonable response.

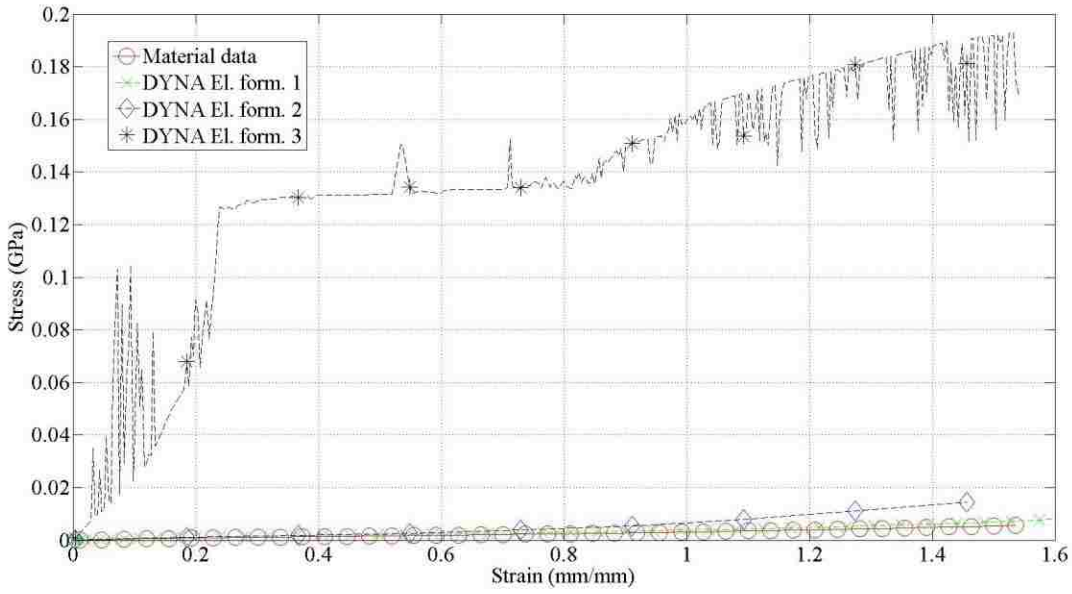

(a)

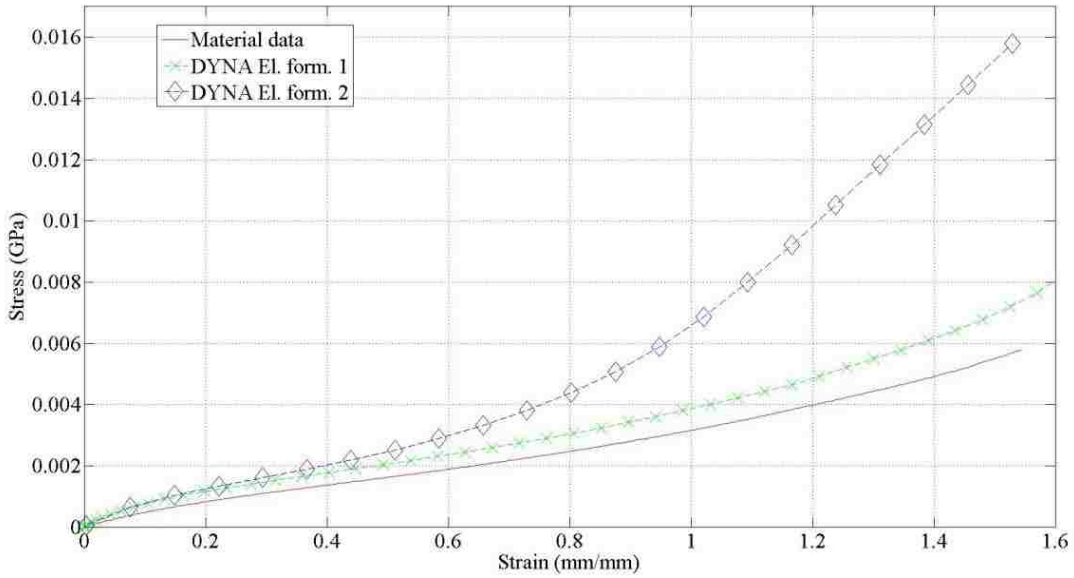

(b)

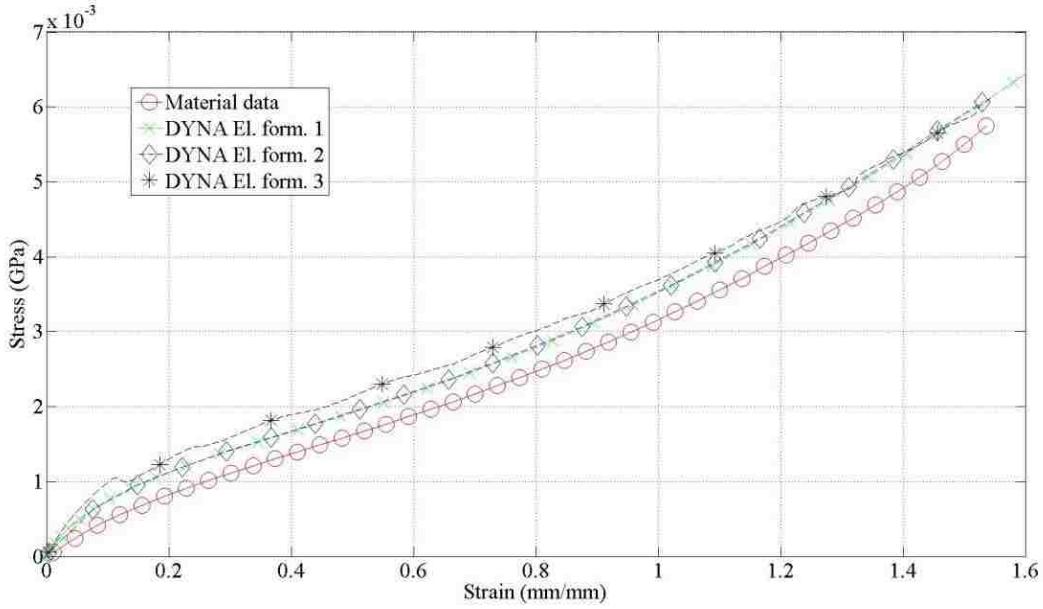

(c)

Figure 49: Planar tension (pure shear) model, hexahedron elements, (a) coarse mesh, (b) coarse mesh, response of element formulation 3 removed, (c) 3rd level of mesh refinement.

Coarse tetrahedron meshes of the planar tension (pure shear) material characterization process with MAT 181 performed very poorly as shown in Figure 50. A refinement of the mesh did not improve the performance of the model in this respect as shown in Figure 51. A 2nd level of mesh refinement yielded fairly accurate results with element formulation 13 (Figure 52). These particular models potentially demonstrated the significant advantage of element formulation 13 over element formulation 10 for near incompressible materials. With another level of refinement of the mesh there was a slight reduction in the accuracy of formulation 13. The computational cost was also very high which necessitated the use of the FIAT computing cluster and a massively parallel processing (MPP) solver. The performance of element formulation 10 was improved but only marginally. The refinement of the mesh to this level also yielded a model for which element formulation 4 would terminate normally.

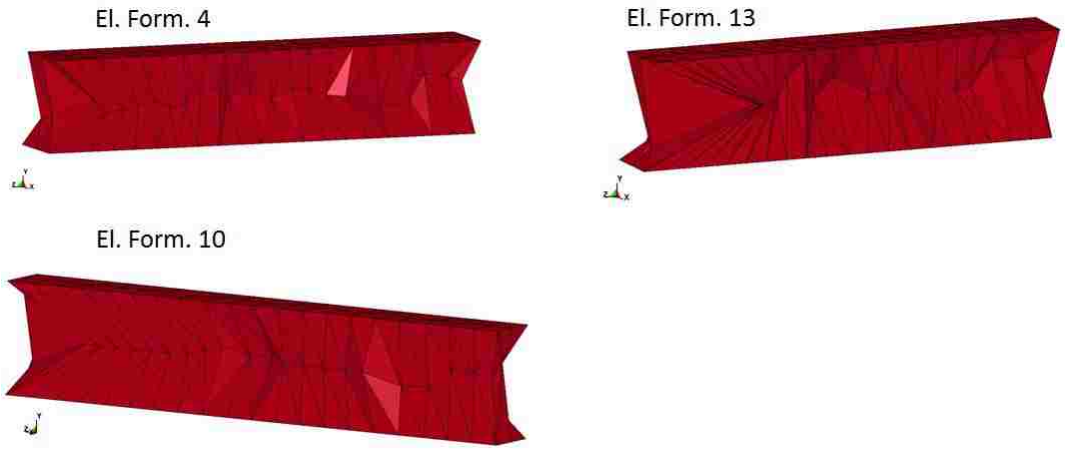

Figure 50: Poor performance of a coarse mesh of tetrahedron elements of the planar tension (pure shear) material characterization process with MAT 181.

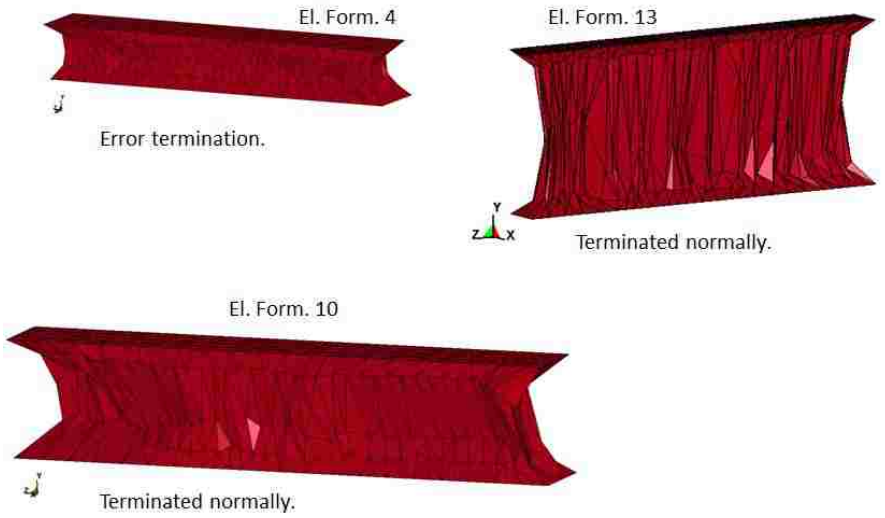

Figure 51: Lack of improvement of results with 1 level of refinement of the tetrahedron mesh of the planar tension (pure shear) material characterization model with MAT 181.

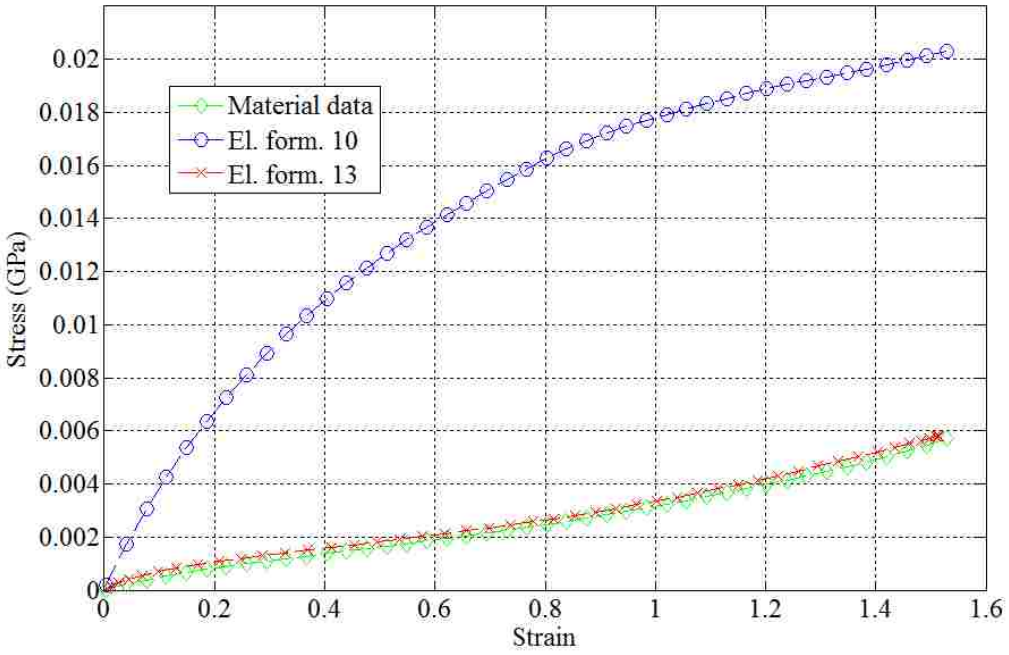

(a)

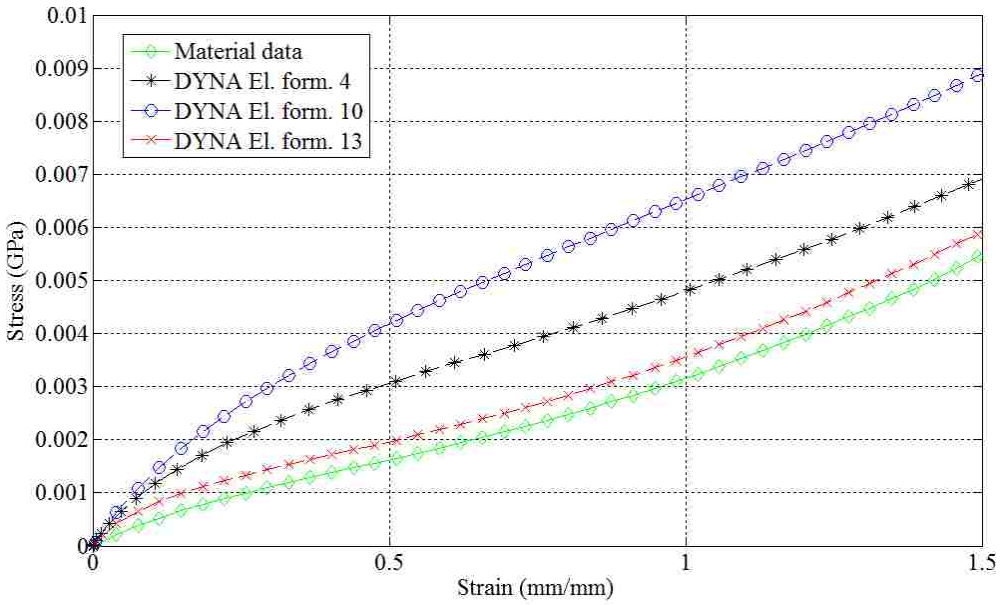

(b)

Figure 52: Stress-strain response of model employing tetrahedron elements, model of planar tension (pure shear) material characterization process, MAT 181, (a) 2nd level of mesh refinement, (b) 3rd level of mesh refinement.

5.2.5 Equibiaxial Tension Finite Element Models (MAT 181)

The equibiaxial tension models provided another excellent method for assessing the capabilities of MAT 181. Equibiaxial tension data cannot strictly be used as an input to the material model although it can be transformed to simple compression data. This is useful for assessing or eliminating the effects of friction on simple compression material characterization data. As shown in Figure 53, with a relatively coarse mesh of the equibiaxial tension material characterization specimen all three hexahedron element formulations performed quite well although element formulation 1 exhibited an instability identified through the D3PLOT animation and also indicated by the oscillations of the stress-strain curve at large strains. Although insignificant with respect to internal and total energy, there was an increasing amount of hourglass energy despite the use of hourglass control. The exact cause of the oscillations is unknown.

Another observation is that the thickness of the specimen decreases significantly due to the biaxial stretching. The aspect ratios of many elements become quite large over time. Despite normal termination of the model LS-PrePost indicates that the maximum aspect ratio approaches 4000 but this is likely associated with what appear to be element inversions. The lack of an error termination does not agree with this observation. With a refined mesh much lower frequency oscillations were observed in the response of the model employing element formulation 3. A clear cause for these oscillations is unknown. As with all models of this material characterization process, large element aspect ratios were observed but the oscillations begin early in the strain history. Element formulation 3 is in theory stiffer than formulations 1 or 2 but this is not apparent considering the stress-strain responses of these models. However, an increased stiffness may explain the oscillations since for a given amount of damping increasing the stiffness would decrease the damping ratio. In terms of accuracy the coarser mesh with element formulation 3 resulted in the most optimal validation metric but considering the CPU time element formulation 2 with a relatively coarse mesh may be the most reasonable combination.

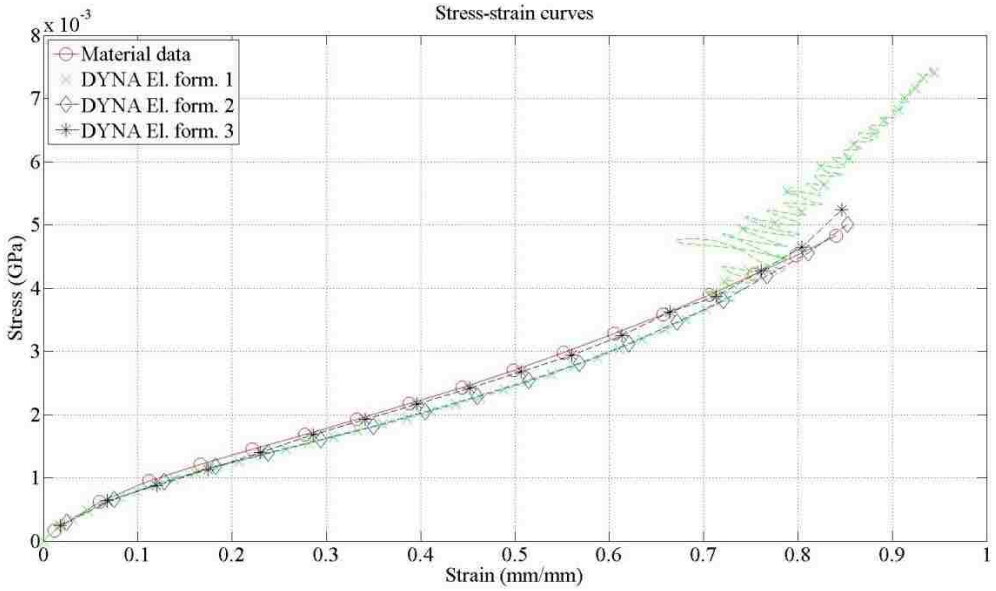

(a)

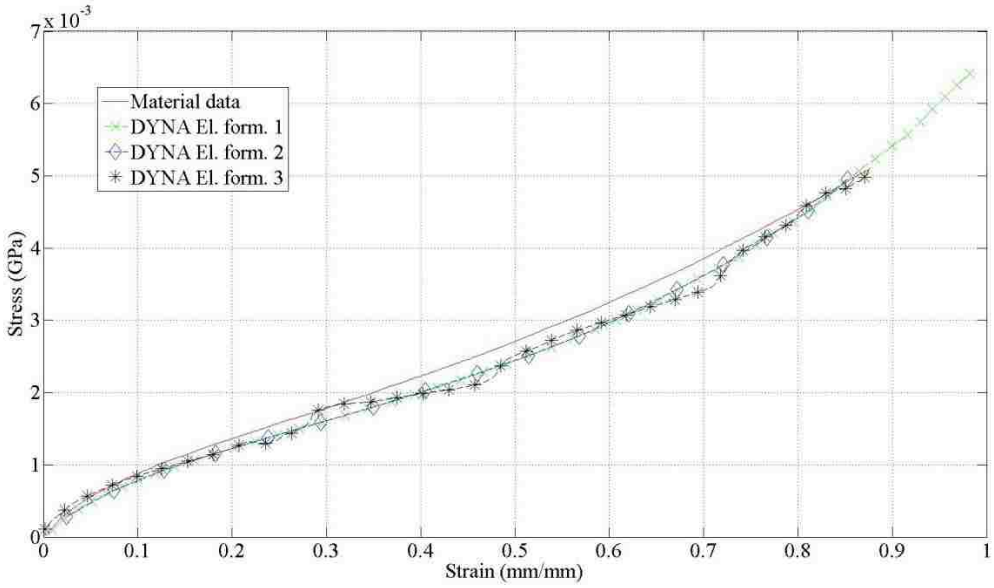

(b)

Figure 53: Equibiaxial tension, MAT 181, (a) coarse hexahedron mesh, (b) 1st level of refinement.

The engineering stress-strain responses for tetrahedron element meshes are shown in Figure 54. Even a relatively coarse mesh resulted in a high level of accuracy. The only tetrahedron element formulation which did not produce an accurate result was element formulation 16, one of the ten node, five point, selectively reduced integration tetrahedron element formulations. The energy balance for this element formulation was very poor. Internal energy and total energy were essentially identical as they should be for the quasi-static condition but external work was much lower. Element formulation 17, another 10 node tetrahedron element, would terminate with an error immediately after initialization.

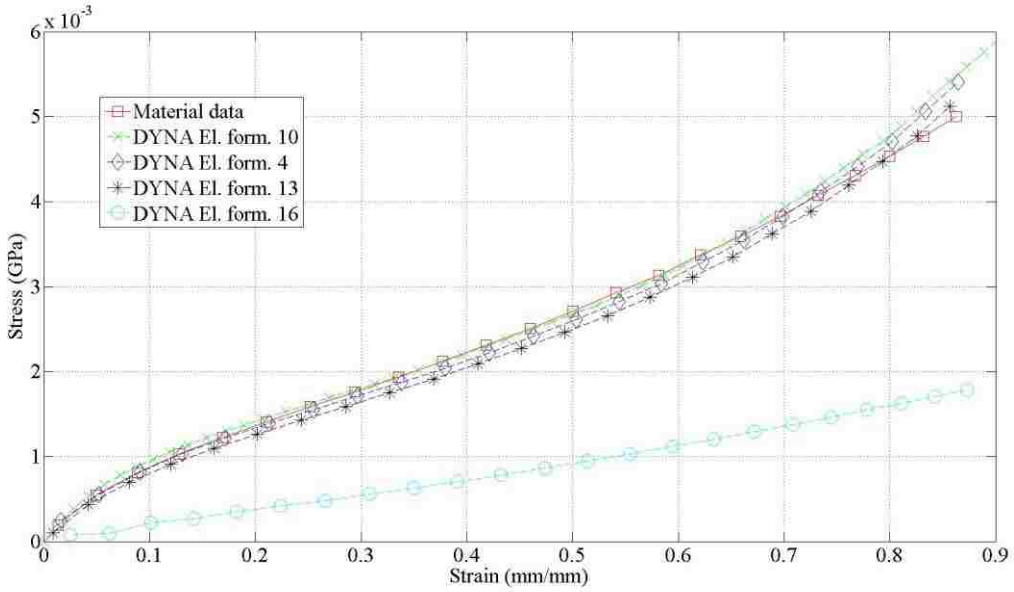

Figure 54: Equibiaxial tension models, coarse tetrahedron mesh.

5.3 Finite Element Modeling of Dynamic Material Characterization by AXEL Products Physical Testing Services

5.3.1 Single Element Models to Validate Strain Rate Sensitivity Capabilities of MAT 181

The capability of MAT 181 to capture strain rate sensitivity by simply providing stress-strain curves at different strain rates is a significant advantage of this material model. While other material models like MAT 77O may be able to capture strain rate sensitivity it would involve more curve fitting with associated error. As shown by Table 22, MAT 181 appears to be capable of essentially perfect replication of each and every stress-strain curve input to the model with an associated strain rate. Mass scaling was necessary to obtain reasonable CPU times. The increase in mass was quite significant but the energy balance showed that kinetic energy was negligible as shown by the energy balance in Figure 55.

Table 21: Mass scaling, single element model, strain rate of 0.01 1/s

Scaled mass	1.2567E-4
Physical mass	1.4125E-7
Ratio	8.8973E2

Table 22: Oberkampf-Trucano validation metric, single element models to assess strain rate sensitivity modeling with MAT 181.

Simple tension, 100 1/s	0.98034
Simple tension, 0.01 1/s	0.99326
Simple compression, 100 1/s	0.96213
Simple compression, 0.01 1/s	0.99116

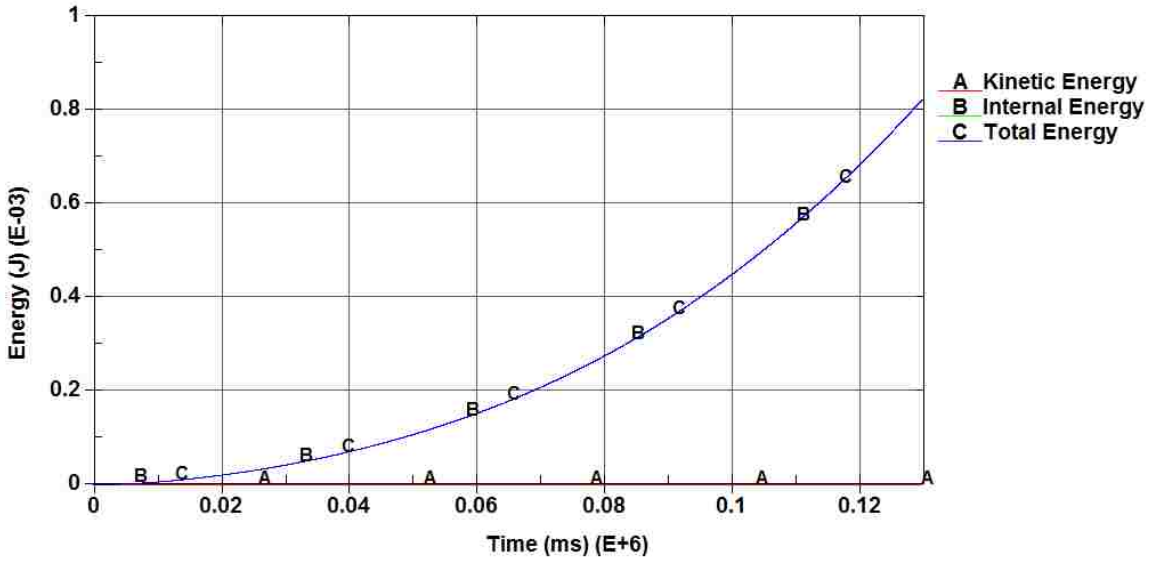

Figure 55: Energy balance, simple tension, strain rate of 0.01 1/s.

5.4 Finite Element Modeling of Quasi-Static Material Characterization with MAT 77O Ogden

The Ogden material model (MAT 77O) was also implemented for the finite element models of the material characterization processes. The material model coefficients were the six coefficients determined using MARC-Mentat. A MATLAB code was later developed that could find any number of coefficients. However, temporal restrictions strongly favoured of the use of the MARC-Mentat coefficients to enhance progress. The MARC-Mentat coefficients may also be advantageous since MARC-Mentat has options to require that all coefficients be positive and perform unknown mathematical checks on the identified coefficients. These steps may result in a more stable model.

5.4.1 Simple Tension Finite Element Models (MAT 77O, 6 Terms)

Figure 56 is the energy balance for element formulation 1. With a very coarse mesh of hexahedron elements and the Ogden material model, LS-DYNA terminated with an error for hexahedron element formulations 2 and 3 (out of range nodal velocities). The instability is visualized in Figure 57 and may be associated with the large element aspect ratios (maximum of approximately 17). The energy balance for the coarse discretization with element formulation 1 is given in Figure 56. Shown in Figure 58 is the stress strain response for a refined mesh. With the refined mesh element formulations 2 and 3 also terminated with an error. The use of a release 6.0.0 solver (the standard solver was R3.2.1) the model using element formulation 2 would terminate normally but exhibited a very poor energy balance beginning at the time at which solver R3.2.1 would terminate with an error.

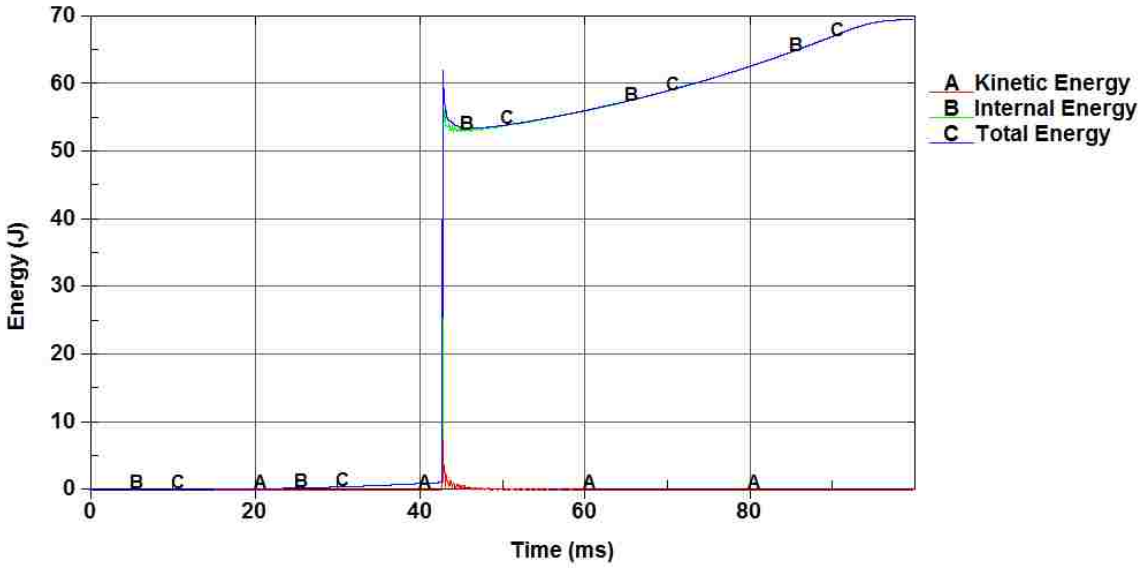

Figure 56: Energy balance plot for element formulation 1, simple tension model, coarse hexahedron element mesh.

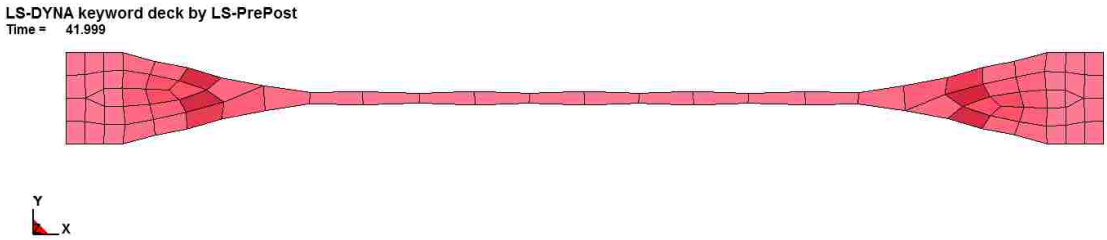

(a)

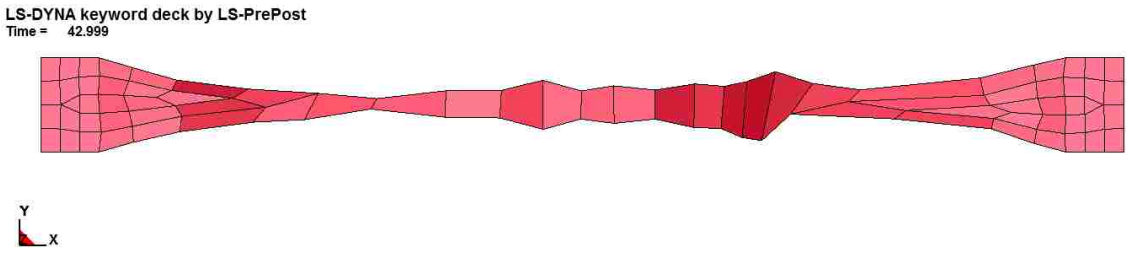

(b)

Figure 57: Element formulation 1, (a) immediately prior to instability, (b) after instability associated with poor energy balance.

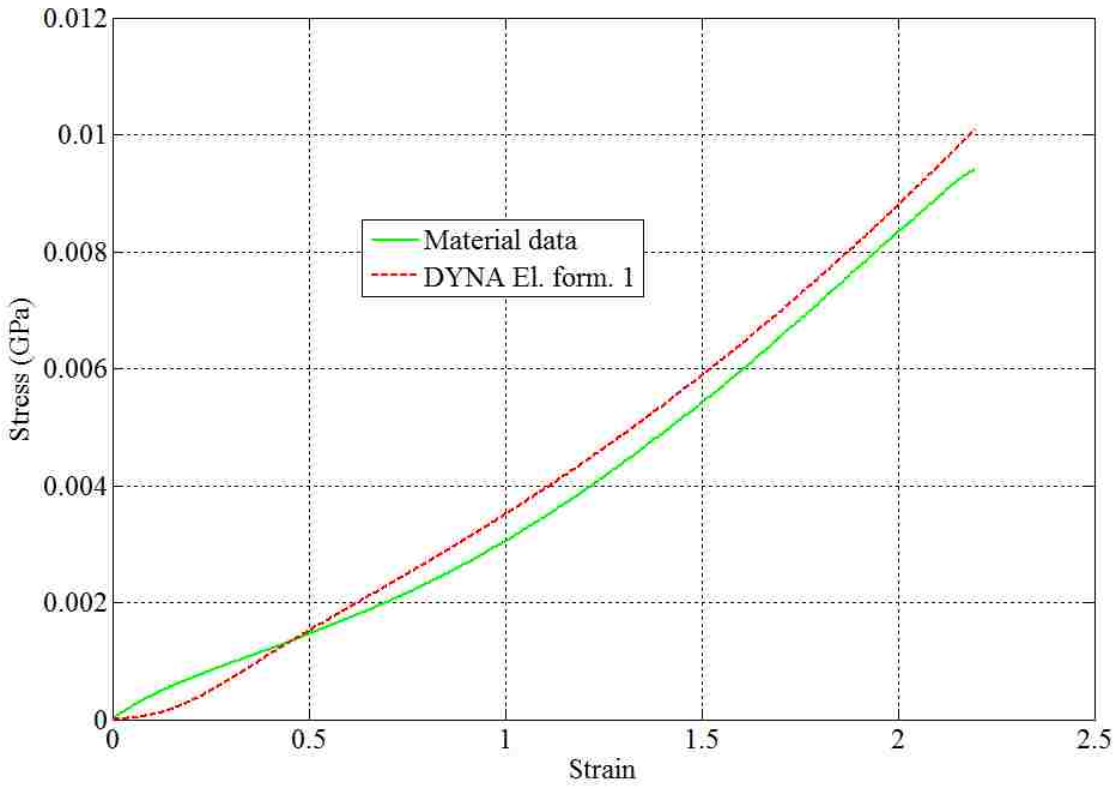

Figure 58: Simple tension model, hexahedron element formulation 1, refined mesh.

The use of tetrahedron elements was much more successful with the Ogden material model (MAT 77O). Element formulations 10 and 13 were found to be accurate, very computationally efficient, and exhibited no significant instabilities as is covered in the Discussion section. A refined mesh marginally reduced the accuracy of the solution. This may be associated with the Ogden model curve fitting. Formulations 4, 16, and 17 terminated with errors. This result was not entirely unexpected for formulations 16 and 17 given their poor performance with MAT 181. However, the essentially complete incompatibility that was observed between element formulation 4 and MAT 77O was surprising.

5.4.2 Simple Tension Finite Element Models (MAT 77O, 8 Terms)

The implementation of the Ogden LS-DYNA material model with 6 terms utilized coefficients obtained with a student version of the finite element software MARC-Mentat. The simple tension, simple compression, planar tension (pure shear), and biaxial tension material data from AXEL was input to MARC-Mentat. This software package offered two options that were assumed would yield a model that would be stable for large strains/deformations. One option was to find Ogden strain energy density function coefficients that are all positive. Since the Ogden strain energy density function is differentiated to obtain stresses, negative coefficients may yield a function that predicts decreasing stress with increasing strain for certain ranges of strain. An increasing applied force may cause the strain to reach this range at which the internal forces would decrease and be unable to match any increase in the applied force. In this case, force equilibrium would not be attained and if viscous forces are not considered the deformation would not be limited. Material failure would be unintentionally modelled. Another option in MARC-Mentat to perform mathematical checks was also used to find the coefficients for the 6 term Ogden model. If more terms were requested MARC-Mentat was not able to find a solution with these two options enabled. Even with the positive coefficients requirement disabled MARC was unable to determine coefficients for an 8 term Ogden model.

To avoid the use of a proprietary piece of software and to gain experience and familiarity with the Ogden model and curve fitting a MATLAB function was developed to find Ogden model coefficients. This simple function, discussed in the methodology section, was capable of finding positive coefficients but did not calculate the mathematical checks of MARC-Mentat. However, this MATLAB function was able to find coefficients for an Ogden model with any number of terms which allowed the largest number of terms for LS-DYNA to be used (eight) which resulted in a model with high accuracy. It was assumed that there existed a distinct possibility that this Ogden model, implemented in LS-DYNA, would not be as stable, in terms of large deformations/strains, as the MARC model.

Figure 59 is an example of the engineering response of the 8 term Ogden model (in LS-DYNA) for simple tension with a coarse mesh of hexahedron elements. With this coarse discretization no hexahedron element formulation employed was capable of modeling large deformations. Shown in the figure is element formulation 41, an element free Galerkin (EFG) formulation. This formulation is at present not compatible with MAT 181 (a Windows Intel64 SMP R6.0.0 solver was used as well as a similar R3.2.1 solver). The response is typical of all hexahedron element formulations employed with this model in that the maximum strain was limited by an error (negative volume) to approximately 125%. With element formulation 1 and R3.2.1 & R6.0.0 solvers were used, the R3.2.1 solver would terminate with an error at a strain of approximately 125%, the R6.0.0 solver would terminate normally but with a very poor energy balance subsequent to the time at which the strain was measured to be 125%.

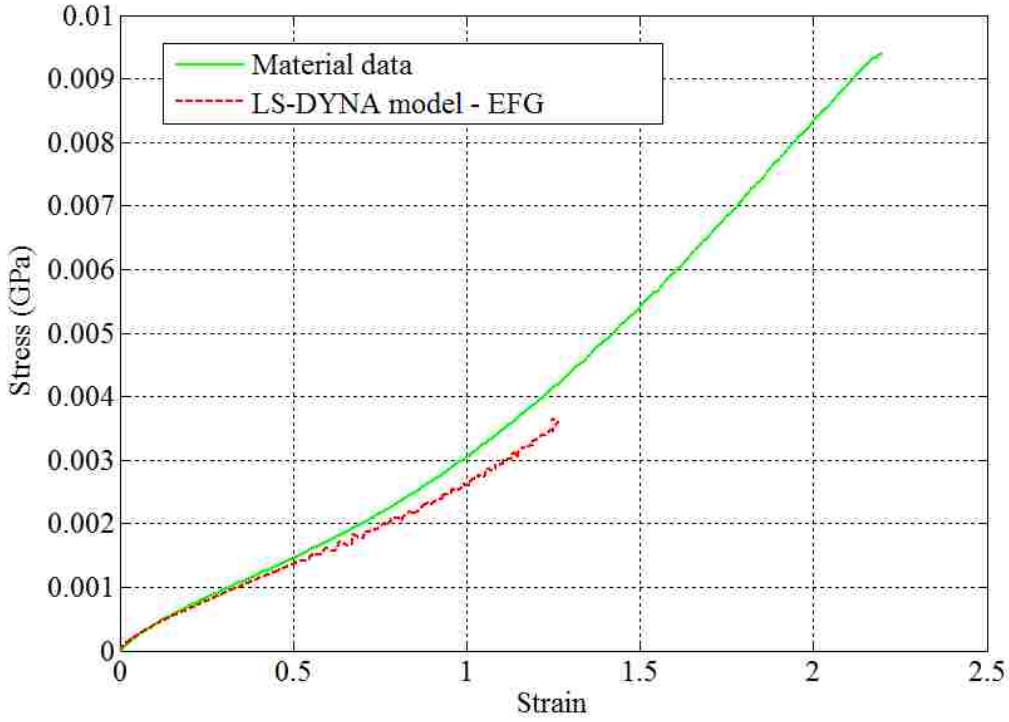

Figure 59: MAT 77O (8 Terms), simple tension finite element model, coarse hexahedron mesh, element formulation 41 (EFG).

With a refined mesh models using hexahedron element formulations 1, 3, and 41 would terminate successfully. Element formulation 1 and 41 were similar in terms of accuracy but element formulation 41 was much more computationally expensive (10X). Element formulation 3 exhibited a high amplitude, high frequency response at large strains which may indicate a potential instability at larger strains. The energy balance for the model using element formulation 3 indicated a significant error approximately midway through the simulation as shown in Figure 60. Figure 61 is a visualization of the model at the time of the initiation of this instability.

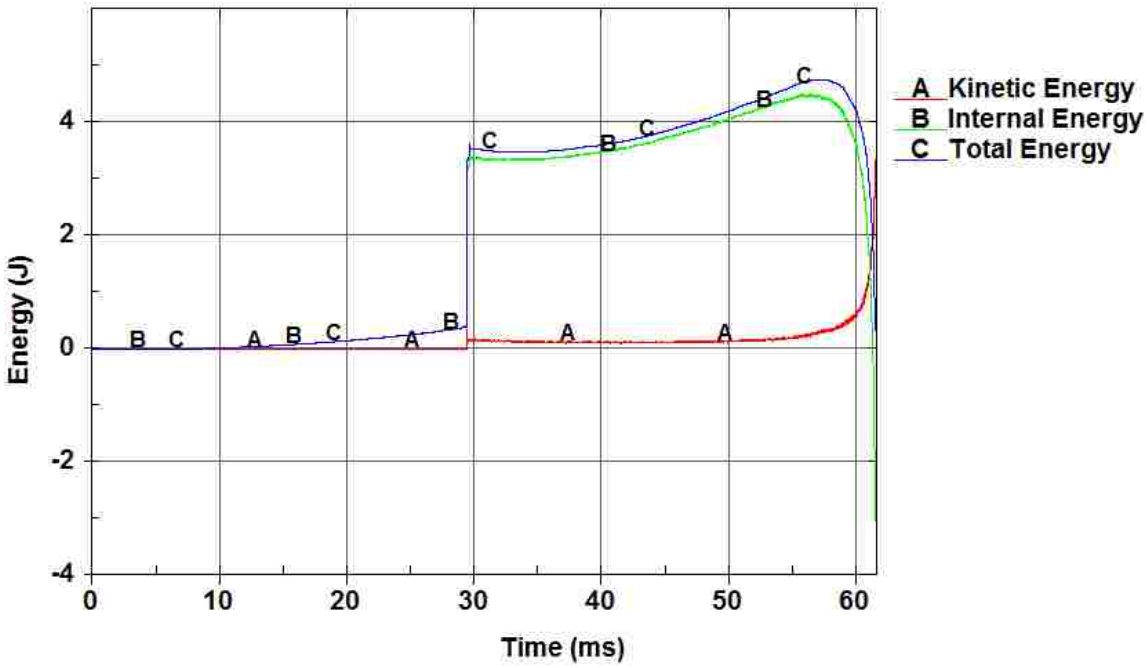

Figure 60: Energy balance of simple tension model using the Ogden material model with 8 terms and element formulation 3.

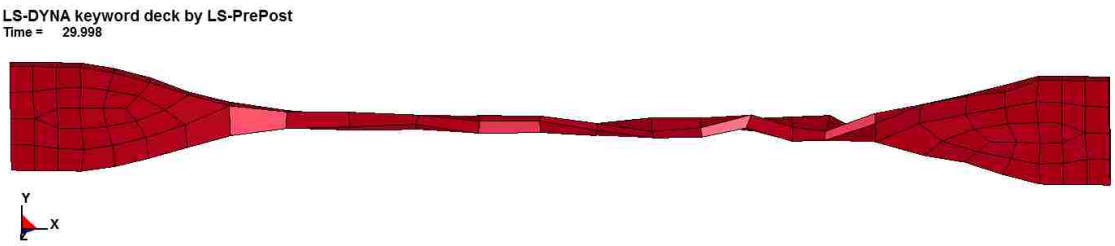

Figure 61: Instability encountered with the 8 term Ogden simple tension model and element formulation 3.

Models using tetrahedron element formulations 4, 10, 13, and 16 with a coarse mesh were compared. The accuracies of element formulations 10, 13, and 16 were consistent with the Ogden model as calculated in MATLAB. Element formulation 16 was very expensive computationally which is to be expected since it is uses 5 point selectively reduced integration. More details on accuracy and computational efficiency are provided in the discussion section. A consistent trend with respect to solver R6.0.0 was observed: for models for which other solvers would terminate with an error R6.0.0 will terminate normally but with poor energy balance initializing at the time at which other solvers terminate abnormally.

5.4.3 Simple Tension Finite Element Models with Automatic Tetrahedron Remeshing (MAT 77O, 8 Terms)

Automatic tetrahedron remeshing may not be practical for use in a model from which nodal or element output quantities are desired. Small oscillations in the nodal displacements used in calculations yield a strain that is non-monotonic over time. Potentially in correspondence with these vibrations is high amplitude high frequency content in the force output shown in Figure 62. The resulting stress-strain output was of very poor quality. Improving this may be challenging. Oscillations in the force and nodal displacement outputs are almost certainly associated with remeshing. The output of strain directly from the one non-remeshed element was possible but the strain was found to reset to zero with each re-mesh.

A significant error was observed with this model. Despite no input to re-mesh the one element used for nodal displacement output this element was often altered (node and element renumbering). One factor that influenced whether or not this element was remeshed was the penalty stiffness scaling factor (PSSF) of the tied contact (*CONTACT_AUTOMATIC_SURFACE_TO_SURFACE_TIEBREAK) used to connect this element to the surrounding deformable elements. Additionally, over the course of many remeshes the nodes of this element would move away from the nodes of surrounding elements until eventually the tied contact failed to tie the nodes together. This is likely another contributor to the reduced quality of the solution over time/strain.

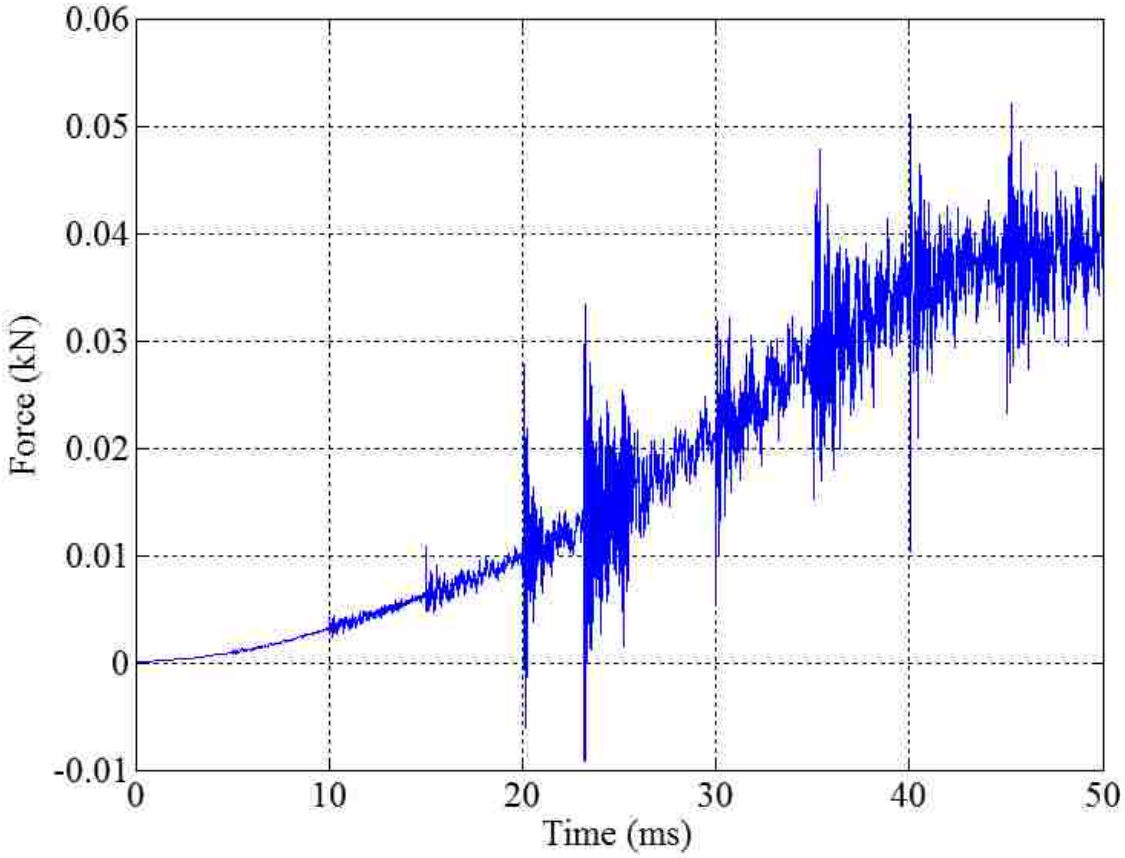

(a)

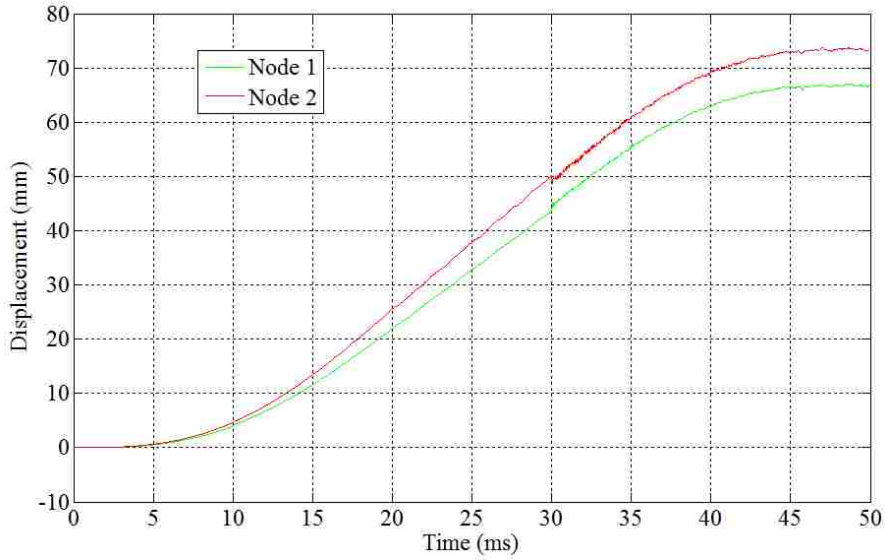

(b)

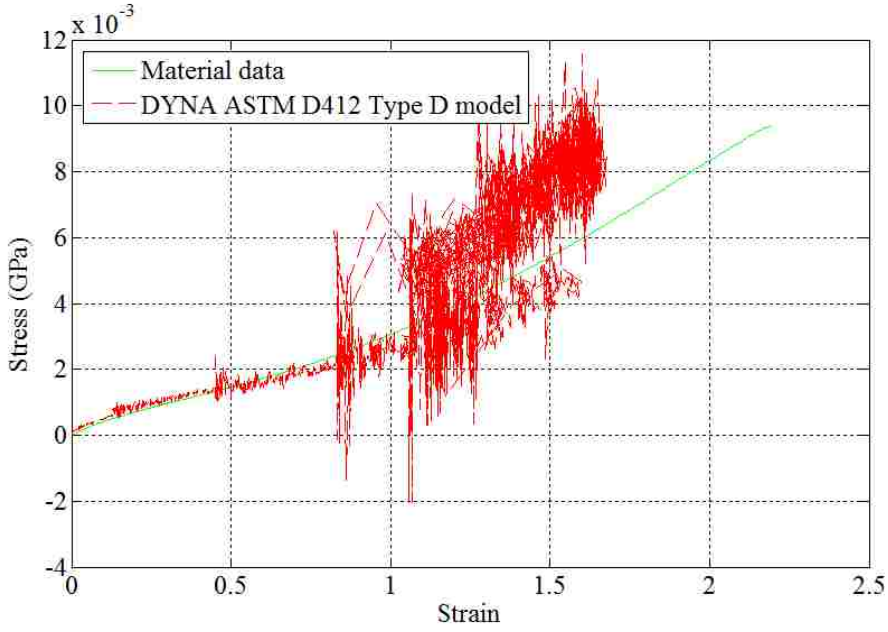

(c)

Figure 62: (a) Force output from simple tension model employing automatic tetrahedron re-meshing, (b) Nodal displacement output (to calculate strain) from simple tension model employing automatic tetrahedron re-meshing, (c) Stress-strain response of simple tension model employing automatic tetrahedron re-meshing.

5.4.4 Simple Compression Finite Element Models (MAT 77O, 6 Terms)

The performance of hexahedron element formulations 1, 2, and 3 with a coarse discretization were studied. All simulations terminated with an error. Element formulation 1 exhibited hourglassing even with hourglass control (Figure 63). Element hourglassing associated with this hourglass energy is shown in Figure 64. Element formulations 2 and 3 may have terminated with an error due to the large maximum compressive strain and the associated large aspect ratios. These topics were studied in more detail by employing a more recent solver release (R6.0.0) and a double precision solver. Neither resulted in a normal termination of the simulation or an increase in the time at which termination occurred.

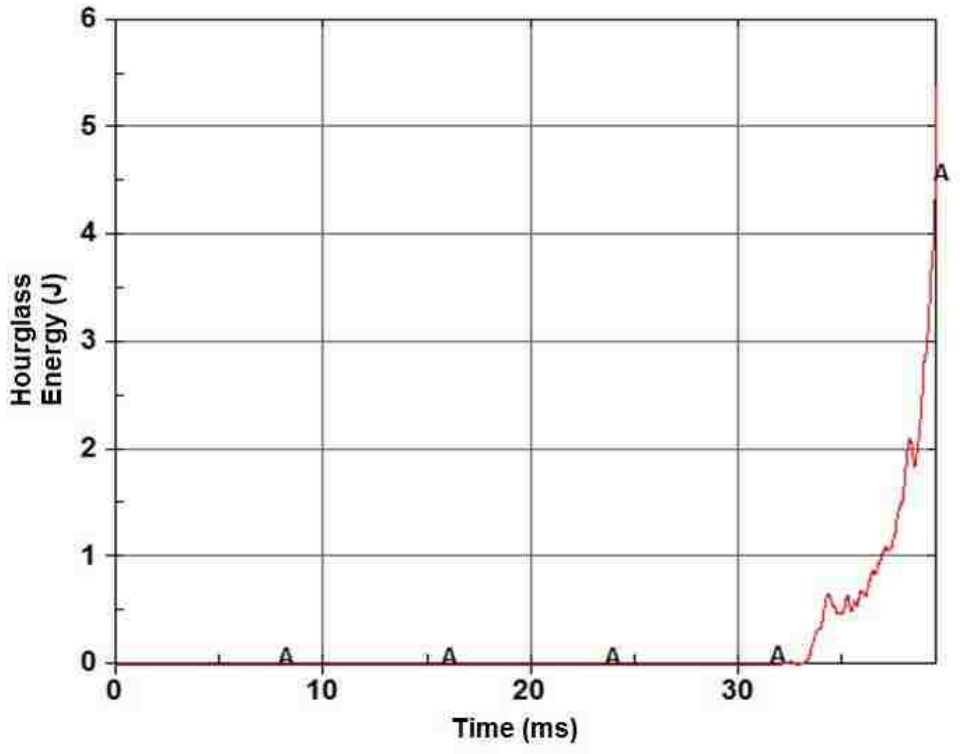

Figure 63: Simple compression finite element model, hexahedron element formulation1 energy balance.

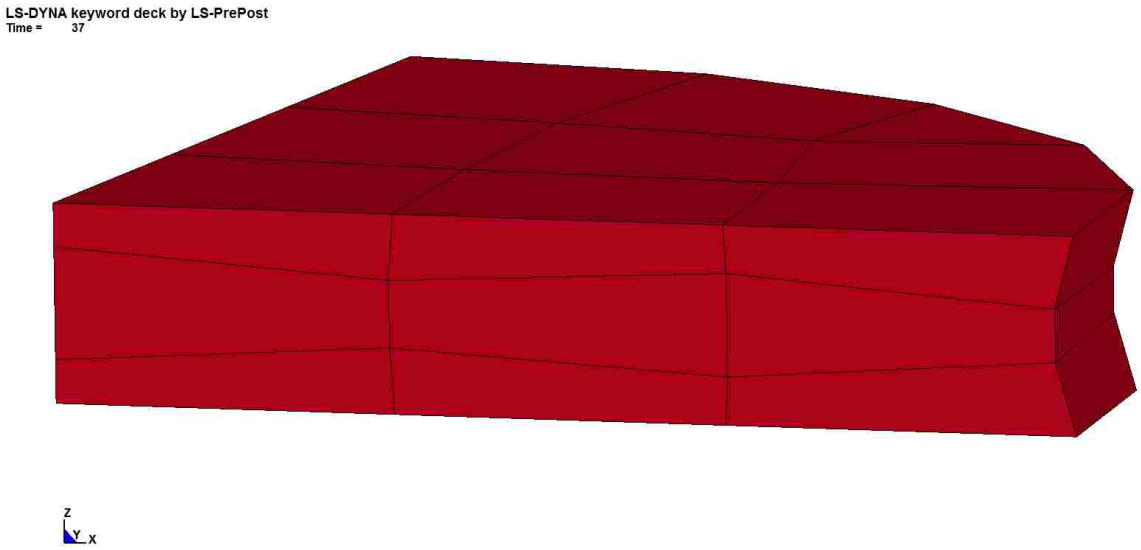

Figure 64: Element hourglassing, simple compression model, element formulation 1, Ogden material model (6 terms).

Refining the mesh did not improve the performance of the model but this should be expected so long as the mesh is refined such that the initial element aspect ratios remain unchanged. As shown in Figure 65, by developing the initial mesh with a relatively poor aspect ratio that would be improved (up to a limit) by compression, normal termination was achieved. The stress-strain response was not particularly accurate due to the Ogden model curve fitting.

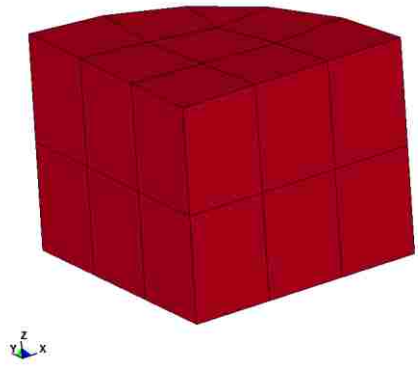

Figure 65: Simple compression model, revised mesh, coarsened through the thickness.

The use of tetrahedron elements improved the stability of the model for coarse and fine meshes. As shown in Figure 66, with a coarse mesh formulations 10 and 13 (identical results, formulation 13 shown) terminated normally and were quite accurate considering the limitations of the Ogden model curve fitting. It can be noted here and for all Ogden models that the computational cost is much lower than MAT 181 Simple Rubber/Foam (see Discussion). Consistent with all models employing the Ogden material model (MAT 77O), element formulation 4 terminated with an error. No significant improvement was observed in the stress-strain responses for element formulations 10 and 13 with a refined mesh.

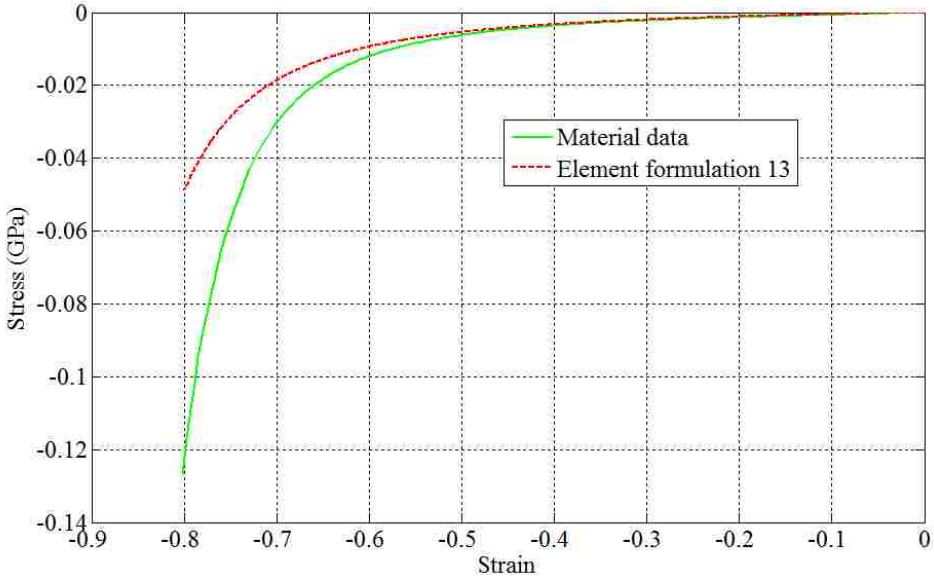

Figure 66: Simple compression finite element models, coarse tetrahedron mesh (MAT 77O, 6 terms), element formulation 13.

5.4.5 Simple compression finite element models (MAT 77O, 8 Terms)

The stress-strain responses for finite element models of the simple compression material characterization process with the Ogden material model (MAT 77O) with 8 terms and coarse meshes of hexahedron elements are shown in Figure 67. Element formulations 2 and 41 were consistent in terms of accuracy and computational cost and were the only two models which terminated normally. Element formulation 1, consistent with the 6

term Ogden model and MAT 181, terminated with an error. Significant hourglass energy and visible hourglassing were observed. Element formulation 3 also terminated with an error at a strain only slightly lower than the maximum of the AXEL experimental simple compression data. With the coarse discretization the accuracy of element formulation 3, not considering the error termination, was very poor. Consistent with the integration scheme this element formulation was also very computationally expensive.

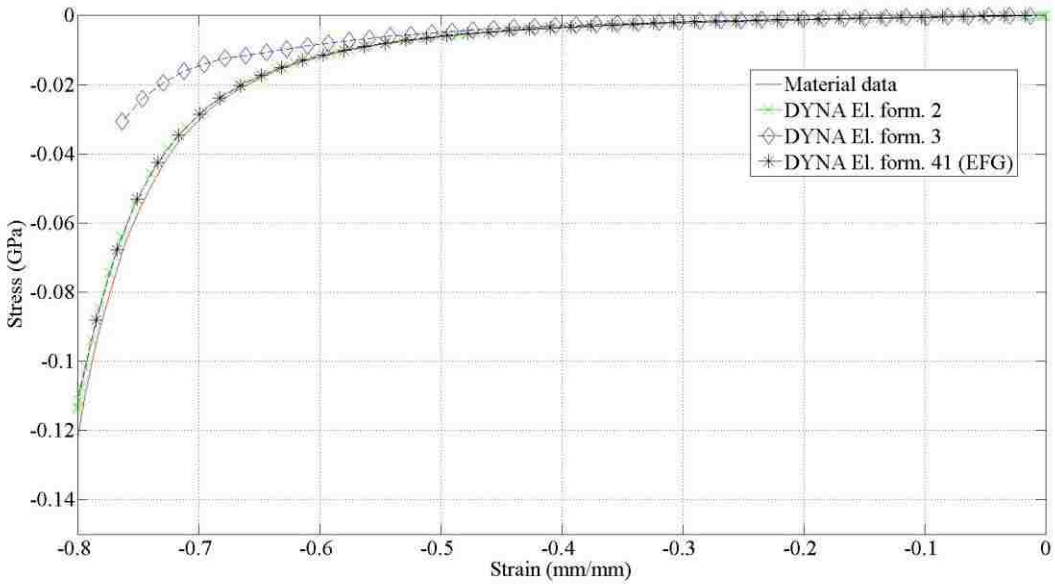

(a)

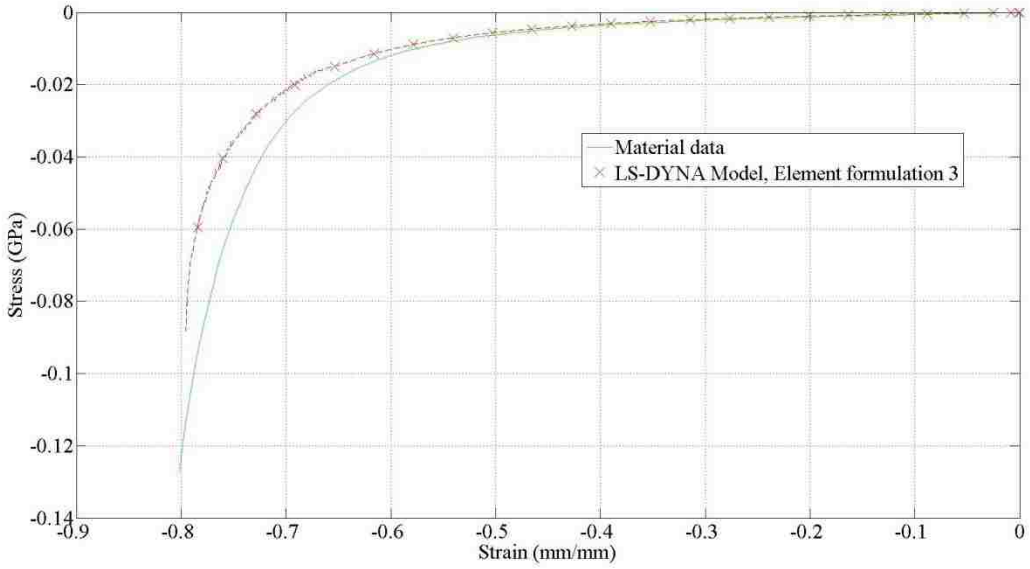

(b)

Figure 67: Simple compression finite element models, MAT 77O (8 Terms), hexahedron element formulations, (a) coarse discretization, (b) refined mesh.

When the mesh was refined significant hourglassing was still observed with element formulation 1. All simple compression models employing element formulation 1 used type 7 hourglass control with the coefficients Q_M, Q_W, and Q_B equal to 0.01. However, of element formulations 2, 3, and 41 the model utilizing element formulation 3 was the only model to terminate normally. The accuracy was significantly improved with respect to the coarse discretization used in the previous set of models.

With a coarse discretization and tetrahedron element formulations only element formulation 13 combined with solver release 6.0.0 terminated normally. Element formulation 10 was capable of reaching a relatively large compressive strain of 75%. Refining the mesh did not greatly affect the results. The models utilizing element formulations 10 and 13 terminated normally with solver release 3.2.1. A slight increase in accuracy was accompanied by a significant increase in CPU time.

5.4.6 Planar Tension (Pure Shear) Finite Element Models (MAT 77O, 6 Terms)

Figure 68 includes stress strain curves for finite element models using hexahedron element formulations and MAT 77O (Ogden). The levels of mesh discretization were consistent with the finite element models using MAT 181. Consistent with the MATLAB calculations, the accuracy of these models was reasonable although the coarsest meshes were deformed excessively with corresponding instabilities and loss of accuracy. An increasingly refined discretization was required to obtain reasonable performance with hexahedron element formulation 3. At the 2nd level of refinement the stress-strain response of formulation 3 became reasonably accurate but with increasing error over the duration of the simulation. A corresponding increasing energy imbalance was observed.

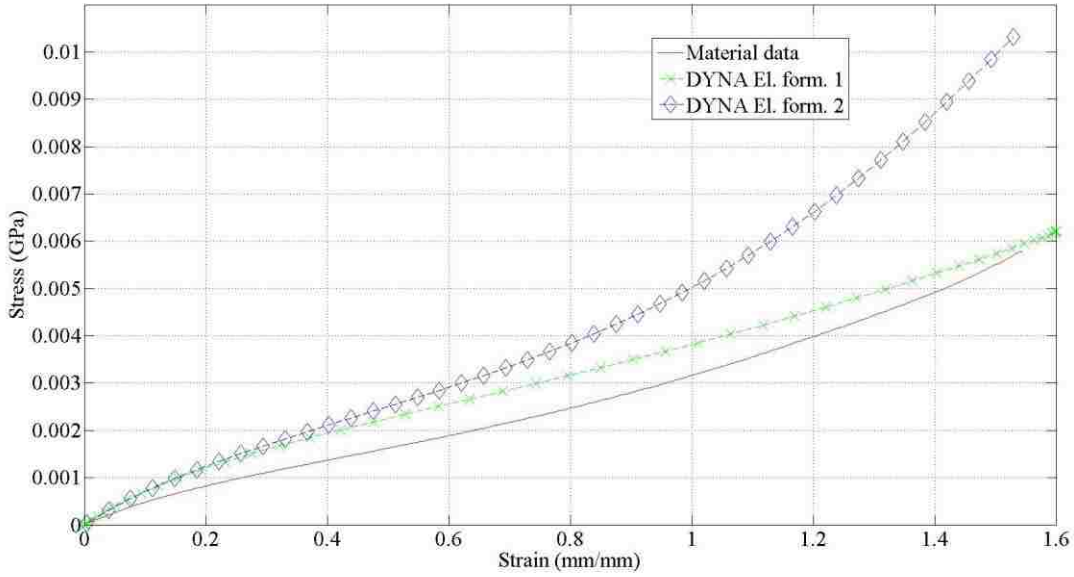

(a)

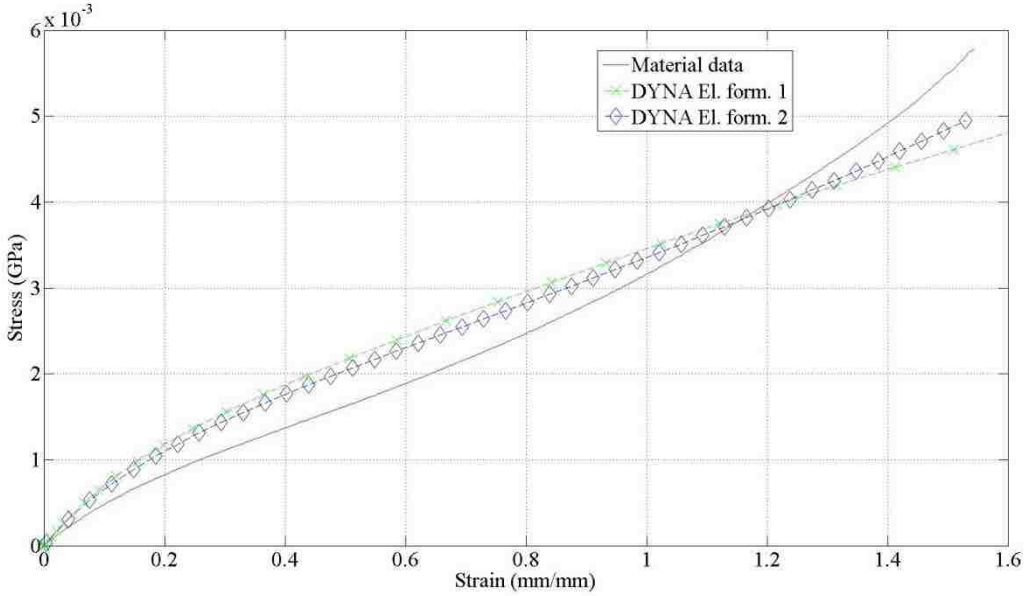

(b)

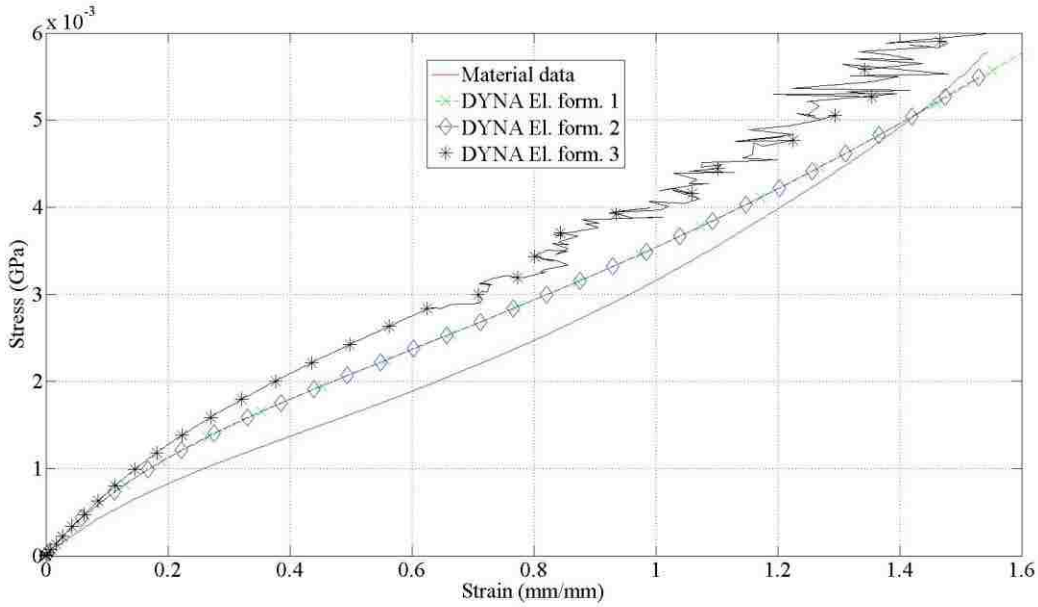

(c)

Figure 68: Planar tension (pure shear) finite element model, (a) coarse hexahedron mesh, (b) first level of mesh refinement, (c) 2nd level of mesh refinement.

Stress-strain responses for finite element models of the planar tension (pure shear) material characterization process using tetrahedron element formulations are shown in Figure 69. With a very coarse discretization element formulation 4 exhibited an instability and element formulations 10 and 13 performed very poorly. With one level of mesh refinement essentially the same behaviour was observed. Two further refinements of the discretization were required to obtain a reasonable degree of accuracy.

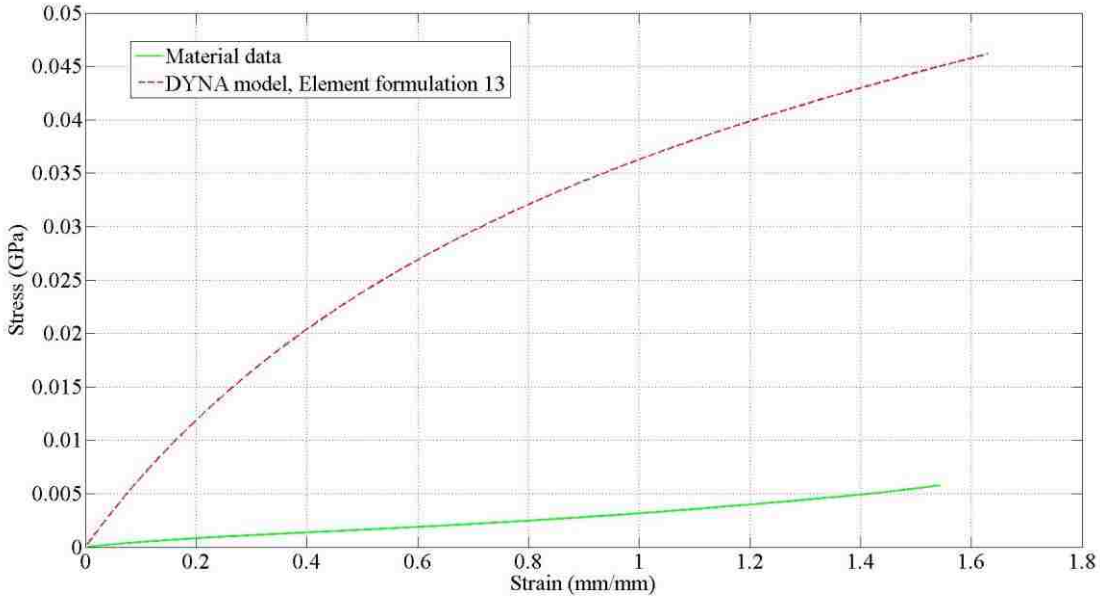

(a)

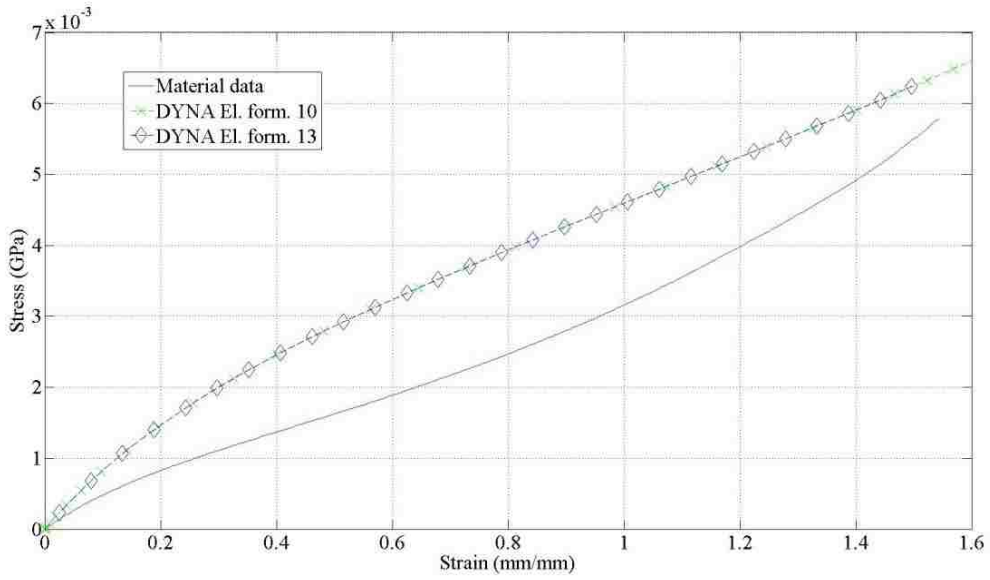

(b)

Figure 69: Stress-strain response of finite element models of the planar tension (pure shear) material characterization process (MAT 77O, 6 terms), tetrahedron element formulations, (a) coarse discretization, (b) 2nd level of mesh refinement.

5.4.7 Planar Tension (Pure Shear) Finite Element Models (MAT 77O, 8 Terms)

Figure 70 provides stress-strain responses of finite element models of the planar tension (pure shear) material characterization process with the 8 term Ogden model (MAT 77O). The models in this figure employed hexahedron element formulations. Element formulation 1 was very accurate, consistent with the theoretical performance of the Ogden model, and had an extremely low computational cost. Element formulation 2 exhibited poor accuracy with a very coarse discretization. This coarse discretization also resulted in minor inconsistencies in the D3PLOT animation but the energy balances were ideal.

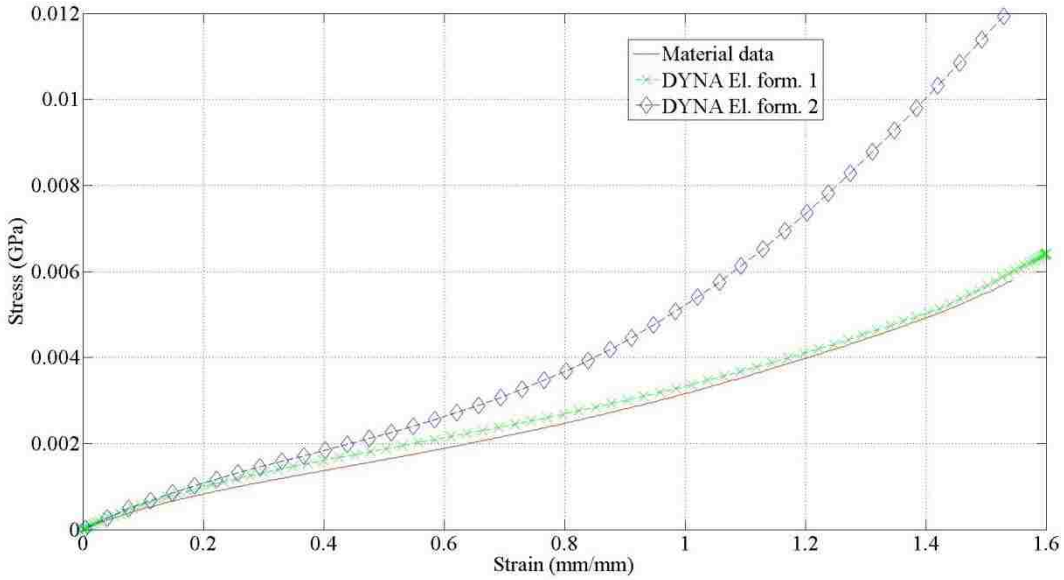
Material data
DYNA El. form. 1
DYNA El. form. 2
Stress (GPa)
Strain (mm/mm)
0.012
0.01
0.008
0.006
0.004
0.002
0
0.2
0.4
0.6
0.8
1
1.2
1.4
1.6

(a)

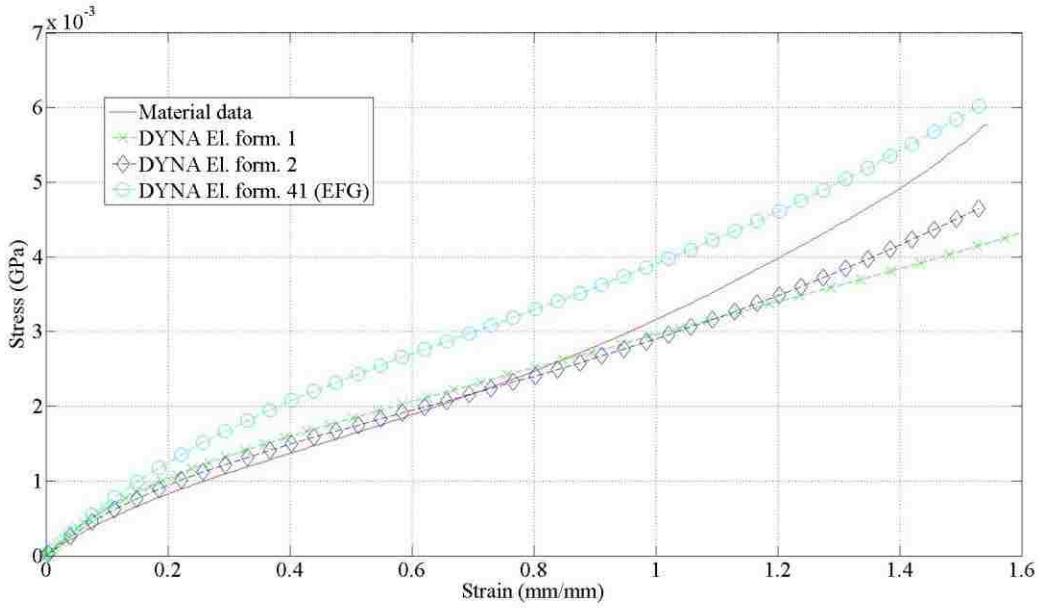
x 10^-3
Material data
DYNA El. form. 1
DYNA El. form. 2
DYNA El. form. 41 (EFG)
Stress (GPa)
Strain (mm/mm)
7
6
5
4
3
2
1
0
0.2
0.4
0.6
0.8
1
1.2
1.4
1.6

(b)

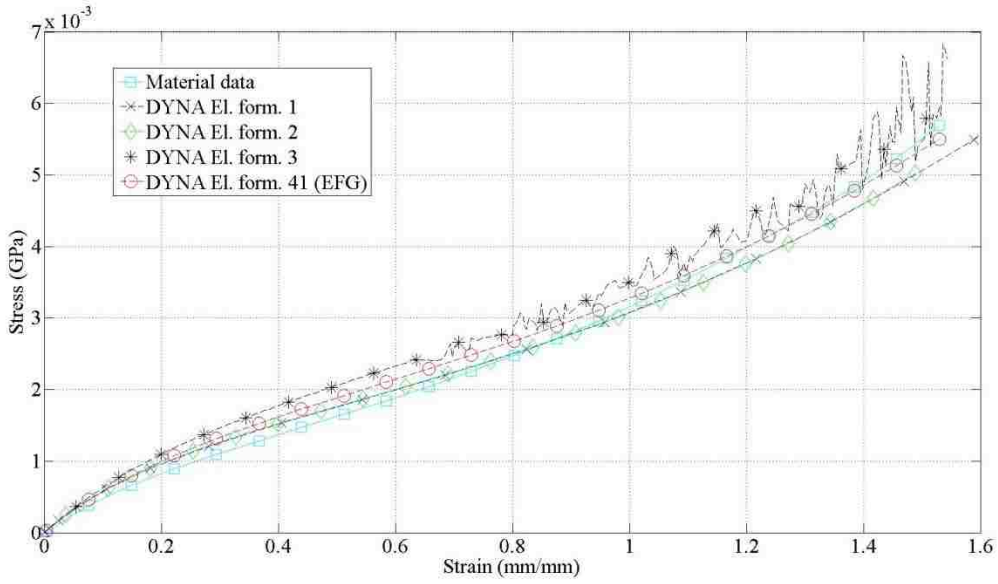

(c)

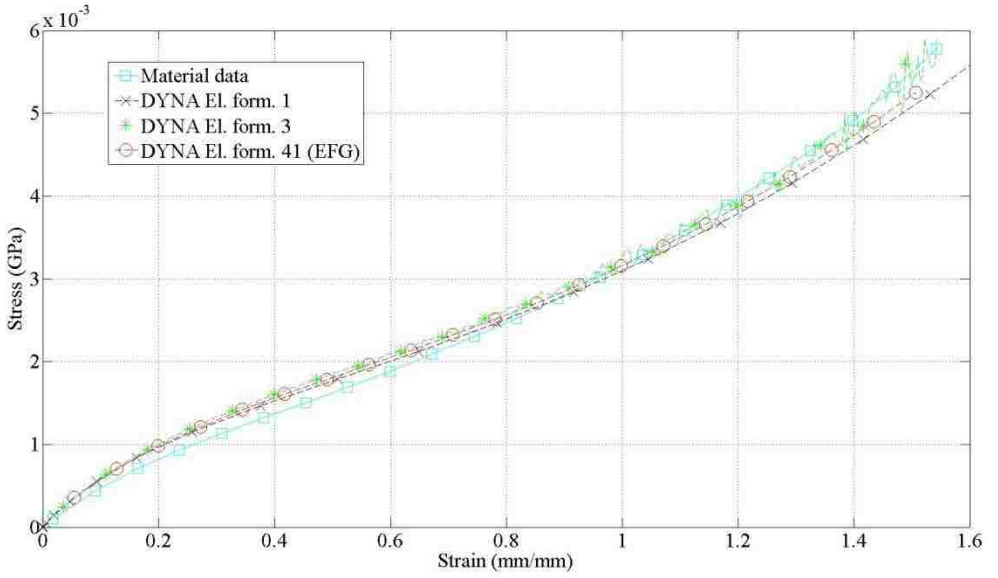

(d)

Figure 70: Planar tension (pure shear) finite element models, MAT 77O (8 Terms), hexahedron element formulations, a) coarse discretization, b) 1st level of mesh refinement, c) 2nd level of mesh refinement, d) 3rd level of mesh refinement.

With one level of mesh refinement there was a significant improvement in the performance of element formulation 2. Element formulation 41 (EFG) also terminated normally and exhibited an accurate stress-strain response. With another refinement of the mesh the results improved considerably with very accurate responses for all element formulations with the exception of element formulation 3 which exhibited a diverging energy balance and high amplitude, high frequency content in the stress-strain response. Refining the mesh once more yielded no significant improvement in the accuracy despite the significant increase in computational expense. Additionally, element formulation 2 terminated with an error.

Stress strain responses for finite element models using tetrahedron element formulations are shown in Figure 71. Element formulations 4, 10, and 13 exhibited poor accuracy with a very coarse discretization. Element formulation 16 was more accurate than 4, 10, or 13 but with respect to the AXEL experimental data the accuracy was poor. With one level of mesh refinement all models exhibited improved accuracy but only element formulation 16 can be referred to as accurate. With another level of refinement of the mesh element formulations 4 and 16 terminated with errors but the performance, in terms of accuracy, of element formulations 10 and 13 became reasonable. With one more refinement of the mesh the accuracy of element formulations 10 and 13 approached the theoretical accuracy limit for the Ogden model as calculated in MATLAB. Element formulations 4 and 16 again terminated with errors.

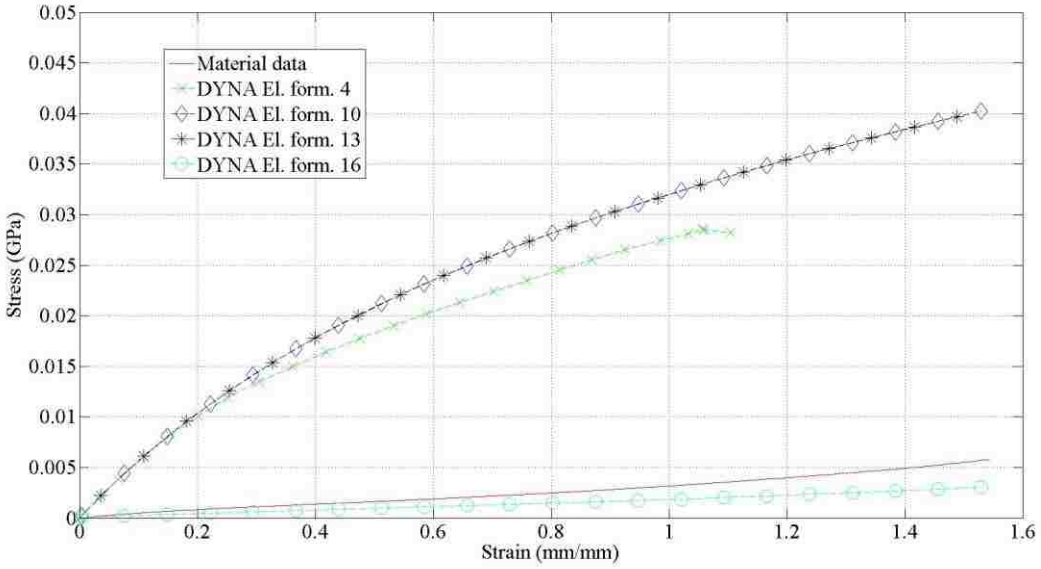
Material data
DYNA El. form. 4
DYNA El. form. 10
DYNA El. form. 13
DYNA El. form. 16
Stress (GPa)
Strain (mm/mm)
0.05
0.045
0.04
0.035
0.03
0.025
0.02
0.015
0.01
0.005
0
0.2
0.4
0.6
0.8
1
1.2
1.4
1.6

(a)

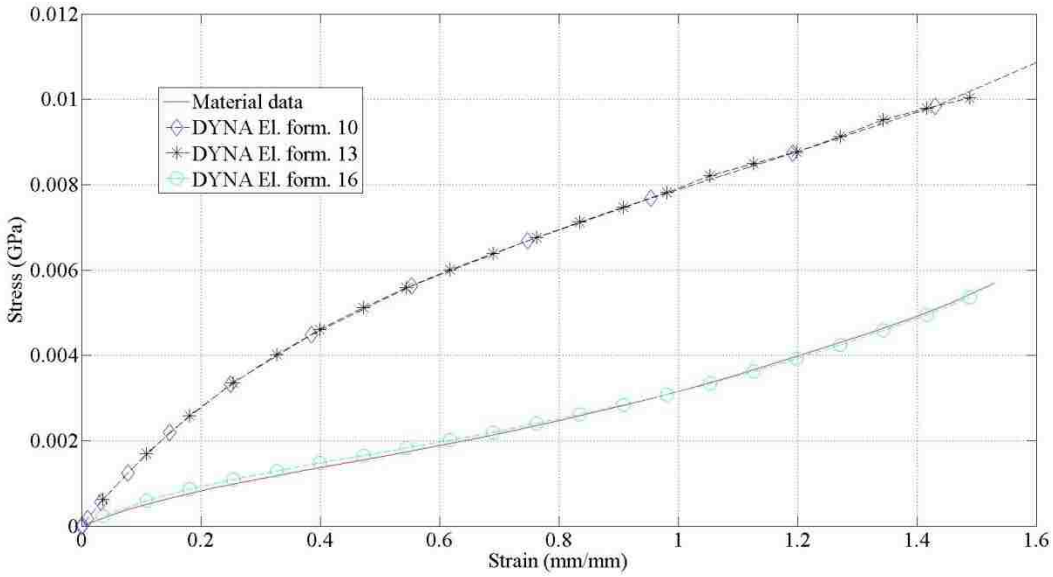
Material data
DYNA El. form. 10
DYNA El. form. 13
DYNA El. form. 16
Stress (GPa)
Strain (mm/mm)
0.012
0.01
0.008
0.006
0.004
0.002
0
0.2
0.4
0.6
0.8
1
1.2
1.4
1.6

(b)

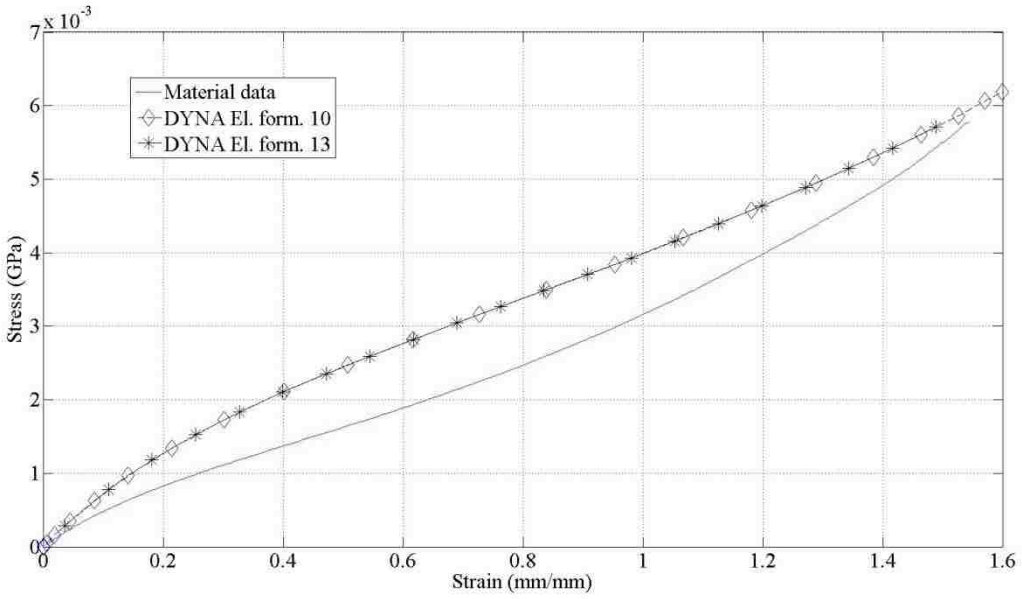

(c)

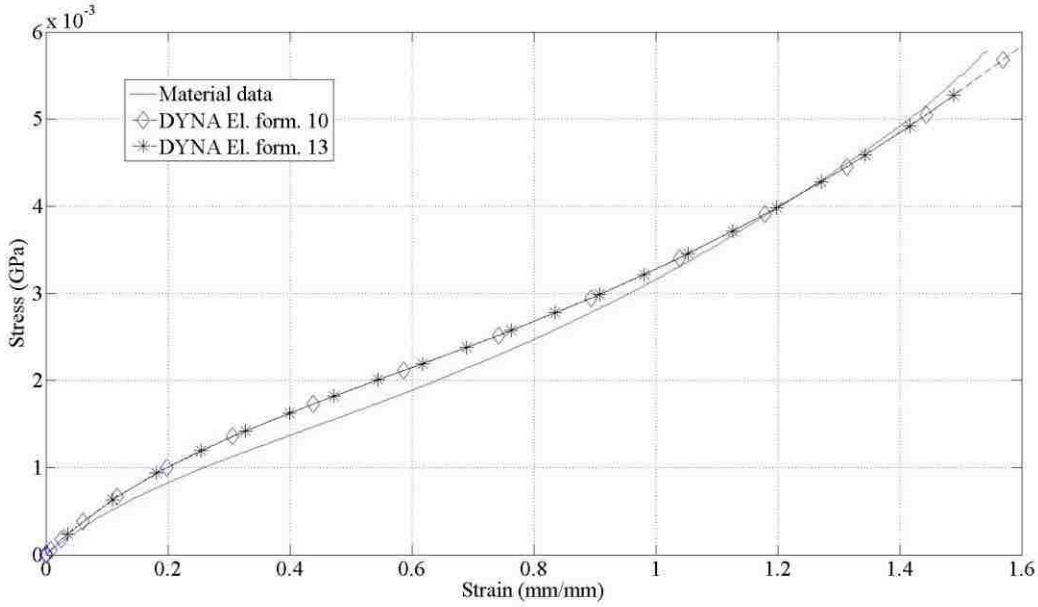

(d)

Figure 71: Planar tension (pure shear) finite element models, MAT 77O (8 Terms), tetrahedron element formulations, (a) coarse discretization, (b) 1st level of mesh refinement, (c) 2nd level of mesh refinement, (d) 3rd level of mesh refinement.

5.4.8 Equibiaxial Tension Finite Element Models (MAT 77O, 6 Terms)

Stress-strain responses for finite element models of the equibiaxial tension material characterization process with hexahedron element formulations are shown in Figure 72. With a coarse discretization the accuracy was very poor even considering the limitations due to the curve fitting of the Ogden model. With one level of mesh refinement the model became consistent with the Ogden material model calculations completed in MATLAB.

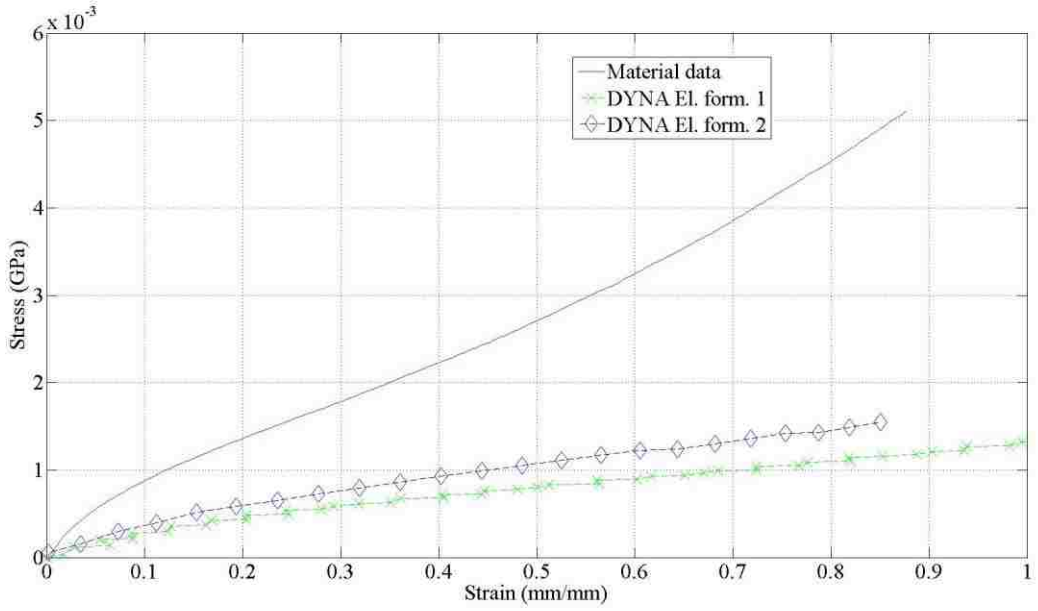

(a)

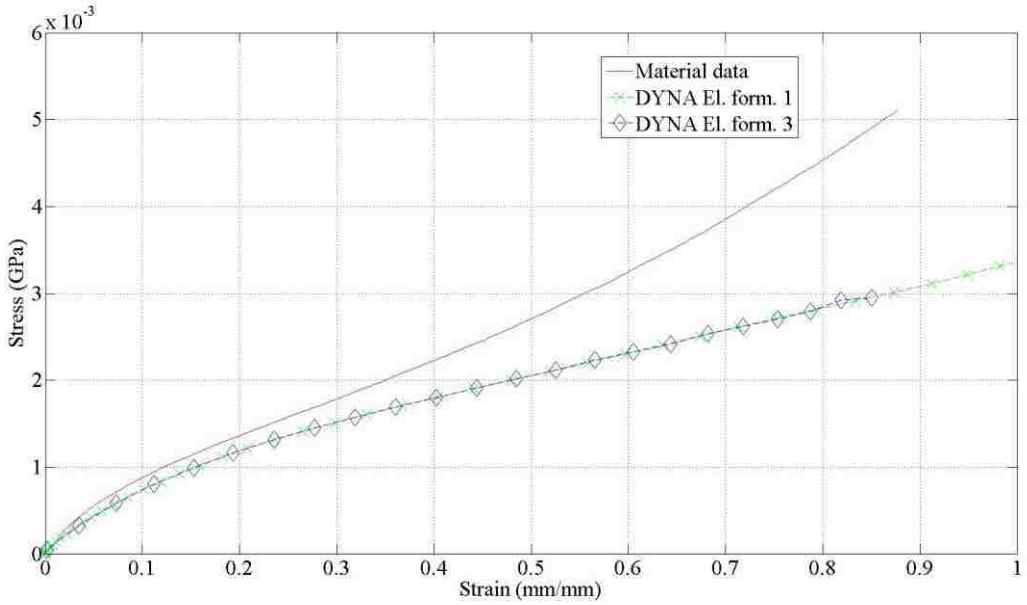

(b)

Figure 72: Stress-strain responses of finite element models of the equibiaxial tension material characterization process (MAT 77O, 6 terms), hexahedron elements, (a) coarse discretization, (b) 2nd level of mesh refinement.

Figure 73 includes stress-strain responses of finite element models of the equibiaxial tension material characterization process (MAT 77O) employing several tetrahedron element formulations. The response was not particularly accurate but was consistent with the MATLAB analysis of the 6 term Ogden model (Figure 25). Mesh refinement did not significantly improve the accuracy of the results although it did eliminate small amplitude vibrations present in the response of the coarse mesh.

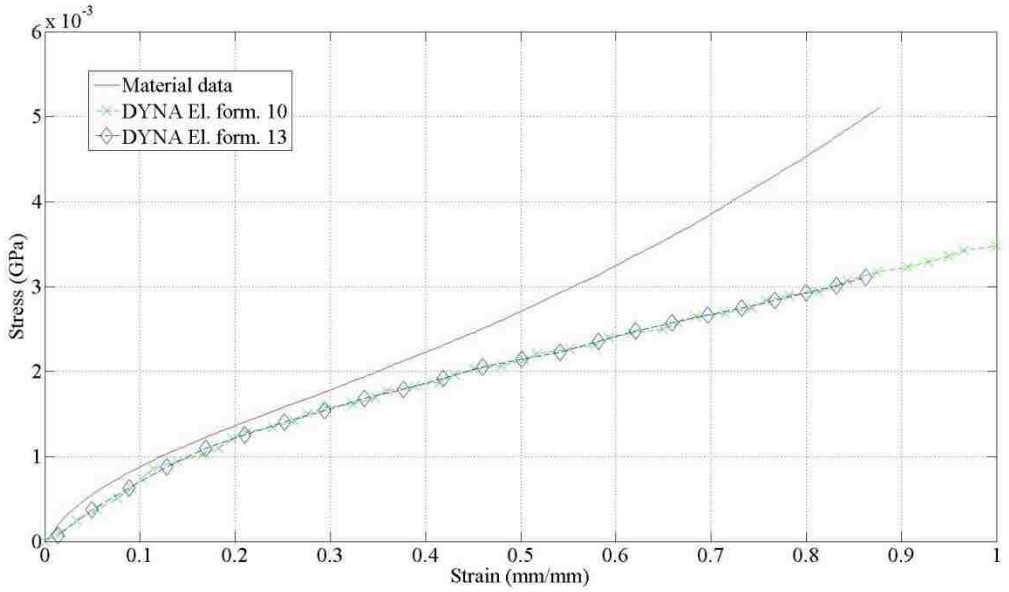

(a)

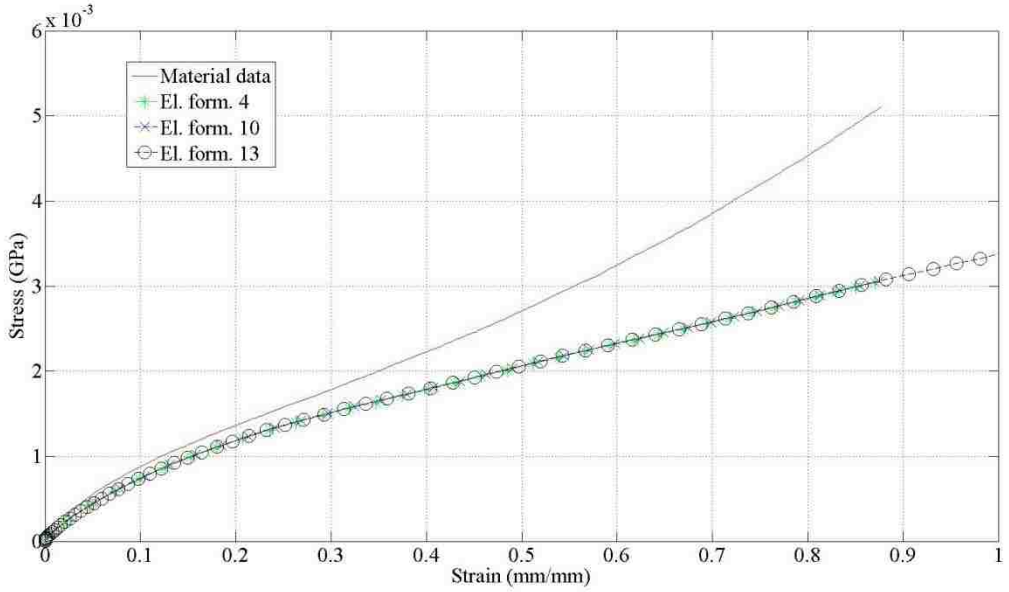

(b)

Figure 73: Stress-strain responses of finite element models of the equibiaxial tension material characterization process, MAT 77O (6 terms), tetrahedron element formulations, (a) coarse discretization, (b) 2nd level of mesh refinement.

5.4.9 Equibiaxial Tension Finite Element Models (MAT 77O, 8 Terms)

Stress strain responses for finite element models of the equibiaxial tension material characterization process with MAT 77O (8 terms), hexahedron element formulations, and a coarse discretization are shown in Figure 74. The use of element formulations 3 and 41 resulted in a very accurate model even with a relatively coarse mesh. With one level of refinement element formulations 2 and 41 terminated with errors. The accuracy of formulation 1 was greatly improved but formulation 3 exhibited high frequency content with the amplitude increasing with time/strain. Another refinement of the mesh did not significantly affect accuracy.

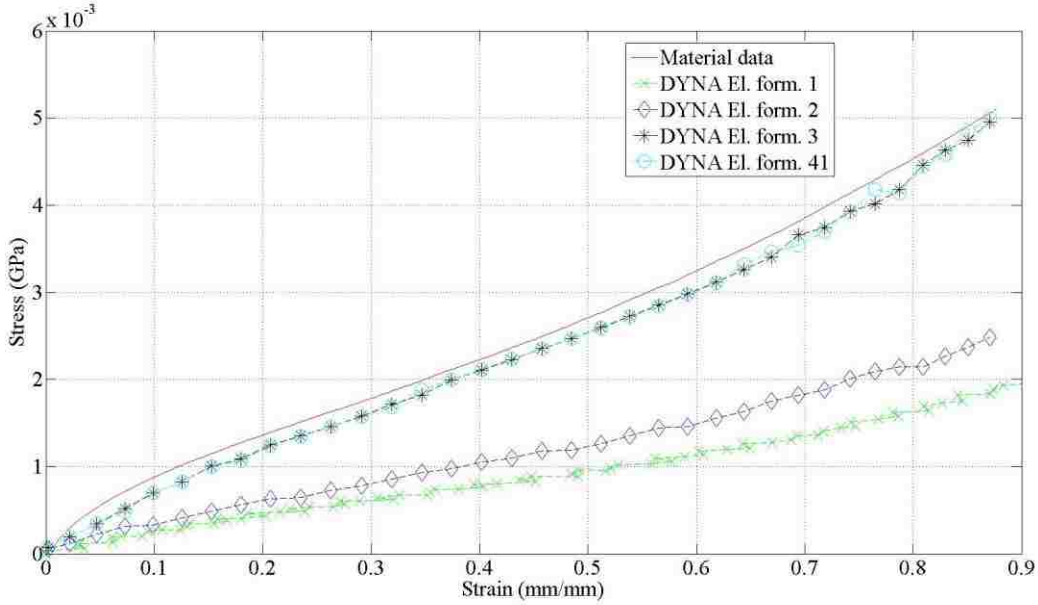

(a)

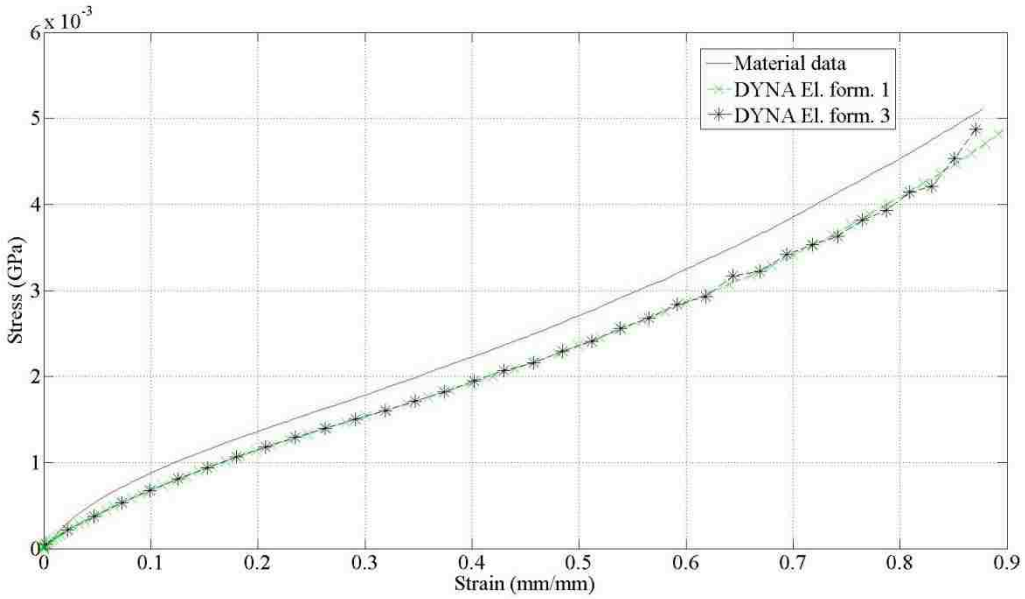

(b)

Figure 74: Stress-strain responses of finite element models of the equibiaxial material characterization process, MAT 77O (8 terms), hexahedron element formulations, (a) coarse discretization, (b) 2nd level of mesh refinement.

Similar models were developed with tetrahedron elements. The stress-strain responses for a coarse discretization are shown in Figure 75. Formulations 10 and 13 were quite accurate. The poor accuracy of element formulation 16 was unexpected. With one and two levels of mesh refinement there were no significant increases in accuracy. Errors were encountered with element formulation 16 in addition to a very high computational cost associated with the halving of the critical time step since the critical length of an element is so reduced by the use of mid-length nodes.

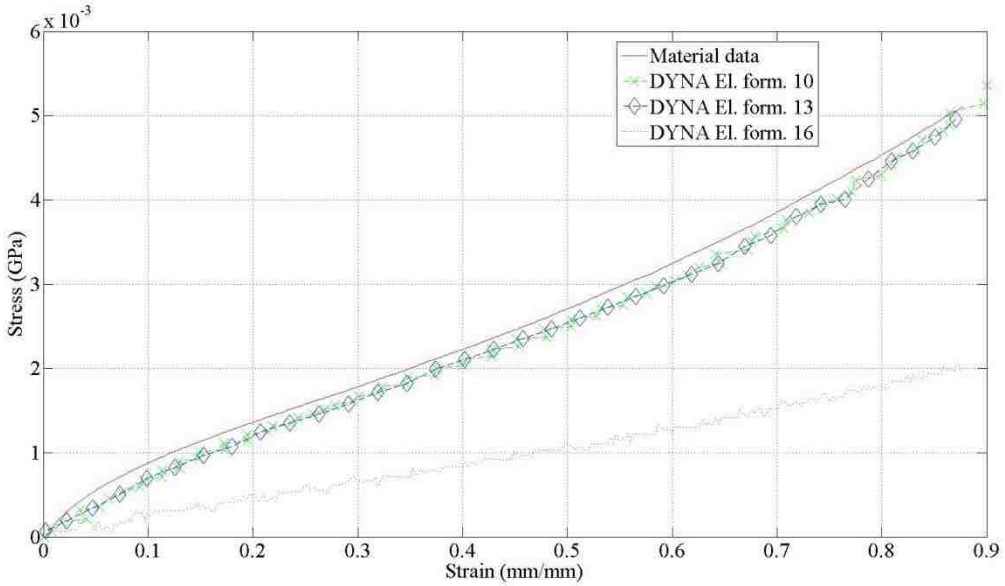

(a)

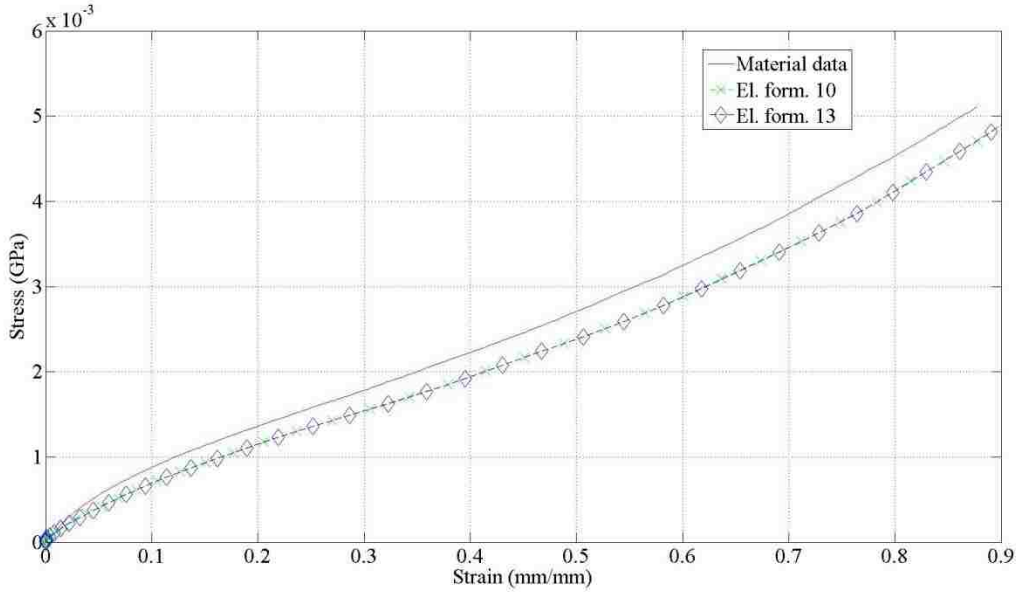

(b)

Figure 75: Stress-strain responses of finite element models of the equibiaxial material characterization process (MAT 77O, 8 terms), tetrahedron element formulations, (a) coarse discretization, (b) 2nd level of mesh refinement.

5.5 Finite Element Models of Chrysler RT Platform Transmission Mount

The first finite element model of the engine mount developed used hexahedron elements with an average element edge length of approximately 1mm. However, this model had a very high computational cost. It was later found that the number of elements was excessive. The resulting CPU time was unreasonable at over 2 hours on 12 CPUs with a massively parallel processing (MPP) single precision (SP) solver. The mesh was coarsened to reduce the number of elements but retained the critical length of 1mm where thin layers of rubber were meshed with solid elements. The use of thick shell elements was discussed but since it offered no benefit in terms of the timestep, and the bonding of the rubber to the metal would prevent bending, this change was never implemented. The most significant effect of including this thin rubber region is likely the effect on local contact stiffness.

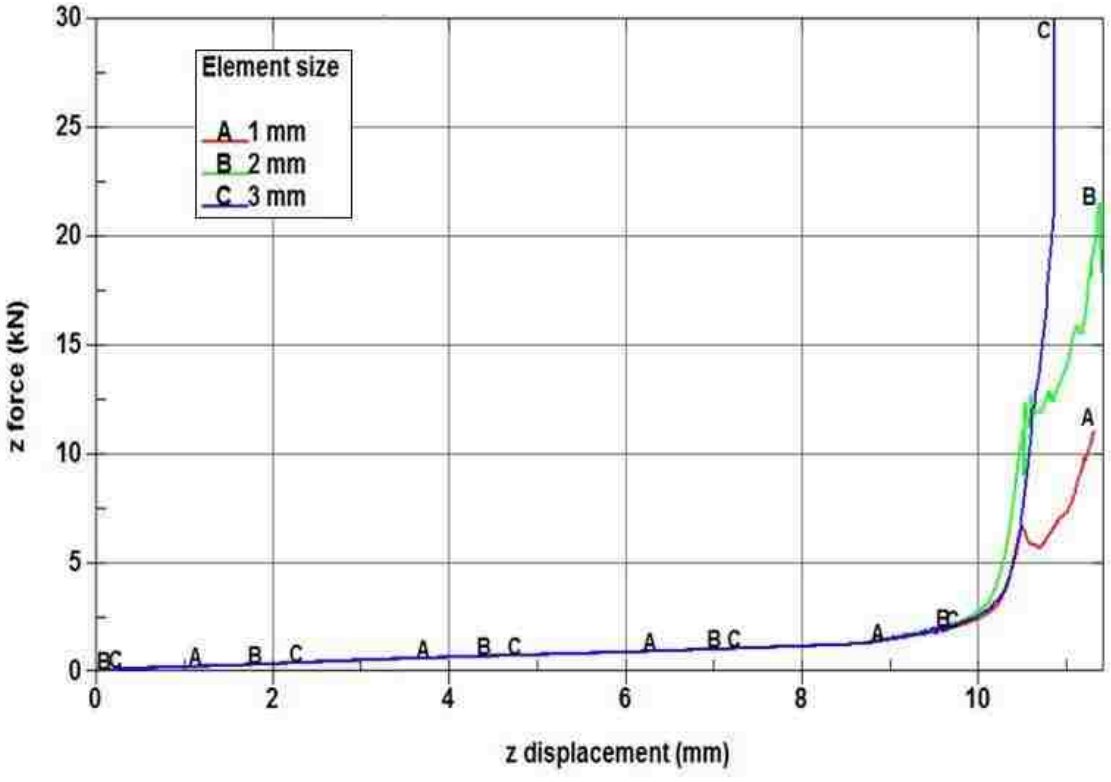

Figure 76: 1mm, 2mm, and 3mm solid hexadron meshes, element formulation 2, solver R5.1.1, hub translation in z-direction.

As shown in Figure 76, the force displacement and external work were not significantly affected by increasing the average element size from 1 mm to 3 mm. These models used element formulation 2. Figure 77 is a comparison of element formulations 1, 2, and 3 for the 2mm solid hexahedron mesh with the hub translating 12 mm in the positive z-direction. Element formulations 2 and 3 exhibit an extremely stiff response with respect to element formulation 1. Only with element formulation 1 does the simulation terminate normally. With formulations 2 and 3 severe element distortions result in an error termination. Solver version was found to be a critical factor, as shown in Figure 78, which essentially eliminates the option of using solver release 5.1.1 with MAT 181.

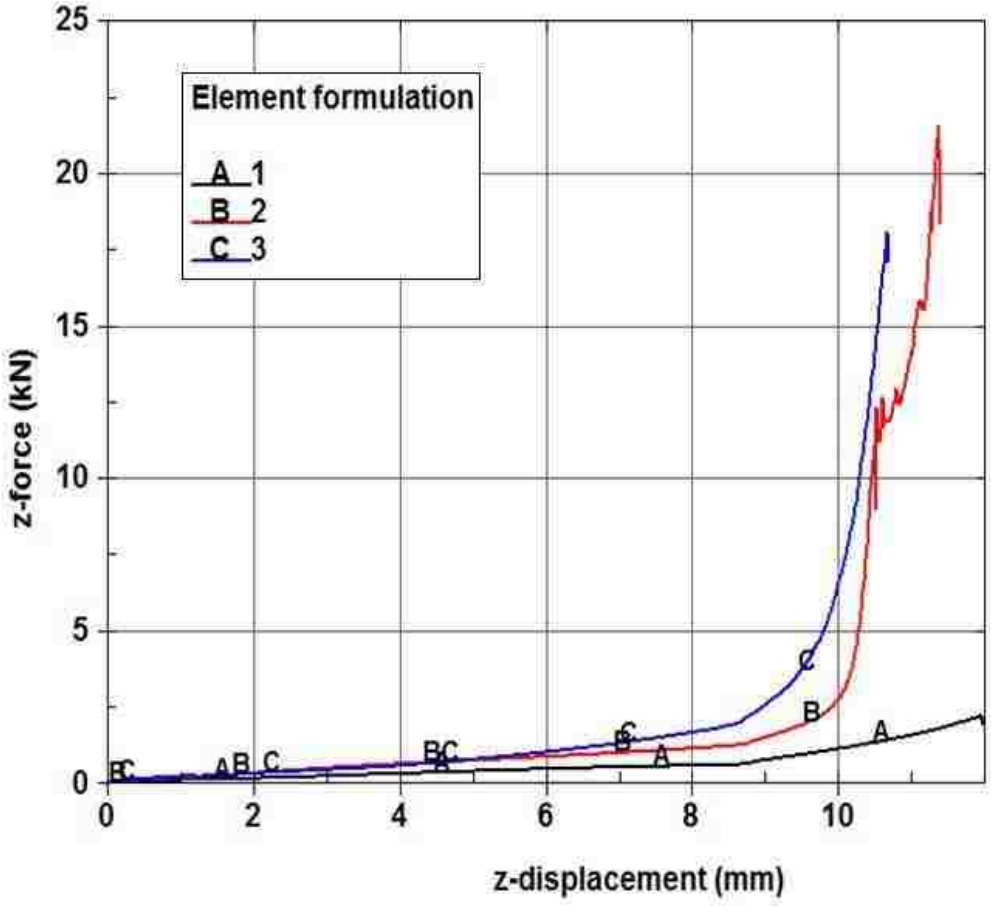

Figure 77: 2mm solid hexahedron mesh, z-translation of hub, study of element formulation (solver R5.1.1).

As shown in Figure 79 the combination of solver version and element formulation is of vital importance. Element formulation 1 with MAT 181 predicted essentially the same response with solvers R3.2.1 and R5.1.1. However, element formulations 2 and 3 combined with MAT 181 were much stiffer with solver release 5.1.1. Other loading configurations were similarly investigated with identical conclusions for, as an example, translation of the hub in the y-direction as shown in Figure 80. For further analyses solver version R5.1.1 was no longer used with MAT 181 for elements of formulations 2 and 3. Another interesting result was observed when y-translation of the hub was modeled. Element 3 exhibited remarkable stiffness with respect to element formulations 1 and 2 even with solver R3.2.1. This is shown in Figure 80 and Figure 81.

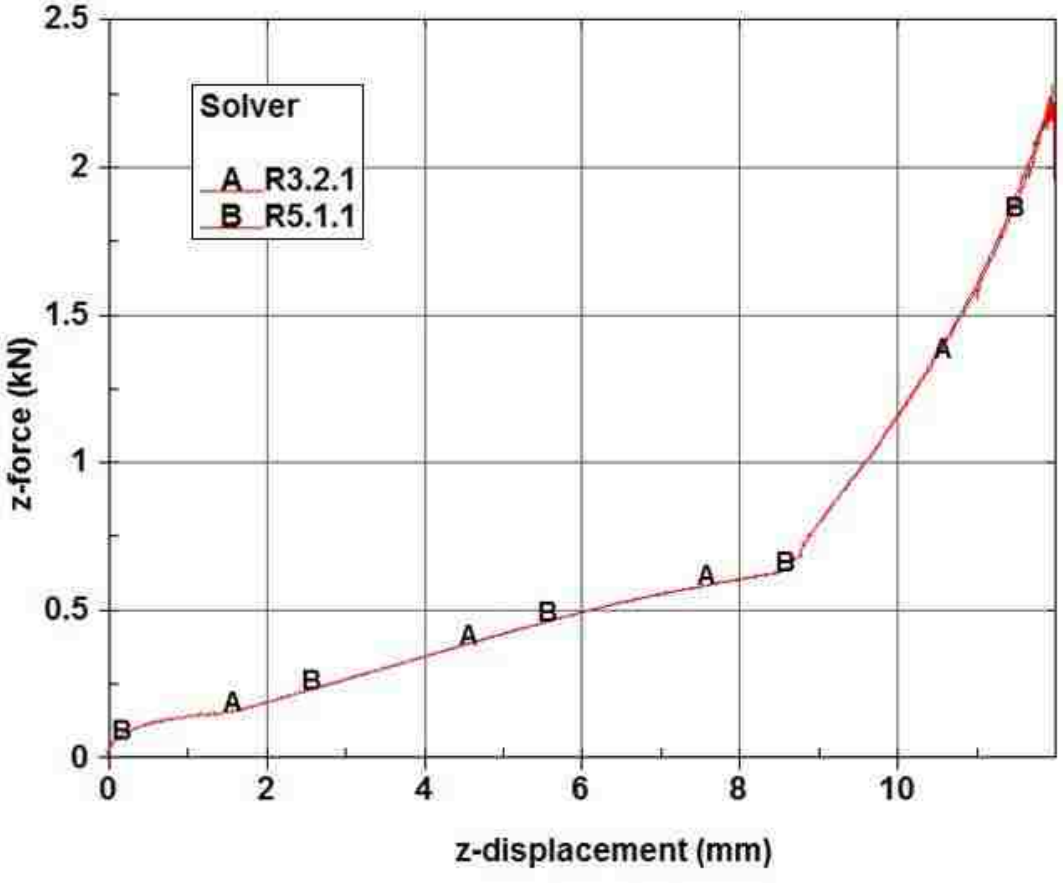

(a)

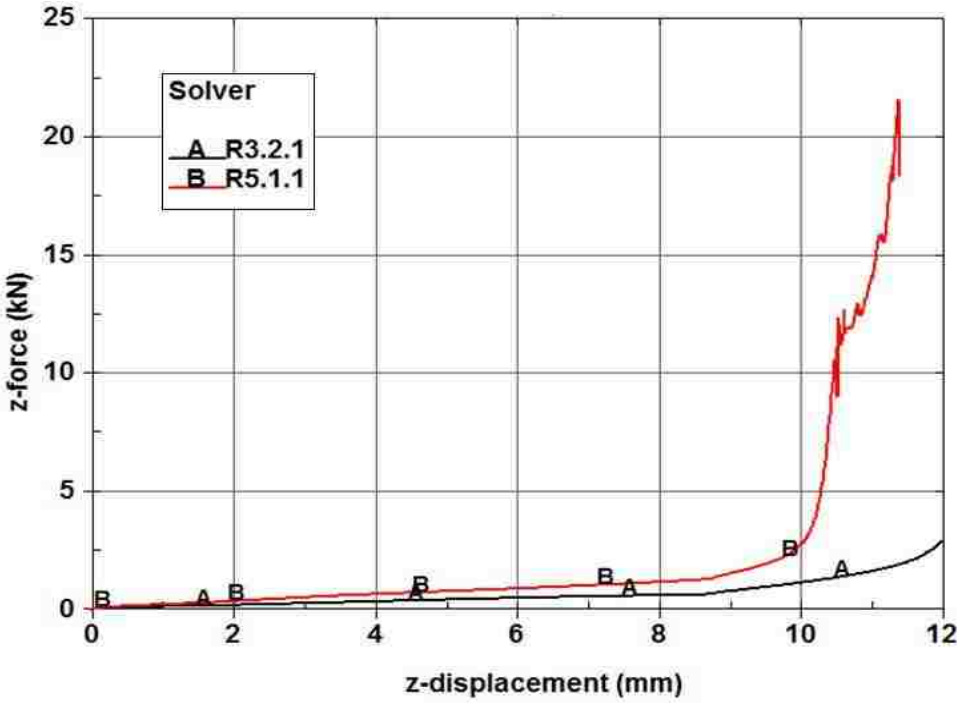

(b)

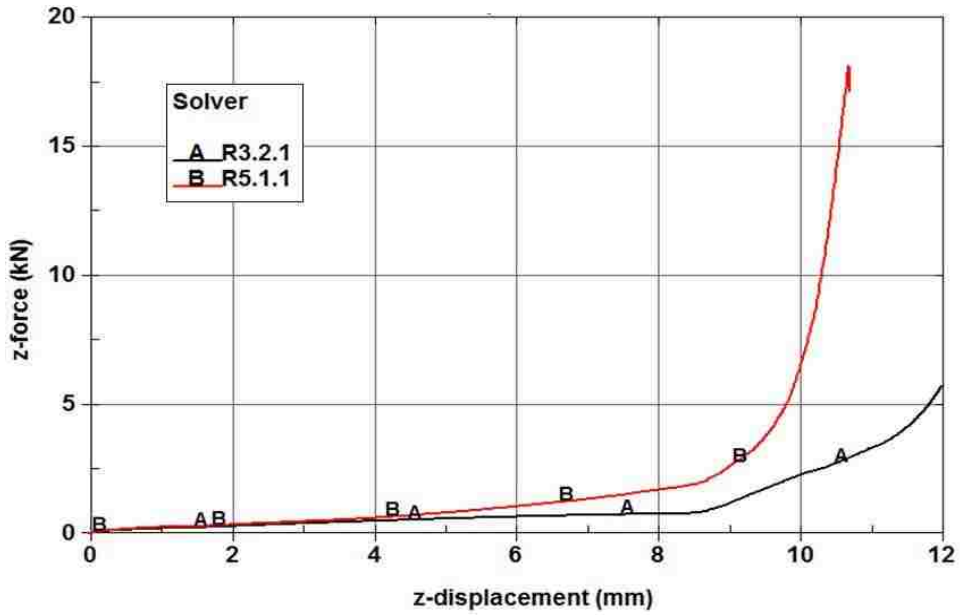

(c)

Figure 78: Study of solver version and element formulation for the 2mm solid hexahedron mesh loaded in the positive z-direction, (a) element formulation 1, (b) element formulation 2, (c) element formulation 3.

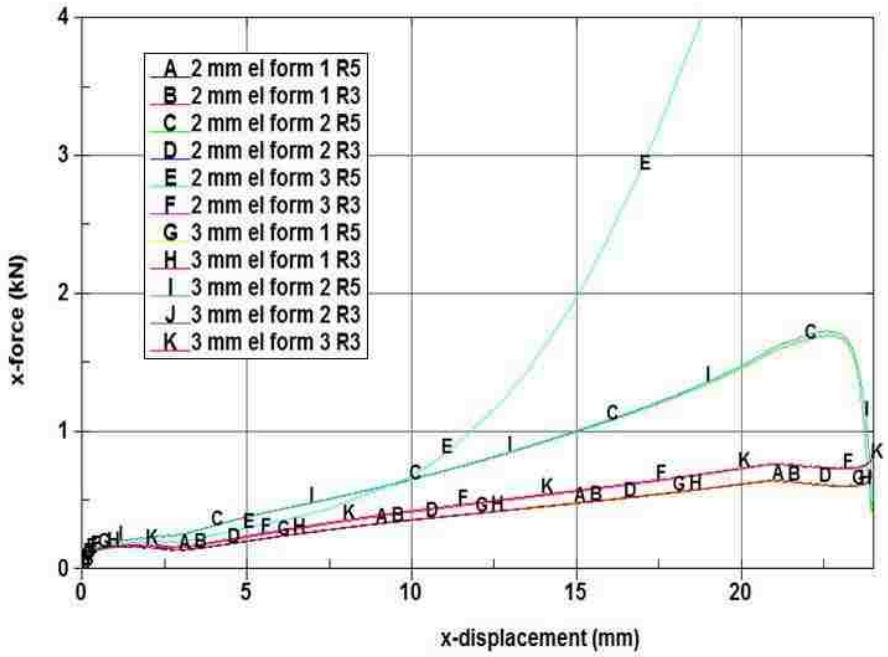

Figure 79: Analysis of solver version, element formulation, and level of discretization with translation of the hub in the x-direction.

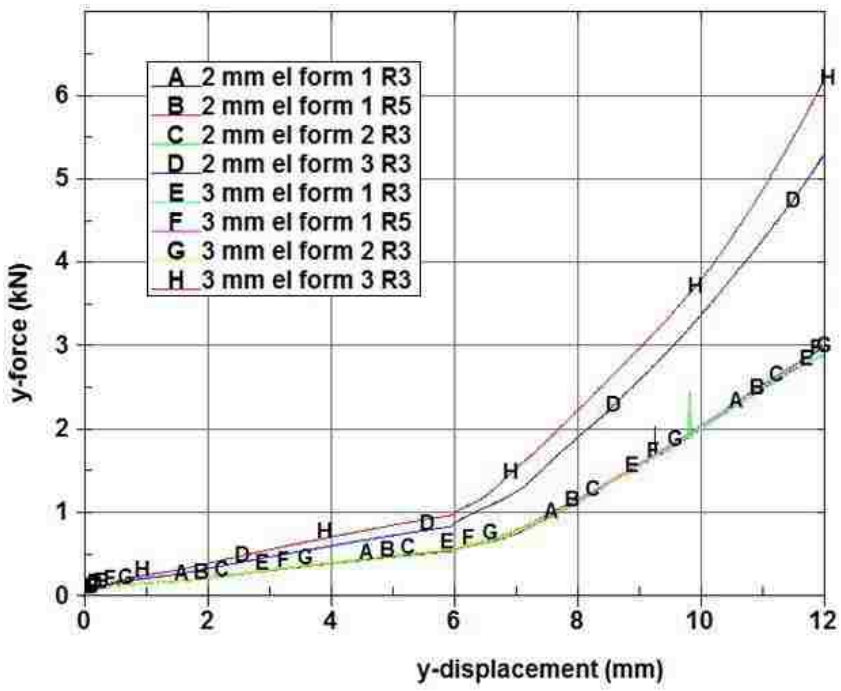

Figure 80: Analysis of element formulation, level of discretization (hexahedron mesh) and solver version with translation of the hub in the y-direction.

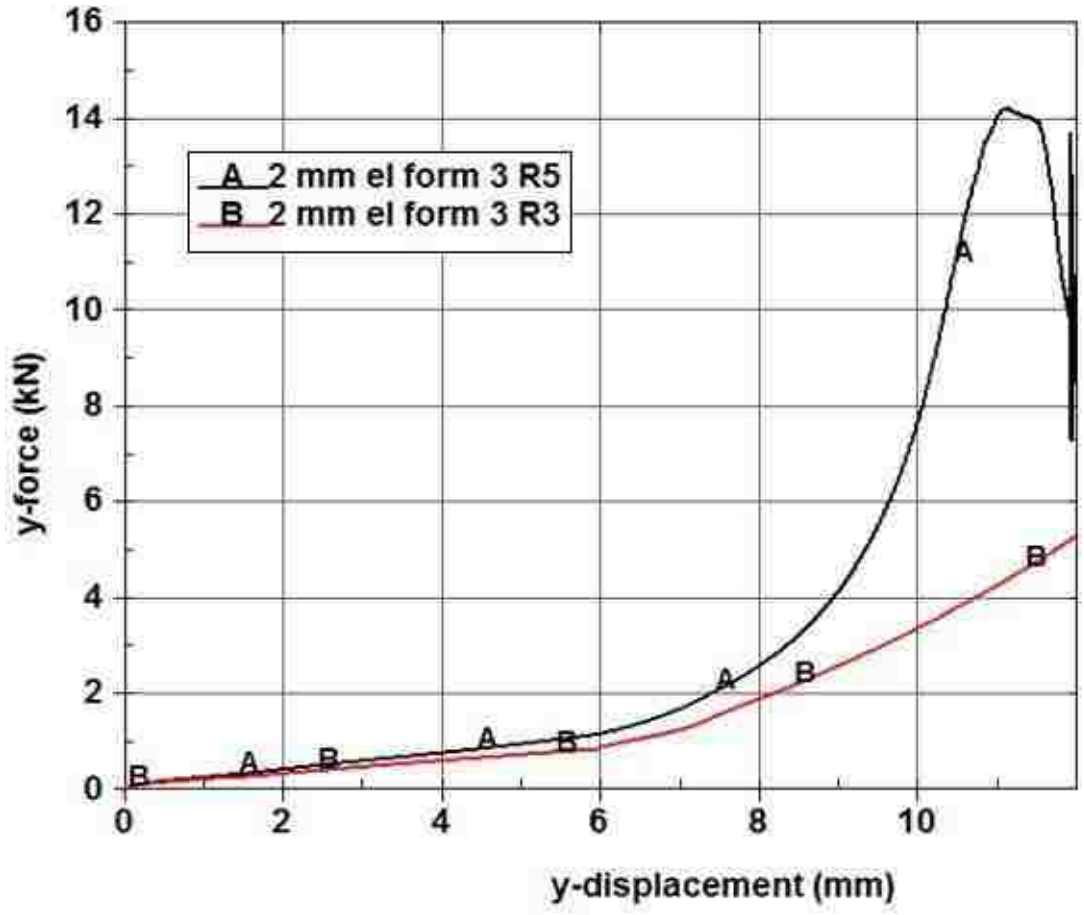

Figure 81: Comparison of element formulation 3 with solvers R3 and R5 for translation of the hub in the y-direction (2mm mesh).

With no significant variation in the force-displacement response of the model with alterations to the level of discretization (1, 2, and 3mm average element edge lengths) further coarsened meshes were developed to identify a limit on the maximum element size. As shown in Figure 82, a mesh using a combination of shell and solid elements with an average element size of 4mm exhibited a force-displacement response similar to the 2 mm hexahedron mesh. The observation of relatively significant increase in the stiffness of models using element formulation 3 continued. Referencing the LS-DYNA theory manual (Hallquist, 2006) it was found that fully integrated hexahedron elements (8 point Gaussian quadrature) exhibit significant locking for constant volume bending modes with incompressible materials. For further analyses element formulation 3 was not considered.

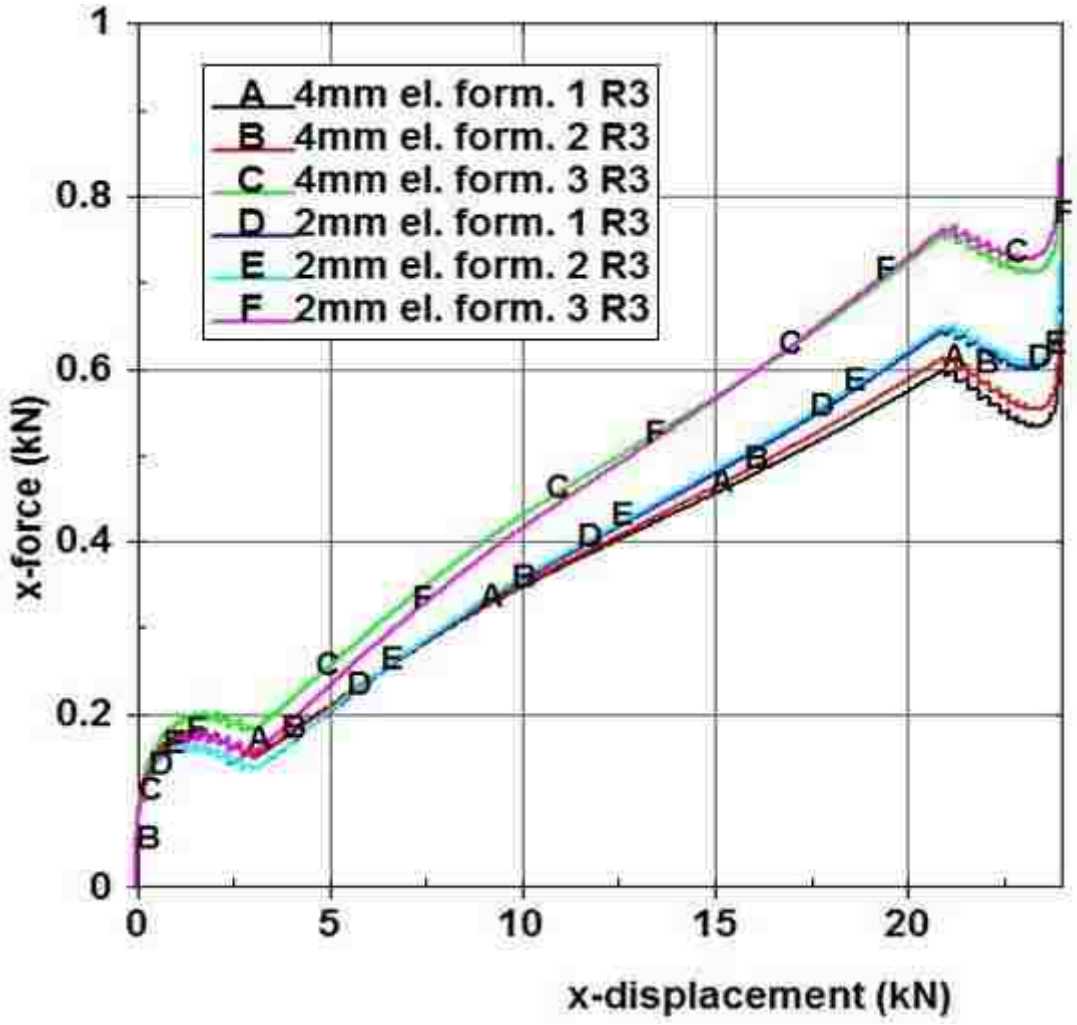

Figure 82: Force-displacement comparison between a 2 mm hexahedron mesh and a 4 mm shell-solid mesh, translation of hub in x-direction.

The discretization supplied by Chrysler, with an average element edge length of 8mm was compared to the 4 mm mesh shown previously. The use of a mesh coarser than 4mm requires additional simplifications to the geometry which is clearly observed comparing the 4mm and 8mm discretizations (shown side-by-side in Figure 31). As shown in Figure 83, for translation of the hub in the x-direction the force-displacement response of the structure is quite different when comparing the 4mm and 8mm meshes with all other modelling parameters as similar as possible. The 4mm mesh may represent an upper limit on element size although depending upon the accuracy required an intermediate mesh size may produce acceptable results.

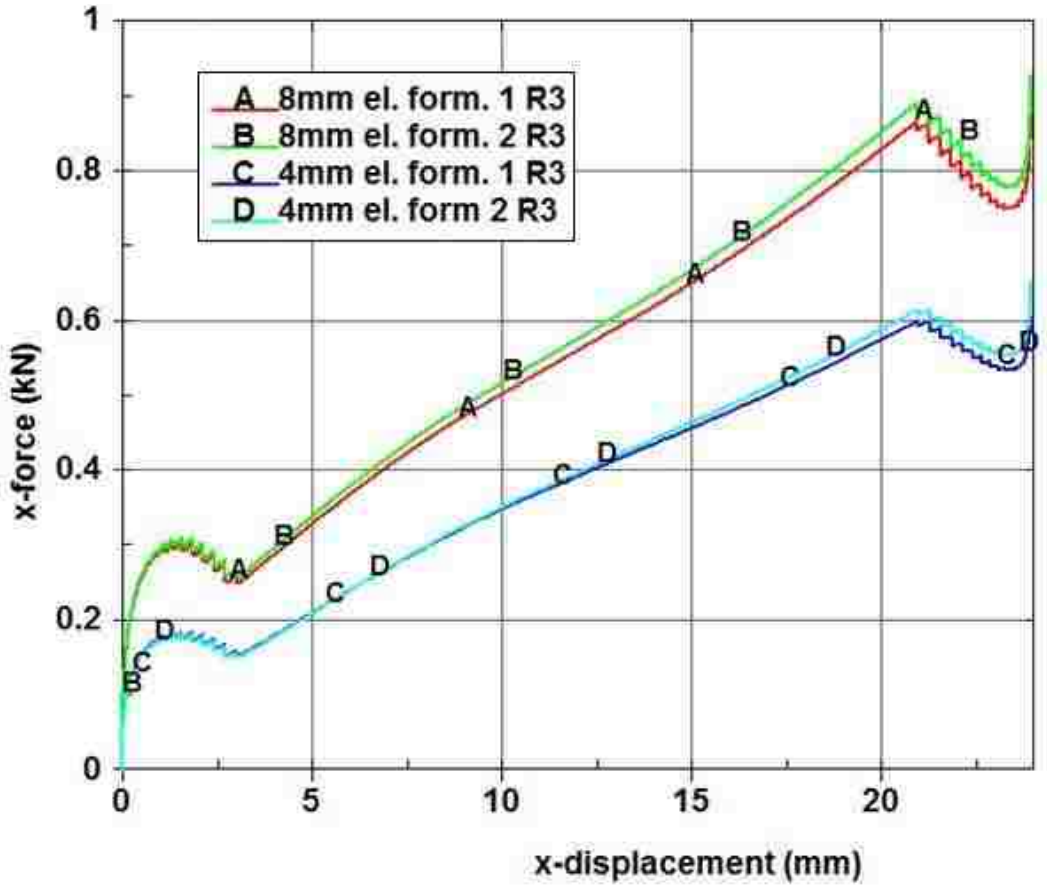

Figure 83: Force-displacement response, 4mm and 8mm meshes, x-translation of hub.

Although a 4mm global average element edge length may be suitable it was found that local refinement is critical to obtain results consistent with globally refined meshes. Figure 84 and Figure 86 are the load-displacement responses with a global average element edge length of 4 mm and with a locally refined mesh respectively where the hub is translated in the z-direction (radially, axis defined by intersection of two planes of symmetry). Mesh refinement is potentially undesirable since the critical timestep is determined by the smallest element. However, local refinement will limit the added mass if mass scaling were used.

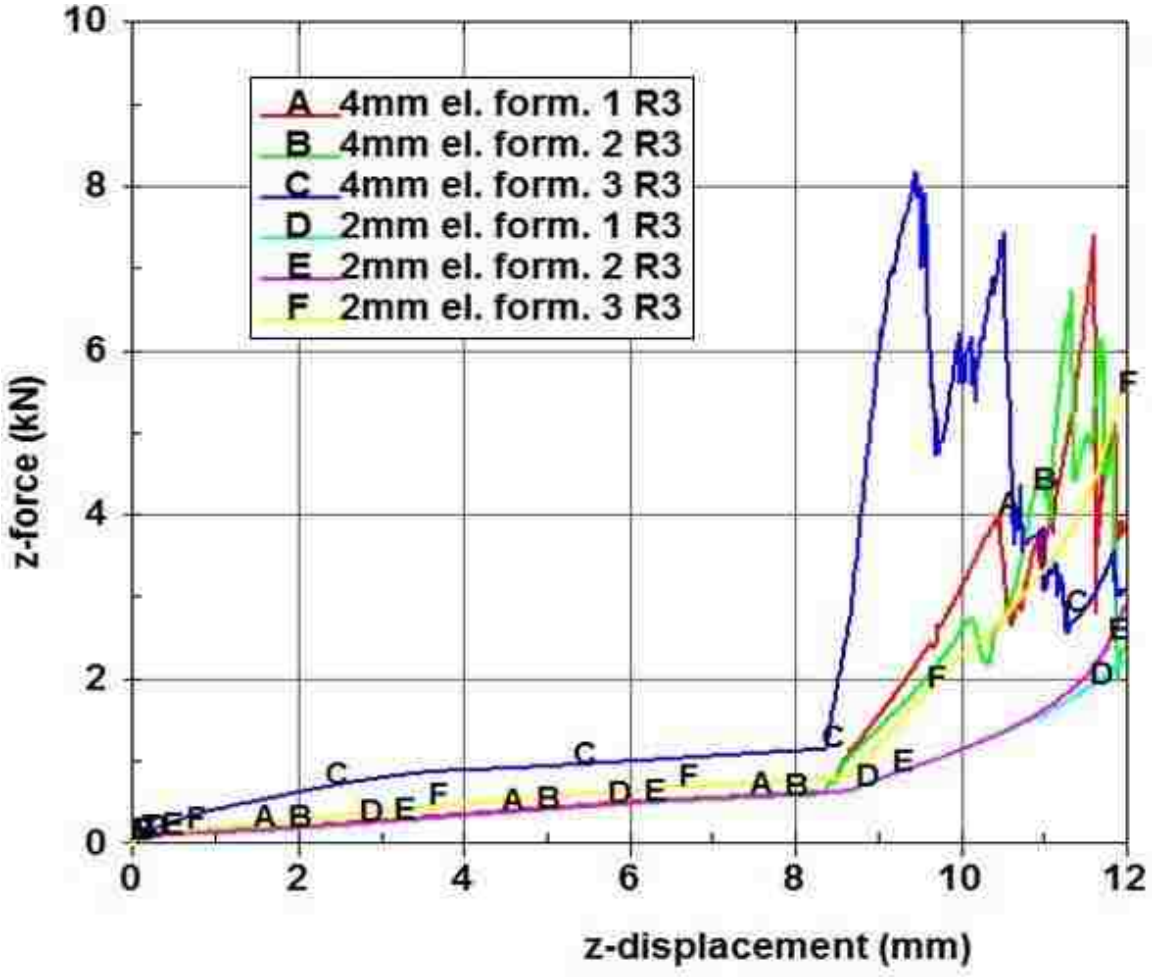

Figure 84: 4 mm global average element edge length, hexahedron solid mesh with shell elements for thin rubber regions, evidence of the need for local refinement of the mesh.

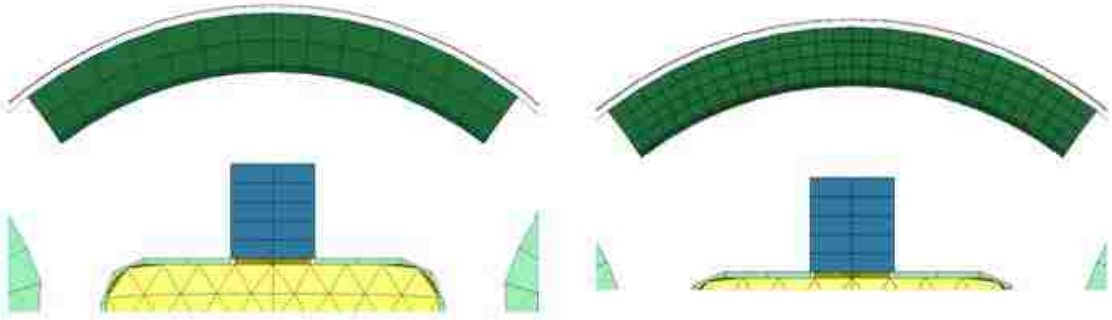

Figure 85: Local refinement of the mesh.

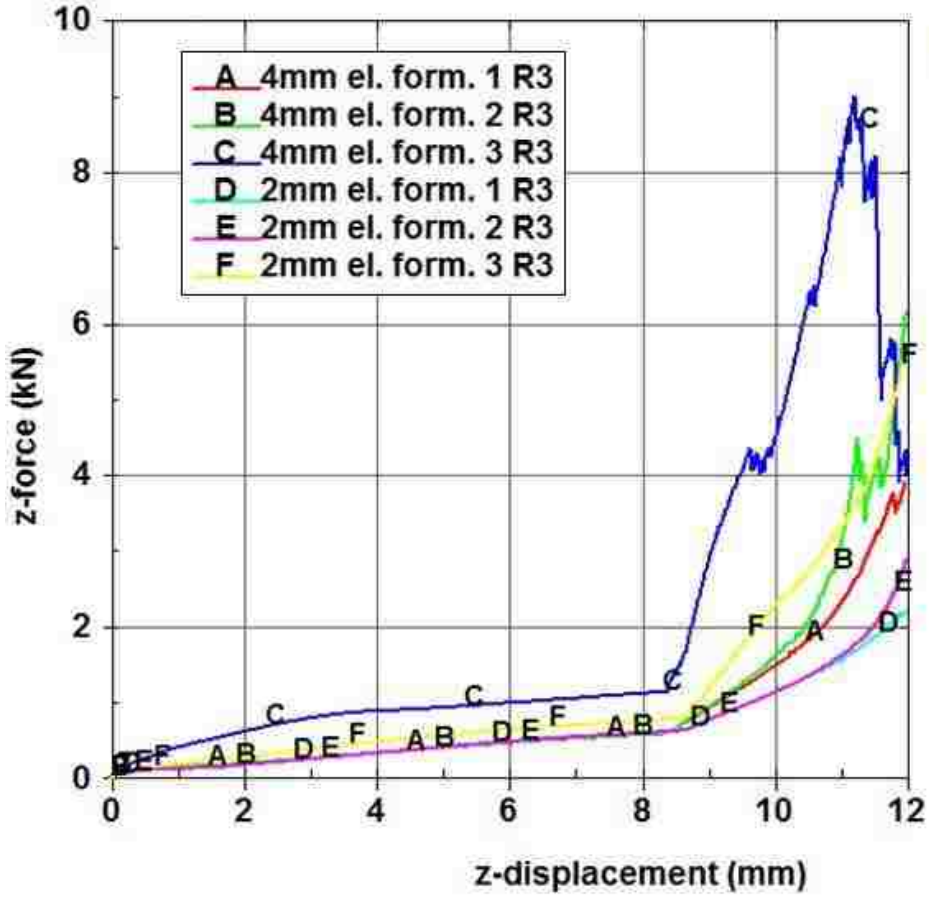

Figure 86: Local mesh refinement yields a force-displacement response more similar to a globally refined mesh.

5.5.1 Hourglass control

The z-direction of loading yielded a region of material distinctly under compression. As observed with the models of simple compression as part of the modelling of the material characterization processes, element formulation 1 exhibits significant deformation in the hourglass deformation mode. Since the chronological progress of this project resulted in the developing of finite element models of the Chrysler transmission mount prior to material characterization and associated modelling, hourglass control was studied using the model of the Chrysler engine mount with the hub displaced radially in the z-direction. Figure 87 provides a comparison of a model identical in all but the method of hourglass control. Hourglass control coefficients were set to the default values. Hourglass control type 7 yielded the least hourglass energy.

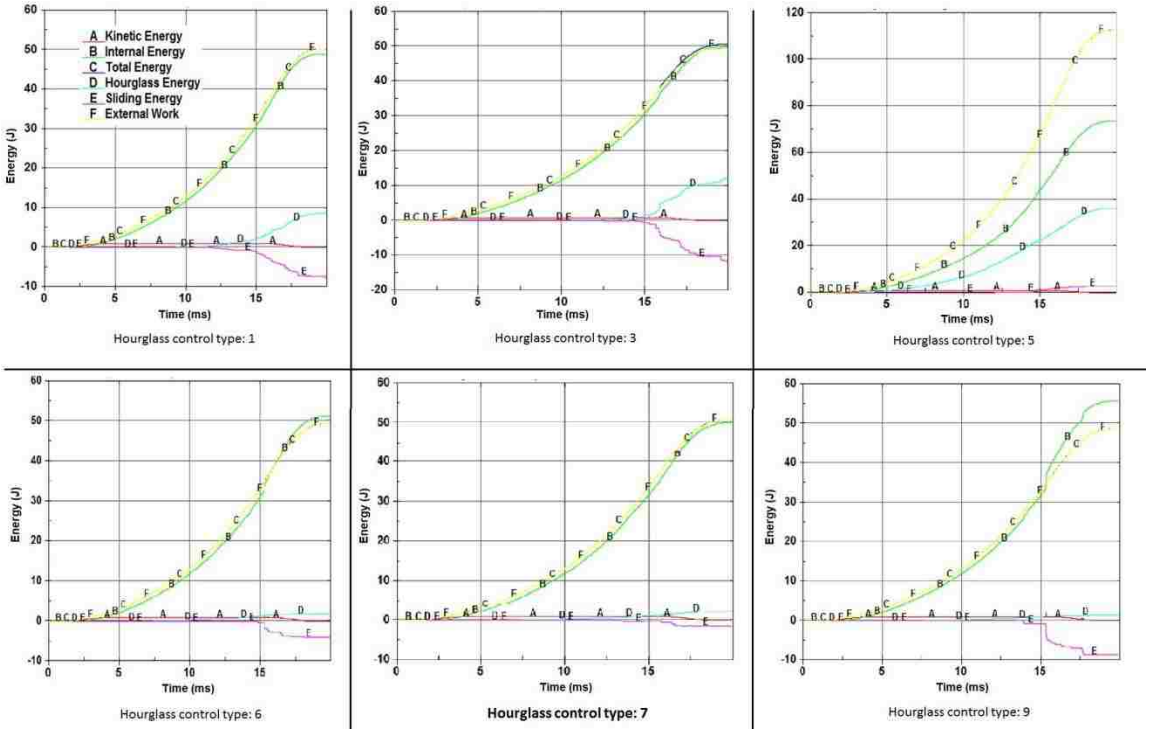

Figure 87: Comparison of different types of hourglass control.

Hourglass control type 7 in LS-DYNA is only valid for solid elements and was developed for visco-elastic materials. It may be ideal for hyperelastic materials since under cyclic loading it returns to the original shape without permanent deformation (LSTC, 2007). Another set of models were developed to identify optimal hourglass control coefficients for hourglass type 7. The results of this parametric study are shown in Figure 88. An interesting result was observed: with decreasing hourglass coefficients and, presumably, decreased hourglass control forces, the hourglass energy is reduced. The external work performed was also reduced which is likely indicative of reduced additional stiffness due to hourglass control.

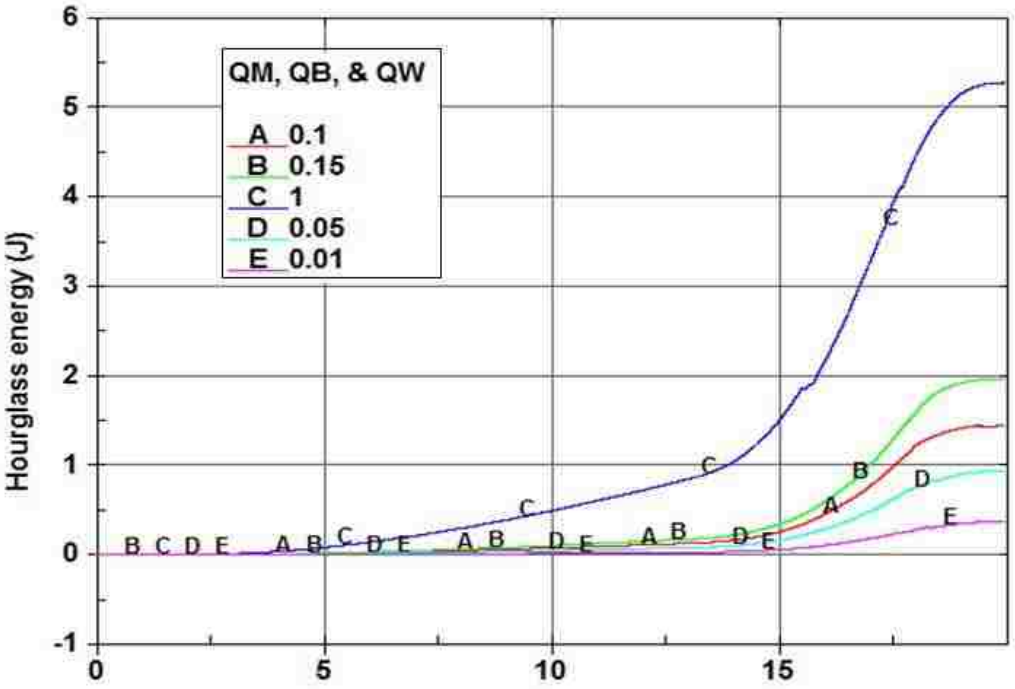

Figure 88: Study of hourglass control coefficients for hourglass control type 7.

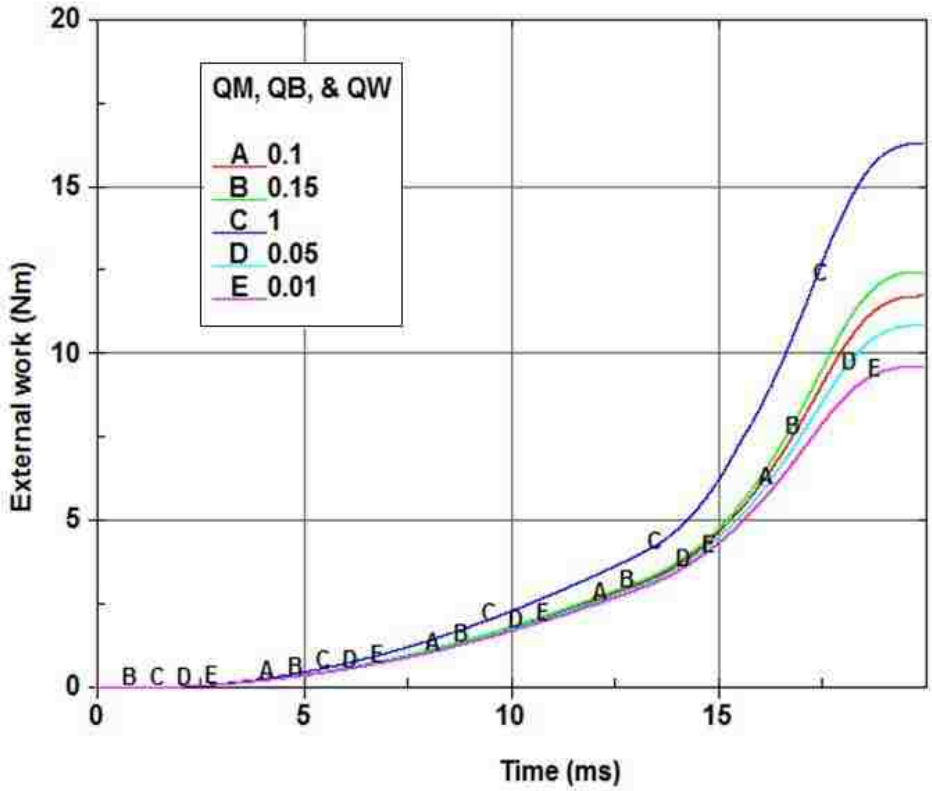

Figure 89: External work, hourglass control type study.

5.5.2 Tetrahedron element formulations and geometry simplifications

Another set of results affected by the chronological completion of the different tasks of this project were associated with the tetrahedron element. This schedule was advantageous in that tetrahedron meshes could be created from the simplified geometry used to create the hexahedron meshes as well as the original geometry (sufficiently defeatured if the tetrahedron mesh was relatively coarse). As shown in Figure 90 all tetrahedron element formulations employed were considerably stiffer than the hexahedron element formulations that were used. Using element formulation 10, two tetrahedron meshes were compared. One mesh was developed using the original unmodified geometry with automatic defeaturing in Hypermesh based upon element size. The other tetrahedron mesh was also built using an automated mesher but the geometry was that used to create the finest hexahedron meshes (models without shell elements). The force displacement responses of these two models were not identical but the difference was much less significant than the difference between the average response of models using tetrahedron elements and the average response of models built from hexahedron elements. It was later realized that there is a special 1 point tetrahedron element for near-incompressible materials, element formulation 13. As shown in Figure 91, this element exhibited a stiffness significantly reduced from that exhibited by element formulations 10 and 4. The response appears to approximate hexahedron element formulation 3.

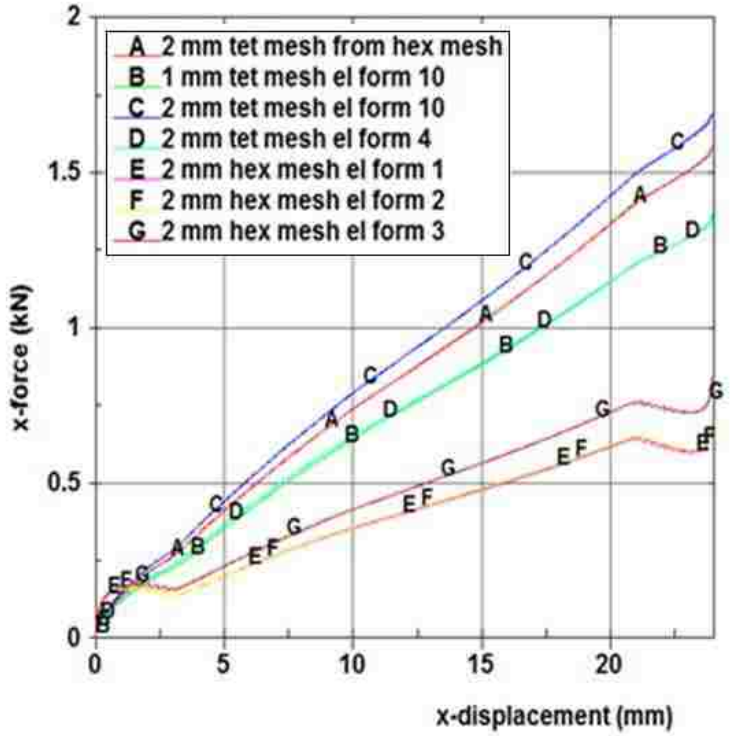

Figure 90: Comparison between hexahedron and tetrahedron meshes from the original unmodified geometry and geometry simplified for meshing with hexahedron elements.

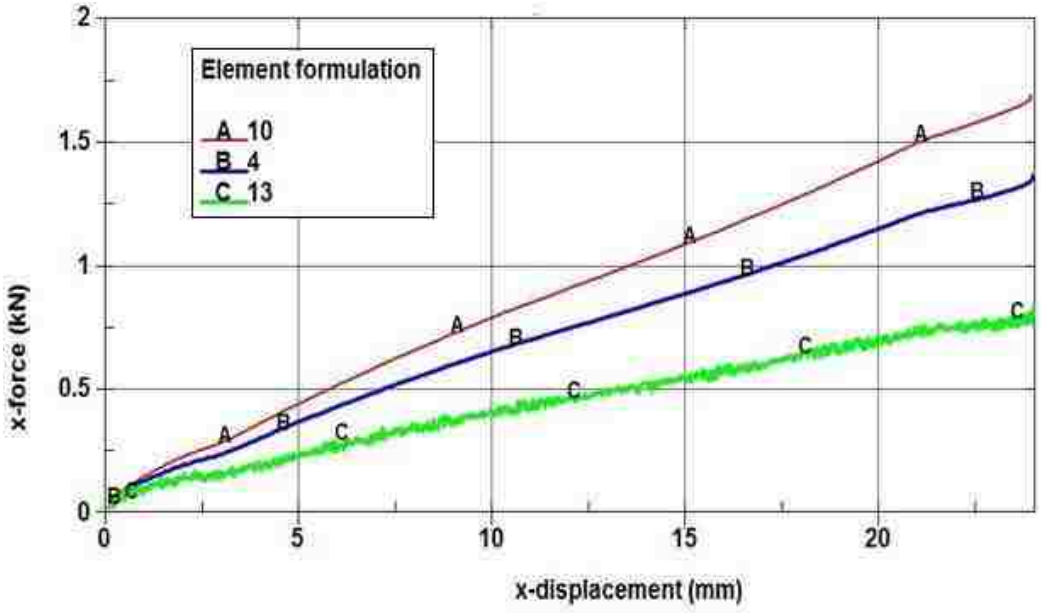

Figure 91: Comparison between tetrahedron element formulations 4, 10, and 13 (2mm element size, mesh generated from unmodified CAD data provided by Chrysler).

5.5.3 Tied Contact

Use of the same mesh that was used with merged nodes (by creating duplicate nodes at the previously merged locations) was the initial approach for implementation of tied contact. The general trend of the force-displacement response was not significantly affected as shown in Figure 92 but significant high frequency content was observed. However, as shown in Figure 93, the energy balance was very poor (element formulation 1 shown, formulations 2 & 3 were similar). This is presumably caused by the shell element thickness causing initial penetrations (equal to half the shell thickness) at every tied node. The poor energy balance was resolved by eliminating the initial penetrations as shown in Figure 94 and employing the contact interfaces shown in Figure 32. An additional tied contact was also found to be necessary. The high frequency content was still present, as shown in Figure 95, but the energy balance was greatly improved Figure 96 (element formulation 1 shown, 2 & 3 were similar).

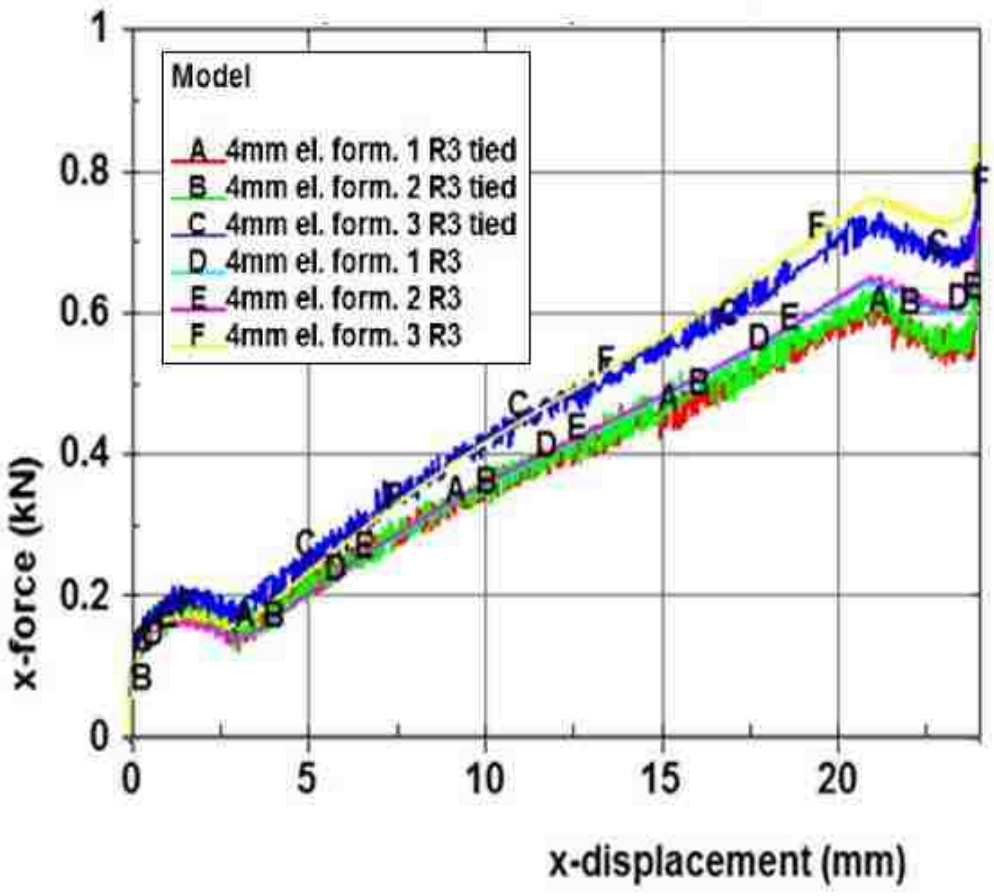

Figure 92: Tied contact implemented with mesh which previously used merged nodes

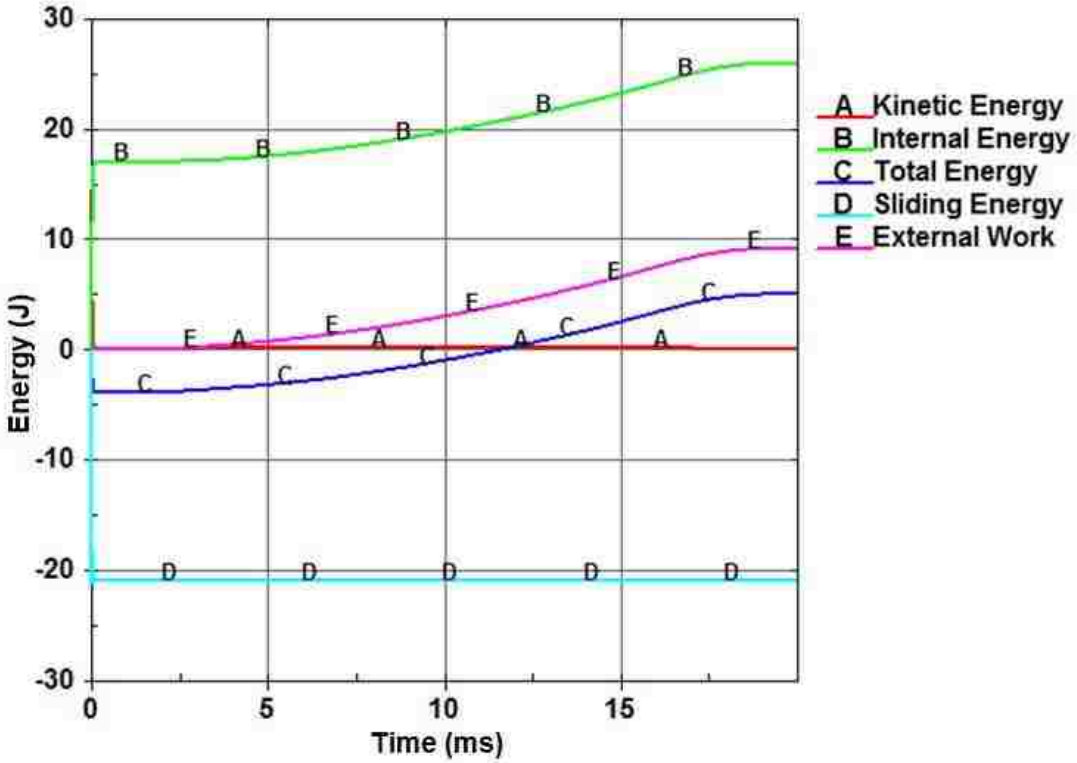

Figure 93: Energy balances for models with tied contact implemented with mesh that had previously used merged nodes, element formulation 1.

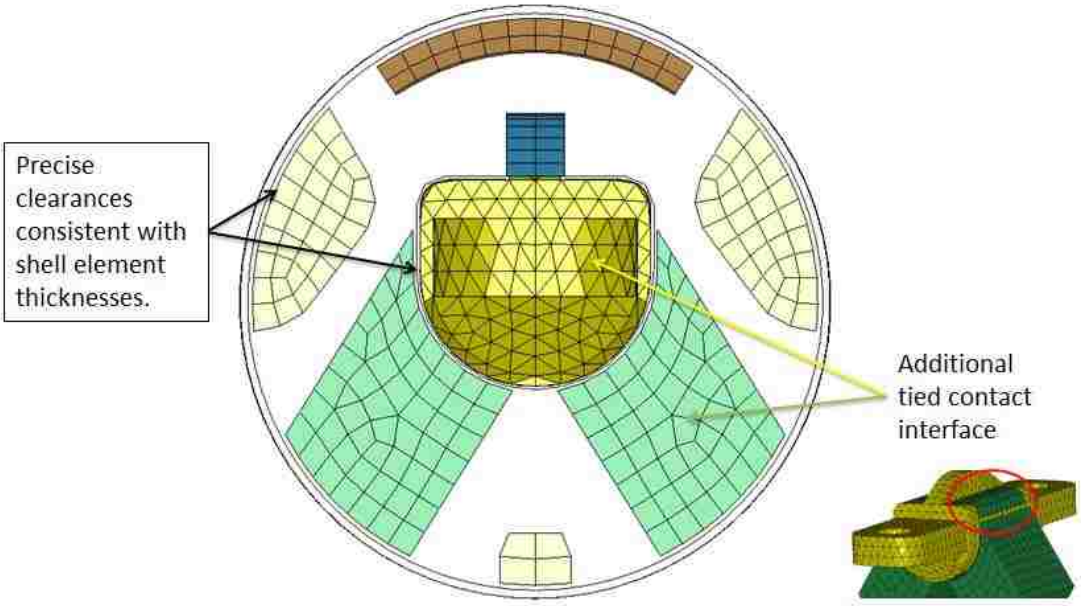

Figure 94: Revised model to improve energy balance with tied contact.

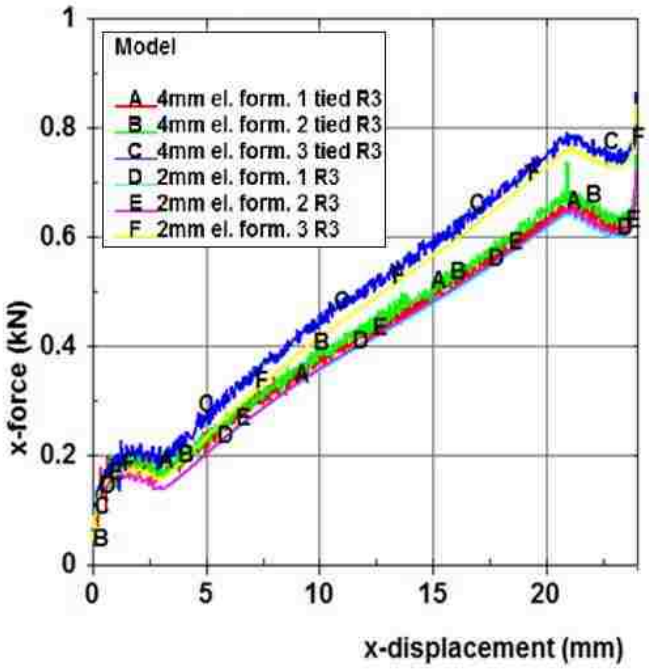

Figure 95: Force displacement response for revised mesh to eliminate initial penetrations of tied contact interfaces.

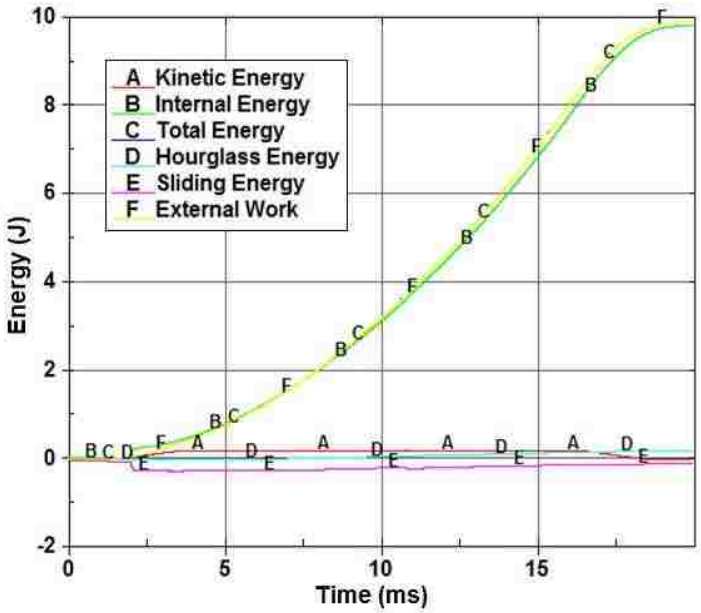

Figure 96: Energy balances for models with tied contact and revised mesh to eliminate initial penetrations, element formulation 1.

5.6 Component Characterization

5.6.1 Fixture Design

Von Mises stresses were considered for the finite element model of the steel equal angle extrusions of the initial fixture design. Peak stresses were on the order of 1000 MPa, considerably higher than the design restriction of the 250 MPa yield strength. Relative motion was also observed between the two steel extrusions bolted together which fundamentally comprise the fixture. These results are reasonably consistent with manual calculations of stress shown below. These calculations make significant assumptions and it was unknown if the predictions of these calculations should be considered reasonable.

A bending stress was calculated for the lower equal angle extrusion, the base of the fixture and the component in direct contact with the lower platen of the testing apparatus. This calculation assumed a simplified model of a cantilever beam with a width of 160 mm and a thickness of 10 mm. It was assumed that this component should be designed to carry the peak load transmitted through the engine mount without yielding. The peak load was estimated from the finite element models of the engine mount. The stress was calculated for an outer surface in the region near the radius.

$$\sigma_{Fixture} = \frac{Mc}{I} = \frac{960\ kN\ mm \cdot 5\ mm}{13333\ mm^4} = 360\ MPa \qquad \text{(Equation 56)}$$

Increasing the thickness of the equal 90 degree angle extrusions was limited by the geometry of the engine mount. Even with the initial design bolt holes were in close proximity to the radius of the 90 degree bend. It was considered that washers would be in contact with the material surrounding the holes which would need to be relatively planar. Thicker pieces of steel required the design be revised, the resulting modified design is shown in Figure 34.

The very large von Mises stresses in the upper half of the base of the fixture, even with the revised design, suggested that the finite element model may have been producing misleading results. The first modification to the finite element model, in an attempt to discover the source of these results and eliminate the misleading output, was to radius sharp edges. Sharp edges may lead to infinite stresses. If one considers stress

concentration factors a sharp edge may be equivalent to a fillet with a radius of zero. Some stress concentration factors approach infinity for edges with a null radius.

Radiusing sharp edges where peak von Mises stresses were located reduced the magnitude of the peak von Mises stresses considerably but did not result in stresses considerably lower than the assumed yield strength of the steel (250 MPa). The next modification to the model was to use a 10 node Tetrahedron element formulation (previous models used a 4 node tetrahedron element formulation). The use of 10 node tetrahedrons in place of 4 node tetrahedrons reduced the peak von Mises stress to 280 MPa (from 350 MPa). However, this was still larger than the assumed yield strength.

The very large stresses in the locations at which there was contact between the washers and the steel brackets of the fixture was unexpected. Additionally, the clearance between the bolt and the holes in the fixture should result in reduced stresses through stress relaxation in the physical part. The washers at the locations of the peak stresses were eliminated as were the loads representing the bolt preload. The corresponding washers for the opposite end of the bolted connections represented remained with their load in place. An unbalanced force on the assembly does not result since the entire fixture is bolted in place. These connections carry a greater load. Overall, the unbalanced bolt preload loading should more severely stress the steel plate of the fixture. Figure 97 depicts the changes made to the model.

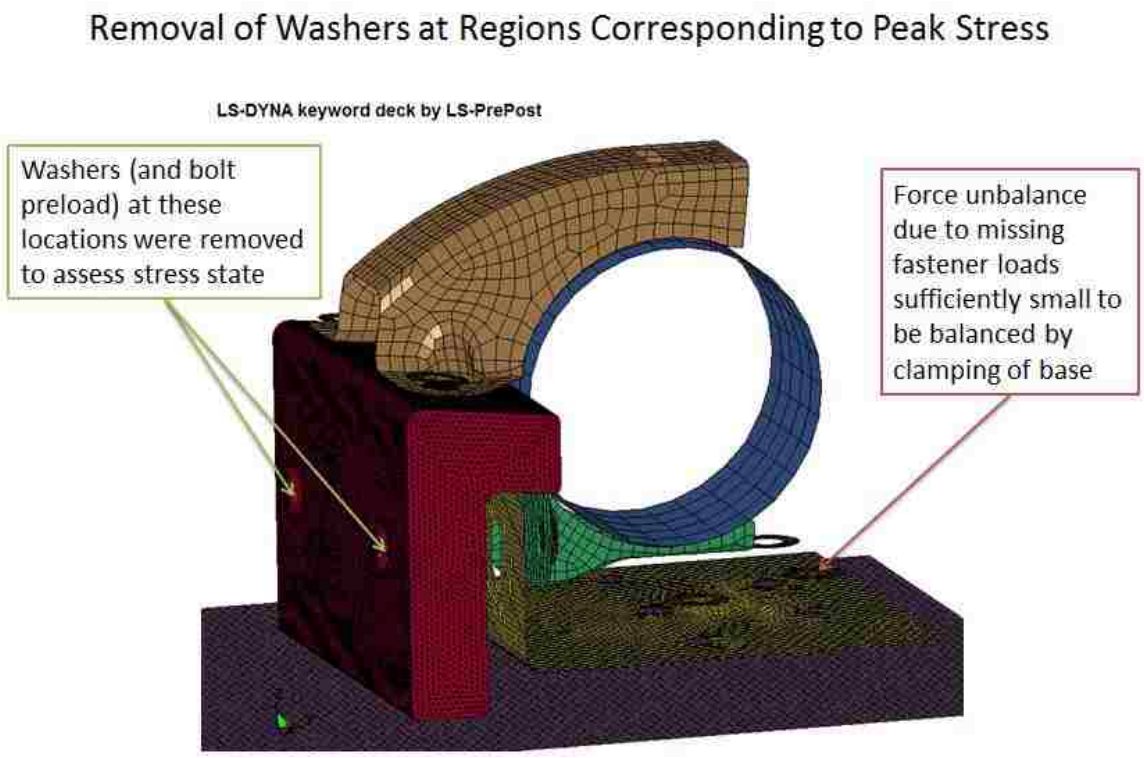

Figure 97: Modifications to finite element model of revised fixture design: removal of washers and corresponding bolt preload.

Von Mises stresses were also considered for the steel fixture plates with the one pair of washers (and corresponding loads) removed (at the previous location of peak von Mises stress). The removal of the two washers (and any loads applied to the nodes of the removed elements) resulted in a significantly different stress state at this location. The stress was reduced from 280 MPa to 34 MPa. The location of the peak von Mises stress was significantly altered. The maximum von Mises stress was also significantly reduced from 280 MPa to 108 MPa.

The last finite element model of the fixture which was developed included all washers but featured a refined mesh and smaller radiuses for filleted edges. The smaller radius was permitted by the use of smaller elements. The reduced fillet radiuses for the edges of the holes with washers increased the area of material of the steel brackets in contact with the

washers. The refined mesh did not result in a significant change in the location or magnitude of the maximum von Mises stress.

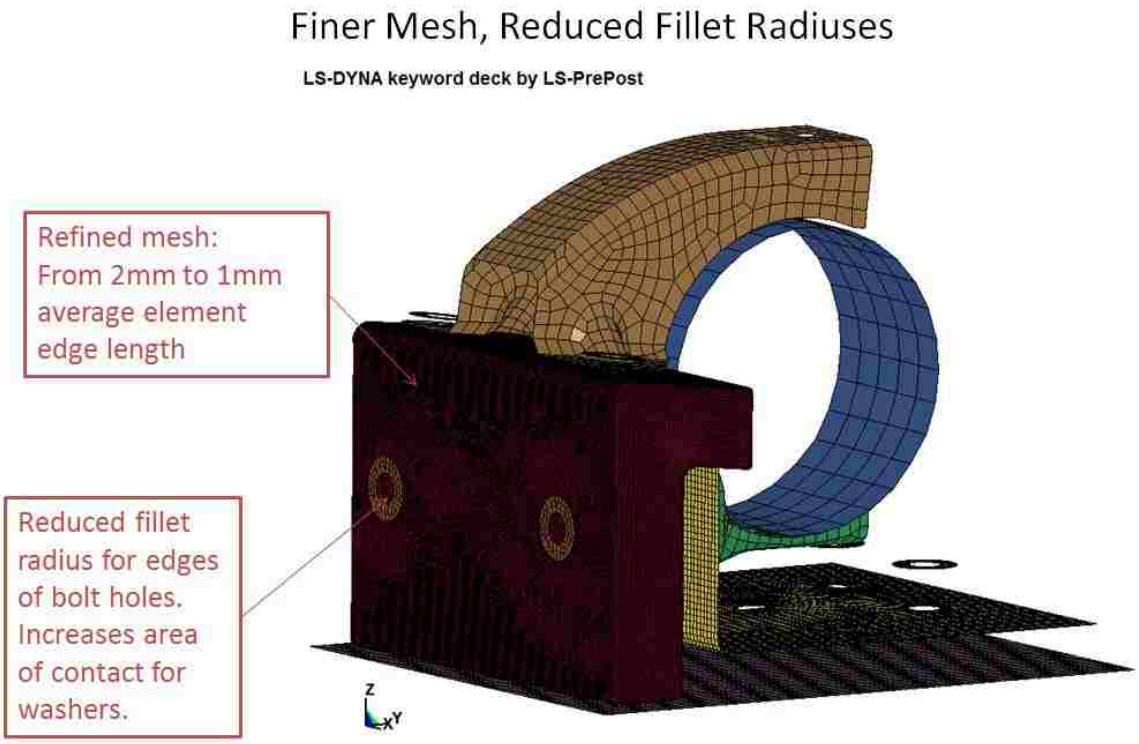

Figure 98: Refined mesh of loading fixture.

5.6.2 Quasi-Static Component Characterization

The quasi-static force-displacement responses of specimens 1 and 2 are shown in Figure 99. Characterization of specimen #1 was completed twice with a delay of approximately 5 minutes. Since there was minimal variation in the force-displacement response during the repeated characterization of specimen #1 only three loading cycles were completed. For all other quasi-static component force-displacement characterizations five loading cycles were completed. Significant variation between the first and second loading cycles was observed. The last four loading cycles were very similar for a given specimen. Shown in Figure 100 is the first loading cycle separated into tensile loading and unloading and compression loading and unloading. A Mullin's effect was observed as shown in Figure 101, plots of the tensile and compression loading for the first and second cycles.

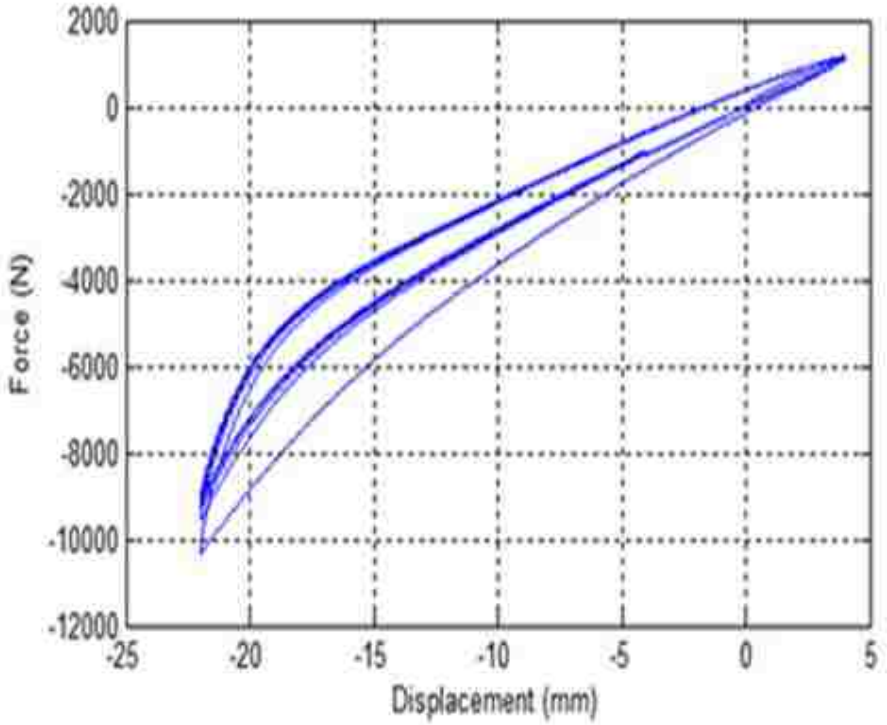
2000
0
-2000
-4000
-6000
-8000
-10000
-12000
Force (N)
-25
-20
-15
-10
-5
0
5
Displacement (mm)

(a)

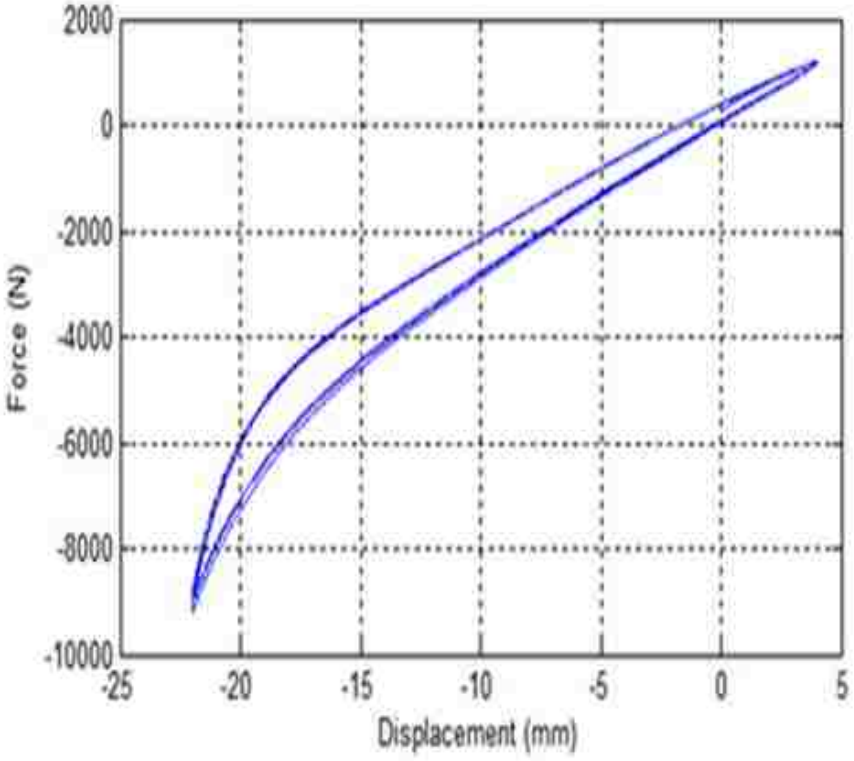
2000
0
-2000
-4000
-6000
-8000
-10000
Force (N)
-25
-20
-15
-10
-5
0
5
Displacement (mm)

(b)

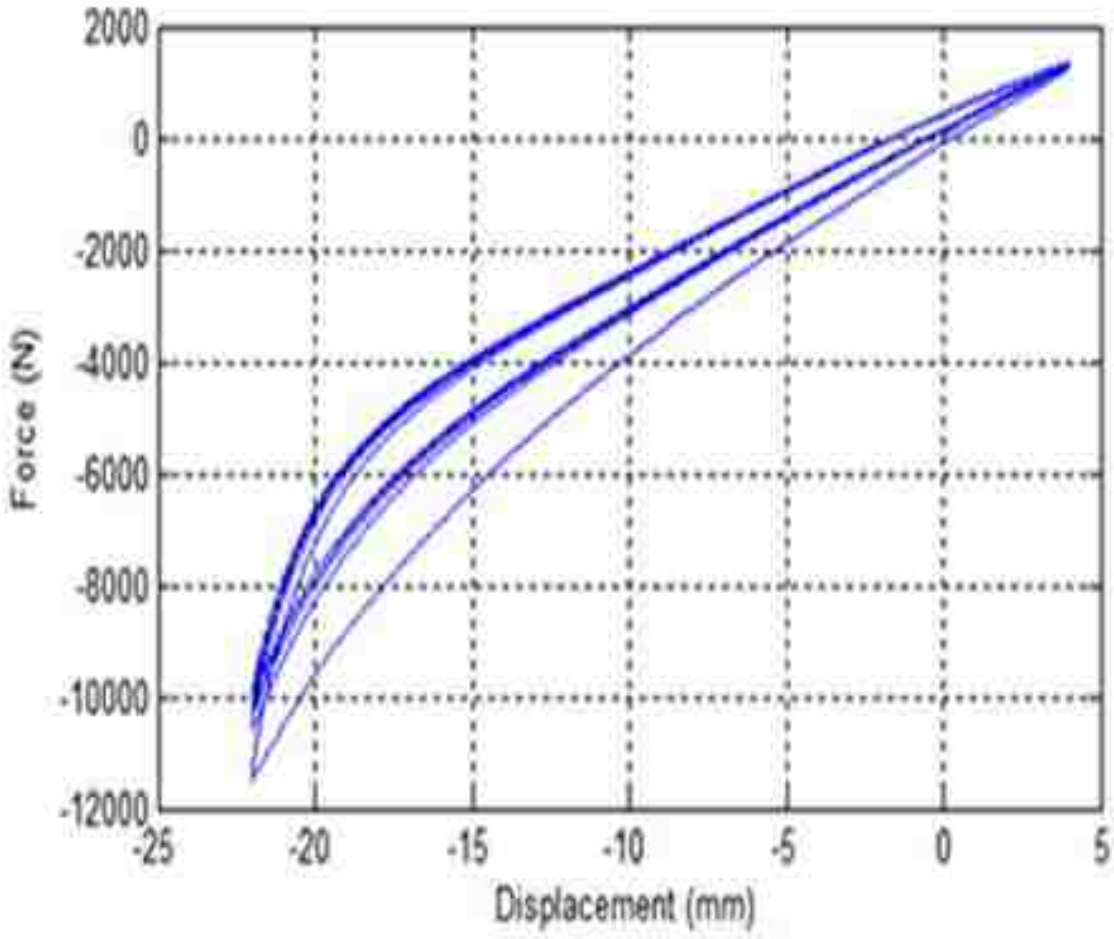

(c)

Figure 99: Quasi-static force displacement response of specimens 1 through 3, (a) test #1 of specimen #1, (b) test #2 of specimen #1, (c) test #1 of specimen #2..

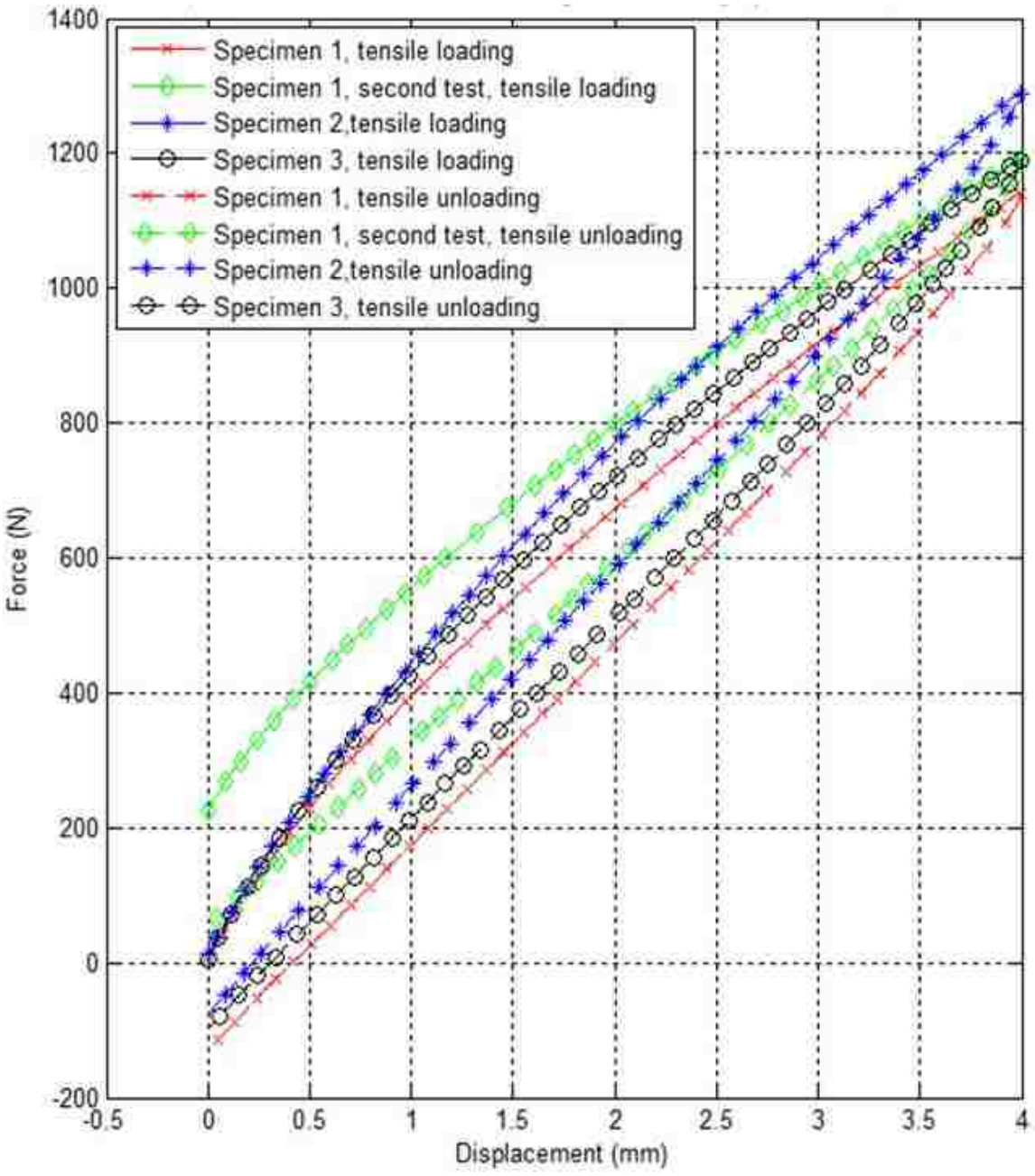
Specimen 1, tensile loading
Specimen 1, second test, tensile loading
Specimen 2,tensile loading
Specimen 3, tensile loading
Specimen 1, tensile unloading
Specimen 1, second test, tensile unloading
Specimen 2,tensile unloading
Specimen 3, tensile unloading
Force (N)
Displacement (mm)
1400
1200
1000
800
600
400
200
0
-200
-0.5
0
0.5
1
1.5
2
2.5
3
3.5
4

(a)

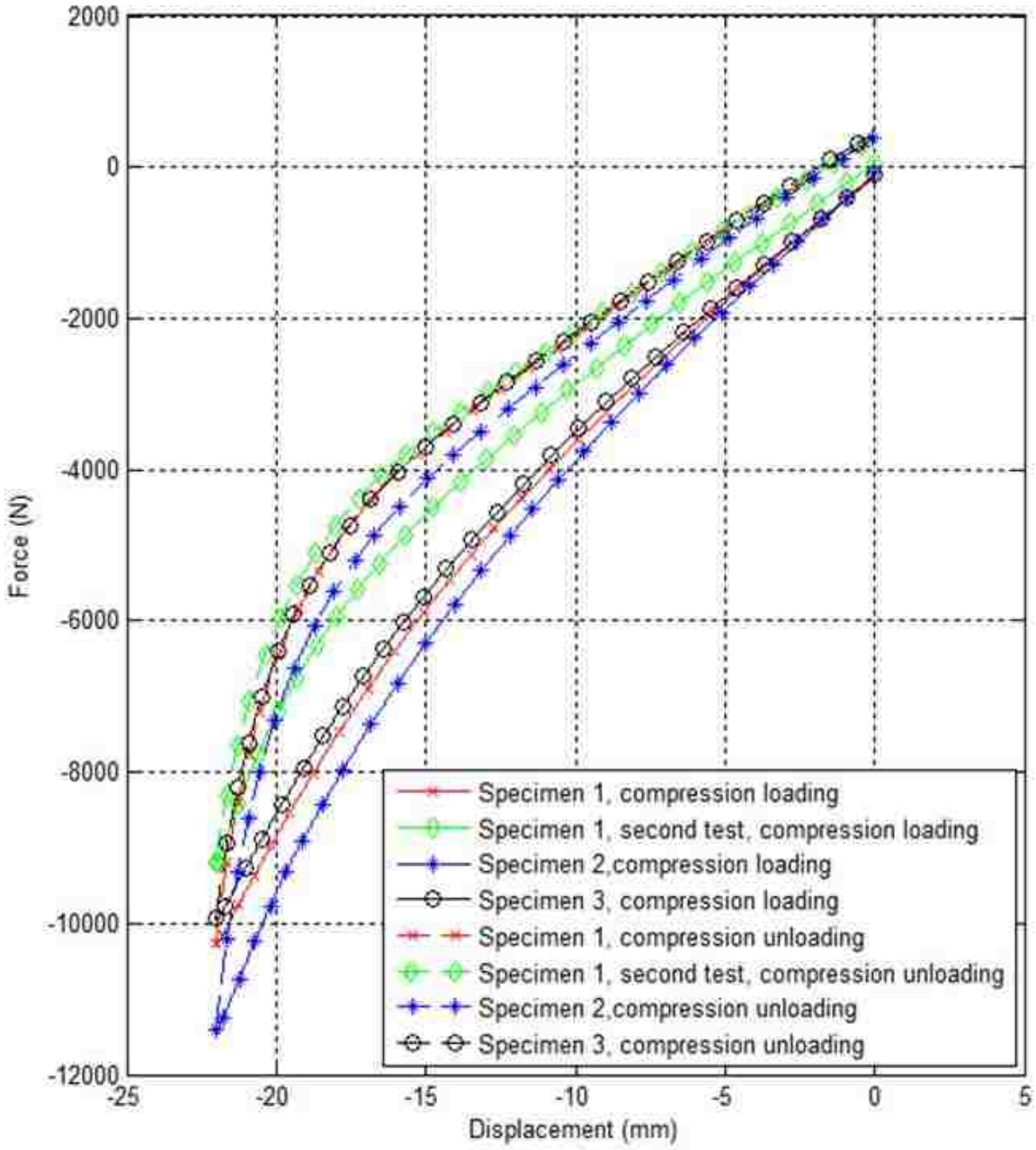

(b)

Figure 100: First loading and unloading cycle, quasi-static component characterization, (a) tension, (b) compression.

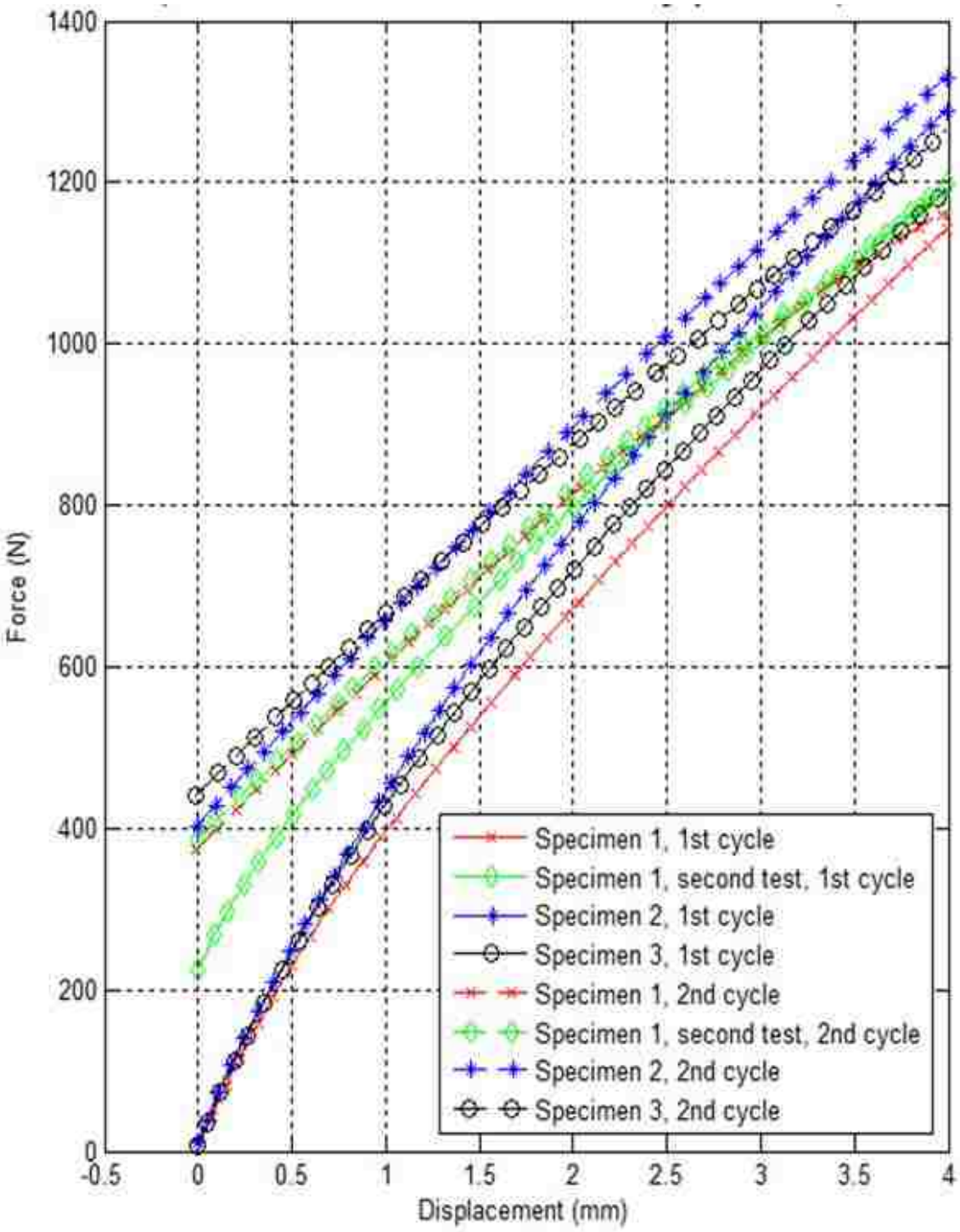
1400
1200
1000
800
600
400
200
0
Force (N)
-0.5
0
0.5
1
1.5
2
2.5
3
3.5
4
Displacement (mm)
Specimen 1, 1st cycle
Specimen 1, second test, 1st cycle
Specimen 2, 1st cycle
Specimen 3, 1st cycle
Specimen 1, 2nd cycle
Specimen 1, second test, 2nd cycle
Specimen 2, 2nd cycle
Specimen 3, 2nd cycle

(a)

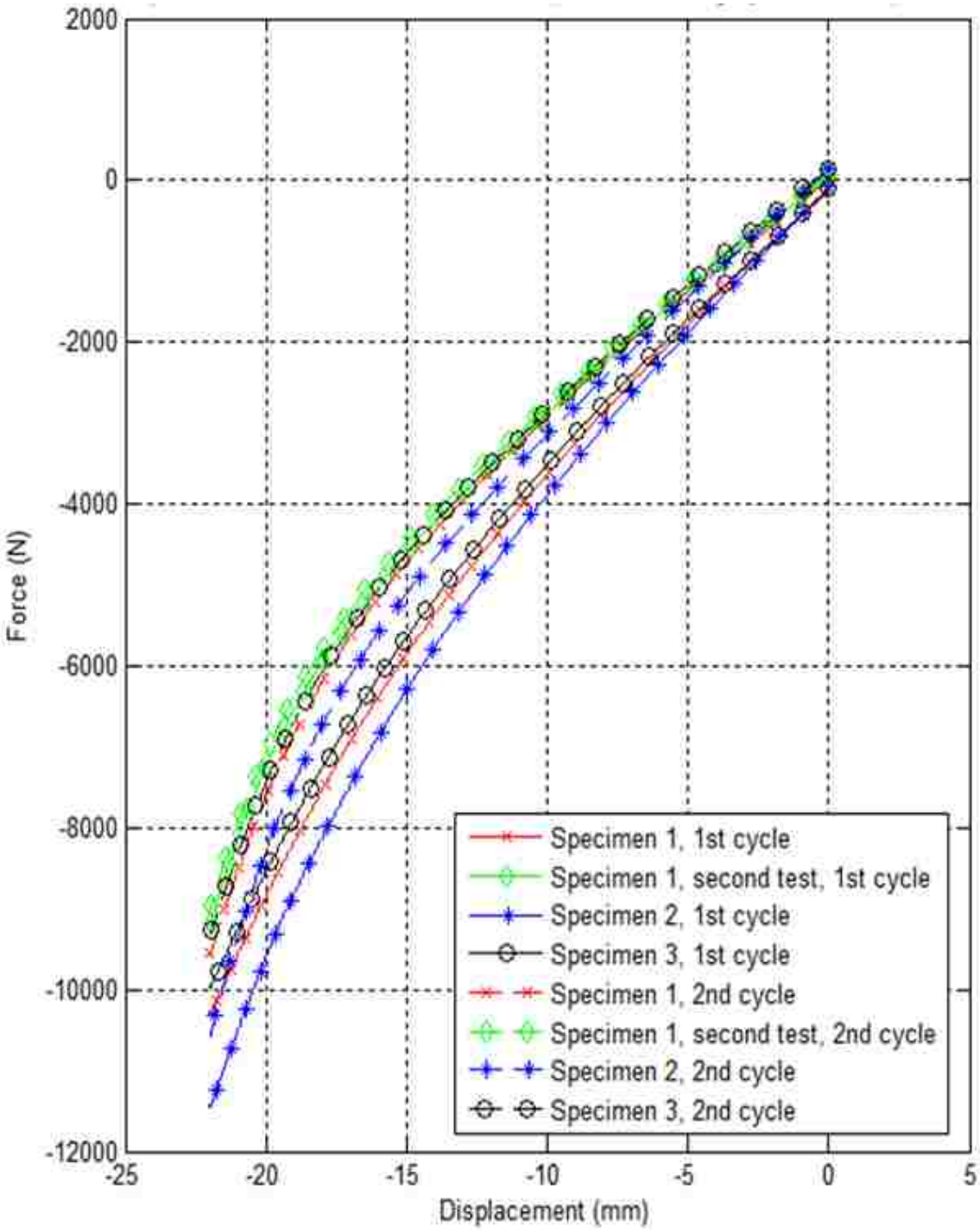

(b)

Figure 101: Tensile and compression loading, first and second cycles, (a) tension, (b) compression.

High resolution photographs of the specimens during the characterization process resulted in important observations. As shown in Figure 102 (undeformed and maximum displacement in compression), the steel brackets of the engine mount deformed such that the measured displacement should either be corrected or finite element models should include the steel brackets. This was consistently observed for all specimens. Another potential source of error was identified for one set of data as shown in Figure 103. A pair of bolts was installed with sufficient torque to provide the necessary clamping force to prevent movement between the two steel plates of the fixture. However, the relative displacement between these plates is minimal.

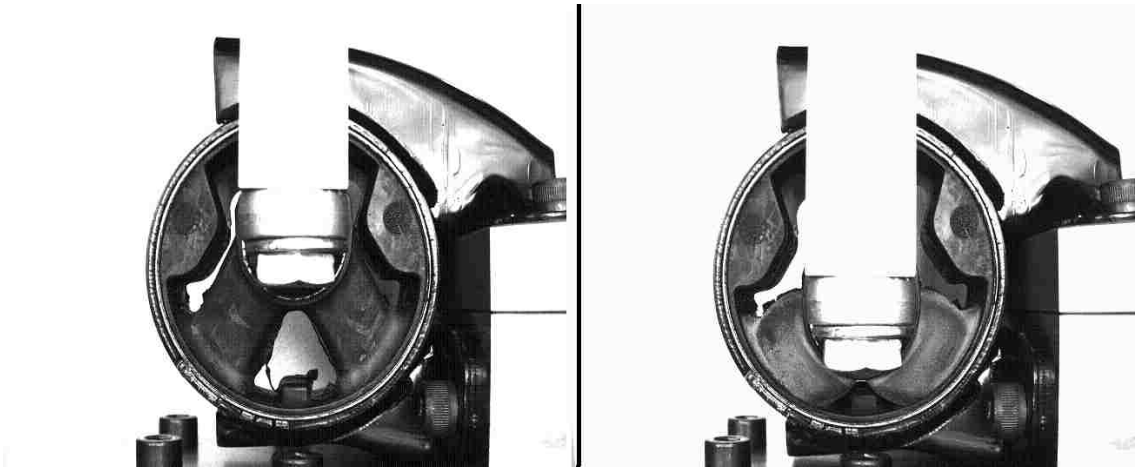

Figure 102: Bracket deformation, specimen #1, test #1.

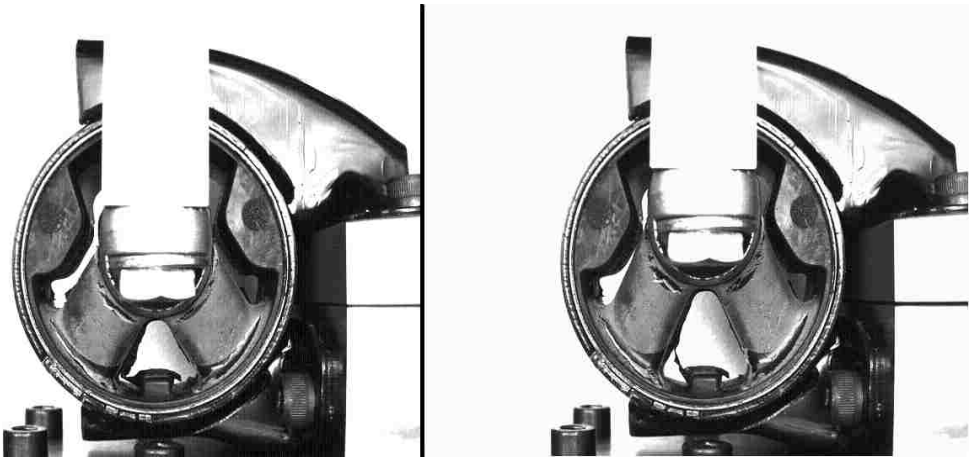

Figure 103: Separation of fixture plates, specimen #1, test #1.

5.6.3 Dynamic Component Characterization

The data acquired during the dynamic characterization process is shown in Figure 104: the displacement over time of the hydraulic cylinder and the force from the load cell. The time displacement profile was essentially identical for all specimens. By identifying the time at which the load cell began registering a load, the data for the position of the hydraulic cylinder could be used to calculate a displacement of the inner hub of the engine mount with respect the base of the metal fixture. This accounted for the initial gap, shown in Figure 36, between the upper half of the fixture and the relatively rigid entity of the DARTEC testing machine against which it was impacted. The resulting dynamic force-displacement responses are shown in Figure 105.

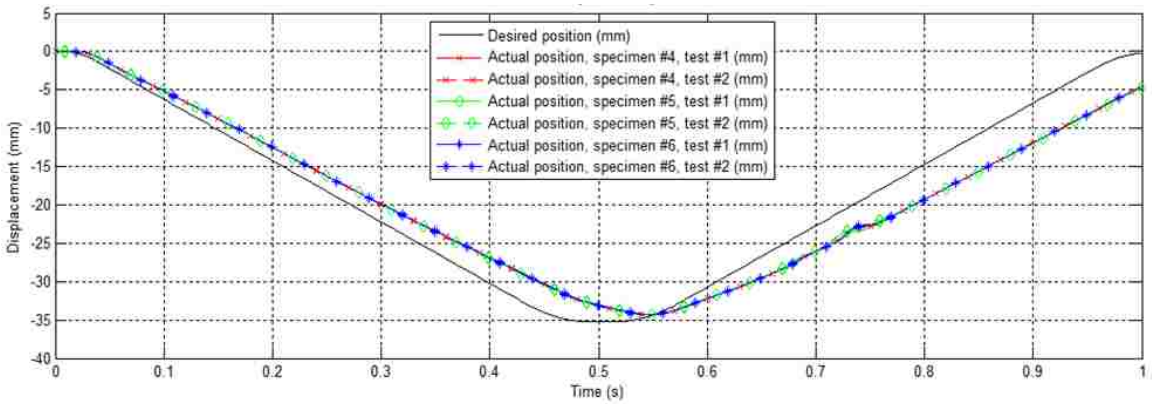

(a)

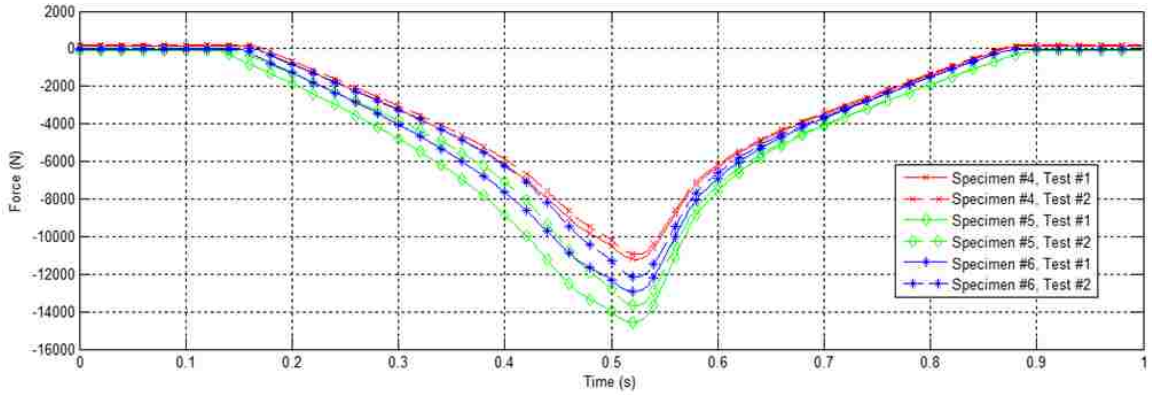

(b)

Figure 104: (a) Displacement of the hydraulic cylinder and (b) force (from load cell) over time.

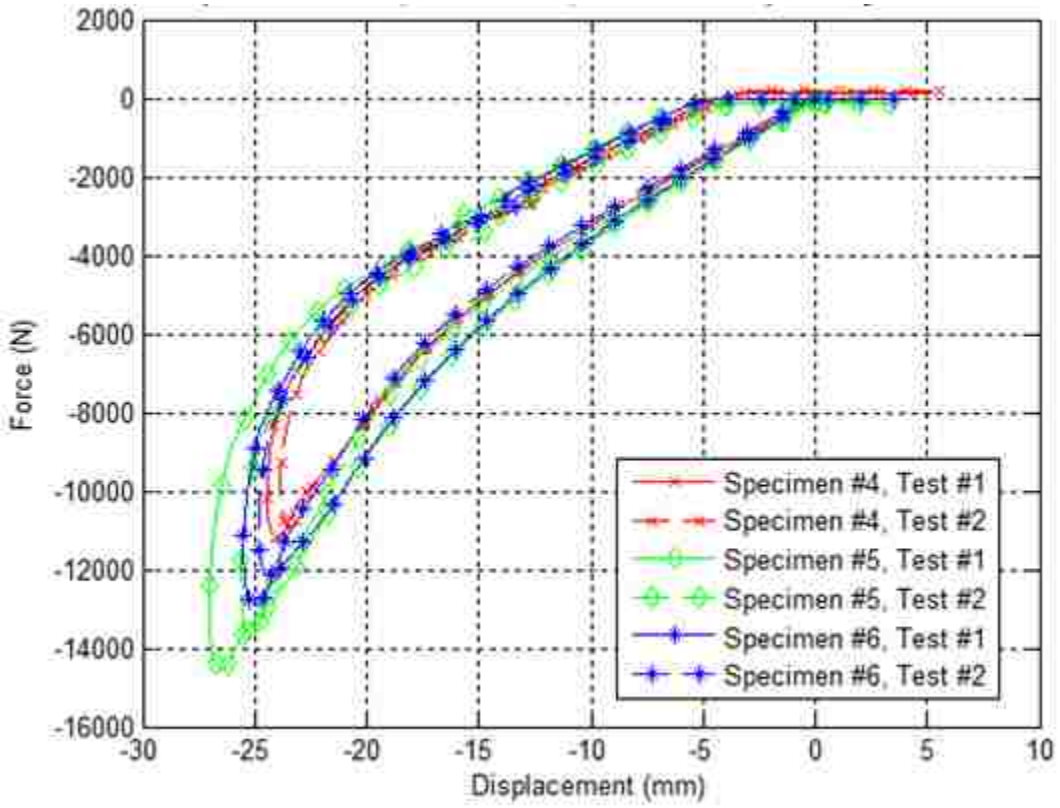

Figure 105: Dynamic force-displacement response of the Chrysler engine mount.

The quasi-static and dynamic force-displacement responses of the Chrysler powertrain suspension component are compared in Figure 106. This component did not exhibit significant strain rate sensitivity under loading. However, the energy dissipation of the component may have significantly increased under dynamic conditions. An alternate explanation for the increased energy absorption is the increased level of deformation. A superposition of these two effects is, accordingly, another possibility.

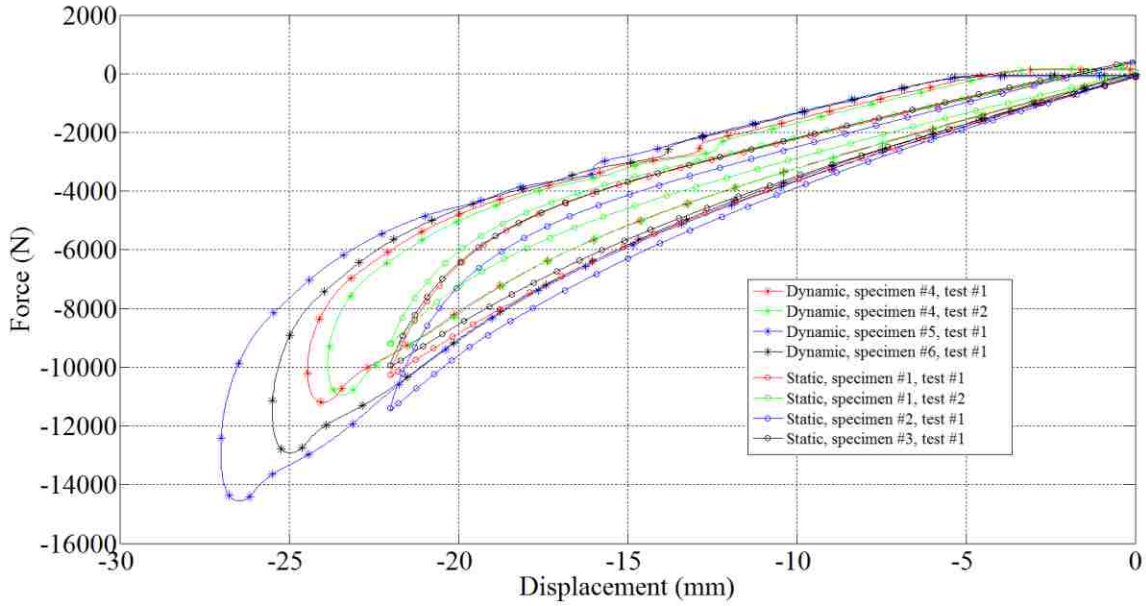

Figure 106: Quasi-static and dynamic force-displacement responses of Chrysler powertrain suspension component.

5.7 Finite Element Model Validation

5.7.1 Quasi-Static Force-Displacement Response

The first validation of the finite element model of the engine mount considered the component characterization data for quasi-static tensile loading of the engine mount. An estimate was made for a termination time sufficiently large to obtain a quasi-static response. A first estimate of this termination time was 20 ms as shown in Figure 107. However, to ensure this termination time was sufficiently large another simulation was completed with a termination time of 40 ms (curve B, the time has been scaled in the figure). The strain rate effects were also removed in another alteration to this model by using only the 0.01 s^{-1} strain rate AXEL data in MAT 181 in place of the tabular input which also included stress-strain data for a strain rate of 100 s^{-1}.

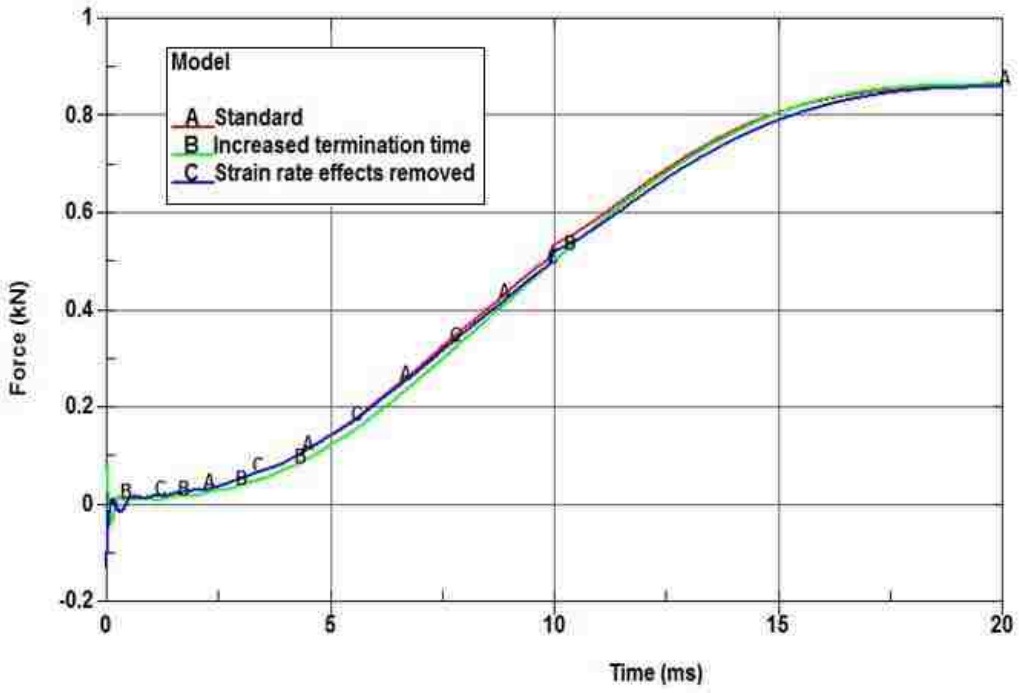

Figure 107: Quasi-static force-displacement characteristics in tension (finite element model).

The quasi-static force displacement response of a finite element model and the tensile quasi-static component characterization data are shown in Figure 108. Force data for all models was filtered in LS-PrePost using a Butterworth filter with a channel frequency class (CFC) of 1000 to remove very high frequency content likely associated with the numerical computation of derivatives. The significant variation between the finite element model and the experimental data led to many alterations to the model in an attempt to improve the accuracy. The reduction in time scaling was not completed to enhance the accuracy since reduced loads would be expected since inertial forces would be reduced. The elimination of strain rate sensitivity modelling was also unrelated to the accuracy concerns. The use of element formulation 2 for element modeling rubber and the alteration of the tied contact interfaces were attempts to increase the accuracy of the model.

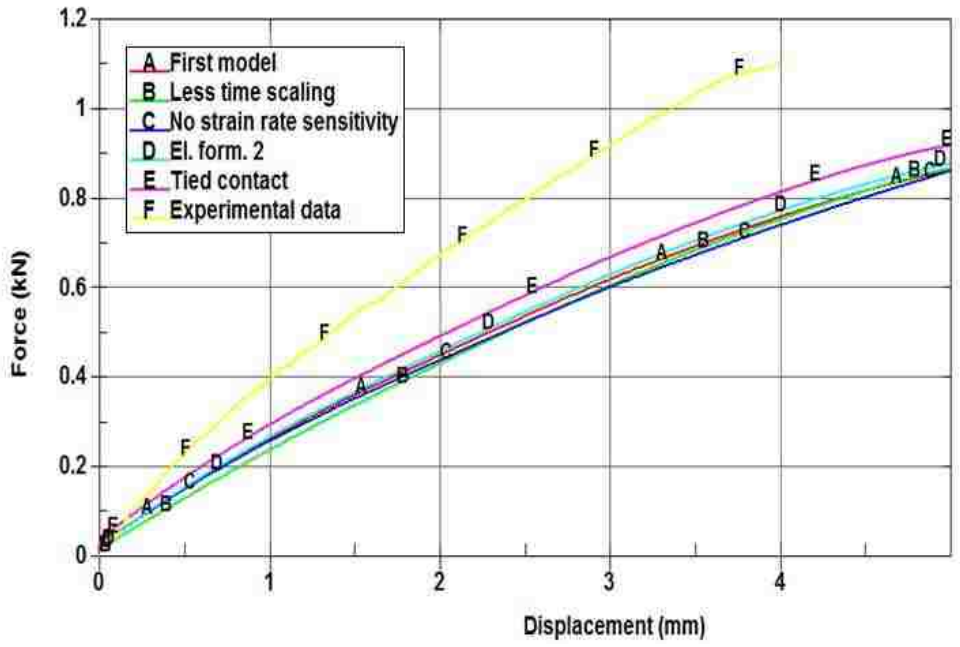

Figure 108: Engine mount finite element model validation, tensile loading, quasi-static characterization

A notable increase in the accuracy of the model resulted from the replacement of tied contact with merged nodes. The process employed in developing the tied contact interfaces was to use *CONTACT_AUTOMATIC_SURFACE_TO_SURFACE_TIED and remove the option Tied to activate the contact checking tool in LS-PrePost. Without the use of this tool contact may have worked well in terms of constraints between nodes but the preloading would result in a significant initial internal energy and a poor energy balance. However, optimal modeling of tied contact without excessive energy imbalance was never achieved. A quick inspection of the D3PLOT output for the models shown in Figure 108 seemed to indicate that the tied contact interfaces were reasonable in terms of nodal constraints and energy balance. However, the force-displacement response and more extensive investigations of the model (in particular considering von Mises stresses at contact interfaces) indicated that the modelling methodology may not be optimal.

As shown in Figure 109, the use of merged coincident nodes greatly increased the stiffness consistent with the observations that the tied contact was not tying many of the nodes. The resulting significant increase in stiffness was not expected. Data set E in

Figure 108 represents a removal of one tied contact interface and replacement with the merging of coincident nodes. The resulting increase in stiffness was not significant. However, as shown in Figure 109, the replacement of all tied contact interfaces with merged nodes yielded a very accurate model. The relative simplicity of this technique (merging nodes) and the presumed reduction in computational cost suggest this methodology may be of considerable benefit. The Oberkampf-Trucano error metric was calculated to be 0.9675.

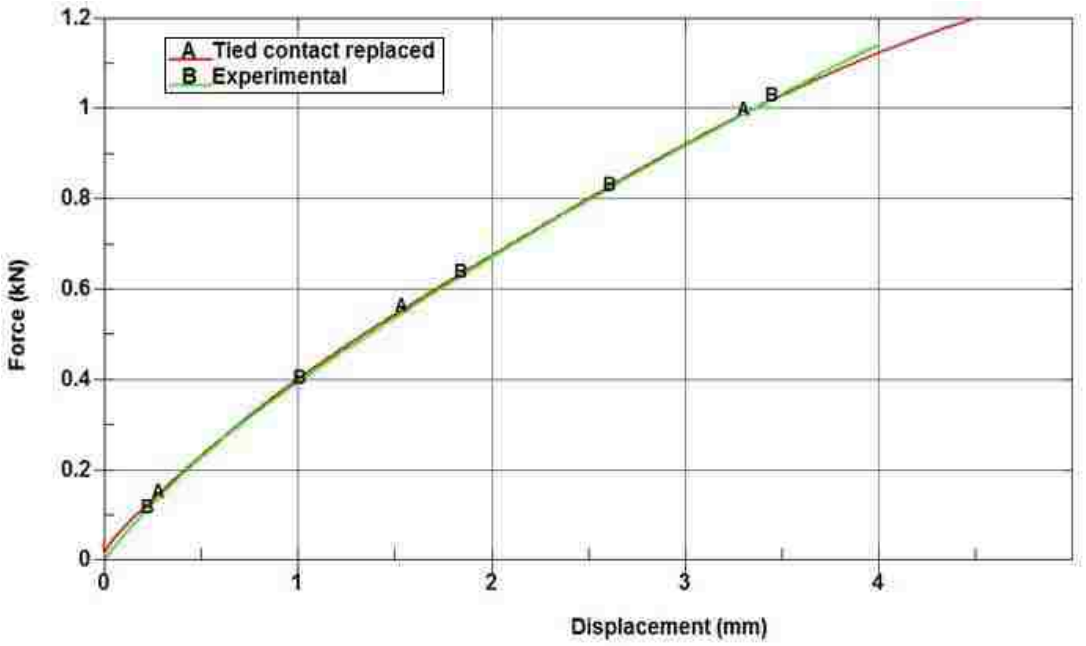

Figure 109: Engine mount finite element model validation, tensile loading, quasi-static characterization, tied contact replaced with constraints.

Excellent correlation between the experimental component characterization data in compression and the finite element model of the engine mount was observed as shown in Figure 110. The Oberkampf-Trucano metric was calculated to be 0.9070 using a slightly modified version of the MATLAB/Octave script in the appendix for validation of simple tension models. The most significant modification to the script was to use the option ‘pchip’ with the interp1 command in MATLAB rather than the Octave option ‘extrap’ (which does not exist in MATLAB). This model worked well with tied contact which likely resulted from the nature of the compressive loading and contact modelling with the default penalty stiffness method.

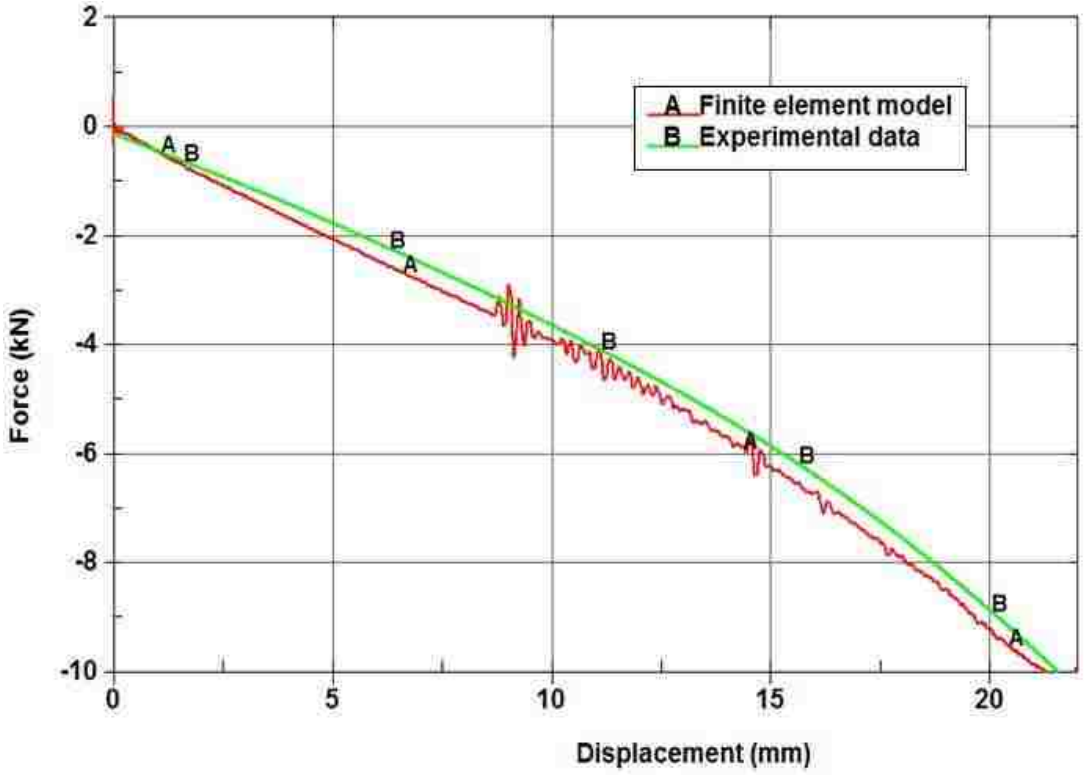

Figure 110: Finite element model validation, compressive loading, quasi-static characterization.

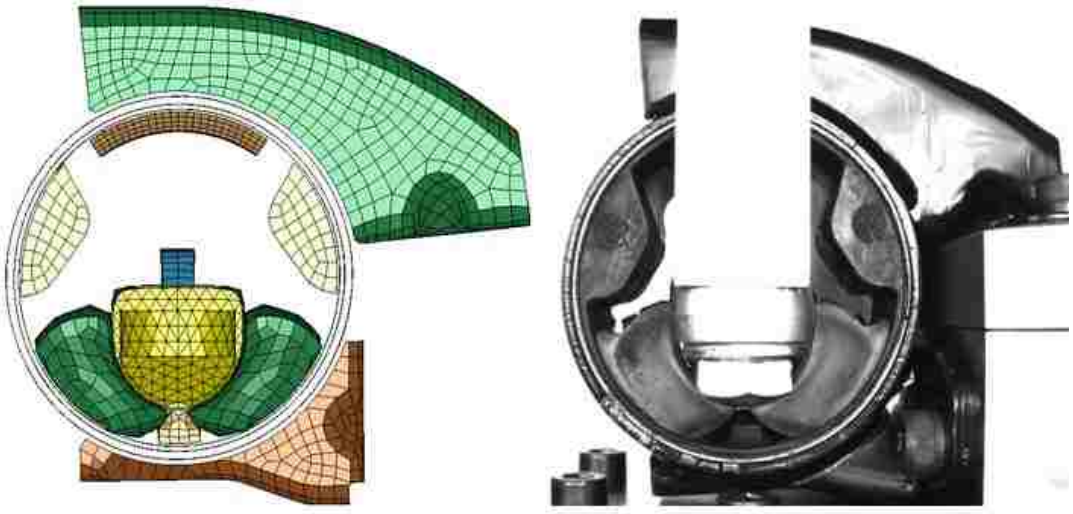

Figure 111: Finite element model of compressive loading and high resolution image.

5.7.2 Dynamic Component Force-Displacement Response

Shown in Figure 112 is the force data captured by the load cell on the Zwick/Roell DARTEC material testing system in DYNLab and the equivalent results from the finite element model shown in Figure 39. The displacement profile for the boundary condition in the finite element model (displacement of the steel brackets of the engine mount) was taken from the data acquired during the first characterization (test #1) of specimen. Correspondingly the force profile in Figure 112 is from this same specimen and test. The time or displacement at which contact between the upper half of the fixture and the upper platen of the DARTEC MTS is consistent between the model and the experimental test. However, the peak load of the numerical model is erroneous with too large a magnitude.

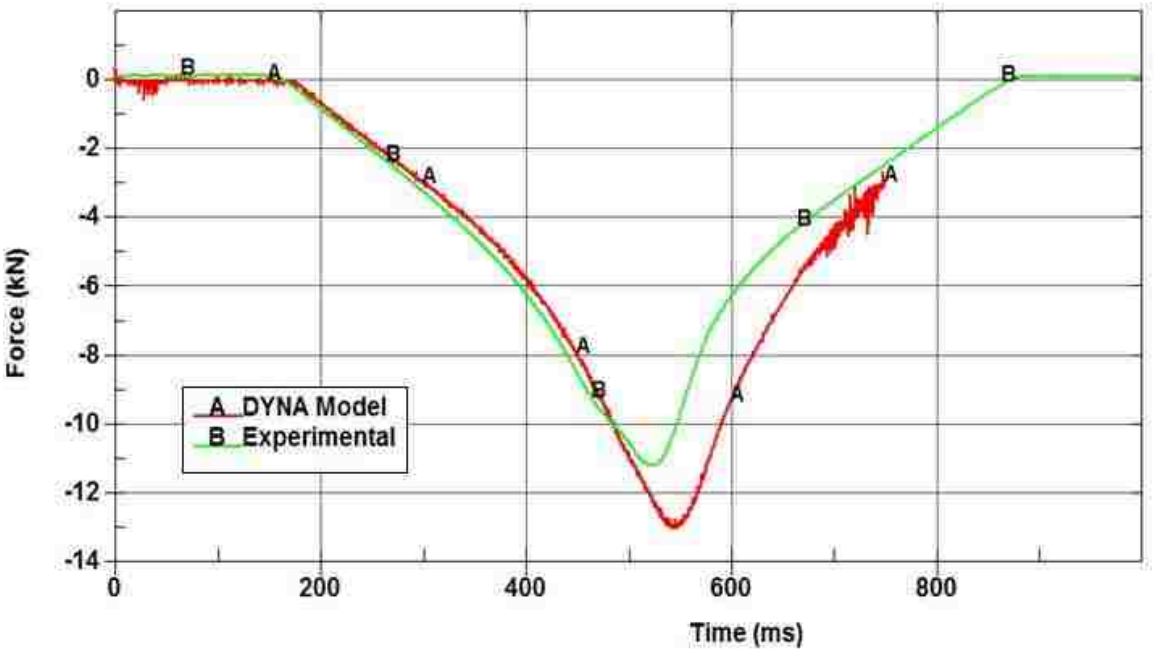

Figure 112: Force-time profile, dynamic component characterization, model validation

Chapter 6: Discussion

6.1 Quasi-Static Material Characterization

Simple tension material characterization was originally proposed to use ASTM D412 Type D specimens and ISO 37 type 2 specimens. The ISO specimens were not used. However, the ASTM specimens are of ideal dimensions whereas the ISO specimens are excessively short and lateral contraction as the specimen is elongated (and volume is essentially constant) is constrained. Shorter specimens can be used for dynamic material characterization since the shorter length assists in achieving higher strain rates. The shorter length also reduces the variation in strain rate since one end of the specimen is fixed and the other is displaced. A more practical reason for using for shorter specimens may be the limitations imposed by the dimensions of the source material.

It was hypothesized that AXEL obtained their material testing specimens from rubber slabs and not directly from components as was done in the FIAT polymer lab. This is based upon the completion of the equibiaxial tension test which requires a large specimen that could not be extracted from an engine mount and their use of stacked discs for simple compression. Simple compression specimen thickness was not limited by the extraction of specimens from the Chrysler engine mount in the FIAT polymer laboratory. The use of stacked discs may explain the discrepancy between the FIAT and AXEL simple compression material data but the excellent correlation between the simple compression data and the converted equibiaxial tension data (Figure 43) suggests that the simple compression data from AXEL is of high quality.

The significant variation in simple compression results in the FIAT laboratory was considered with no adequate solution found. The poor specimen dimensional accuracy was considered as a possible contributor to the variation. It may be a combination of factors difficult to account for. It may be worthwhile to develop finite element models of specimens with poor dimensional accuracy (i.e. out of roundness, non-parallel faces, etc.) and determine the effects of these factors on the stress-strain response. A previous study (Day JR, 2000) considered friction and found its affects to be significant with shear strains that may be greater than the compressive strains.

Planar tension (pure shear) testing was originally planned to be completed in the FIAT Mirafiori polymer laboratory. The procedure used by FIAT is different from that of AXEL Products Physical Testing Services. FIAT uses an adhesive to attach rubber specimens to aluminum fixtures. AXEL clamps the rubber specimen in a manner similar to that used for simple tension. With the AXEL methodology, as a result of the significant deformation, the material flows in the clamps. Finite element models of the planar tension (pure shear) material characterization process were based upon the FIAT models which greatly simplified the application of boundary conditions. The theoretical conditions for the planar tension characterization process, an element strained in one direction, no strain in an orthogonal direction, and no stress in the other mutually orthogonal directions may be more similar to the FIAT process.

6.2 Finite Element Modeling of Quasi-Static Material Characterization

6.2.1 Single Element Models

The superior accuracy of MAT 77O (Ogden) and MAT 77H with respect to MAT 181 was unexpected since (Kolling S, 2005) states that MAT 181 can very accurately represent any input stress-strain data. This is dependent upon the model being quasi-static but this condition was easily met with the single element models. In other single element models, not presented here, it was found that the bulk modulus, one of the material model inputs for MAT 181, significantly influenced the uniaxial stress state accuracy of MAT 181. This may be explained by the influence of volumetric change on the stress-strain relationship of the material model. The material model may also have fundamental assumptions that the volume of each element is constant (Equation 15), a condition that is not true unless the bulk modulus is infinite. Correspondingly, increasing the bulk modulus increased the accuracy of MAT 181. However, the bulk modulus is not infinite for any material and, at least for rubber, is commonly measured in the laboratory to determine a finite value that may or not be used in the material model. For this research the bulk modulus was provided by Chrysler engineers.

The increase in accuracy of MAT 181 with the addition of compressive data to the input to the material model (for a simulation of an element in pure tension) was unexpected. The decrease in performance of MAT 77 is sensible since the curve fitting was completed internally by LS-DYNA not considering that the model would be in a state of pure tension and the compressive portion of the stress-strain curve was of less importance. Therefore, since the same expression was required to be fit to a curve with a larger domain with a more complex response, a decrease of the accuracy in pure tension was expected. It may be noted that the decrease in accuracy was essentially insignificant. This is likely due to the use of a large number of terms which is sufficient to not only accurately capture a uniaxial stress strain curve but also to represent reasonably well the characteristics of the material for equibiaxial tension and pure shear.

6.2.2 Simple Tension Finite Element Models

Table 23 compares the simple tension finite element models employing MAT 181 and MAT 77O (6 Terms). MAT 77H was not used since the strain energy function upon which is it based is a subset of the Ogden strain energy function of MAT 77O (Equation 16 and Equation 21). The most and least accurate models using each material model are highlighted as are the models that are most and least computationally expensive. MAT 181 was consistently more accurate and more stable as judged by the many models that ran to termination with MAT 181 but terminated with errors when the material model was changed to different implementations of MAT 77O (with no other alterations). MAT 77O (Ogden) was much more computationally efficient. The internal procedures that allow MAT 181 to essentially perfectly replicate input uniaxial stress strain curves likely resulted in this relatively high computational expense.

Table 23: Comparison between simple tension models using MAT 181 and MAT 77O (6 terms).

MAT 181

Element Formulation	Element Size (mm)	Validation Metric	CPU Time (min)
16	2.5	0.98041	32
1	1	0.98008	12
2	1	0.97986	68
10	1	0.97893	48
13	2.5	0.97674	7
13	1	0.97665	54
10	2.5	0.96868	3
16	1	0.95305	301
4	1	0.95019	30
4	2.5	0.9323	7
3	1	0.92681	51
2	2.5	0.8428	1
1	2.5	0.61712	0.3
3	2.5	0.50203	2.3

MAT 77O
Ogden
6 terms

Element Formulation	Element Size (mm)	Validation Metric	CPU Time (min)
4	1	-	-
1	1	0.90454	4.333
16	1	0.90383	330
10	2.5	0.89845	1
13	2.5	0.89845	1
10	1	0.89264	9
13	1	0.89264	9
16	2.5	0.88319	8
1	2.5	0	0.3
2	2.5	0	-
3	2.5	0	-
2	1	0	-
3	1	0	-
4	2.5	0	-

A similar comparison is given in Table 24 where the coefficients of the Ogden material model have been increased (8 term model, 16 coefficients). These coefficients were identified in MATLAB as discussed in the methodology section. It was expected that the 6 term model would be capable of modeling larger deformations since the coefficients were found using MARC. More specifically, this behaviour was expected since the option, within MARC, to find positive coefficients was utilized. Additionally, an option within MARC to perform mathematical analyses of potential coefficients was also activated. Considering Table 23, for many models the 6 term Ogden material model terminated with an error while the corresponding models employing MAT 181 terminated normally (shown by the reduced number of entries in the columns for MAT

77 with respect to the entries for MAT 181). Considering Table 24, the 8 term Ogden model had fewer models which terminated normally but the difference is not especially significant. One final observation: the accuracy and computational efficiency of the 6 term and 8 term Ogden models are comparable.

Table 24: Comparison between simple tension models using MAT 181 and MAT 77O (8 terms).

MAT 181

Element Formulation	Element Size (mm)	Validation Metric	CPU Time (min)
16	2.5	0.98041	32
1	1	0.98008	12
2	1	0.97986	68
10	1	0.97893	48
13	2.5	0.97674	7
13	1	0.97665	54
10	2.5	0.96868	3
16	1	0.95305	301
4	1	0.95019	30
4	2.5	0.9323	7
3	1	0.92681	51
2	2.5	0.8428	1
1	2.5	0.61712	0.3
3	2.5	0.50203	2.3

MAT 77O Ogden 8 Terms

Element Formulation	Element Size (mm)	Validation Metric	CPU Time (min)
10	2.5	0.90729	0.383
13	2.5	0.90729	0.417
16	1	0.90365	89
16	2.5	0.90319	3.6
13	1	0.90287	9.8
10	1	0.90274	7
1	1	0.89173	4.633
41	1	0.89105	0.867
3	1	0.88978	72

6.2.3 Simple Compression Finite Element Models

Table 25 compares MAT 181 and MAT 77O (6 terms, determined using MARC) in simple compression with hexahedron and tetrahedron element formulations. Many discretizations which, with MAT 181, terminated normally without unrealistic behaviour or poor energy balance would not successfully reach the termination time (and associated level of deformation) successfully when the material model was changed to MAT 77 Ogden. No other changes were made to the model, solver, or computer used to run the models. As was expected with the ability of MAT 181 to replicate uniaxial stress-strain input data, MAT 181 was more accurate than this 6 term implementation of MAT 77O. However, MAT77O was considerably less computationally expensive than MAT 181. If it were not for the reduced ability to model large deformations, MAT 77O might be worth considering for use in this crashworthiness application.

Table 25: Comparison between simple compression finite element models using MAT 181 and MAT 77O (6 terms)

MAT 181

Element Formulation	Element Size (mm)	Validation Metric	CPU Time (min)
10	2	0.98387	3
13	2	0.98364	3
4	2	0.98267	14
13	5	0.97613	0.117
2	5	0.97548	0.167
4	5	0.97494	0.417
10	5	0.97456	0.117
3	2	0.95116	9
2	2	0.9496	2
3	5	0.93275	0.433
1	2	0.8697	0.917
1	5	0.85099	0.133

MAT 77O Ogden, 6 terms (MARC)

Element Formulation	Element Size (mm)	Validation Metric	CPU Time (min)
10	2	0.79086	1
13	2	0.79086	1
10	5	0.7813	0.033
13	5	0.7813	0.033
2*	5	0.78126	0.1

* Revised mesh to reduce peak aspect ratio.

Table 26 is a similar comparison between the MAT 181 and the 8 term Ogden model with coefficients identified in MATLAB. The 8 term model was not particularly less stable than the 6 term model but was significantly more accurate. This is consistent with a comparison of the curve fitting as analyzed in MATLAB. However, even with 8 terms the Ogden model was not as accurate as MAT 181. The significantly decreased computational cost of MAT 77O with respect to MAT 181 was still observed.

Table 26: Comparison between simple compression finite element models using MAT 181 and MAT 77O (8 terms).

MAT 181

Element Formulation	Element Size (mm)	Validation Metric	CPU Time (min)
10	2	0.98387	3
13	2	0.98364	3
4	2	0.98267	14
13	5	0.97613	0.117
2	5	0.97548	0.167
4	5	0.97494	0.417
10	5	0.97456	0.117
3	2	0.95116	9
2	2	0.9496	2
3	5	0.93275	0.433
1	2	0.8697	0.917
1	5	0.85099	0.133

MAT 77O Ogden, 8 terms

Element Formulation	Element Size (mm)	Validation Metric	CPU Time (min)
10	2	0.87854	0.933
13	2	0.87854	0.95
2	5	0.86772	0.083
41	5	0.86758	0.117
13	5	0.86737	0.033
3	2	0.78655	5

6.2.4 Planar Tension (Pure Shear) Finite Element Models

Table 27 compares finite element models of the planar tension (pure shear) method of material characterization using MAT 181 and the 6 term implementation of MAT 77 Ogden both with hexahedron elements. A consistent trend with previous results for simple tension and compression was observed: increased accuracy with MAT 181 but decreased computational cost with MAT 77O. The reduced ability to model large

deformations with MAT 77O was not as significant for the deformation mode of this model. For very fine meshes there was also a possible trend towards MAT 77O becoming more accurate which would be reasonable since the coefficients of the Ogden strain energy function were determined considering the planar tension (pure shear) AXEL data.

Table 27: Comparison between planar tension (pure shear) models using MAT 181 and MAT 77O (6 terms), hexahedron element formulations.

MAT 181

Element Formulation	Element Size (mm)	Validation Metric	CPU Time (min)
2	1.25	0.85958	19
2	0.625	0.81518	214
1	0.625	0.81389	20
1	0.3125	0.80375	480
2	0.3125	0.79853	2400
1	1.25	0.79286	5
3	0.3125	0.71481	7200
1	2.5	0.71154	0.3
3	0.625	0.43938	337
2	2.5	0.31677	2
3	1.25	0.10673	86
3	2.5	0	6

MAT 77O Ogden 6 terms (MARC)

Element Formulation	Element Size (mm)	Validation Metric	CPU Time (min)
2	1.25	0.82534	210
1	0.625	0.80645	10
2	0.625	0.80546	40
1	0.3125	0.80106	50
1	1.25	0.77759	0.667
3	0.3125	0.76392	1680
1	2.5	0.72622	0
3	0.625	0.65614	130
2	2.5	0.47143	0.333
3	2.5	0	-
3	1.25	0	-
2	0.3125	0	-

Table 28 is a similar comparison between MAT 181 and MAT 77O (6 terms) but for tetrahedron elements. Coarse discretizations yielded poor results with either material model. MAT 77O did not accurately capture the engineering stress-strain response of the specimen even with a very fine discretization. With MAT 181 the potential advantage of element formulation 13 over element formulation 10 for modeling rubber may be observed. Element formulations 10 and 13 are both 4 node, 1 point integration tetrahedron elements. However, element formulation 13 is less prone to volumetric locking and is more suitable for incompressible and near incompressible materials.

Table 28: Comparison between planar tension (pure shear) models using MAT 181 and MAT 77O (6 terms), tetrahedron element formulations.

MAT 181

Element Formulation	Element Size (mm)	Validation Metric	CPU Time (min)
4	2.5	All element formulations exhibited instabilities in planar tension for coarse discretization.	
10	2.5		
13	2.5		
4	1.25		
10	1.25		
13	1.25		
4	0.625		
13	0.625	0.85893	150
13	0.3125	0.78443	440
4	0.3125	0.41877	3600
10	0.3125	0.18182	440
10	0.625	0.001	150

MAT 77O Ogden 6 terms (MARC)

Element Formulation	Element Size (mm)	Validation Metric	CPU Time (min)
10	0.3125	0.75453	240
13	0.3125	0.75453	240
10	0.625	0.51901	43
13	0.625	0.51901	43
10	1.25	0.05571	5
13	1.25	0.05571	5
4	2.5	0	-
10	2.5	0	0.333
13	2.5	0	0.833
4	1.25	0	-
4	0.625	0	-
4	0.3125	0	-

Comparable tables for the 8 term Ogden model are given in Table 29 and Table 30. For these models, since the Ogden material model coefficients were obtained taking directly into consideration the AXEL planar tension (pure shear) data the accuracy of MAT 77O with 8 terms was generally superior to that of MAT 181. However, for reasonable modeling parameter selections the accuracy of MAT 181 was quite good. The 8 term implementation of MAT 77O was also consistent with the 6 term model in terms of the poor accuracy with coarse tetrahedron meshes. One may also note, for all models, that element formulations 16 (10 node, 5 point integration tetrahedron) and 41 (element free Galerkin) were considered for the 8 term Ogden model. Neither formulation worked well with MAT 181 (EFG is essentially completely unsupported). Neither was particularly impressive, especially in terms of capability to model large deformations. This may be a limitation imposed by the material model.

Table 29: Comparison between planar tension (pure shear) models using MAT 181 and MAT 77O (8 terms), hexahedron element formulations.

MAT 181

Element Formulation	Element Size (mm)	Validation Metric	CPU Time (min)
2	1.25	0.85958	19
2	0.625	0.81518	214
1	0.625	0.81389	20
1	0.3125	0.80375	480
2	0.3125	0.79853	2400
1	1.25	0.79286	5
3	0.3125	0.71481	7200
1	2.5	0.71154	0.3
3	0.625	0.43938	337
2	2.5	0.31677	2
3	1.25	0.10673	86
3	2.5	0	6

MAT 77O Ogden 8 terms

Element Formulation	Element Size (mm)	Validation Metric	CPU Time (min)
1	0.625	0.91562	2
1	0.3125	0.91437	40
2	0.625	0.91433	11
41	0.3125	0.91288	300
3	0.3125	0.90409	960
41	0.625	0.90024	14
2	1.25	0.8963	0.75
1	2.5	0.89325	0
1	1.25	0.84575	0.1
3	0.625	0.82117	27
41	1.25	0.69281	0.95
2	2.5	0.5083	0.05

Table 30: Comparison between planar tension (pure shear) models using MAT 181 and MAT 77O (8 terms), tetrahedron element formulations.

MAT 181

Element Formulation	Element Size (mm)	Validation Metric	CPU Time (min)
4	2.5	All element formulations exhibited instabilities in planar tension for coarse discretization.	
10	2.5		
13	2.5		
4	1.25		
10	1.25		
13	1.25		
4	0.625		
13	0.625	0.85893	150
13	0.3125	0.78443	440
4	0.3125	0.41877	3600
10	0.3125	0.18182	440
10	0.625	0.001	150

MAT 77O Ogden 8 terms

Element Formulation	Element Size (mm)	Validation Metric	CPU Time (min)
16	1.25	0.94784	50
10	0.625	0.89565	195
13	0.3125	0.89565	195
10	0.625	0.67445	9
13	0.625	0.67445	9
16	2.5	0.59701	0.4
10	1.25	0.09239	1
13	1.25	0.09238	1
10	2.5	0	0.067
13	2.5	0	0.167

6.2.5 Equibiaxial Tension Finite Element Models

Table 31 compares finite element models (hexahedron element formulations) of the equibiaxial tension material characterization process employing MAT 181 and MAT 77O (6 terms). This is another clear example of the increased accuracy of MAT 181 at the expense of computational cost. The high accuracy of MAT 181 was surprising since the input to this material model is nothing more than a uniaxial engineering stress-strain curve. This material model (MAT 181) is based upon the Ogden strain energy functional (Kolling S, 2005) which in theory has the capability to model the equibiaxial tension stress state quite accurately as shown by the 8 term Ogden model developed in MATLAB.

Table 31: Comparison between equibiaxial tension models using MAT 181 and MAT 77O (6 terms), hexahedron element formulations.

MAT 181

Element Formulation	Element Size (mm)	Validation Metric	CPU Time (min)
3	2	0.96035	8
2	0.5	0.92599	720
1	0.5	0.9256	120
3	0.5	0.92555	1800
2	2	0.9246	4
2	1	0.91616	43
1	1	0.91518	8
3	1	0.91222	80
1	2	0.89263	1

MAT 77O Ogden 6 terms

Element Formulation	Element Size (mm)	Validation Metric	CPU Time (min)
2	1	0.82534	3.5
1	0.5	0.80645	10
2	0.5	0.80546	40
1	1	0.77759	0.667
1	2	0.72622	0
3	0.5	0.65614	130
2	2	0.47143	0.333
3	2	0	-
3	1	0	-

Table 32 is a similar comparison of equibiaxial tension finite element models using tetrahedron elements. The models which use MAT 181 were fairly consistent in producing accurate results. The response of MAT 77 Ogden was much less accurate but this was a limitation imposed by the curve fitting. The Oberkampf Trucano validation metric is limited to the value calculated in MATLAB (0.79863, see Table 13) when the coefficients for this 6 term Ogden model were identified using MARC.

Table 32: Comparison between equibiaxial tension models using MAT 181 and MAT 77O (6 terms), tetrahedron element formulations.

MAT 181

Element Formulation	Element Size (mm)	Validation Metric	CPU Time (min)
4	2	0.964	26
10	2	0.95785	5
10	1	0.951	60
10	0.5	0.94681	690
13	1	0.93734	60
13	2	0.93272	5
13	0.5	0.924	690
4	1	0.86856	372
16	1	0.4926	7200
16	2	0.40952	52
4	0.5	0	-

MAT 77O Ogden 6 terms (MARC)

Element Formulation	Element Size (mm)	Validation Metric	CPU Time (min)
10	1	0.7742	23
13	1	0.7742	23
4	1	0.77165	110
10	2	0.76822	2
13	2	0.76822	2
10	0.5	0.7637	300
13	0.5	0.7637	300
4	0.5	0.75998	690
4	2	0	-

Similar tables for the 8 term implementation of MAT 77O are given in Table 33 (hexahedron elements) and Table 34 (tetrahedron elements). Even with 8 terms (the maximum for LS-DYNA) implemented in MAT 77O, MAT 181 was more accurate in equibiaxial tension. Consistent with previous results, MAT 181 was significantly more expensive computationally but if only a small portion of a full vehicle model consists of rubber components this should not be significant. The finer mesh that may be necessary with MAT 77O may be more problematic if the critical timestep for the entire model was dictated by one of the rubber elements.

Table 33: Comparison between equibiaxial tension models using MAT 181 and MAT 77O (8 terms), hexahedron element formulations.

MAT 181

Element Formulation	Element Size (mm)	Validation Metric	CPU Time (min)
3	2	0.96035	8
2	0.5	0.92599	720
1	0.5	0.9256	120
3	0.5	0.92555	1800
2	2	0.9246	4
2	1	0.91616	43
1	1	0.91518	8
3	1	0.91222	80
1	2	0.89263	1

MAT 77O Ogden 8 terms

Element Formulation	Element Size (mm)	Validation Metric	CPU Time (min)
3	2	0.89381	1.45
41	2	0.8925	3
3	0.5	0.85815	675
1	0.5	0.85569	46
3	1	0.85467	62
1	1	0.84165	3.35
2	2	0.49997	15
1	2	0.42099	2.3

Table 34: Comparison between equibiaxial tension models using MAT 181 and MAT 77O (8 terms), tetrahedron element formulations.

MAT 181

Element Formulation	Element Size (mm)	Validation Metric	CPU Time (min)
4	2	0.964	26
10	2	0.95785	5
10	1	0.951	60
10	0.5	0.94681	690
13	1	0.93734	60
13	2	0.93272	5
13	0.5	0.924	690
4	1	0.86856	372
16	1	0.4926	7200
16	2	0.40952	52
4	0.5	0	-

MAT 77O Ogden 8 terms

Element Formulation	Element Size (mm)	Validation Metric	CPU Time (min)
13	2	0.89367	1.9
10	2	0.89366	1.867
10	1	0.89115	20
13	1	0.89115	20
10	0.5	0.86354	240
13	0.5	0.86354	240
16	1	0.59326	185
16	2	0.44216	15.25

6.3 Finite Element Model of Chrysler Engine Mount

For many of the force displacement results presented there are obvious dynamic effects at small and large displacements due to the use of the *DEFINE_CURVE_SMOOTH keyword (ie. Figure 82 and Figure 83). While this keyword may be advantageous since the derivative of this curve is smooth it also results in relatively rapid changes in the dependent variable if the rise time is not sufficiently large as was the case for some models. However, all models presented use identical load-displacement curves defined using this keyword. Therefore, comparing different models to identify trends should be reasonable despite the less than optimal use of this keyword.

An important consideration when meshing was that the clearances between different surfaces which may come into contact should be accurate with respect to the physical component. This is especially important if experimental validation is performed by obtaining load-displacement data for the physical component. A numerical validation metric is significantly affected by an offset of two sets of data that are compared. The very coarse 8 mm mesh may be problematic in this regard since the geometrical simplifications are extensive.

A brief analysis of the computational expense of meshes using tetrahedron and hexahedron elements was presented. Considering the models of the material characterization process it is possible to estimate the respective accuracy. Considering Table 23 and Table 24 for simple tension the coarsest hexahedron mesh is generally less accurate than the coarsest tetrahedron mesh but the computational expense is greatly reduced. In simple compression (Table 25 and Table 26) the accuracy and computational expense are similar. For planar tension (Table 27, Table 28, Table 29, and Table 30) the combination of large deformations and significant constraints results in poor performance of the tetrahedron elements with coarse discretizations. Drawing conclusions here is difficult. For equibiaxial tension (Table 31, Table 32, Table 33 and Table 34) both types of elements are quite accurate but the models using tetrahedron elements have a slight advantage. Hexahedron elements were generally less expensive computationally.

6.3.1 Hourglass control

An additional study of hourglass control may be worthwhile. Significant hourglass energy and error terminations were observed for the finite element models of the simple compression material characterization process with element formulation 1. These models used the optimal hourglass control method identified using the model of the Chrysler transmission mount. It would be interesting to complete an additional study of hourglass control with the simple compression models. The hourglass control method study with the engine mount produced odd results: reduced hourglass energy with reduced hourglass control. Such an inconsistency warrants further consideration.

6.3.2 Tetrahedron element formulations and geometry simplifications

A significant increase in stiffness with tetrahedron elements was only clearly observed for some material characterization finite element models with very coarse discretizations. Nevertheless, when tetrahedron elements were used to model the Chrysler transmission mount the response was very stiff for element formulation 4, which features selectively reduced integration, and element formulation 10. It was also stiffer than element formulation 13 for the refined tetrahedron model of the planar tension (pure shear) material characterization process, a model which was a particularly valuable assessment of modelling techniques including element formulation. Element formulation 13 performs quite well which is consistent with the general performance of this element formulation for the models of material characterization processes.

6.3.3 Tied Contact

Tied contact was challenging to implement. A larger study of modelling parameters related to this modelling tool may be very worthwhile. It was found that the use of tied contact required a high quality mesh with careful attention at very preliminary stages to ensure the CAD data upon which the mesh was created was precise with consistent offsets between tied surfaces. While tied contact may function with lower quality models the energy balance was entirely unreasonable. The inability to assess the validity of the

model through the energy balance was not acceptable. One limitation that was encountered was associated with the massively parallel processing (MPP) solvers on the FIAT computing clusters. *CONTACT_TIED contact algorithms are not supported with these solvers. Share memory parallel (SMP) solvers were available on FIAT computing clusters but the selection of releases was greatly reduced (the selection of MPP solver release versions is already not especially extensive). The reduced efficiency in parallel execution and limited computational resources may have made use of SMP solvers impractical.

The problems associated with tied contact are likely the result of the different magnitudes of force when rubber is loaded in tension or in compression. In an attempt to find a solution to this problem two contact algorithms were used at each interface, one a tied contact algorithm and the other a normal penalty based contact algorithm. If the tied contact could be specified to be capable of modeling relatively small tensile loading the larger loads associated with compressive loading could be resolved by the penalty stiffness algorithm. However, a balanced pair of contact algorithms as proposed could not be found that avoided the previous issues of insufficient or excessive stiffness and poor energy balance.

6.4 Component Characterization

6.4.1 Fixture Design

Significant assumptions were made in the initial design of the fixture to complete simple manual calculations of maximum stresses. Stress concentrations due to radiused edges or holes were not considered. Additionally, stresses resulting from the contact between different components (e.g. steel brackets and washers) were not considered. Simple assumptions could also have been made to obtain approximations of these contributions to the stress state at critical locations in the fixture material. Such simple calculations were later completed to assess the results from finite element models. As an example, two similar models predicted very different stress states. One model included washers

through which bolt preloading was applied. The other model removed these washers and directly associated bolt preloading.

With the washers and associated bolt preloading loads removed, the peak von Mises stress due to the loading of the engine mount was 34 MPa. With the washers and bolt preloading the respective von Mises stress was approximately 280 MPa. If the contribution to the stress state due to the washer bolt preload is calculated assuming a direct normal stress the resulting von Mises stress should be less than 105 MPa. Even if the area of contact between a particular washer and a steel bracket is significantly less than the surface area of one side of the washer (assumed to be the area below, annular ring with an inner diameter of 10 mm and an outer diameter of 20 mm) the resulting maximum stress should be less than 200 MPa (assuming the surface area is 50% of 235.6 mm^2).

$$\sigma_{Bolt\ preload} = \frac{F_{Bolt\ preload}}{\pi({r_{washer\ inner}}^2 - {r_{washer\ outer}}^2)} = \frac{16.7\ kN}{235.6\ mm^2} = 70.9\ MPa \quad \text{(Equation 57)}$$

A potential source of error in the process of designing the fixture with finite element models may exist. While mesh dependency was assessed by reducing the average element size the geometry of the model was also altered by reducing the radius of filleted edges. Ideally, the model should not have been altered in any way other than the use of smaller, on average, elements. However, stress concentration factors generally increase with sharper edges. Since the objective of the finite element modeling process was to ensure maximum von Mises stress was less than the yield strength of the material, the observed reduction in maximum von Mises stress with decreased element size (and edge radius) suggests that the design is acceptable.

6.4.2 Quasi-Static Component Characterization

The quasi-static component characterization process included five loading cycles of each engine mount since it was relatively easy to complete such a testing procedure. For the current application this data may not be particularly useful but a single loading and unloading cycle may be relevant for crashworthiness performance. The data for a larger

number of cycles may, however, be valuable considering the loading cycles due to normal use. It is interesting to observe that after one loading cycle the remaining loading cycles are essentially identical. A second characterization of specimen #1 did not reveal significant variation between the first and second cycles which may indicate that the material was damaged due to the relatively large strains during the first cycle.

If the variation between cycles was due to a Mullin's effect it was expected that the variation between the first and second cycles would have been observed. However, the time between the repeated tests of a specimen may not have been sufficient for complete material recovery. Another significant observation was the clearly identifiable hysteresis. In an informal discussion with Lorenzo Peroni at the DYNLab at the PdT in Vercelli this researcher indicated that the hysteresis may be indicative of a moderately strain rate sensitive material. This is an interesting hypothesis since very little strain rate sensitivity was observed with the material characterization completed by AXEL Products Physical Testing Services.

6.4.3 Dynamic Component Characterization

The essentially identical displacement profiles but variation in force (Figure 104) may be associated with unnoticed changes of the initial gap shown in Figure 36. This hypothesis was generated considering the variation in the time at which a non-zero load was registered by the load cell. The significant variation between the characterizations of specimen #5 may have been the result of human error: improper usage of the DARTEC software resulted in a significant error in the initial position of the hydraulic cylinder.

6.5 Finite Element Model Validation

6.5.1 Quasi-static component characterization model validation

With minor alterations to some models the force-displacement responses of the finite element models of the Chrysler engine mount were very accurate as quantified with the Oberkampf-Trucano error metric. It may have been very valuable to obtain force-displacement data at larger displacements to better assess contact between internal regions of the rubber of the engine mount. An interesting observation was that the use of significant time scaling, thereby significantly increasing the loading rate, did yield a significant increase in stiffness even though the material model considered strain rate sensitivity. This may be the result of the relatively small increase in stiffness observed in the material characterization completed by AXEL. An analysis of kinetic, total, and internal energy, shown in Figure 113, confirmed that kinetic energy was very low and a quasi-static loading was modeled.

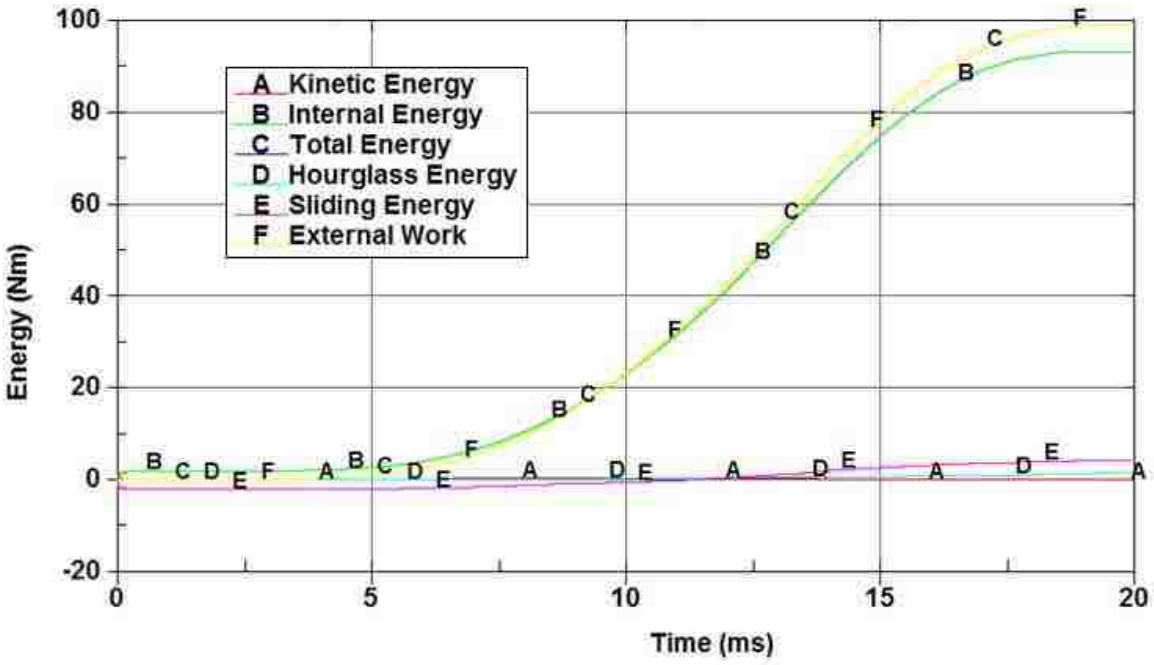

Figure 113: Energy balance, model of quasi-static component characterization, significant time scaling.

6.5.2 Dynamic component characterization model validation

Dynamic loading of the engine mount was accurately modeled. However, the transition to unloading and unloading process was much less accurate. It was expected that the unloading process would not be modeled with great accuracy since the material model did not account for hysteresis effects. Stress-strain data for uniaxial unloading processes would have allowed the hysteresis modeling capabilities of MAT 183 to be investigated. Another option may be to use the damping coefficient parameter. An iterative process may allow this modeling parameter to be determined.

Chapter 7: Conclusions

7.1 Quasi-Static Material Characterization

Material characterization processes for the purposes of developing finite element models can depend upon the type of material, the finite element software, the material model, loading condition, and the application, in this case crashworthiness. Quasi-static material characterization for this research was completed consistent with the recommended process of AXEL Products Physical Testing Services. The material model to be used was unspecified, identifying an optimal material model was an objective. While some models are able to use simple tension, simple compression, planar shear, and equibiaxial tension data rather directly some material models may only use a portion of this data set. However, additional data may be used to provide a valuable assessment of the capabilities of the model.

Material characterization was completed in two separate laboratories (SHPB testing at the PdT in Vercelli not included). Ideally, there would be overlap between the data obtained from each lab which would allow comparison of data from the different sources. This would provide a strong assurance that high quality data had been obtained. It may also be useful for the laboratories so they might consider the procedures they employ. Unfortunately, material characterization was not completed in sufficient detail to allow such validation of collected data or to be particularly useful for the laboratories. Simple tension and simple compression characterization processes were completed at both the FIAT Mirafiori polymer laboratory and by AXEL Products Physical Testing Services. There was excellent correlation between simple tension data from both laboratories. However, there was variation in the simple compression data. The data from AXEL was used since the simple compression data was consistent with a transformation of the radial stress-strain data from equibiaxial tension material characterization.

7.2 Dynamic Material Characterization

Dynamic material characterization was completed by AXEL Products Physical Testing Services. The dynamic material characterization completed by AXEL consisted of simple tension and simple compression material characterization processes completed at elevated loading rates with the specimen geometry modified to provide further control over the strain rate. The SHPB may be a better apparatus for studying strain rate sensitivity. Some of the data from AXEL may support this, for some data sets very high stiffness was observed at low strain rates.

7.3 Finite Element Modeling of Quasi-Static Material Characterization

Finite element models of quasi-static material characterization processes were developed to assess hyperelastic material models available in LS-DYNA and ensure proper user input of data and parameters. Two material models were investigated: MAT 77O (Ogden strain energy function) and MAT 181 (Simple Rubber/Foam). The Ogden strain energy function is of a general format which can be simplified to yield other models including Mooney-Rivlin type strain energy functions. MAT 77O allows the user to provide a uniaxial stress-strain curve and automatically determines the parameters of the strain energy function or allows these parameters to be input directly. The latter course of action may be superior since the coefficients can be determined for a set of material characterization data which may include planar tension (pure shear) and equibiaxial tension stress-strain data. MAT 181 only accepts a uniaxial stress-strain curve as input but can replicate this response with minimal error by piecemeal curve fitting. MAT 181 is also capable of modeling strain rate sensitivity, material failure, and hysteresis.

The internal (to the LS-DYNA solver) curve fitting of MAT 77O was not utilized extensively. A MATLAB/Octave program was developed to determine Ogden strain energy function parameters from a given set of data. As a concomitant method the finite element preprocessor Mentat (associated with the FE solver MARC) was also used to find Ogden model parameters. Mentat was unable to determine coefficients if restricted to finding positive coefficients and if it was specified that unknown mathematical analyses were to be completed (and produce acceptable results). The MATLAB/Octave

script was advantageous in that it would always identify coefficients although the result was not always highly accurate. Additionally, it should be considered that the accuracy of the curve fitting becomes an upper limit on the accuracy of the model. A coarse discretization could further reduce the accuracy.

Models were developed for the simple tension, simple compression, planar tension (pure shear), and equibiaxial tension material characterization processes with two versions of each model: one using MAT 77O and the other using MAT 181. These models yielded a great number of important observations which are summarized in Table 23 through Table 34 which are collectively presented in Appendix D. In Appendix D the results are arranged by the magnitude of the validation metric. It may be noted that every model with a validation metric in excess of 0.95 (maximum of 1) uses MAT 181. MAT 181 was, however, fairly computationally expensive (only 20% of models with a CPU time of less than 1 minute employed MAT 181, see Appendix E in which the results are sorted by CPU time). However, if only a small portion of a full vehicle model, as an example, consists of components requiring a hyperelastic material model the relative computational cost between these two material models may not be especially important. Another critical observation was the relative stability of MAT 181. For many models solely changing the material model from MAT 181 to MAT 77O resulted in a termination due to an error (e.g. negative speed of sound or out of bound velocity) at a rather high level of deformation of the mesh.

Other conclusions include: with MAT 77O the selectively reduced integration tetrahedron element formulation 4 performed very poorly. This element formulation did not exhibit any particular problems with MAT 181. However, element formulation 10 (one point integration tetrahedron) performed poorly in some cases with MAT 181. This was not entirely unexpected. There exists an alternative element formulation (formulation 13) which is essentially identical to 10 but designed for near incompressible materials. The use of this formulation in place of 10 yielded an improved performance of MAT 181. For hexahedron elements formulation 3 (fully integrated) should not be used with incompressible materials since the element will lock up in constant volume bending

modes. Hourglassing was also found to be problematic with under-integrated hexahedron elements (formulation 1) in compression.

One of the most important findings may be that the advantages of MAT 181 may simplify the experimental material characterization that should be completed. If this material can only accept uniaxial stress-strain (or force-displacement) data any additional data is not necessary (although it can be beneficial for model validation). With sufficient experience with this model it might be found that the tabulated Ogden model implementation is a reasonable representation for hyperelastic materials under other loading conditions.

7.4 Finite Element Modeling of the Chrysler Engine Mount

Finite element models of the Chrysler engine mount were initially developed prior to obtaining material stress-strain data. A preliminary estimate of the stress-strain behaviour data was provided by Chrysler engineers as well as CAD data and a preliminary finite element mesh. Finite element meshes were built using the Altair Hyperworks package Hypermesh. Several models were developed with different average element sizes and element types. The first models developed used solid hexahedron or tetrahedron elements. Tetrahedron elements were advantageous in that meshing could be automated and fewer geometrical simplifications were required. However, for a given volume and average mesh edge length a greater number of tetrahedron elements are generally required which may increase computational cost. LS-DYNA tetrahedron element formulations 4 and 10 were found to be significantly stiffer than element formulation 13 with material model MAT 181.

Several meshes were developed using hexahedron elements with different densities with varying average element edge lengths. One of the first meshes used elements with 1 mm average element edge lengths. A progressive coarsening of the mesh did not yield any significant changes in the stiffness of the model until the average element edge length increased to 4 mm. However, a mesh this coarse required shell elements to model regions with rubber of a thickness of approximately 1 mm. Shell elements were required to

eliminate this dimension as a constraint on the explicit time integration critical time step. Local refinements to the mesh were also necessary to accurately model contact internally within the engine mount between different regions of the rubber at large levels of deformation.

Investigations of other modeling parameter/techniques were completed using the engine mount models and yielded important observations. Hourglass control type 7 was found to minimize hourglass energy with element formulation 1. Additionally, small hourglass control coefficients yielded minimal hourglass energy and internal energy for a given level of deformation. This may indicate that the stiffness of the structure decreased with decreasing hourglass control coefficients. This is a surprising result since it seems to indicate that less hourglass control better controlled hourglassing and avoided excessive artificial stiffening of the structure. Further investigation of this topic may be worthwhile. Another important observation was the significant variation in stiffness of the model when different releases of the LS-DYNA solver were used with specific model parameters. The material model may be a critical factor. LS-DYNA solver release R3.2.1 (v971) did not yield any unexpected significant increases in stiffness. However, release 5.1.1 (MPP solvers on a FIAT computing cluster were used) yielded erroneous increases in stiffness with MAT 181 and element formulations 2 and 3.

7.5 Component Characterization

Quasi-static and dynamic component characterization was completed in the DYNLab at the PdT campus in Vercelli, Italy under the supervision of Lorenzo Peroni. A fixture was designed using an implicit LS-DYNA solver to adapt the Chrysler engine mount to equipment in this laboratory. Quasi-static force-displacement data for 5 loading and unloading cycles was acquired as well as a single dynamic loading and unloading cycle. A significant Mullin's effect was not observed. A reduction in force from the first to the second cycle was observed but further cycles did not yield a reduced load.

7.6 Validation of Finite Element Models of the Chrysler Engine Mount

A finite element model of the Chrysler engine mount, including steel brackets, was developed from earlier models and validated with respect to the data from component characterization in the DYNLab at the PdT Vercelli campus. The quasi-static force displacement response of the finite element model was very accurate (Oberkampf-Trucano validation metric of 0.9675 for tensile loading and 0.9070 for compressive loading) with only minor revisions to the model, the most significant of which was the removal of tied contact and replacement with merged nodes. Unloading behaviour was not investigated since the material model was not specified to be capable of modeling this phenomenon. The loading behaviour of the model under dynamic conditions was accurate but a significant improvement may be possible at large levels of deformation and for unloading. Investigations of these topics may continue.

References

ASTM International. (2008). ASTM D3767 - 03(2008) Standard Practice for Rubber—Measurement of Dimensions. West Conshohocken, PA.

ASTM International. (2009). ASTM D412 - 06ae2 Standard Test Methods for Vulcanized Rubber and Thermoplastic Elastomers—Tension. West Conshohocken, PA.

ASTM International. (2010). ASTM D3183 - 10 Standard Practice for Rubber—Preparation of Pieces for Test Purposes from Products. West Conshohocken, PA.

ASTM International. (2012). ASTM D575 - 91(2012) Standard Test Methods for Rubber Properties in Compression. West Conshohocken, PA.

Bancroft. (1941). The velocity of Longitudinal Waves in Cylindrical Bars. *Physical Review, 59*(59), 588-593.

CDC. (2010). *Web-based injury statistics query and reporting system*. Retrieved July 18, 2011, from CDC: http://www.cdc.gov/injury/wisqars

CDC. (2011). *Injury prevention & control: motor vehicle safety*. Retrieved July 18, 2011, from CDC: http://www.cdc.gov/Motorvehiclesafety/statecosts/index.html

CDC. (2011). Nonfatal, motor vehicle-occupant injuries (2009) and seat belt use (2008) among adults - United States. *Vital Signs, 59*.

Charlton D, Y. J. (1993). A review of methods to characterize rubber elastic behaviour for use in finite element analysis. *Rubber Chemistry and Technology, 67*, 481-503.

Chen J, W. C. (1997). On computational issues in large deformation analysis of rubber bushings. *Mechanics of Structures and Machines, 25*(3), 287-309.

Chen R, H. S. (2009). A modified Kolsky bar system for testing ultrasoft materials under intermediate strain rates. *Review of Scientific Instruments, 80*.

Chen W, L. F. (2002, May). Dynamic Compression Testing of Soft Materials. *ASME Transactions: Journal of Applied Mechanics, 69*, 214-223.

Chen W, Z. B. (1999, June). A Split Hopkinson Bar Technique for Low-impedance Materials. *Experimental Mechanics, 39*(2), 81-85.

Chen Y, T. T. (2003). Dynamic Testing and CAE Modeling of Engine Mounts and the Application in Vehicle Crash Analysis. *SAE World Congress.* Detroit, Michigan: SAE Technical Paper Series.

Chen Y, T. T. (2003). Dynamic Testing and CAE Modeling of Body Mount - An Application in the Frontal Impact Analysis of a Body-on-Frame Vehicle. *SAE World Congress.* Detroit, Michigan: SAE Technical Paper Series.

Cook, R. (1995). *Finite Element Modeling for Stress Analysis.* New York, NY: John Wiley & Sons Inc.

Davies, R. (1948). A critical study of the Hopkinson pressure bar. *Phil. Trans. A., 240*, 375-457.

Day JR, M. K. (2000). Equibiaxial Stretching of Elastomeric Sheets, An Analytical Verification of Experimental Technique. *ABAQUS 2000 User's Conference Proceedings.* Newport, Rhode Island.

Dharwadkar N, A. K. (2011). *Modelling of Engine Suspension Components for Crash Simulations.* Göteborg, Sweden: Department of Applied Mechanics, Division of Vehicle Safety, Chalmers University of Technology.

Dick, J. (2001). *Rubber Technology, Compounding and Testing for Performance.* Munich: Carl Hanser Verlag.

Duffy J, C. J. (1971). On the Use of a Torsional Split Hopkinson Bar to Study Rate Effects in 1100-0 Aluminum. *ASME Transactions: Journal of Applied Mechanics, 37*, 83-91.

Eguia M, H. M. (2005). Impact Testing of Lower Control Arm for Crashworthiness Simulation. *2005 SAE World Congress, Advances in Modeling and Testing of Materials and Vehicle Structures for Crash Safety Applications.* Detroit, Michigan: SAE Technical Paper Series.

Eguia M, T. T. (2006). Impact Testing of Bushings for Crashworthiness Simulation. *2006 SAE World Congress: Modeling Testing & Design of Materials Dummies & Structures for Crash Safety Applications.* Detroit, Michigan: SAE Technical Paper Series.

Finney R, K. A. (1988). Development of material constants for nonlinear finite-element analysis. *Rubber Chemistry & Technology, 61*, 879-891.

Genta G, M. L. (2009). *The Automotive Chassis, Volume 2: System Design.* Berlin: Springer Science+Business Media.

Hallquist, J. (2006). *LS-DYNA Theory Manual.* Livermore, California: LSTC.

Hauser, F. (1966). Technique for measuring stress-strain relations at high strain rates. *Experimental Mechanics, 6*(8), 395-402.

Hock L, B. S. (1926). *Kautschuk, 2*, 130.

Holt, W. (1931). Behaviour of Rubber under Repeated Stresses. *Industrial & engineering chemistry, 23*(12), 1471-1475.

Hopkinson, B. (1914). A method of measuring the pressure produced in the detonation of high explosives or by the impact of bullets. *Philosophical Transactions of the Royal Society of London. Series A, Containing Papers of a Mathematical or Physical Character, 213*, 437-456.

Huang M, E. M. (2005). Crashworthiness Simulation of Lower Control Arm Impact Tests. *SAE World Congress: Advances in Modeling and Testing of Materials and Vehicle Structures for Crash Safety Applications.* Detroit, Michigan: SAE Technical Paper Series.

Kadlowec J, W. A. (2003). Elastomer bushing response: experiments and finite element modeling. *Acta Mechanica, 163*, 25-38.

Kolling S, D. P. (2005). A Simplified Rubber Model with Damage. *LS-DYNA Anwenderforum, Crash II* (pp. BII-1 - BII-10). Bamberg: Dynamore GmbH.

Kolsky, H. (1949). An investigation of the mechanical properties of materials at very high rates of loading. *Proc. Phys. Soc. (London), B62*, 676-700.

Koppel S, C. J. (2008). How important is vehicle safety in the new vehicle purchase process? *Accident Analysis and Prevention, 40*, 994-1004.

Li M, C. Y. (2005). Testing and Modeling of Mounts for Improved Safet Design and Crashworthiness Analysis. *SAE World Congree: Safety Test Methodology and Structural Crashworthiness.* Detroit, Michigan: SAE Technical Paper Series.

LSTC. (2007). *LS-DYNA Keyword User's Manual.* Livermore, California: Livermore Software Technology Corporation (LSTC).

MasterHD. (2008, April 26). *File:Resonance.PNG*. Retrieved December 28, 2012, from Wikipedia: http://commons.wikimedia.org/wiki/File:Resonance.PNG

McMaster-Carr. (n.d.). *Steel Angle Bars*. Retrieved September 4, 2012, from McMaster-Carr: http://www.mcmaster.com/#steel-angle-bars/=j2ne51

Mooney, M. (1940). A Theory of Large Elastic Deformation. *Journal of Applied Physics, 11*(9), 582-591.

Morello L, R. L. (2011). *The Automotive Body, Volume II: System Design.* Dordrecht Heidelberg London New York: Springer Science + Business Media.

Morman K, P. T. (1988). Application of finite-element analysis in the design of automotive elastomeric components. *Rubber Chemistry & Technology, 61*, 503-533.

Mullins, L. (1969). Softening of rubber by deformation. *Rubber Chemistry & Technology, 42*(1), 339-362.

Nie X, S. B. (2009). Dynamic Tensile Testing of Soft Materials. *Experimental Mechanics, 49*, 451-458.

Oberkampf W, T. T. (2002). Verification and validation in computational fluid dynamics. *Progress in Aerospace Sciences*, 209-272.

Park S, K. M. (2004). FE modeling and validation of vehicle rubber mount preloading and impact response. *International LS-DYNA Users Conference* (pp. 23-32). LSTC.

Reddy, J. (1993). *An Introduction to the Finite Element Method.* Boston MA: McGraw Hill.

Rivlin, R. (1956). Chapter 10. In E. F, *Rheology* (Vol. 1, p. 351). New York: Academic Press.

Shaw M, Y. E. (1988). Rubber elasticity and fracture. *Journal of Engineering Materials and Technology, 110*, 258-265.

SMARTRISK. (2009). *The Economic Burden of Injury in Canada.* Toronto, ON: SMARTRISK.

Song B, G. Y. (2007). Radial Inertia Effects in Kolsky Bar Testing of Extra-soft Specimens. *Experimental Mechanics, 47*, 659-670.

Song B, S. C. (2008). A Long Split Hopkinson Pressure Bar (LSHPB) for Intermediate-rate Characterization of Soft Materials. *Experimental Mechanics, 48*, 809-815.

Treloar, L. (2009). *Physics of Rubber Elasticity.* Oxford: Clarendon Press.

Treloar, L. (2009). *Physics of Rubber Elasticity, Chapter 2: Internal Energy & Entropy Changes on Deformation.* Oxford: Clarendon Press.

Weinong W Chen, B. S. (2011). *Split Hopkinson (Kolsky) Bar: Design, Testing, and Applications.* New York: Springer.

WHO. (2004). *World report on road traffic injury prevention - summary.* Geneva: World Health Organization.

WHO. (2011). *United Nations road safety collaboration*. Retrieved July 18, 2011, from WHO: http://www.who.int/roadsafety/en/

Yeoh, O. (1990). Characterization of elastic properties of carbon black filled rubber vulcanizates. *Rubber Chemistry and Technology, 63*, 792-805.

Zhao H, G. G. (1997). On the use of a viscoelastic split Hopkinson pressure bar. *International Journal of Impact Engineering, 19*(4), 319-330.

Appendix A

MATLAB/Octave script to compute Oberkampf-Trucano error metric for LS-DYNA model of ASTM D412 simple tension material characterization process

Line wrapping may need to be corrected if this script is copied to be used in Octave.

```
% read in material stress strain curve
mat_data=dlmread('set2_tension.csv',',',1,0);

% plot material stress strain curve
figure(1)
plot(mat_data(:,1),mat_data(:,2))
title('Material stress strain curve, tensile specimen D412 #1')
xlabel('Strain (mm/mm)')
ylabel('Stress (GPa)')

% read in force and displacement data from LS-DYNA
force_LS-DYNA=dlmread('set2_force.csv',',',1,0);
force_LS-DYNA(:,2)=-force_LS-DYNA(:,2); % reference frame results in negative x-force for specimen in tension
disp_LS-DYNA=dlmread('set2_disp.csv',',',1,0);
disp2_LS-DYNA=dlmread('set2_disp2.csv',',',1,0);

% plot force over time
figure(2)
plot(force_LS-DYNA(:,1),force_LS-DYNA(:,2))
title('Force vs time, LS-DYNA')
xlabel('Time (ms)')
ylabel('Force (kN)')

% plot disp over time
figure(3)
plot(disp_LS-DYNA(:,1),disp_LS-DYNA(:,2),'r',disp2_LS-DYNA(:,1),disp2_LS-DYNA(:,2),'r')
title('Displacement of two neighbouring nodes vs time, LS-DYNA')
xlabel('Time (ms)')
ylabel('Displacement (mm)')
legend('Node 1','Node 2')

% calculate engineering stress from load from LS-DYNA bndout data
Stress_LS-DYNA=force_LS-DYNA(:,2)/(3*1.5); % stress in GPa
 % calculate engineering strain from LS-DYNA nodout data
```

```
L0=4.125; % initial length of LS-DYNA model in mm
Strain_LS-DYNA=abs(disp_LS-DYNA(:,2)-disp2_LS-DYNA(:,2))/L0; % (mm/mm)

% plot stress-strain curves
figure(4)
plot(mat_data(:,1),mat_data(:,2),'g',Strain_LS-DYNA,Stress_LS-DYNA,'--r')
title('Stress-strain curves')
xlabel('Strain (mm/mm)')
ylabel('Stress (GPa)')
legend('Material data','LS-DYNA ASTM D412 Type D model')

% interpolate LS-DYNA data to obtain equal number of data points
Stress_LS-DYNA_int=interp1(Strain_LS-DYNA,Stress_LS-
DYNA,mat_data(:,1),'extrap');

% plot interpolated data
figure(5)
plot(mat_data(:,1),mat_data(:,2),'g',mat_data(:,1),Stress_LS-DYNA_int,'--r')
title('Stress-strain curves')
xlabel('Strain (mm/mm)')
ylabel('Stress (GPa)')
legend('Material data','LS-DYNA ASTM D412 Type D model')

% calculate Oberkampf-Trucano metric
for i=1:length(mat_data(:,2))
   if mat_data(i,2)==0
      if i>(length(mat_data)-3)
      mat_data(i,2)=(mat_data(i-1,2)+mat_data(i-2,2))/2;
      else
      mat_data(i,2)=(mat_data(i+1,2)+mat_data(i+2,2))/2;
      end
   end
end
OTmetric=1-1/length(mat_data(:,1))*sum(tanh(abs((Stress_LS-DYNA_int-
mat_data(:,2))./mat_data(:,2))))

% compare element formulations 1, 2, and 3
Elform2SS=dlmread('Elform2StressStrain.txt');
Elform3SS=dlmread('Elform3StressStrain.txt');

figure(6)
plot(mat_data(:,1),mat_data(:,2),'r',mat_data(:,1),Stress_LS-DYNA_int,'--
g',Elform2SS(:,1),Elform2SS(:,2),'--b',Elform3SS(:,1),Elform3SS(:,2),'--k')
title('Stress-strain curves')
xlabel('Strain (mm/mm)')
ylabel('Stress (GPa)')
legend('Material data','LS-DYNA El. form. 1','LS-DYNA El. form. 2','LS-DYNA El.
form. 3')
```

Appendix B

MATLAB/Octave script to determine Ogden material model coefficients

```
close all
clear all

% This first section imports and plots AXEL data

% read in biaxial tension data
BT=dlmread('ChryslerC0EBT0.01Cleaned.txt');
BT(:,2)=BT(:,2)/1000; % convert MPa to GPa
BT2=BT(:,1)+1; % convert engineering strain to stretch ratio

% read in planar tension (pure shear) data
PT=dlmread('ChryslerC0EPT0.01Cleaned.txt');
PT(:,2)=PT(:,2)/1000; % convert MPa to GPa
PT2=PT(:,1)+1; % convert engineering strain to stretch ratio

% import AXEL simple tension results
ST=dlmread('set2_tension.csv');
ST2(:,1)=ST(:,1)+1; % convert strain to stretch ratio

% import simple compression AXEL data
SC=dlmread('set2_compression.csv');
SC2=SC(:,1)+1; % calculate stretch ratio from strain

% % plot biaxial tension and planar tension data
% figure(1)
% plot(BT(:,1),BT(:,2),'r',PT(:,1),PT(:,2),'g')
% title('Equibiaxial tension and planar tension test data from AXEL')
% xlabel('Strain')
% ylabel('Stress (MPa)')
% legend('Equibiaxial tension','Planar tension')
%
%
%%%%%%%%%%%%%%%%%%%%%%%%%%%%%%%%%%%%%%%%%%%%%%%%%%%%%%%%%%%%%%%
%
% % calculate strain energy density for planar tension
SED_PT=cumtrapz(PT(:,1),PT(:,2));
% % In planar tension along the axis of loading there is stress and strain
% % For the other two orthogonal axes, for one there is stress but no strain
% % For the other there is strain but no stress
% % An integral of the loading axis stress strain curve is therefore the
% % strain energy density?
%
% % plot strain energy density vs strain for planar tension
% figure(2)
% plot(PT(:,1),SED_PT)
% title('Strain energy density for planar tension')
% xlabel('Strain')
```

```
% ylabel('Strain energy density')
%
%%%%%%%%%%%%%%%%%%%%%%%%%%%%%%%%%%%%%%%%%%%%%%%%%%%%%%%
%
% % Pure shear (planar tension) data was imported into MARC and coefficients
% % for the Ogden material model (4 terms) was found
%
% % MARC-Mentat Ogden model (only planar shear data)
% mu1=7.74217E-10;
% mu2=0.00115883;
% mu3=1.25757E-5;
% mu4=2.86218E-10;
% alpha1=2.29459;
% alpha2=3.32686;
% alpha3=2.35069;
% alpha4=3.61581;
lambda=PT(:,1)+1;
%
% % calculate the strain energy density for these coefficients to compare to
% % the cumulative integral of the AXEL data
%
% SED_MARC=mu1/alpha1*(lambda.^alpha1+lambda.^-alpha1-
2)+mu2/alpha2*(lambda.^alpha2+lambda.^-alpha2-2)+...
% mu3/alpha3*(lambda.^alpha3+lambda.^-alpha3-2)+mu4/alpha4*(lambda.^alpha4+lambda.^-alpha4-2);
%
%
% % plot cumulative integral of AXEL pure shear stress strain data and Ogden strain energy function with
MARC
% % coefficients
% % plot MATLAB-MARC Ogden model
% figure(3)
% subplot(2,1,1)
% plot(PT(:,1),SED_PT,'r',PT(:,1),SED_MARC,'g')
% title('Strain energy density - Ogden model')
% xlabel('Strain')
% ylabel('Strain energy density')
% legend('Integral of stress-strain curve (AXEL planar shear)','Ogden model computed in Matlab with
MARC coefficients (AXEL data)')
%
% % calculate stress with publication formula using the MARC coefficients
% Stress=mu1*((PT(:,1)+1).^(alpha1-1)-(PT(:,1)+1).^(-1-alpha1))+mu2*((PT(:,1)+1).^(alpha2-1)-
(PT(:,1)+1).^(-1-alpha2))+...
% mu3*((PT(:,1)+1).^(alpha3-1)-(PT(:,1)+1).^(-1-alpha3))+mu4*((PT(:,1)+1).^(alpha4-1)-(PT(:,1)+1).^(-
1-alpha4));
%
% % plot this calculated stress over strain and the AXEL pure shear stress
% % strain curve
% subplot(2,1,2)
% plot(PT(:,1),PT(:,2),'r',PT(:,1),Stress,'g')
% title('Stress strain curve')
% xlabel('Strain')
% ylabel('Stress')
% legend('AXEL data','Ogden model, coefficients from MARC')

%%%%%%%%%%%%%%%%%%%%%%%%%%%%%%%%%%%%%%%%%%%%%%%%%%%%%%%
%%%%%%%%%%%%%%%%%%%%%%%%%%%%%%%%%%%%%%%%%%%%%%%%%%%%%%%
```

```
%%%%%%%%%%%%%%%%%%%%%%%%%%%%%%%%%%%%%%%%%%%%%%%%%%%%%%%

% % Use a Matlab optimization function to find Ogden coefficients for pure
% % shear data (to avoid using MARC)
%
% % Initialize coeff vector for finding Ogden coeff.
% coeffGuess=1.0*[0.001 0.001 0.001 0.001 1 1 1 1]; % initial guess
% [goodcoeff FVEC]=fminsearch(@Ogden4th,coeffGuess)
%
% % Matlab/Octave solution - pure shear
% StressOctave=goodcoeff(1)*((PT(:,1)+1).^(goodcoeff(5)-1)-(PT(:,1)+1).^(-1-
goodcoeff(5)))+goodcoeff(2)*((PT(:,1)+1).^(goodcoeff(6)-1)-(PT(:,1)+1).^(-1-goodcoeff(6)))+...
% goodcoeff(3)*((PT(:,1)+1).^(goodcoeff(7)-1)-(PT(:,1)+1).^(-1-
goodcoeff(7)))+goodcoeff(4)*((PT(:,1)+1).^(goodcoeff(8)-1)-(PT(:,1)+1).^(-1-goodcoeff(8)));
%
% % plot Ogden (Matlab curve fit) to input data
% figure(4)
% plot(PT(:,1),PT(:,2),'r',PT(:,1),StressOctave,'g')
% title('Stress strain curve')
% xlabel('Strain')
% ylabel('Stress')
% legend('AXEL data','Ogden model, coefficients from Matlab')

%%%%%%%%%%%%%%%%%%%%%%%%%%%%%%%%%%%%%%%%%%%%%%%%%%%%%%%
%%%%%%%%%%%%%%%%%%%%%%%%%%%%%%%%%%%%%%%%%%%%%%%%%%%%%%%
%%%%%%%%%%%%%%%%%%%%%%%%%%%%%%%%%%%%%%%%%%%%%%%%%%%%%%%

% Input all AXEL data to MARC and find best fit for Ogden model
% coefficients

% MARC-Mentat Ogden model (all data: uniaxial, shear, biaxial)
mu1_2=0.00123168;
mu2_2=2.95657E-6;
mu3_2=8.77739E-5;
mu4_2=0.000230026;
alpha1_2=1.76178;
alpha2_2=2.20847;
alpha3_2=4.57289;
alpha4_2=2.45609;

% Calculate strain energy density
SED_MARC_2=mu1_2/alpha1_2*(lambda.^alpha1_2+lambda.^-alpha1_2-
2)+mu2_2/alpha2_2*(lambda.^alpha2_2+lambda.^-alpha2_2-2)+...
mu3_2/alpha3_2*(lambda.^alpha3_2+lambda.^-alpha3_2-
2)+mu4_2/alpha4_2*(lambda.^alpha4_2+lambda.^-alpha4_2-2);

% Calculate stress for pure shear test
Stress_2=mu1_2*((PT(:,1)+1).^(alpha1_2-1)-(PT(:,1)+1).^(-1-
alpha1_2))+mu2_2*((PT(:,1)+1).^(alpha2_2-1)-(PT(:,1)+1).^(-1-alpha2_2))+...
mu3_2*((PT(:,1)+1).^(alpha3_2-1)-(PT(:,1)+1).^(-1-alpha3_2))+mu4_2*((PT(:,1)+1).^(alpha4_2-1)-
(PT(:,1)+1).^(-1-alpha4_2));

% plot MATLAB-MARC Ogden model (plot strain energy density for pure shear)
figure(5)
```

```
subplot(3,2,1)
plot(PT(:,1),SED_PT,'r',PT(:,1),SED_MARC_2,'g')
title('Strain energy density - Ogden model')
xlabel('Strain')
ylabel('Strain energy density')
legend('Integral of stress-strain curve (AXEL planar shear)','Ogden model computed in Matlab with MARC
coefficients (AXEL data)')

% plot Ogden (MARC curve fit) to input data
% compare AXEL stress to stress derived from Ogden model with MARC best fit
% coefficients for all AXEL data
subplot(3,2,2)
plot(PT(:,1),PT(:,2),'r',PT(:,1),Stress_2,'g')
title('Pure shear stress-strain curve')
xlabel('Strain')
ylabel('Stress')
legend('AXEL data','Ogden model, coefficients from MARC')

% calculate simple tension response of MARC curve fit
Stress_tensile=mu1_2*(ST2(:,1).^(alpha1_2-1)-ST2(:,1).^-
(1+0.5*alpha1_2))+mu2_2*(ST2(:,1).^(alpha2_2-1)-ST2(:,1).^-(1+0.5*alpha2_2))+...
mu3_2*(ST2(:,1).^(alpha3_2-1)-ST2(:,1).^-(1+0.5*alpha3_2))+mu4_2*(ST2(:,1).^(alpha4_2-1)-
ST2(:,1).^-(1+0.5*alpha4_2));

% plot AXEL tensile data and MARC Ogden curve fit
subplot(3,2,3)
plot(ST(:,1),ST(:,2),'r',ST(:,1),Stress_tensile,'g')
title('Comparison - AXEL simple tension and Ogden curve fit')
xlabel('Strain')
ylabel('Stress (GPa)')
legend('AXEL simple tension','4 term Ogden model')

% calculate simple compression for Ogden model
Stress_compression=mu1_2*(SC2(:,1).^(alpha1_2-1)-SC2(:,1).^-
(1+0.5*alpha1_2))+mu2_2*(SC2(:,1).^(alpha2_2-1)-SC2(:,1).^-(1+0.5*alpha2_2))+...
mu3_2*(SC2(:,1).^(alpha3_2-1)-SC2(:,1).^-(1+0.5*alpha3_2))+mu4_2*(SC2(:,1).^(alpha4_2-1)-
SC2(:,1).^-(1+0.5*alpha4_2));

% plot and compare simple compression
subplot(3,2,4)
plot(SC(:,1),SC(:,2),'r',SC(:,1),Stress_compression,'g')
title('Simple compression comparison, AXEL and Ogden model')
xlabel('Engineering strain')
ylabel('Engineering stress (GPa)')
legend('AXEL data (0.01 1/s)','Ogden model, 4 terms')

% import biaxial tension AXEL data
BT=dlmread('ChryslerC0EBT0.01Cleaned.txt');
BT2=BT(:,1)+1; % calculate stretch ratio from engineering strain
BT(:,2)=BT(:,2)/1000; % convert MPa to GPa

% calculate radial stress-strain from Ogden coefficients
Radial_stress=mu1_2*(BT2.^(alpha1_2-1)-BT2.^-(1+2*alpha1_2))+mu2_2*(BT2.^(alpha2_2-1)-BT2.^-
(1+2*alpha2_2))+...
```

```
mu3_2*(BT2.^(alpha3_2-1)-BT2.^-(1+2*alpha3_2))+mu3_2*(BT2.^(alpha3_2-1)-BT2.^-(1+2*alpha3_2));

% plot to compare AXEL biaxial stress-strain and Ogden curve fit derived stress-strain
subplot(3,2,5)
plot(BT(:,1),BT(:,2),'r',BT(:,1),Radial_stress,'g')
title('Radial stress-strain, AXEL experimental and Ogden model')
xlabel('Engineering strain')
ylabel('Engineering stress (GPa)')
legend('AXEL data','Equibiaxial tension - 4 term Ogden model')

% OT metric for simple tension
for i=1:length(ST(:,2))
   if ST(i,2)==0
      if i>(length(ST)-3)
      ST(i,2)=(ST(i-1,2)+ST(i-2,2))/2;
      else
      ST(i,2)=(ST(i+1,2)+ST(i+2,2))/2;
      end
   end
end
OTmetric_simple_tension_4=1-1/length(ST(:,2))*sum(tanh(abs((Stress_tensile-ST(:,2))./ST(:,2))))

% OT metric for simple compression
for i=1:length(SC(:,2))
   if SC(i,2)==0
      if i>(length(SC)-3)
      SC(i,2)=(SC(i-1,2)+SC(i-2,2))/2;
      else
      SC(i,2)=(SC(i+1,2)+SC(i+2,2))/2;
      end
   end
end
OTmetric_simple_compression_4=1-1/length(SC(:,2))*sum(tanh(abs((Stress_compression-
SC(:,2))./SC(:,2))))

% OT metric for planar tension (pure shear)
for i=1:length(PT(:,2))
   if PT(i,2)==0
      if i>(length(PT)-3)
      PT(i,2)=(PT(i-1,2)+PT(i-2,2))/2;
      else
      PT(i,2)=(PT(i+1,2)+PT(i+2,2))/2;
      end
   end
end
OTmetric_pure_shear_4=1-1/length(PT(:,2))*sum(tanh(abs((Stress_2-PT(:,2))./PT(:,2))))

% OT metric for equibiaxial tension
for i=1:length(BT(:,2))
   if BT(i,2)==0
      if i>(length(BT)-3)
      BT(i,2)=(BT(i-1,2)+BT(i-2,2))/2;
      else
      BT(i,2)=(BT(i+1,2)+BT(i+2,2))/2;
      end
```

```
    end
end
OTmetric_equibiaxial_tension_4=1-1/length(BT(:,2))*sum(tanh(abs((Radial_stress-BT(:,2))./BT(:,2))))

%%%%%%%%%%%%%%%%%%%%%%%%%%%%%%%%%%%%%%%%%%%%%%%%%%%%%%%%%%%%%%%%%%%%%%%%%%%%
%%%%%%%%%%%%%%%%%%%%%%%%%%%%%%%%%%%%%%%%%%%%%%%%%%%%%%%%%%%%%%%%%%%%%%%%%%%%

% 6 term Ogden model fit to all AXEL data (using MARC)
mu1_3=0.000222631;
mu2_3=0.000199656;
mu3_3=6.38978E-5;
mu4_3=0.000294451;
mu5_3=0.000143757;
mu6_3=0.000719426;
alpha1_3=1.96928;
alpha2_3=1.13113;
alpha3_3=3.13473;
alpha4_3=2.1394;
alpha5_3=4.20627;
alpha6_3=1.32728;

% pure shear stress
Stress_shear_6=mu1_3*((PT(:,1)+1).^(alpha1_3-1)-(PT(:,1)+1).^(-1-
alpha1_3))+mu2_3*((PT(:,1)+1).^(alpha2_3-1)-(PT(:,1)+1).^(-1-alpha2_3))+...
mu3_3*((PT(:,1)+1).^(alpha3_3-1)-(PT(:,1)+1).^(-1-alpha3_3))+mu4_3*((PT(:,1)+1).^(alpha4_3-1)-
(PT(:,1)+1).^(-1-alpha4_3))+...
mu5_3*((PT(:,1)+1).^(alpha5_3-1)-(PT(:,1)+1).^(-1-alpha5_3))+mu6_3*((PT(:,1)+1).^(alpha6_3-1)-
(PT(:,1)+1).^(-1-alpha6_3));

% plot Ogden (MARC curve fit) to input data
figure(6)
subplot(2,2,1)
plot(PT(:,1),PT(:,2),'r',PT(:,1),Stress_shear_6,'g')
title('Pure shear stress-strain curve')
xlabel('Strain')
ylabel('Stress')
legend('AXEL data','6 term Ogden model')
grid on

% calculate simple tension response of MARC curve fit
Stress_tensile_6=mu1_3*(ST2(:,1).^(alpha1_3-1)-ST2(:,1).^-
(1+0.5*alpha1_3))+mu2_3*(ST2(:,1).^(alpha2_3-1)-ST2(:,1).^-(1+0.5*alpha2_3))+...
mu3_3*(ST2(:,1).^(alpha3_3-1)-ST2(:,1).^-(1+0.5*alpha3_3))+mu4_3*(ST2(:,1).^(alpha4_3-1)-
ST2(:,1).^-(1+0.5*alpha4_3))+...
mu5_3*(ST2(:,1).^(alpha5_3-1)-ST2(:,1).^-(1+0.5*alpha5_3))+mu6_3*(ST2(:,1).^(alpha6_3-1)-
ST2(:,1).^-(1+0.5*alpha6_3));

% plot AXEL tensile data and MARC Ogden curve fit
subplot(2,2,2)
plot(ST(:,1),ST(:,2),'r',ST(:,1),Stress_tensile_6,'g')
title('Comparison - AXEL simple tension and Ogden curve fit')
xlabel('Strain')
ylabel('Stress (GPa)')
legend('AXEL simple tension','6 term Ogden model')
grid on
```

```
% calculate simple compression for Ogden model
Stress_compression_6=mu1_3*(SC2(:,1).^(alpha1_3-1)-SC2(:,1).^-
(1+0.5*alpha1_3))+mu2_3*(SC2(:,1).^(alpha2_3-1)-SC2(:,1).^-(1+0.5*alpha2_3))+...
mu3_3*(SC2(:,1).^(alpha3_3-1)-SC2(:,1).^-(1+0.5*alpha3_3))+mu4_3*(SC2(:,1).^(alpha4_3-1)-
SC2(:,1).^-(1+0.5*alpha4_3))+...
mu5_3*(SC2(:,1).^(alpha5_3-1)-SC2(:,1).^-(1+0.5*alpha5_3))+mu6_3*(SC2(:,1).^(alpha6_3-1)-
SC2(:,1).^-(1+0.5*alpha6_3));

% plot and compare simple compression
subplot(2,2,3)
plot(SC(:,1),SC(:,2),'r',SC(:,1),Stress_compression_6,'g')
title('Simple compression comparison, AXEL and Ogden model')
xlabel('Engineering strain')
ylabel('Engineering stress (GPa)')
legend('AXEL data (0.01 1/s)','Ogden model, 6 terms')
grid on

% calculate radial stress-strain from Ogden coefficients
Radial_stress_6=mu1_3*(BT2.^(alpha1_3-1)-BT2.^-(1+2*alpha1_3))+mu2_3*(BT2.^(alpha2_3-1)-BT2.^-
(1+2*alpha2_3))+...
mu3_3*(BT2.^(alpha3_3-1)-BT2.^-(1+2*alpha3_3))+mu4_3*(BT2.^(alpha4_3-1)-BT2.^-
(1+2*alpha4_3))+...
mu5_3*(BT2.^(alpha5_3-1)-BT2.^-(1+2*alpha5_3))+mu6_3*(BT2.^(alpha6_3-1)-BT2.^-(1+2*alpha6_3));

% plot to compare AXEL biaxial stress-strain and Ogden curve fit derived stress-strain
subplot(2,2,4)
plot(BT(:,1),BT(:,2),'r',BT(:,1),Radial_stress_6,'g')
title('Radial stress-strain, AXEL experimental and Ogden model (6 terms)')
xlabel('Engineering strain')
ylabel('Engineering stress (GPa)')
legend('AXEL data','6 term Ogden model')
grid on

% OT metric for simple tension
for i=1:length(ST(:,2))
   if ST(i,2)==0
      if i>(length(ST)-3)
      ST(i,2)=(ST(i-1,2)+ST(i-2,2))/2;
      else
      ST(i,2)=(ST(i+1,2)+ST(i+2,2))/2;
      end
   end
end
OTmetric_simple_tension_6=1-1/length(ST(:,2))*sum(tanh(abs((Stress_tensile_6-ST(:,2))./ST(:,2))))

% OT metric for simple compression
for i=1:length(SC(:,2))
   if SC(i,2)==0
      if i>(length(SC)-3)
      SC(i,2)=(SC(i-1,2)+SC(i-2,2))/2;
      else
      SC(i,2)=(ST(i+1,2)+SC(i+2,2))/2;
      end
   end
```

```
end
OTmetric_simple_compression_6=1-1/length(SC(:,2))*sum(tanh(abs((Stress_compression_6-
SC(:,2))./SC(:,2))))

% OT metric for planar tension (pure shear)
for i=1:length(PT(:,2))
   if PT(i,2)==0
      if i>(length(PT)-3)
      PT(i,2)=(PT(i-1,2)+PT(i-2,2))/2;
      else
      PT(i,2)=(ST(i+1,2)+PT(i+2,2))/2;
      end
   end
end
OTmetric_pure_shear_6=1-1/length(PT(:,2))*sum(tanh(abs((Stress_shear_6-PT(:,2))./PT(:,2))))

% OT metric for equibiaxial tension
for i=1:length(BT(:,2))
   if BT(i,2)==0
      if i>(length(BT)-3)
      BT(i,2)=(BT(i-1,2)+BT(i-2,2))/2;
      else
      BT(i,2)=(BT(i+1,2)+BT(i+2,2))/2;
      end
   end
end
OTmetric_equibiaxial_tension_6=1-1/length(BT(:,2))*sum(tanh(abs((Radial_stress_6-BT(:,2))./BT(:,2))))

%%%%%%%%%%%%%%%%%%%%%%%%%%%%%%%%%%%%%%%%%%%%%%%%%%%%%%%%%%%%%%%%%%%%%%%%%%%%
%%%%%%%%%%%%%%%%%%%%%%%%%%%%%%%%%%%%%%%%%%%%%%%%%%%%%%%%%%%%%%%%%%%%%%%%%%%%
%%%%%%%%%%%%%%%%%%%%%%%%%%%%%%%%%%%%%%%%%%%%%%%%%%%%%%%%%%%%%%%%%%%%%%%%%%%%

% % Use a Matlab optimization function to find Ogden coefficients for all AXEL data (to avoid using
MARC)
%
% % Initialize coeff vector for finding Ogden coeff.
% coeffGuess8=1.0*[0.001 0.001 0.001 0.001 0.001 0.001 0.001 0.001 1 1 1 1 1 1 1 1]; % initial guess
% % coeffGuess8=goodcoeff8;
% options=optimset('MaxFunEvals',10^6,'MaxIter',10^6,'TolFun',0.001);
% [goodcoeff8 FVEC8 exitflag]=fminsearch(@(coeff)Ogden8th(coeff,PT,SC,ST,BT),coeffGuess8,options)
%
% mu1_5=goodcoeff8(1);
% mu2_5=goodcoeff8(2);
% mu3_5=goodcoeff8(3);
% mu4_5=goodcoeff8(4);
% mu5_5=goodcoeff8(5);
% mu6_5=goodcoeff8(6);
% mu7_5=goodcoeff8(7);
% mu8_5=goodcoeff8(8);
% alpha1_5=goodcoeff8(9);
% alpha2_5=goodcoeff8(10);
% alpha3_5=goodcoeff8(11);
% alpha4_5=goodcoeff8(12);
% alpha5_5=goodcoeff8(13);
% alpha6_5=goodcoeff8(14);
```

```
% alpha7_5=goodcoeff8(15);
% alpha8_5=goodcoeff8(16);
%
% % Matlab/Octave solution - pure shear
% StressOctave8=mu1_5*((PT(:,1)+1).^(alpha1_5-1)-(PT(:,1)+1).^(-1-
alpha1_5))+mu2_5*((PT(:,1)+1).^(alpha2_5-1)-(PT(:,1)+1).^(-1-alpha2_5))+...
% mu3_5*((PT(:,1)+1).^(alpha3_5-1)-(PT(:,1)+1).^(-1-alpha3_5))+mu4_5*((PT(:,1)+1).^(alpha4_5-1)-
(PT(:,1)+1).^(-1-alpha4_5))+...
% mu5_5*((PT(:,1)+1).^(alpha5_5-1)-(PT(:,1)+1).^(-1-alpha5_5))+mu6_5*((PT(:,1)+1).^(alpha6_5-1)-
(PT(:,1)+1).^(-1-alpha6_5))+...
% mu7_5*((PT(:,1)+1).^(alpha7_5-1)-(PT(:,1)+1).^(-1-alpha7_5))+mu8_5*((PT(:,1)+1).^(alpha8_5-1)-
(PT(:,1)+1).^(-1-alpha8_5));
%
% % Matlab Octave solution - simple tension
% Simple_tension8=mu1_5*(ST2.^(alpha1_5-1)-ST2.^-(1+0.5*alpha1_5))+mu2_5*(ST2.^(alpha2_5-1)-
ST2.^-(1+0.5*alpha2_5))+...
% mu3_5*(ST2.^(alpha3_5-1)-ST2.^-(1+0.5*alpha3_5))+mu4_5*(ST2.^(alpha4_5-1)-ST2.^-
(1+0.5*alpha4_5))+mu5_5*(ST2.^(alpha5_5-1)-ST2.^-(1+0.5*alpha5_5))+...
% mu6_5*(ST2.^(alpha6_5-1)-ST2.^-(1+0.5*alpha6_5))+mu7_5*(ST2.^(alpha7_5-1)-ST2.^-
(1+0.5*alpha7_5))+mu8_5*(ST2.^(alpha8_5-1)-ST2.^-(1+0.5*alpha8_5));
%
% % compute simple compression stress for Ogden model
% Simple_compression8=mu1_5*(SC2.^(alpha1_5-1)-SC2.^-
(1+0.5*alpha1_5))+mu2_5*(SC2.^(alpha2_5-1)-SC2.^-(1+0.5*alpha2_5))+...
% mu3_5*(SC2.^(alpha3_5-1)-SC2.^-(1+0.5*alpha3_5))+mu4_5*(SC2.^(alpha4_5-1)-SC2.^-
(1+0.5*alpha4_5))+mu5_5*(SC2.^(alpha5_5-1)-SC2.^-(1+0.5*alpha5_5))+...
% mu6_5*(SC2.^(alpha6_5-1)-SC2.^-(1+0.5*alpha6_5))+mu7_5*(SC2.^(alpha7_5-1)-SC2.^-
(1+0.5*alpha7_5))+mu8_5*(SC2.^(alpha8_5-1)-SC2.^-(1+0.5*alpha8_5));
%
% % calculate radial stress-strain from Ogden coefficients
% Radial_stress8=mu1_5*(BT2.^(alpha1_5-1)-BT2.^-(1+2*alpha1_5))+mu2_5*(BT2.^(alpha2_5-1)-
BT2.^-(1+2*alpha2_5))+...
% mu3_5*(BT2.^(alpha3_5-1)-BT2.^-(1+2*alpha3_5))+mu4_5*(BT2.^(alpha4_5-1)-BT2.^-
(1+2*alpha4_5))+...
% mu5_5*(BT2.^(alpha5_5-1)-BT2.^-(1+2*alpha5_5))+mu6_5*(BT2.^(alpha6_5-1)-BT2.^-
(1+2*alpha6_5))+...
% mu7_5*(BT2.^(alpha7_5-1)-BT2.^-(1+2*alpha7_5))+mu8_5*(BT2.^(alpha8_5-1)-BT2.^-
(1+2*alpha8_5));
%
% % plot Ogden (Matlab curve fit) and input data (pure shear)
% figure(7)
% subplot(2,2,1)
% plot(PT(:,1),PT(:,2),'r',PT(:,1),StressOctave8,'g')
% title('Stress strain curve')
% xlabel('Strain')
% ylabel('Stress')
% legend('AXEL data - planar tension (pure shear)','Ogden model, coefficients calculated in Matlab')
%
% subplot(2,2,2)
% plot(ST(:,1),ST(:,2),'r',ST(:,1),Simple_tension8,'g')
% title('Stress strain curve')
% xlabel('Strain')
% ylabel('Stress')
% legend('AXEL data - simple tension','Ogden model, coefficients calculated in Matlab')
%
% subplot(2,2,3)
```

```
% plot(SC(:,1),SC(:,2),'r',SC(:,1),Simple_compression8,'g')
% title('Stress strain curve')
% xlabel('Strain')
% ylabel('Stress')
% legend('AXEL data - simple compression','Ogden model, coefficients calculated in Matlab')
%
% subplot(2,2,4)
% plot(BT(:,1),BT(:,2),'r',BT(:,1),Radial_stress8,'g')
% title('Stress strain curve')
% xlabel('Strain')
% ylabel('Stress')
% legend('AXEL data - equibiaxial tension','Ogden model, coefficients calculated in Matlab')

%%%%%%%%%%%%%%%%%%%%%%%%%%%%%%%%%%%%%%%%%%%%%%%%%%%%
%%%%%%%%%%%%%%%%%%%%%%%%%%%%%%%%%%%%%%%%%%%%%%%%%%%%

% generalized Ogden model coefficient identifier

% how many terms?
n=8; % eight terms (16 coefficients)

% Initialize coeff vector for finding Ogden coeff.
for i=1:1:n
coeffGuessn(i)=0.0005; % initial guess
end

for i=n+1:1:2*n
coeffGuessn(i)=1;
end

coeffGuessn=[0.001430401833915,0.000984372703989,-
0.001111333343152,0.001509515368452,0.000750418628958,0.000036961648425,0.000859486995073,0
.002028371017567,...
-0.730528305376716,-1.635323159935653,-2.208012055364714,1.008884805631591,-
1.496740689986303,5.656411001322061,0.975554388605357,0.759739009642598];

% coeffGuess8=goodcoeff8;
optionsn=optimset('MaxFunEvals',10^5,'MaxIter',10^5);
[goodcoeffn FVECn
exitflagn]=fminsearch(@(coeff)Ogdennth(coeff,n,PT,SC,ST,BT),coeffGuessn,optionsn)

% compute planar tension stress for Ogden model
Stress_pure_shearn=0;
for i=1:n
Stress_pure_shearn=Stress_pure_shearn+goodcoeffn(i)*(PT2.^(goodcoeffn(i+n)-1)-PT2.^-
(1+goodcoeffn(i+n)));
end

% compute simple compression stress for Ogden model
Simple_compressionn=0;
for i=1:n
Simple_compressionn=Simple_compressionn+goodcoeffn(i)*(SC2.^(goodcoeffn(i+n)-1)-SC2.^-
(1+0.5*goodcoeffn(i+n)));
end
```

```
% compute simple tension stress for Ogden model
Simple_tensionn=0;
for i=1:n
Simple_tensionn=Simple_tensionn+goodcoeffn(i)*(ST2.^(goodcoeffn(i+n)-1)-ST2.^-
(1+0.5*goodcoeffn(i+n)));
end

% calculate radial stress-strain from Ogden coefficients
Radial_stressn=0;
for i=1:n
Radial_stressn=Radial_stressn+goodcoeffn(i)*(BT2.^(goodcoeffn(i+n)-1)-BT2.^-(1+2*goodcoeffn(i+n)));
end

% plot Ogden (Matlab curve fit) and input data (pure shear)
figure(8)
subplot(2,2,1)
plot(PT(:,1),PT(:,2),'r',PT(:,1),Stress_pure_shearn,'g')
title('Stress strain curve')
xlabel('Strain')
ylabel('Stress')
legend('AXEL data - planar tension (pure shear)','Ogden model, coefficients calculated in Matlab')
grid on

subplot(2,2,2)
plot(ST(:,1),ST(:,2),'r',ST(:,1),Simple_tensionn,'g')
title('Stress strain curve')
xlabel('Strain')
ylabel('Stress')
legend('AXEL data - simple tension','Ogden model, coefficients calculated in Matlab')
grid on

subplot(2,2,3)
plot(SC(:,1),SC(:,2),'r',SC(:,1),Simple_compressionn,'g')
title('Stress strain curve')
xlabel('Strain')
ylabel('Stress')
legend('AXEL data - simple compression','Ogden model, coefficients calculated in Matlab')
grid on

subplot(2,2,4)
plot(BT(:,1),BT(:,2),'r',BT(:,1),Radial_stressn,'g')
title('Stress strain curve')
xlabel('Strain')
ylabel('Stress')
legend('AXEL data - equibiaxial tension','Ogden model, coefficients calculated in Matlab')
grid on

% OT metric for simple tension
for i=1:length(ST(:,2))
   if ST(i,2)==0
      if i>(length(ST)-3)
      ST(i,2)=(ST(i-1,2)+ST(i-2,2))/2;
      else
      ST(i,2)=(ST(i+1,2)+ST(i+2,2))/2;
      end
   end
end
```

```
OTmetric_simple_tension_n=1-1/length(ST(:,2))*sum(tanh(abs((Simple_tensionn-ST(:,2))./ST(:,2))))

% OT metric for simple compression
for i=1:length(SC(:,2))
   if SC(i,2)==0
      if i>(length(SC)-3)
      SC(i,2)=(SC(i-1,2)+SC(i-2,2))/2;
      else
      SC(i,2)=(ST(i+1,2)+SC(i+2,2))/2;
      end
   end
end
OTmetric_simple_compression_n=1-1/length(SC(:,2))*sum(tanh(abs((Simple_compressionn-
SC(:,2))./SC(:,2))))

% OT metric for planar tension (pure shear)
for i=1:length(PT(:,2))
   if PT(i,2)==0
      if i>(length(PT)-3)
      PT(i,2)=(PT(i-1,2)+PT(i-2,2))/2;
      else
      PT(i,2)=(ST(i+1,2)+PT(i+2,2))/2;
      end
   end
end
OTmetric_pure_shear_n=1-1/length(PT(:,2))*sum(tanh(abs((Stress_pure_shearn-PT(:,2))./PT(:,2))))

% OT metric for equibiaxial tension
for i=1:length(BT(:,2))
   if BT(i,2)==0
      if i>(length(BT)-3)
      BT(i,2)=(BT(i-1,2)+BT(i-2,2))/2;
      else
      BT(i,2)=(BT(i+1,2)+BT(i+2,2))/2;
      end
   end
end
OTmetric_equibiaxial_tension_n=1-1/length(BT(:,2))*sum(tanh(abs((Radial_stressn-BT(:,2))./BT(:,2))))

% identify optimal initial guess for finding `n` Ogden coefficients
% [goodcoeffn_ig FVECn_ig
exitflagn_ig]=fminsearch(@(guess1)OgdenInitialGuess(guess1,n,PT,SC,ST,BT,optionsn),goodcoeffn)
```

Appendix C

MATLAB/Octave function used with a minimization function (in the previous script) to determine Ogden material model coefficients

```
function errmetric=Ogdennth(coeff,n,PT,SC,ST,BT)

% n is the desired number of terms for the Ogden model

% this function is fed to the Matlab function fminsearch to minimize 'err metric'
% fminunc in Octave may also work

% read in planar tension (pure shear) AXEL data
% PT=dlmread('ChryslerC0EPT0.01Cleaned.txt');
% PT(:,2)=PT(:,2)/1000; % convert MPa to GPa
PT2=PT(:,1)+1; % calculate stretch ratio from engineering strain

% import simple compression AXEL data
% SC=dlmread('set2_compression.csv');
SC2=SC(:,1)+1; % calculate stretch ratio from strain

% import AXEL simple tension results
% ST=dlmread('set2_tension.csv');
ST2(:,1)=ST(:,1)+1; % convert strain to stretch ratio

% import biaxial tension AXEL data
% BT=dlmread('ChryslerC0EBT0.01Cleaned.txt');
BT2=BT(:,1)+1; % calculate stretch ratio from engineering strain
% BT(:,2)=BT(:,2)/1000; % convert MPa to GPa

% optimization function only accepts one input but it can be a vector
% de-vectorize Ogden material parameters:
% mu1=coeff(1);
% mu8=coeff(8);
% alpha1=coeff(9);
% alpha8=coeff(16);
% this is just sort of notes to make the following easier, vestigial from
% when this function had a specific version to get a specific number of
% terms for the Ogden model

% compute planar tension stress for Ogden model
Stress_pure_shear=0;
for i=1:n
Stress_pure_shear=Stress_pure_shear+coeff(i)*(PT2.^(coeff(i+n)-1)-PT2.^-(1+coeff(i+n)));
end

% compute simple compression stress for Ogden model
Simple_compression=0;
for i=1:n
```

```
Simple_compression=Simple_compression+coeff(i)*(SC2.^(coeff(i+n)-1)-SC2.^-(1+0.5*coeff(i+n)));
end

% compute simple tension stress for Ogden model
Simple_tension=0;
for i=1:n
Simple_tension=Simple_tension+coeff(i)*(ST2.^(coeff(i+n)-1)-ST2.^-(1+0.5*coeff(i+n)));
end

% calculate radial stress-strain from Ogden coefficients
Radial_stress=0;
for i=1:n
Radial_stress=Radial_stress+coeff(i)*(BT2.^(coeff(i+n)-1)-BT2.^-(1+2*coeff(i+n)));
end

% least squares error metric
% if coeff>0
errmetric=4*sum(abs(Stress_pure_shear-PT(:,2)))+2*sum(abs(Simple_compression-
SC(:,2)))+sum(abs(Simple_tension-ST(:,2)))+...
4*sum(abs(Radial_stress-BT(:,2)))+...
4*sum((Stress_pure_shear-PT(:,2)).^2)+2*sum((Simple_compression-SC(:,2)).^2)+sum((Simple_tension-
ST(:,2)).^2)+...
4*sum((Radial_stress-BT(:,2)).^2);
% else errmetric=10*(4*sum(abs(Stress_pure_shear-PT(:,2)))+2*sum(abs(Simple_compression-
SC(:,2)))+sum(abs(Simple_tension-ST(:,2)))+...
% 4*sum(abs(Radial_stress-BT(:,2)))+...
% 4*sum((Stress_pure_shear-PT(:,2)).^2)+2*sum((Simple_compression-
SC(:,2)).^2)+sum((Simple_tension-ST(:,2)).^2)+...
% 4*sum((Radial_stress-BT(:,2)).^2));
% end
```

Appendix D

Summary of material characterization models parametric studies – sorted by validation metric

Element Type	Material Characterization Process	Material Model	Element Formulation	Element Size (mm)	Validation Metric	CPU Time (min)
Tetrahedron	Simple compression	MAT 181	10	2	0.98387	3
Tetrahedron	Simple compression	MAT 181	13	2	0.98364	3
Tetrahedron	Simple compression	MAT 181	4	2	0.98267	14
Tetrahedron	Simple tension	MAT 181	16	2.5	0.98041	32
Hexahedron	Simple tension	MAT 181	1	1	0.98008	12
Hexahedron	Simple tension	MAT 181	2	1	0.97986	68
Tetrahedron	Simple tension	MAT 181	10	1	0.97893	48
Tetrahedron	Simple tension	MAT 181	13	2.5	0.97674	7
Tetrahedron	Simple tension	MAT 181	13	1	0.97665	54
Tetrahedron	Simple compression	MAT 181	13	5	0.97613	0.117
Hexahedron	Simple compression	MAT 181	2	5	0.97548	0.167
Tetrahedron	Simple compression	MAT 181	4	5	0.97494	0.417
Tetrahedron	Simple compression	MAT 181	10	5	0.97456	0.117
Tetrahedron	Simple tension	MAT 181	10	2.5	0.96868	3
Tetrahedron	Equibiaxial tension	MAT 181	4	2	0.964	26
Hexahedron	Equibiaxial tension	MAT 181	3	2	0.96035	8
Tetrahedron	Equibiaxial tension	MAT 181	10	2	0.95785	5
Tetrahedron	Simple tension	MAT 181	16	1	0.95305	301
Hexahedron	Simple compression	MAT 181	3	2	0.95116	9
Tetrahedron	Equibiaxial tension	MAT 181	10	1	0.951	60
Tetrahedron	Simple tension	MAT 181	4	1	0.95019	30

Hexahedron	Simple compression	MAT 181	2	2	0.9496	2
Tetrahedron	Planar tension	MAT 77O 8 terms	16	1.25	0.94784	50
Tetrahedron	Equibiaxial tension	MAT 181	10	0.5	0.94681	690
Tetrahedron	Equibiaxial tension	MAT 181	13	1	0.93734	60
Hexahedron	Simple compression	MAT 181	3	5	0.93275	0.433
Tetrahedron	Equibiaxial tension	MAT 181	13	2	0.93272	5
Tetrahedron	Simple tension	MAT 181	4	2.5	0.9323	7
Hexahedron	Simple tension	MAT 181	3	1	0.92681	51
Hexahedron	Equibiaxial tension	MAT 181	2	0.5	0.92599	720
Hexahedron	Equibiaxial tension	MAT 181	1	0.5	0.9256	120
Hexahedron	Equibiaxial tension	MAT 181	3	0.5	0.92555	1800
Hexahedron	Equibiaxial tension	MAT 181	2	2	0.9246	4
Tetrahedron	Equibiaxial tension	MAT 181	13	0.5	0.924	690
Hexahedron	Equibiaxial tension	MAT 181	2	1	0.91616	43
Hexahedron	Planar tension	MAT 77O 8 terms	1	0.625	0.91562	2
Hexahedron	Equibiaxial tension	MAT 181	1	1	0.91518	8
Hexahedron	Planar tension	MAT 77O 8 terms	1	0.3125	0.91437	40
Hexahedron	Planar tension	MAT 77O 8 terms	2	0.625	0.91433	11
Hexahedron	Planar tension	MAT 77O 8 terms	41	0.3125	0.91288	300
Hexahedron	Equibiaxial tension	MAT 181	3	1	0.91222	80
Tetrahedron	Simple tension	MAT 77O 8 terms	10	2.5	0.90729	0.383
Tetrahedron	Simple tension	MAT 77O 8 terms	13	2.5	0.90729	0.417
Hexahedron	Simple tension	MAT 77O 6 terms	1	1	0.90454	4.333
Hexahedron	Planar tension	MAT 77O 8 terms	3	0.3125	0.90409	960
Tetrahedron	Simple tension	MAT 77O 6 terms	16	1	0.90383	330
Tetrahedron	Simple tension	MAT 77O 8 terms	16	1	0.90365	89
Tetrahedron	Simple tension	MAT 77O 8 terms	16	2.5	0.90319	3.6
Tetrahedron	Simple tension	MAT 77O 8 terms	13	1	0.90287	9.8
Tetrahedron	Simple tension	MAT 77O 8 terms	10	1	0.90274	7
Hexahedron	Planar tension	MAT 77O 8 terms	41	0.625	0.90024	14
Tetrahedron	Simple tension	MAT 77O 6 terms	10	2.5	0.89845	1
Tetrahedron	Simple tension	MAT 77O 6 terms	13	2.5	0.89845	1
Hexahedron	Planar tension	MAT 77O 8 terms	2	1.25	0.8963	0.75
Tetrahedron	Planar tension	MAT 77O 8 terms	10	0.625	0.89565	195
Tetrahedron	Planar tension	MAT 77O 8 terms	13	0.3125	0.89565	195

Hexahedron	Equibiaxial tension	MAT 77O 8 terms	3	2	0.89381	1.45
Tetrahedron	Equibiaxial tension	MAT 77O 8 terms	13	2	0.89367	1.9
Tetrahedron	Equibiaxial tension	MAT 77O 8 terms	10	2	0.89366	1.867
Hexahedron	Planar tension	MAT 77O 8 terms	1	2.5	0.89325	0
Tetrahedron	Simple tension	MAT 77O 6 terms	10	1	0.89264	9
Tetrahedron	Simple tension	MAT 77O 6 terms	13	1	0.89264	9
Hexahedron	Equibiaxial tension	MAT 181	1	2	0.89263	1
Hexahedron	Equibiaxial tension	MAT 77O 8 terms	41	2	0.8925	3
Hexahedron	Simple tension	MAT 77O 8 terms	1	1	0.89173	4.633
Tetrahedron	Equibiaxial tension	MAT 77O 8 terms	10	1	0.89115	20
Tetrahedron	Equibiaxial tension	MAT 77O 8 terms	13	1	0.89115	20
Hexahedron	Simple tension	MAT 77O 8 terms	41	1	0.89105	0.867
Hexahedron	Simple tension	MAT 77O 8 terms	3	1	0.88978	72
Tetrahedron	Simple tension	MAT 77O 6 terms	16	2.5	0.88319	8
Tetrahedron	Simple compression	MAT 77O 8 terms	10	2	0.87854	0.933
Tetrahedron	Simple compression	MAT 77O 8 terms	13	2	0.87854	0.95
Hexahedron	Simple compression	MAT 181	1	2	0.8697	0.917
Tetrahedron	Equibiaxial tension	MAT 181	4	1	0.86856	372
Hexahedron	Simple compression	MAT 77O 8 terms	2	5	0.86772	0.083
Hexahedron	Simple compression	MAT 77O 8 terms	41	5	0.86758	0.117
Tetrahedron	Simple compression	MAT 77O 8 terms	13	5	0.86737	0.033
Tetrahedron	Equibiaxial tension	MAT 77O 8 terms	10	0.5	0.86354	240
Tetrahedron	Equibiaxial tension	MAT 77O 8 terms	13	0.5	0.86354	240
Hexahedron	Planar tension	MAT 181	2	1.25	0.85958	19
Tetrahedron	Planar tension	MAT 77O 6 terms	13	0.625	0.85893	150
Hexahedron	Equibiaxial tension	MAT 77O 8 terms	3	0.5	0.85815	675
Hexahedron	Equibiaxial tension	MAT 77O 8 terms	1	0.5	0.85569	46
Hexahedron	Equibiaxial tension	MAT 77O 8 terms	3	1	0.85467	62
Hexahedron	Simple compression	MAT 181	1	5	0.85099	0.133
Hexahedron	Planar tension	MAT 77O 8 terms	1	1.25	0.84575	0.1
Hexahedron	Simple tension	MAT 181	2	2.5	0.8428	1
Hexahedron	Equibiaxial tension	MAT 77O 8 terms	1	1	0.84165	3.35

Hexahedron	Equibiaxial tension	MAT 77O 6 terms	2	1	0.82534	3.5
Hexahedron	Planar tension	MAT 77O 6 terms	2	1.25	0.82534	210
Hexahedron	Planar tension	MAT 77O 8 terms	3	0.625	0.82117	27
Hexahedron	Planar tension	MAT 181	2	0.625	0.81518	214
Hexahedron	Planar tension	MAT 181	1	0.625	0.81389	20
Hexahedron	Planar tension	MAT 77O 6 terms	1	0.625	0.80645	10
Hexahedron	Equibiaxial tension	MAT 77O 6 terms	1	0.5	0.80645	10
Hexahedron	Planar tension	MAT 77O 6 terms	2	0.625	0.80546	40
Hexahedron	Equibiaxial tension	MAT 77O 6 terms	2	0.5	0.80546	40
Hexahedron	Planar tension	MAT 181	1	0.3125	0.80375	480
Hexahedron	Planar tension	MAT 77O 6 terms	1	0.3125	0.80106	50
Hexahedron	Planar tension	MAT 181	2	0.3125	0.79853	2400
Hexahedron	Planar tension	MAT 181	1	1.25	0.79286	5
Tetrahedron	Simple compression	MAT 77O 6 terms	10	2	0.79086	1
Tetrahedron	Simple compression	MAT 77O 6 terms	13	2	0.79086	1
Hexahedron	Simple compression	MAT 77O 8 terms	3	2	0.78655	5
Tetrahedron	Planar tension	MAT 77O 6 terms	13	0.3125	0.78443	440
Tetrahedron	Simple compression	MAT 77O 6 terms	10	5	0.7813	0.033
Tetrahedron	Simple compression	MAT 77O 6 terms	13	5	0.7813	0.033
Hexahedron	Simple compression	MAT 77O 6 terms	2*	5	0.78126	0.1
Hexahedron	Planar tension	MAT 77O 6 terms	1	1.25	0.77759	0.667
Hexahedron	Equibiaxial tension	MAT 77O 6 terms	1	1	0.77759	0.667
Tetrahedron	Equibiaxial tension	MAT 77O 6 terms	10	1	0.7742	23
Tetrahedron	Equibiaxial tension	MAT 77O 6 terms	13	1	0.7742	23
Tetrahedron	Equibiaxial tension	MAT 77O 6 terms	4	1	0.77165	110
Tetrahedron	Equibiaxial tension	MAT 77O 6 terms	10	2	0.76822	2
Tetrahedron	Equibiaxial tension	MAT 77O 6 terms	13	2	0.76822	2
Hexahedron	Planar tension	MAT 77O 6 terms	3	0.3125	0.76392	1680
Tetrahedron	Equibiaxial tension	MAT 77O 6 terms	10	0.5	0.7637	300
Tetrahedron	Equibiaxial tension	MAT 77O 6 terms	13	0.5	0.7637	300
Tetrahedron	Equibiaxial tension	MAT 77O 6 terms	4	0.5	0.75998	690
Tetrahedron	Planar tension	MAT 77O 6 terms	10	0.3125	0.75453	240

Tetrahedron	Planar tension	MAT 77O 6 terms	13	0.3125	0.75453	240
Hexahedron	Planar tension	MAT 77O 6 terms	1	2.5	0.72622	0
Hexahedron	Equibiaxial tension	MAT 77O 6 terms	1	2	0.72622	0
Hexahedron	Planar tension	MAT 181	3	0.3125	0.71481	7200
Hexahedron	Planar tension	MAT 181	1	2.5	0.71154	0.3
Hexahedron	Planar tension	MAT 77O 8 terms	41	1.25	0.69281	0.95
Tetrahedron	Planar tension	MAT 77O 8 terms	10	0.625	0.67445	9
Tetrahedron	Planar tension	MAT 77O 8 terms	13	0.625	0.67445	9
Hexahedron	Planar tension	MAT 77O 6 terms	3	0.625	0.65614	130
Hexahedron	Equibiaxial tension	MAT 77O 6 terms	3	0.5	0.65614	130
Hexahedron	Simple tension	MAT 181	1	2.5	0.61712	0.3
Tetrahedron	Planar tension	MAT 77O 8 terms	16	2.5	0.59701	0.4
Tetrahedron	Equibiaxial tension	MAT 77O 8 terms	16	1	0.59326	185
Tetrahedron	Planar tension	MAT 77O 6 terms	10	0.625	0.51901	43
Tetrahedron	Planar tension	MAT 77O 6 terms	13	0.625	0.51901	43
Hexahedron	Planar tension	MAT 77O 8 terms	2	2.5	0.5083	0.05
Hexahedron	Simple tension	MAT 181	3	2.5	0.50203	2.3
Hexahedron	Equibiaxial tension	MAT 77O 8 terms	2	2	0.49997	15
Tetrahedron	Equibiaxial tension	MAT 181	16	1	0.4926	7200
Hexahedron	Planar tension	MAT 77O 6 terms	2	2.5	0.47143	0.333
Hexahedron	Equibiaxial tension	MAT 77O 6 terms	2	2	0.47143	0.333
Tetrahedron	Equibiaxial tension	MAT 77O 8 terms	16	2	0.44216	15.25
Hexahedron	Planar tension	MAT 181	3	0.625	0.43938	337
Hexahedron	Equibiaxial tension	MAT 77O 8 terms	1	2	0.42099	2.3
Tetrahedron	Planar tension	MAT 77O 6 terms	4	0.3125	0.41877	3600
Tetrahedron	Equibiaxial tension	MAT 181	16	2	0.40952	52
Hexahedron	Planar tension	MAT 181	2	2.5	0.31677	2
Tetrahedron	Planar tension	MAT 77O 6 terms	10	0.3125	0.18182	440
Hexahedron	Planar tension	MAT 181	3	1.25	0.10673	86
Tetrahedron	Planar tension	MAT 77O 8 terms	10	1.25	0.09239	1
Tetrahedron	Planar tension	MAT 77O 8 terms	13	1.25	0.09238	1
Tetrahedron	Planar tension	MAT 77O 6 terms	10	1.25	0.05571	5
Tetrahedron	Planar tension	MAT 77O 6 terms	13	1.25	0.05571	5
Tetrahedron	Planar tension	MAT 77O 6 terms	10	0.625	0.001	150
Tetrahedron	Planar tension	MAT 77O 8 terms	10	2.5	0	0.067
Tetrahedron	Planar tension	MAT 77O 8 terms	13	2.5	0	0.167

Hexahedron	Simple tension	MAT 77O 6 terms	1	2.5	0	0.3
Tetrahedron	Planar tension	MAT 77O 6 terms	10	2.5	0	0.333
Tetrahedron	Planar tension	MAT 77O 6 terms	13	2.5	0	0.833
Hexahedron	Planar tension	MAT 181	3	2.5	0	6
Tetrahedron	Simple tension	MAT 77O 6 terms	4	1	0	-
Hexahedron	Simple tension	MAT 77O 6 terms	2	2.5	0	-
Hexahedron	Simple tension	MAT 77O 6 terms	3	2.5	0	-
Hexahedron	Simple tension	MAT 77O 6 terms	2	1	0	-
Hexahedron	Simple tension	MAT 77O 6 terms	3	1	0	-
Tetrahedron	Simple tension	MAT 77O 6 terms	4	2.5	0	-
Hexahedron	Planar tension	MAT 77O 6 terms	3	2.5	0	-
Hexahedron	Planar tension	MAT 77O 6 terms	3	1.25	0	-
Hexahedron	Planar tension	MAT 77O 6 terms	2	0.3125	0	-
Tetrahedron	Planar tension	MAT 77O 6 terms	4	2.5	0	-
Tetrahedron	Planar tension	MAT 77O 6 terms	4	1.25	0	-
Tetrahedron	Planar tension	MAT 77O 6 terms	4	0.625	0	-
Tetrahedron	Planar tension	MAT 77O 6 terms	4	0.3125	0	-
Tetrahedron	Equibiaxial tension	MAT 181	4	0.5	0	-
Hexahedron	Equibiaxial tension	MAT 77O 6 terms	3	2	0	-
Hexahedron	Equibiaxial tension	MAT 77O 6 terms	3	1	0	-
Tetrahedron	Equibiaxial tension	MAT 77O 6 terms	4	2	0	-

Appendix E

Summary of material characterization models parametric studies – sorted by CPU time

Element Type	Material Characterization Process	Material Model	Element Formulation	Element Size (mm)	Validation Metric	CPU Time (min)
Hexahedron	Planar tension	MAT 77O 8 terms	1	2.5	0.89325	0
Hexahedron	Planar tension	MAT 77O 6 terms	1	2.5	0.72622	0
Hexahedron	Equibiaxial tension	MAT 77O 6 terms	1	2	0.72622	0
Tetrahedron	Simple compression	MAT 77O 8 terms	13	5	0.86737	0.033
Tetrahedron	Simple compression	MAT 77O 6 terms	10	5	0.7813	0.033
Tetrahedron	Simple compression	MAT 77O 6 terms	13	5	0.7813	0.033
Hexahedron	Planar tension	MAT 77O 8 terms	2	2.5	0.5083	0.05
Tetrahedron	Planar tension	MAT 77O 8 terms	10	2.5	0	0.067
Hexahedron	Simple compression	MAT 77O 8 terms	2	5	0.86772	0.083
Hexahedron	Planar tension	MAT 77O 8 terms	1	1.25	0.84575	0.1
Hexahedron	Simple compression	MAT 77O 6 terms	2*	5	0.78126	0.1
Tetrahedron	Simple compression	MAT 181	13	5	0.97613	0.117
Tetrahedron	Simple	MAT 181	10	5	0.97456	0.117
Hexahedron	Simple compression	MAT 77O 8 terms	41	5	0.86758	0.117
Hexahedron	Simple compression	MAT 181	1	5	0.85099	0.133
Hexahedron	Simple compression	MAT 181	2	5	0.97548	0.167

Tetrahedron	Planar tension	MAT 77O 8 terms	13	2.5	0	0.167
Hexahedron	Planar tension	MAT 181	1	2.5	0.71154	0.3
Hexahedron	Simple tension	MAT 181	1	2.5	0.61712	0.3
Hexahedron	Simple tension	MAT 77O 6 terms	1	2.5	0	0.3
Hexahedron	Planar tension	MAT 77O 6 terms	2	2.5	0.47143	0.333
Hexahedron	Equibiaxial tension	MAT 77O 6 terms	2	2	0.47143	0.333
Tetrahedron	Planar tension	MAT 77O 6 terms	10	2.5	0	0.333
Tetrahedron	Simple tension	MAT 77O 8 terms	10	2.5	0.90729	0.383
Tetrahedron	Planar tension	MAT 77O 8 terms	16	2.5	0.59701	0.4
Tetrahedron	Simple compression	MAT 181	4	5	0.97494	0.417
Tetrahedron	Simple tension	MAT 77O 8 terms	13	2.5	0.90729	0.417
Hexahedron	Simple compression	MAT 181	3	5	0.93275	0.433
Hexahedron	Planar tension	MAT 77O 6 terms	1	1.25	0.77759	0.667
Hexahedron	Equibiaxial tension	MAT 77O 6 terms	1	1	0.77759	0.667
Hexahedron	Planar tension	MAT 77O 8 terms	2	1.25	0.8963	0.75
Tetrahedron	Planar tension	MAT 77O 6 terms	13	2.5	0	0.833
Hexahedron	Simple tension	MAT 77O 8 terms	41	1	0.89105	0.867
Hexahedron	Simple compression	MAT 181	1	2	0.8697	0.917
Tetrahedron	Simple compression	MAT 77O 8 terms	10	2	0.87854	0.933
Tetrahedron	Simple compression	MAT 77O 8 terms	13	2	0.87854	0.95
Hexahedron	Planar tension	MAT 77O 8 terms	41	1.25	0.69281	0.95
Tetrahedron	Simple tension	MAT 77O 6 terms	10	2.5	0.89845	1
Tetrahedron	Simple tension	MAT 77O 6 terms	13	2.5	0.89845	1

Hexahedron	Equibiaxial tension	MAT 181	1	2	0.89263	1
Hexahedron	Simple tension	MAT 181	2	2.5	0.8428	1
Tetrahedron	Simple compression	MAT 77O 6 terms	10	2	0.79086	1
Tetrahedron	Simple compression	MAT 77O 6 terms	13	2	0.79086	1
Tetrahedron	Planar tension	MAT 77O 8 terms	10	1.25	0.09239	1
Tetrahedron	Planar tension	MAT 77O 8 terms	13	1.25	0.09238	1
Hexahedron	Equibiaxial tension	MAT 77O 8 terms	3	2	0.89381	1.45
Tetrahedron	Equibiaxial tension	MAT 77O 8 terms	10	2	0.89366	1.867
Tetrahedron	Equibiaxial tension	MAT 77O 8 terms	13	2	0.89367	1.9
Hexahedron	Simple compression	MAT 181	2	2	0.9496	2
Hexahedron	Planar tension	MAT 77O 8 terms	1	0.625	0.91562	2
Tetrahedron	Equibiaxial tension	MAT 77O 6 terms	10	2	0.76822	2
Tetrahedron	Equibiaxial tension	MAT 77O 6 terms	13	2	0.76822	2
Hexahedron	Planar tension	MAT 181	2	2.5	0.31677	2
Hexahedron	Simple tension	MAT 181	3	2.5	0.50203	2.3
Hexahedron	Equibiaxial tension	MAT 77O 8 terms	1	2	0.42099	2.3
Tetrahedron	Simple compression	MAT 181	10	2	0.98387	3
Tetrahedron	Simple compression	MAT 181	13	2	0.98364	3
Tetrahedron	Simple tension	MAT 181	10	2.5	0.96868	3
Hexahedron	Equibiaxial tension	MAT 77O 8 terms	41	2	0.8925	3
Hexahedron	Equibiaxial tension	MAT 77O 8 terms	1	1	0.84165	3.35
Hexahedron	Equibiaxial tension	MAT 77O 6 terms	2	1	0.82534	3.5
Tetrahedron	Simple tension	MAT 77O 8 terms	16	2.5	0.90319	3.6
Hexahedron	Equibiaxial tension	MAT 181	2	2	0.9246	4
Hexahedron	Simple tension	MAT 77O 6 terms	1	1	0.90454	4.333

Hexahedron	Simple tension	MAT 77O 8 terms	1	1	0.89173	4.633
Tetrahedron	Equibiaxial tension	MAT 181	10	2	0.95785	5
Tetrahedron	Equibiaxial tension	MAT 181	13	2	0.93272	5
Hexahedron	Planar tension	MAT 181	1	1.25	0.79286	5
Hexahedron	Simple compression	MAT 77O 8 terms	3	2	0.78655	5
Tetrahedron	Planar tension	MAT 77O 6 terms	10	1.25	0.05571	5
Tetrahedron	Planar tension	MAT 77O 6 terms	13	1.25	0.05571	5
Hexahedron	Planar tension	MAT 181	3	2.5	0	6
Tetrahedron	Simple tension	MAT 181	13	2.5	0.97674	7
Tetrahedron	Simple tension	MAT 181	4	2.5	0.9323	7
Tetrahedron	Simple tension	MAT 77O 8 terms	10	1	0.90274	7
Hexahedron	Equibiaxial tension	MAT 181	3	2	0.96035	8
Hexahedron	Equibiaxial tension	MAT 181	1	1	0.91518	8
Tetrahedron	Simple tension	MAT 77O 6 terms	16	2.5	0.88319	8
Hexahedron	Simple compression	MAT 181	3	2	0.95116	9
Tetrahedron	Simple tension	MAT 77O 6 terms	10	1	0.89264	9
Tetrahedron	Simple tension	MAT 77O 6 terms	13	1	0.89264	9
Tetrahedron	Planar tension	MAT 77O 8 terms	10	0.625	0.67445	9
Tetrahedron	Planar tension	MAT 77O 8 terms	13	0.625	0.67445	9
Tetrahedron	Simple tension	MAT 77O 8 terms	13	1	0.90287	9.8
Hexahedron	Planar tension	MAT 77O 6 terms	1	0.625	0.80645	10
Hexahedron	Equibiaxial tension	MAT 77O 6 terms	1	0.5	0.80645	10
Hexahedron	Planar tension	MAT 77O 8 terms	2	0.625	0.91433	11
Hexahedron	Simple tension	MAT 181	1	1	0.98008	12
Tetrahedron	Simple compression	MAT 181	4	2	0.98267	14
Hexahedron	Planar tension	MAT 77O 8 terms	41	0.625	0.90024	14

Hexahedron	Equibiaxial tension	MAT 77O 8 terms	2	2	0.49997	15
Tetrahedron	Equibiaxial tension	MAT 77O 8 terms	16	2	0.44216	15.25
Hexahedron	Planar tension	MAT 181	2	1.25	0.85958	19
Tetrahedron	Equibiaxial tension	MAT 77O 8 terms	10	1	0.89115	20
Tetrahedron	Equibiaxial tension	MAT 77O 8 terms	13	1	0.89115	20
Hexahedron	Planar tension	MAT 181	1	0.625	0.81389	20
Tetrahedron	Equibiaxial tension	MAT 77O 6 terms	10	1	0.7742	23
Tetrahedron	Equibiaxial tension	MAT 77O 6 terms	13	1	0.7742	23
Tetrahedron	Equibiaxial tension	MAT 181	4	2	0.964	26
Hexahedron	Planar tension	MAT 77O 8 terms	3	0.625	0.82117	27
Tetrahedron	Simple tension	MAT 181	4	1	0.95019	30
Tetrahedron	Simple tension	MAT 181	16	2.5	0.98041	32
Hexahedron	Planar tension	MAT 77O 8 terms	1	0.3125	0.91437	40
Hexahedron	Planar tension	MAT 77O 6 terms	2	0.625	0.80546	40
Hexahedron	Equibiaxial tension	MAT 77O 6 terms	2	0.5	0.80546	40
Hexahedron	Equibiaxial tension	MAT 181	2	1	0.91616	43
Tetrahedron	Planar tension	MAT 77O 6 terms	10	0.625	0.51901	43
Tetrahedron	Planar tension	MAT 77O 6 terms	13	0.625	0.51901	43
Hexahedron	Equibiaxial tension	MAT 77O 8 terms	1	0.5	0.85569	46
Tetrahedron	Simple tension	MAT 181	10	1	0.97893	48
Tetrahedron	Planar tension	MAT 77O 8 terms	16	1.25	0.94784	50
Hexahedron	Planar tension	MAT 77O 6 terms	1	0.3125	0.80106	50
Hexahedron	Simple tension	MAT 181	3	1	0.92681	51
Tetrahedron	Equibiaxial tension	MAT 181	16	2	0.40952	52
Tetrahedron	Simple tension	MAT 181	13	1	0.97665	54
Tetrahedron	Equibiaxial tension	MAT 181	10	1	0.951	60
Tetrahedron	Equibiaxial tension	MAT 181	13	1	0.93734	60

Hexahedron	Equibiaxial tension	MAT 77O 8 terms	3	1	0.85467	62
Hexahedron	Simple tension	MAT 181	2	1	0.97986	68
Hexahedron	Simple tension	MAT 77O 8 terms	3	1	0.88978	72
Hexahedron	Equibiaxial tension	MAT 181	3	1	0.91222	80
Hexahedron	Planar tension	MAT 181	3	1.25	0.10673	86
Tetrahedron	Simple tension	MAT 77O 8 terms	16	1	0.90365	89
Tetrahedron	Equibiaxial tension	MAT 77O 6 terms	4	1	0.77165	110
Hexahedron	Equibiaxial tension	MAT 181	1	0.5	0.9256	120
Hexahedron	Planar tension	MAT 77O 6 terms	3	0.625	0.65614	130
Hexahedron	Equibiaxial tension	MAT 77O 6 terms	3	0.5	0.65614	130
Tetrahedron	Planar tension	MAT 77O 6 terms	13	0.625	0.85893	150
Tetrahedron	Planar tension	MAT 77O 6 terms	10	0.625	0.001	150
Tetrahedron	Equibiaxial tension	MAT 77O 8 terms	16	1	0.59326	185
Tetrahedron	Planar tension	MAT 77O 8 terms	10	0.625	0.89565	195
Tetrahedron	Planar tension	MAT 77O 8 terms	13	0.3125	0.89565	195
Hexahedron	Planar tension	MAT 77O 6 terms	2	1.25	0.82534	210
Hexahedron	Planar tension	MAT 181	2	0.625	0.81518	214
Tetrahedron	Equibiaxial tension	MAT 77O 8 terms	10	0.5	0.86354	240
Tetrahedron	Equibiaxial tension	MAT 77O 8 terms	13	0.5	0.86354	240
Tetrahedron	Planar tension	MAT 77O 6 terms	10	0.3125	0.75453	240
Tetrahedron	Planar tension	MAT 77O 6 terms	13	0.3125	0.75453	240
Hexahedron	Planar tension	MAT 77O 8 terms	41	0.3125	0.91288	300
Tetrahedron	Equibiaxial tension	MAT 77O 6 terms	10	0.5	0.7637	300
Tetrahedron	Equibiaxial tension	MAT 77O 6 terms	13	0.5	0.7637	300
Tetrahedron	Simple tension	MAT 181	16	1	0.95305	301

Tetrahedron	Simple tension	MAT 77O 6 terms	16	1	0.90383	330
Hexahedron	Planar tension	MAT 181	3	0.625	0.43938	337
Tetrahedron	Equibiaxial tension	MAT 181	4	1	0.86856	372
Tetrahedron	Planar tension	MAT 77O 6 terms	13	0.3125	0.78443	440
Tetrahedron	Planar tension	MAT 77O 6 terms	10	0.3125	0.18182	440
Hexahedron	Planar tension	MAT 181	1	0.3125	0.80375	480
Hexahedron	Equibiaxial tension	MAT 77O 8 terms	3	0.5	0.85815	675
Tetrahedron	Equibiaxial tension	MAT 181	10	0.5	0.94681	690
Tetrahedron	Equibiaxial tension	MAT 181	13	0.5	0.924	690
Tetrahedron	Equibiaxial tension	MAT 77O 6 terms	4	0.5	0.75998	690
Hexahedron	Equibiaxial tension	MAT 181	2	0.5	0.92599	720
Hexahedron	Planar tension	MAT 77O 8 terms	3	0.3125	0.90409	960
Hexahedron	Planar tension	MAT 77O 6 terms	3	0.3125	0.76392	1680
Hexahedron	Equibiaxial tension	MAT 181	3	0.5	0.92555	1800
Hexahedron	Planar tension	MAT 181	2	0.3125	0.79853	2400
Tetrahedron	Planar tension	MAT 77O 6 terms	4	0.3125	0.41877	3600
Hexahedron	Planar tension	MAT 181	3	0.3125	0.71481	7200
Tetrahedron	Equibiaxial tension	MAT 181	16	1	0.4926	7200
Tetrahedron	Simple tension	MAT 77O 6 terms	4	1	0	-
Hexahedron	Simple tension	MAT 77O 6 terms	2	2.5	0	-
Hexahedron	Simple tension	MAT 77O 6 terms	3	2.5	0	-
Hexahedron	Simple tension	MAT 77O 6 terms	2	1	0	-
Hexahedron	Simple tension	MAT 77O 6 terms	3	1	0	-
Tetrahedron	Simple tension	MAT 77O 6 terms	4	2.5	0	-
Hexahedron	Planar tension	MAT 77O 6 terms	3	2.5	0	-
Hexahedron	Planar tension	MAT 77O 6 terms	3	1.25	0	-

Hexahedron	Planar tension	MAT 77O 6 terms	2	0.3125	0	-
Tetrahedron	Planar tension	MAT 77O 6 terms	4	2.5	0	-
Tetrahedron	Planar tension	MAT 77O 6 terms	4	1.25	0	-
Tetrahedron	Planar tension	MAT 77O 6 terms	4	0.625	0	-
Tetrahedron	Planar tension	MAT 77O 6 terms	4	0.3125	0	-
Tetrahedron	Equibiaxial tension	MAT 181	4	0.5	0	-
Hexahedron	Equibiaxial tension	MAT 77O 6 terms	3	2	0	-
Hexahedron	Equibiaxial tension	MAT 77O 6 terms	3	1	0	-
Tetrahedron	Equibiaxial tension	MAT 77O 6 terms	4	2	0	-

Vita Auctoris

Name: Matthew Bondy

Place of Birth: Windsor, Ontario, Canada

Year of Birth: 1986

Education:

- St. Anne's High School
  2000 – 2004
- St. Clair College
  2005 – 2007
- University of Windsor
  2007 - 2012
- Politecnico di Torino
  2011 - 2012